Laboratory Study and Constitutive Model Development on Collapse and Torsional Shear Behaviour of Kaolin Under Hydro-Mechanical Loadings

Thesis submitted in the partial fulfilment of the requirements

for the award of the degree

of

Doctor of Philosophy

by

Ankti Srivastava

Roll no. 166104101

Indian Institute of Technology Guwahati

Department of Civil Engineering

July 2023

Certificate

This is to certify that the thesis, entitled **"Laboratory Study and Constitutive Model Development on Collapse and Torsional Shear Behaviour of Kaolin Under Hydro-Mechanical Loadings"**, being submitted by Mr. Ankti Srivastava, a research scholar in the Department of Civil Engineering, Indian Institute of Technology Guwahati, for the award of Doctor of Philosophy, is a record of original research work carried out by him under my supervision. The thesis work, in our opinion, has reached the standard, fulfilling the requirements for the said degree. Further, we certify that this submission is Mr. Ankti own work and that, to the best of our knowledge and belief, it contains no material previously published or written by another person which to a substantial extent, has been accepted for the award of any other degree or diploma of any University or Institute.

Dr. T.V. Bharat
Professor of Geotechnical Engineering
Department of Civil Engineering
IIT Guwahati
Guwahati-781039, India

Acknowledgement

At the very outset, I would like to express my heartfelt thanks and a deep sense of gratitude to my supervisor Prof. T.V. Bharat, for his meticulous guidance and support during my entire PhD study. During this entire PhD period, I have been fortunate enough to gain precious learning experiences with him. My gratitude is extended to the members of my Doctoral Committee, Prof. Arbind Kumar Singh, Dr. Abhishek Kumar Sharma, and Prof. Sachin Singh Gautam, for reviewing my work and providing their valuable inputs that helped in improving my thesis. I would also like to thank the other faculty members of Civil Engineering and other departments for providing me to credit several courses of my interests during my PhD period in which they provided an in-depth conceptual understanding of their specialized area. I thank all office staff members of the Civil Engineering Department for their cooperation in official work. I sincerely thank my fellow research scholars, friends, and colleagues of IIT Guwahati, whose generous help and support will always be remembered. I want to give special thanks to the other group members in my supervisor's lab, namely, Dr. Dhanesh Sing Das, Mr. Himanshu Yadav, and Dr. Partha Das, for all the support and productive discussions related to my research. I humbly thank Central Instruments Facility (IITG) staff and Biotech Park Facility (IITG) for allowing me to carry out various sample analyses when required. Lastly, I am extremely grateful to my parents for their unconditional love, encouragement, and endless support throughout the journey toward a PhD.

Abstract

Aeolian and kaolin deposits contribute to significant infrastructural damage during the rainy seasons due to massive collapse settlements. The stability of the engineering structures built on such soils depends on the volume change and shear strength characteristics of the underlying soil. A comprehensive study on wetting-induced collapse and large shear deformation behaviour is pivotal. However, majority of the existing laboratory studies on collapsible soils are carried out at near saturation state (i.e., optimum moisture conditions). And, only a limited number of laboratory studies are currently available to understand the deformation response of collapsible soils compacted at an initially lower degree of saturation (air-dry state) that simulate field conditions. This study investigated the compression, yielding, and collapse response of two different partially saturated compacted kaolin soils using suction-controlled compression experiments conducted in one-dimensional oedometer apparatus. The measured yielding data were validated against the well-known Basic Barcelona model (BBM). A significant discrepancy was found between the model and measured data. The reason for deviation was investigated from a microstructural perspective. The effect of particle orientation resulting from various initial compaction conditions, drying path, and wetting path on the yielding behaviour of soil was investigated. It was found that the initial clay fabric of compacted kaolin has a significant influence on its yielding behaviour.

Further, constitutive models are required for predicting the collapsible soil behaviour. Majority of the theoretical models utilize the wetting and drying behaviour of soils using the soil water characteristic curve (SWCC), which demands additional complex and time-consuming laboratory experiments to estimate the model parameters. Furthermore, the existing constitutive models are validated on soils at near saturation state only. Thus, in this

study, a general constitutive model was developed from the suction-controlled compression and wetting-induced collapse tests. A novel comprehensive model is proposed by considering the wetting-induced changes to the clay fabric associations in compacted soils. The proposed method was capable of predicting three crucial mechanical characteristics, viz., loading-collapse yield, compression, and collapse behaviour from the basic compression data at air-dry compaction state. The model shows excellent agreement with the measured data for two different kaolin soils from the present work and several collapsible soils from the literature studies. The generalized model predicts mechanical behaviour for all types of collapsible soils with various initial compaction states and loading stress history.

Apart from the collapse characteristics of clays, the shear strength response is also important for clays subjected to extensive shear deformation in the slope stability analysis. The normal stress, strain rate, and pore-fluid chemistry significantly influence the large-strain shear resistance of clays. The effect of inundation pressure, consolidation pressure, pH of aqueous solutions, and di-electric on the shear response of kaolin was experimentally investigated. The strain-softening behaviour was observed under normally consolidated (NC) conditions, similar to the past studies on different clays. However, this anomalous shear response with volumetric contraction is not understood. Thus, for the first time, the strain-softening behaviour of NC clays was addressed from an effective stress approach using physico-chemical analysis of kaolin. In this study, the drained shear strength response of NC kaolin was investigated under physico-chemical influence using ring shear tests. A theoretical framework was developed by including micro-mechanism of clay fabric evolution during shear and explicit expressions for electro-chemical forces. The proposed framework was used to estimate the shear resistance from the modified effective stress approach to interpret the experimental results. The proposed framework provides useful expressions for predicting the shear strength behaviour of kaolin clays, which were validated with

experimental data from the present study and literature studies. The new conceptual framework satisfactorily explained the peak and residual shear strength variations under different chemo-mechanical loading for NC conditions. The proposed model adequately predicted the effective stress paths, peak, and residual envelopes in ring shear stress conditions for normally consolidated kaolin soils.

Engineering intervention to minimize the subsidence of the surface under wetting condition is essential. The geopolymerization technique gained much attention over the last decade to enhance the mechanical performance of problematic clays. However, earlier research have not investigated the wetting-induced collapse potential in treated kaolin soils. The application of existing laboratory techniques for field application are complex, as the field mixing of alkali and maintaining the desired concentration is challenging. This work investigates the volume change behaviour of compacted kaolin treated with a sodium-based alkaline solution and activator as sodium silicate at different concentrations and inundation pressures. The treated kaolin samples were cured for eight days to improve mechanical characteristics. The cured samples were subjected to one-dimensional compression and inundation tests at different pressures in an oedometer set-up. The collapse potential of treated kaolin reduced significantly at optimal concentrations of alkali activator solution. Finally, a most effective, simple method was proposed based on laboratory procedure to apply in field to minimize collapse deformations.

Key Words: Collapsible soils, compression, mechanical behaviour, wetting, yield, shear strength, pore fluid chemistry, alkali solution, concentration.

Table of Contents

List of Figures

List of Tables

Abbreviations

AAMs	Alkali-activated materials
BBM	Barcelona basic model
BET	Brunauer-Emmett-Teller
CP	Collapse potential
ESV	Equilibrium sediment volume
IEP_{edge}	Isoelectric point of the edge
LC	Loading-collapse
MDD	Maximum dry density
MIP	Mercury intrusion porosimetry
MPK	Monash-Peradeniya-Kodikara
NC	Normally consolidated
OMC	Optimum moisture content
OPC	Ordinary Portland Cement
PSD	Pore size distribution
SBS	State boundary surface
SEM	Scanning electron microscope
SWRC	Soil water characteristics curve
UCS	Unconfined compressive strength
XRD	X-ray diffraction

Nomenclature

k_{sc}	Soaking gradient
$\kappa(0)$	Slope of the elastic re-compression line
$\lambda(0)$	Slope of virgin consolidation line
s	Suction (kPa)
$p_y(s)$	Yield stress with associated suction, s (kPa)
$p_y(0)$	Yield stress at saturated state (kPa)
A	Effective inter-particle attractive pressure (kPa)
R	Effective inter-particle repulsive pressure (kPa)
$\bar{\sigma}$	Mineral-to-mineral contact stress (kPa)
a_m	Fraction of total inter-particle area that is mineral to mineral contact (m^2)
σ'	Effective stress (kPa)
u_w	Effective pore water pressure (kPa)
u_a	Effective pore air pressure (kPa)
σ	External applied normal stress on a unit area (kPa)
e	Void ratio
ρ	Electrical surface charge density (C/m^2)
ρ_e	Electrical edge charge density (C/m^2)
t	Thickness of particle (m)
ε_o	Vacuum permittivity (F/m)
ε_r	Di-electric constant of pore medium
y	Distance between the particles (m)
F_{ff}	Electrostatic force of repulsion (N)

F_{ef}	Electrostatic force of attraction (N)
F_w	Van der Waals attractive pressure (N/m^2)
A_H	Hamaker's coefficient (ergs)
a_{eff}	Effective area of interaction (m^2)
α	Particle orientation angle
Q	Vertical applied load (kN)
c	Cohesion of soil (kPa)
K_p	Passive earth pressure coefficient

Chapter 1

Introduction

1.1 General

Partially saturated soils that go through particle re-arrangement and volume reduction due to wetting under constant mechanical load are called collapsible soils. Collapsible soils such as loess and kaolin are distributed worldwide, including China, India, Southern Europe, United States of America, Northern Russia, and South America (Lehmann et al. 2021). These soils show collapse (volume reduction) upon wetting due to rainfall infiltration at constant overburden pressure. Infrastructures built on collapsible soils have suffered substantial damage from collapse and other collapse-related problems such as differential settlement, ground subsidence, and landslides (Derbyshire, 2001; Li et al., 2016; Opukumo et al., 2022). The presence of loess (Jiang et al., 2012; Mu et al., 2022), kaolin (Sridharan et al., 1973; Wheeler & Sivakumar 1995; Thorel et al., 2011; Choudhury & Bharat, 2018), and laterites (Das & Thyagaraj, 2018; Rao & Revanasiddappa, 2002; Thyagaraj & Das, 2017) contribute to such wetting-induced collapse although the collapse mechanism is different in these soils (Choudhury & Bharat, 2018). The North-Eastern part of India consists of both laterite and kaolin deposits to a deeper depth, where damages due to subsidence are reported during various infrastructure development projects. A significantly high mean annual rainfall of 2000 mm further contributes to such damages frequently. The loss of economy due to subsidence problems is thus extremely high in the various part of the world with such geology during infrastructural development without engineering interventions (Vilar et al., 1981; Silveira & Rodrigues, 2020). Thus, comprehensive knowledge of wetting-induced collapse behaviour is pivotal.

The study of wetting-induced collapse potential and compressibility behaviour at different saturated states is essential for field applications. And most of the laboratory testing on the collapsible soils was carried out at near saturation state. Thus, only limited number of laboratory studies are currently available to understand the deformation response of collapsible soil compacted at an initially lower degree of saturation (air-dry state) that simulate natural field conditions.

In addition to past laboratory test studies, quick constitutive models are required for prediction of the behaviour. Thus, several constitutive models are developed to predict the mechanical response (i.e., volume change and shear strength) of clays under hydro-mechanical loadings. The majority of existing theoretical models utilize the soil wetting and drying behaviour by incorporating soil water characteristic curve (SWCC) parameters. This demands additional complex and time-consuming laboratory experiments to estimate model parameters from the observed SWCC data. Furthermore, these constitutive models are validated on soils that are initially compacted at an optimum moisture content (OMC) or high saturation state.

Apart from the volume change study, over the last few decades, there has been growing interest in the shear strength characteristics of kaolin soils subjected to extensive shear deformation for slope stability applications. The large-strain shear resistance of kaolin is the key parameter for the design and analysis of slopes that have undergone large shear deformation due to new and reactivated landslides (Skempton 1964, 1977; Gibo et al., 1987; Rahardjo et al., 1995; Timothy et al., 1997; Tiwari et al., 2005). Some of the available studies showed that the stability of the slip surface of both new and reactivated landslides strongly depends on the residual shear strength of the soil (Bishop et al., 1971; Mesri et al., 2003; Mesri & Sarihan 2012; Li et al., 2017). The minimal constant value of shear strength along the slip plane, in which the soil particles are reoriented and subjected to sufficiently large

displacements, is known as the residual shear strength of soil (Skempton 1964, 1985). Other studies showed that the residual shear resistance of active and non-active clays is mainly affected by the clay content, mineral composition, rate of shearing, and pore-fluid chemistry (Skempton 1985; Moore 1991; Mesri et al., 2003; Duong et al., 2018). Interestingly, some researchers found that normally consolidated (NC) clays showed peak behaviour followed by a strain softening response during mobilization of shear resistance (Skempton 1985, Li et al. 2017, Lian et al. 2020, Yao et al. 2020). However, the strain softening behaviour under NC conditions with volumetric contraction contradicts the general understanding of the NC behavior of clays. This anomalous behavior is yet to be addressed.

The peak shear response of NC clays in ring shear tests is found to be influenced by the pore-fluid salinity concentrations (Yao et al. 2020). Thus, the strain-softening response of the NC clays appears to be related to micro-fabric evolution during shear under physico-chemical effects. The inter-particle interactive forces and particle configuration play a crucial role in controlling elasto-plastic volume change response of compacted kaolin clays (Pedrotti & Tarantino 2014, 2018). The electro-chemical forces such as coulombic attraction/repulsion and van der Waals attraction depend on pH and other pore-fluid characteristics in kaolin clays. However, the nature of these interparticle interactions under the mechanical loading conditions is unknown. Further, in the ring shear tests, the torque is applied to shear the sample under a constant vertical normal stress, σ_v (i.e., K_o-condition). The mobilized shear stress on the shear plane of the soil element due to the applied torque changes during the shear and achieves a stable value at residual state. Thus, deviatoric stress, $q = (\sigma'_v - \sigma'_h)$ and effective mean normal stress, $p' = \left[(\sigma'_v + 2\sigma'_h)/3\right]$ will not be constant in clays that undergo significant shearing in ring shear tests unlike the existing constitutive model frameworks. Where σ'_v and σ'_h are vertical and horizontal normal effective stresses,

respectively. It indicates that the inter-particle forces play a role in controlling the shear resistance, which is responsible for changes in effective stress. Therefore, it is essential to consider the effect of electro-chemical forces in estimating the effective stresses for interpreting the shear response. Moreover, currently there is no theoretical framework available to explain the torsional shear response of clays.

Engineering involvement to minimize the subsidence of the surface under wetting condition is essential. According to past studies (Corrêa-Silva et al., 2019; Coudert et al., 2022; Cristelo et al., 2011; Matalkah et al., 2020; Rios et al., 2016; Singhi et al., 2016; Wilkinson et al., 2010), alkali-activated materials (AAMs) have been successfully utilized to stabilize a variety of soils, including clayey soil, sandy clay, marl, marlstone, silty sand, road aggregates, meta kaolin, and kaolin. Alkali solute such as as sodium hydroxide (NaOH) is introduced in alumina (Al_2O_3) and silica (SiO_2)-rich source materials such as fly ash, kaolin, red mud, and metakaolin (Heah et al., 2013; Songpiriyakij et al., 2010). The polycondensation of silico-aluminate structure produces geopolymers. The geopolymers products exhibit high mechanical strength and chemical stability (Wang et al., 2005). Geopolymers have also been created using kaolinite minerals as a source of aluminosilicate oxide (Xu & Van Deventer, 2002). Since kaolinite mineral contains alumino-silicate compounds, which can directly react with sodium hydroxide and sodium silicate solution to form geopolymer products with improved mechanical characteristics. The extent of geopolymerization with the enhanced mechanical behaviour of kaolin slurry by alkali activation was examined in past studies (Heah et al., 2011, 2013; Hounsi et al., 2014; Vitale et al., 2017). Limited studies have explored the mechanical characteristics of compacted kaolin soil treated with AAMs; most studies focus on the slurry state. Recently, it was found that the alkali-treated compacted kaolin had improved compression and shear strength characteristics over raw kaolin (Coudert et al., 2022). However, the wetting-induced collapse

settlements in treated compacted kaolin soil have not been examined in the previous studies. The application of existing laboratory procedures for field application are difficult as the alkali concentration is sensitive to equilibrium strength and curing time. Mixing alkali activators with compacted kaolin deposits in the field is tedious and requires a vast quantity of costly alkali activators. Moreover, mixing cannot be done in field conditions where kaolin deposits are found at higher depths. The field mixing of alkali and maintaining the desired concentration is challenging. Thus, a new cost-effective suitable procedure is required that can be employed in the field.

1.2 Organization of Thesis

The organization of the thesis was discussed here. The thesis consists of eight chapters, including four contributing chapters. **Chapter 1** presents the introduction to the problem, the motivation behind the research work, and the objectives of the present work. A detailed review of the available literature relating to the volume change and shear strength behaviour of kaolin soils and existing stabilization techniques to arrest the collapse in kaolin soil was presented in **Chapter 2**. The chapter also provides a detailed discussion of the existing experimental and modeling studies on mechanical behavior of compacted collapsible soils. The critical appraisal of the available related work leading to the objectives of the present study was also presented in this chapter. **Chapter 3** provides detailed information on the properties of soils and initial compaction conditions used in the experimental program throughout the present study. Oedometer compression tests were the practical laboratory methodology for exploring the volume change behaviour of air-dry compacted kaolin soils under different saturation states. A torsional ring shear device was used to investigate the volume change and shear strength behaviour under different inundation pressures, and various pore fluids were presented in this chapter. The proposed procedure for controlling the collapse volume change of compacted kaolin under the influence of various solution

concentration and inundation pressures was also discussed in this chapter. Results and discussion from the study are presented in chapters 4 - 7. **Chapter 4** presents the effect of initial matric suction and clay fabric on the compression, yielding, and collapse response of the compacted kaolin. The deviation of the yielding response of kaolin from the BBM was explained from a microstructural perspective through Scanning Electron Microscopy (SEM) of the soil fabric evolution with changes in inter-particle forces due to wetting and drying from different initial compaction states. **Chapter 5** presents the formulation of generic constitutive modeling based on past and current experimental results to account for wetting explicitly and inter-particle forces implicitly, which BBM was not able to capture. The proposed model validity was checked for the soils from the present study and collapsible soils from various past literature. The effect of inundation pressure, consolidation pressure, and pore fluid chemistry on shear strength and volume change characteristics was explored in **Chapter 6**. The laboratory investigation of large-strain shear resistance response and the theoretical framework for modeling the large-strain shear resistance behaviour under chemo-mechanical loadings was presented. **Chapter 7** presents the volume change behaviour of the compacted kaolin soil under the influence of various alkali activator solution concentrations and at different inundation pressures. The effect of solution concentration of the alkaline solution and normal stresses on the compression and collapse behaviour of the compacted kaolin was presented. A new method procedure based on laboratory study was proposed to reduce the collapse potential of kaolin soils in the field condition. Important conclusions and scope for future work were discussed in **Chapter 8** based on the detailed investigation of the results and limitations in the present work.

Chapter 2

Background and Literature Review

2.1 General

This work focuses on kaolin (i.e. dominated by kaolinite mineral) due to its wetting-induced collapsible nature and high abundance in various regions worldwide. Kaolinite predominantly exists in tropical regions that receive high average annual rainfall, as shown in Fig. 2.1. An important aspect of kaolinite mineral effects is their impact on soil mechanical behaviour, which plays a significant role in natural hazards (Regmi et al., 2013; Skempton, 1985). The soil deposits which contain kaolinite minerals, such as kaolin causes

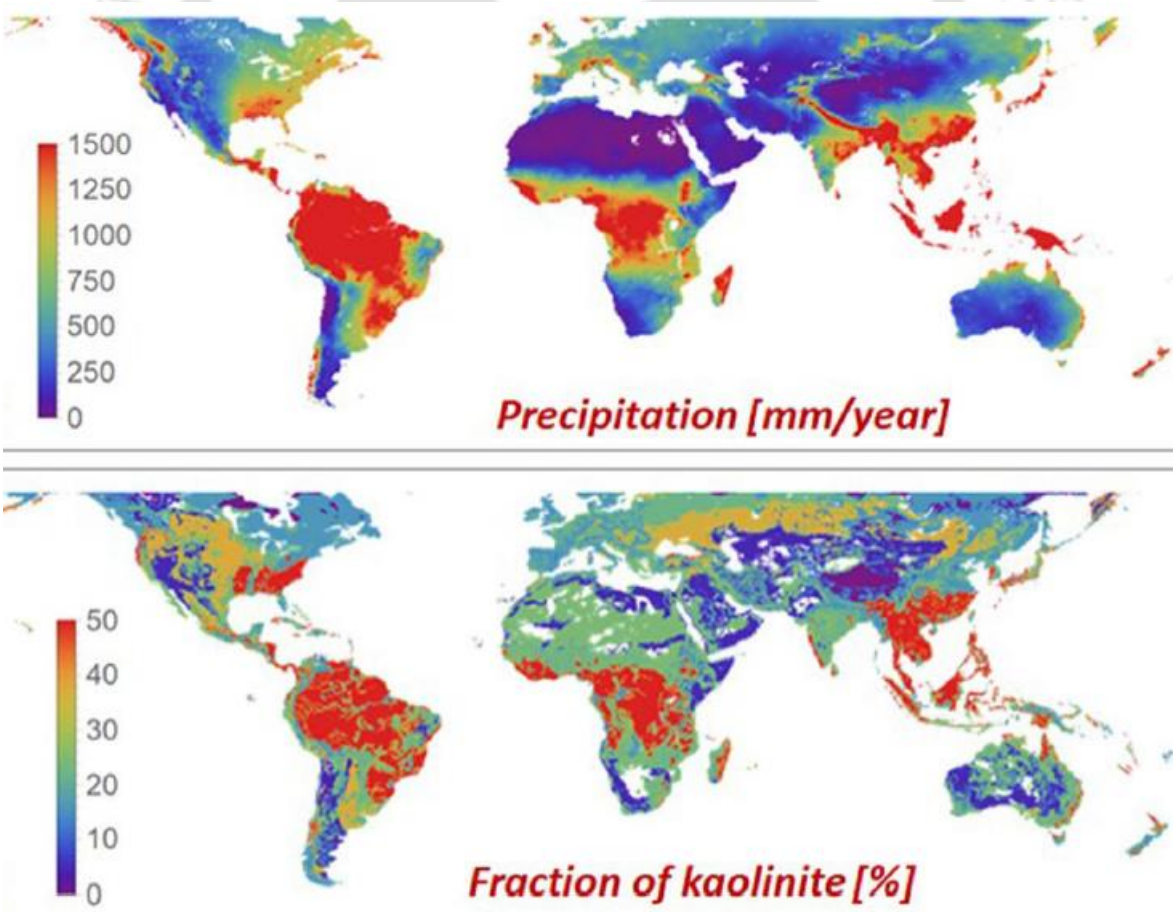

Fig. 2.1. Global distribution of kaolinite clay in tropical regions controlled by precipitation patterns (Lehmann et. al., 2021)

extensive damage to civil engineering structures; as a result, huge loss of economy and, in some cases, loss of life (Houston et al., 2002; Zheng et al., 2013; Silveira & Rodrigues, 2020; Opukumo et al., 2022). Thus, it is essential to understand the fundamental aspects of kaolinite minerals, including microstructure and particle interaction. The kaolinite microstructure and clay particle interactions were discussed in the next section.

2.2 Kaolinite Structure and Nature of Particle Interaction

The basic unit layers of kaolinite (Fig. 2.2(a)) combined through hydrogen bonds to form a single particle (Fig. 2.2(b)). The tetrahedral and octahedral faces (Fig. 2.2) of kaolinite particles always contain a permanent negative charge due to isomorphic substitution. The octahedral faces also include some pH-dependent charges (Choudhury & Bharat, 2018; Van Olphen, 1977). The magnitude of edge charges varies with the pH of the pore fluid environment due to the protonation and de-protonation of termination sites of hydroxyl groups at the edges (Braggs, 1994; Mitchell & Soga, 2005; Wang & Siu, 2006a).

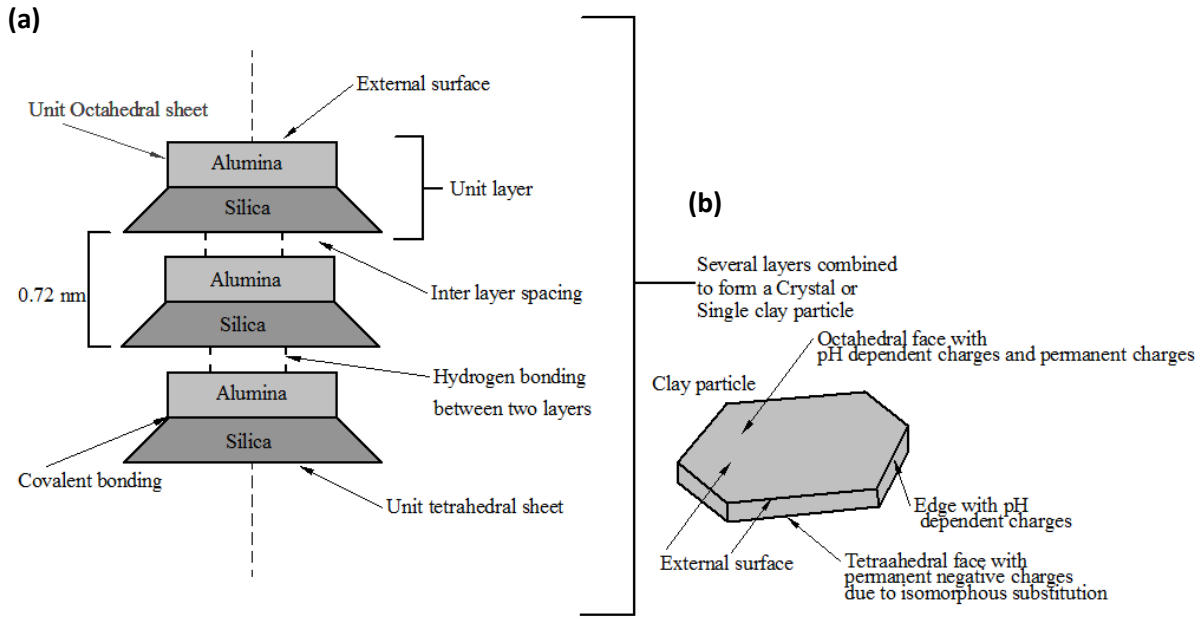

Fig. 2.2. Structure of Kaolinite mineral.

The sedimentation analysis of kaolinite particles gives insight into the role of inter-particle forces such as coulomb and van der Waals forces in settling, sediment deposition, and particle configurations (Michaels & Bolger, 1962; Wang & Siu, 2006a). The inter-particle forces and associated clay fabric formations can lead to different sediment volumes under different pore fluid environments. The variation of sediment volume of clay suspension at equilibrium final deposition states against pore fluid characteristics parameters such as pH and di-electric constants is called the equilibrium sediment volume curve (ESV).

From the ESV curve, the information regarding clay particle arrangement can be understood. The pH of the pore fluid suspension at which the net charge on the kaolin particle edges becomes zero is known as the isoelectric point of the edge, IEP_{edge} (Rand & Melton, 1977; Wang & Siu, 2006a). The edges of kaolinite become negatively charged when pH > IEP_{edge} and positively charged when pH < IEP_{edge}. Accordingly, clay fabric transition from ESV curve can be identified.

The particle interactions in kaolinite are controlled by the electrostatic forces such as coulombic attraction/repulsion and intermolecular force of van der Waals attraction (Van Olphen, 1991; Santamarina et al., 2001; Pedrotti &Tarantino, 2014, 2018). The attractive coulomb force and attractive van der Waals forces act between the positively charged edge and negatively charged face when pH < IEP_{edge} in kaolin and give raise to edge-to-face particle association, as shown in Fig. 2.3(a). Coulombic repulsion and van der Waals attraction exist between the negatively charged faces when pH > IEP_{edge}, which gives raise to face-to-face particle arrangement, as shown in Fig. 2.3(b). The inter-particle electro-chemical forces depend not only on the pH of the pore medium; but also on the di-electric permittivity of the medium and the distance between the clay particles according to Coulomb's law. The two distinct kaolinite clay particle configurations (i.e., edge-to-face and face-to-face) offer significantly different shear resistance under the applied normal stresses.

It indicates that the electro-chemical forces could significantly resist external loading and control elasto-plastic mechanical response (Pedrotti &Tarantino, 2014, 2018). Thus, it is crucial to explore the mechanical characteristics of kaolin under mechanical loadings with consideration of electro-chemical forces. Available experimental studies related to the compression, yielding, and collapse behaviour of partially saturated compacted collapsible soils are discussed below.

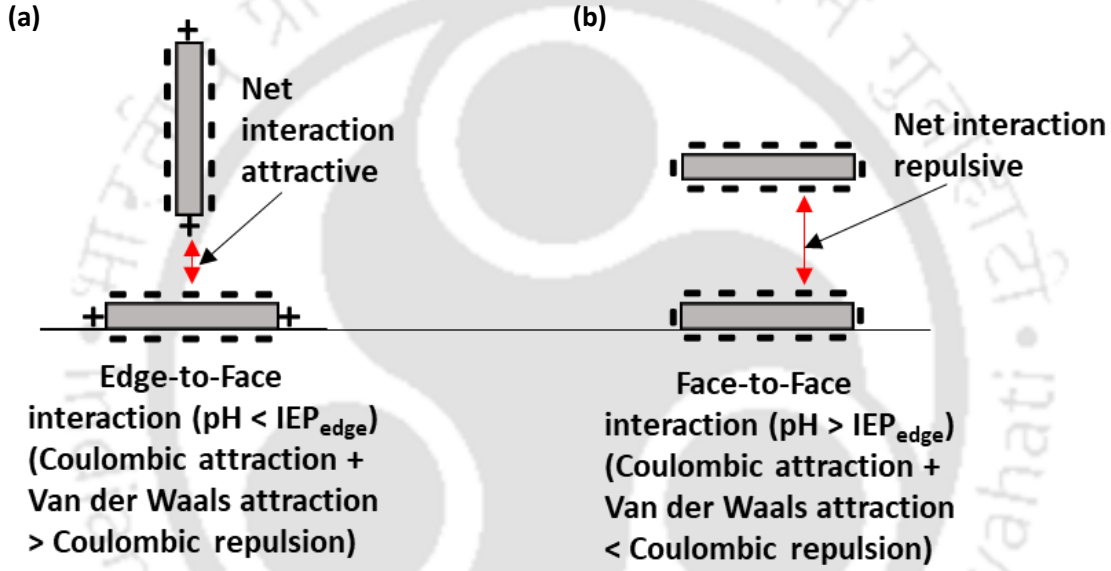

Fig. 2.3. Electrical interaction between the kaolinite particles under different pH conditions.

2.3 Influencing Factors for Mechanical response of Collapsible Soils

The initial compaction parameters, such as suction/moisture content and soil structure, significantly influence the mechanical behaviour of compacted collapsible soils (Sivakumar & Wheeler, 2000; Sun et al., 2007b; Sivakumar et al., 2006; Thu et al., 2007; Sivakumar et al., 2010; Thyagaraj & Das, 2017; Xu et al., 2021; Ge et., 2021). Sivakumar & Wheeler (2000) studied the influence of compaction characteristics on the suction-controlled compression and yielding behaviour of kaolin clay due to wetting under isotropic loading conditions. The loading-collapse (LC) yield curve positions and normal compression lines

for various suction levels were influenced by compaction pressure and strongly affected by the compaction water content, indicating some effect of the initial compaction-induced soil fabric.

Suction-controlled triaxial tests are conducted by Sun et al. (2007b) to study the effect of initial density and suction on the volume change behaviour of pearl clay. The volume change due to a decrease in suction is mainly influenced by the mean net stress and the initial void ratio. The maximum collapse was observed when the mean net stress was equal to the initial yield net stress of the unsaturated soil.

The effect of wetting and drying stress paths on the compression and yielding behaviour of kaolin initially compacted near maximum dry density (MDD) and OMC was explored by (Sivakumar et al., 2006). Two different series of experiments are performed under suction-controlled conditions using the axis-translation technique in twin-cell triaxial cell equipment. In the first series of tests, three compacted specimens were subjected to controlled wetting until equilibrium suctions of 300, 200, and 0 kPa were achieved at an inundation pressure of 50 kPa. Subsequently, samples were subjected to compression under specified constant suctions. The second series of experiments initially involved wetting all three samples until 50 kPa suction. Drying was performed in subsequent steps to attain equilibrium suction of 100, 200, and 300 kPa, respectively. The yield curves established from suction-controlled compression tests showed that the samples subjected to only wetting in the first series of experiments yielded at higher normal stresses than those of the samples that underwent both wetting and drying.

The results of suction-controlled isotropic compression experiments in modified triaxial apparatus on identical samples of kaolin clay compacted at MDD and OMC showed that the yield stress increased with matric suction (Thu et al., 2007). The matric suction influenced

the loading and unloading normal compression curves and intercepts of normal compression curves.

Sivakumar et al. (2010) carried out suction-controlled compression experiments in twin cell apparatus on kaolin to study the effect of stress histories, viz., anisotropic and isotropic stress states on compaction, yielding, and pore size distributions. The yielding of samples with two different stress histories showed significant differences. The LC yield locus had a substantially distinct size and shape for the samples with two different stress histories.

The physico-chemical influence on compressibility and loading-collapse yield behaviour is studied by Thyagaraj & Das (2017). The compression response in the elastic range was found to be independent for residual soils of initial matric suction and pore fluid osmotic suction for the samples prepared using different pore fluids and compacted at similar void ratios. However, the yield stress was influenced by the initial matric suction and pore fluid osmotic suction for the studied compacted samples.

Influence of particle orientation for the in-situ intact loess soil and re-constituted loess soil compacted to the in-situ void ratio and moisture content on the mechanical response was investigated by Xu et al. (2021) using suction-controlled compression oedometer tests. It is found that the yield stress of the field sample is higher than that of re-constituted specimens under constant suction due to differences in the particle arrangement. The compressibility of laboratory compacted loess was higher than that of natural field specimen under the same suction.

The one-dimensional compression, micro-structural analysis, including scanning electron microscope (SEM), and pore size distribution (PSD), confirmed that the collapsible soil micro-structure significantly affects the collapse potential in compacted loess soil (Ge et al., 2021). The influence was more prominent for the loess soil compacted on the dry side of the

optimum, indicating the initial suction and clay fabric controls volume change response in collapsible soils. After full saturation in one-dimensional compression testing, a partial collapse mechanism was seen at intermediate and higher normal stresses. Results from mercury intrusion porosimetry (MIP) and SEM indicated significant differences in PSD and structural organization amongst the specimens that attained the same vertical effective stress via various loading and saturation pathways.

It is shown from several literature studies are available on the volume change and yielding response of collapsible soils compacted near saturation conditions (i.e., optimum moisture condition). The volume change behaviour depends on the initial suction/moisture content and particle association, as reported by the previous studies. In actual field conditions, dry soil deposits undergo massive collapse settlement due to wetting/saturation. Because of this, the compression and yielding behaviour might be significantly distinct compared to soil compacted to near saturation conditions. Thus, the mechanical characteristics of collapsible soils initially compacted at a dry state need to be explored. The features of the various existing predictive constitutive models for compacted collapsible soils are illustrated in the next section.

2.4 Constitutive Models for Prediction of Mechanical Response of Unsaturated Clays

Several theoretical studies are available in developing constitutive models to predict laboratory studies on partially saturated soil behaviour. The most popular model in the elastoplastic framework is Barcelona basic model (BBM). The BBM predicts wetting-induced volume change behavior, yielding, and shear response in isotropic conditions for moderately expansive soils.

BBM was developed by Alonso et al. (1990) for predicting unsaturated elasto-plastic mechanical behaviour of moderately expansive soils under isotropic triaxial stress state

conditions. Alonso et al. (1990) simplified the BBM by substituting volume change due to wetting using

$$N(0)-N(s)=k_s \ln\left[\frac{s+p_{at}}{p_{at}}\right] \quad [2.1]$$

where s is matric suction; p_{at} is atmospheric pressure; and k_s is the ratio of soil volume change due to change in matric suction during the soaking, which is defined as a soaking gradient in this work. The $k_s > 0$ for collapse upon wetting, $k_s < 0$ for swelling, and $k_s = 0$ for no volume change. The volume change response of compacted soil under unloading and wetting conditions is given by (Alonso et al., 1990)

$$N(s)-\lambda(s)\ln\left[\frac{p_y(s)}{p^c}\right]+\kappa(0)\ln\left[\frac{p_y(s)}{p_y(0)}\right]+k_s \ln\left[\frac{s+p_{at}}{p_{at}}\right]=N(0)-\lambda(0)\ln\left[\frac{p_y(0)}{p^c}\right] \quad [2.2]$$

The equation for the yield curve was obtained by combining eq. (2.1) and (2.2),

$$\frac{p_y(s)}{p^c}=\left[\frac{p_y(0)}{p^c}\right]^{(\lambda(0)-\kappa(0))/(\lambda(s)-\kappa(0))} \quad [2.3]$$

where $p_y(s)$ is the yield stress with associated suction, s; p^c is reference pressure; $p_y(0)$ is yield stress at saturated state; $\lambda(0)$ is the slope of virgin consolidation line for the saturated condition; $\kappa(0)$ is the slope of the elastic re-compression line for s = 0 and $\lambda(s)$ is the slope of normal compression line, according to

$$\lambda(s)=\lambda(0)\left[(1-r)\exp(-\beta s)+r\right] \quad [2.4]$$

where r and β are the model parameters and can be determined by the best fit of eq. (2.4) on experimental data. The estimation of parameter k_s is complex as it is a material constant. The yield function (eq. 2.3) does not take wetting behaviour into account because the wetting parameter k_s is not considered in eq. (2.2). Moreover, while deriving eq. (2.3) volume change due to both swelling and unloading was considered, but volume change due to collapse was

not considered. Therefore, the inclusion of wetting-induced collapse behaviour is important for the complete wetting response of soils.

Josa et al. (1992); Wheeler & Sivakumar (1995) modified BBM model to address some limitations. Josa et al. (1992) enhanced the BBM to capture the maximum collapse potential observed in loose unsaturated soils. Wheeler & Sivakumar (1995) developed a framework that is very similar to the BBM; simplified the procedure to obtain the model parameters.

Several modified models (Wheeler et al., 2003; Sun et al., 2007a; Thu et al., 2007; Alonso et al., 2013; Rojas et al., 2015; Xie et al., 2018; Kodikara et al., 2020) incorporated hydraulic hysteresis or SWCC and microstructural behaviour of soils into the mechanical response. Wheeler & Sivakumar (2003) formulated an elasto-plastic constitutive model for unsaturated soils at isotropic stress conditions by integrating SWCC with mechanical behaviour. Bishop's stress tensor is introduced in this framework. The stress-strain behaviour is influenced by the plastic changes in the saturation state, and plastic volumetric strains influence the water retention behaviour. This model simulation qualitatively explained the measured data of maximum collapse potential and volume change behaviour upon saturation.

Sun et al. (2007) proposed an elasto-plastic model in isotropic stress conditions for partially saturated soils to predict hydraulic (SWCC) and stress-strain behaviour. The model considered the effect of the degree of saturation on stress-strain behaviour, the influence of void ratio on water retention behaviour (SWCC), and the impact of suction. The proposed model predicts stress-strain response for the compacted clay along constant suction or net stress paths. The measured data of water retention, compression, and stress-strain response of the pearl clay compacted at the moisture content of 26 % close to the saturation state produced from triaxial experiments are validated with the model.

A framework that incorporated micro-structural behaviour and water retention behaviour (SWCC) into BBM is developed by Alonso et al. (2013) to predict compressibility, collapse, and the yielding response of unsaturated soils. The micro-structural effect is incorporated in BBM by including an additional single microstructure state variable, ξ_m, which is the ratio of the micro void to the total void ratio. This model also requires water retention parameters, similar to Wheeler & Sivakumar (2003). The experimentally measured suction-controlled oedometer compression and wetting response are validated with the proposed model for collapsible Barcelona silty clay, which is initially compacted on the dry and wet side of optimum moisture contents (i.e., near saturation state)

A Monash-Peradeniya-Kodikara (MPK) model was developed by Kodikara et al. (2020) to predict volumetric yield surface obtained from soil compacted at constant moisture content, loading-collapse (LC) yield curve based on plastic strain and SWCC. The model equations for isotropic stress state used Bishop's effective stress and conjugate strains to represent coupled hydro-mechanical behaviour for allowing the transition from partially saturated to saturated behaviour. The model is qualitatively validated on kaolin, a mixture of kaolin and bentonite samples compacted at different moisture contents near OMC from previous studies. In some cases, model predictions are unsatisfactory. Further, the model requires 16 model parameters and poses difficulty in determining some of the parameters.

In summary, the existing theoretical models did not incorporate collapse response to predict soil behaviour. Further, the models can predict soil behaviour only under certain conditions, such as isotropic and near-saturation conditions. In actual field conditions, significant collapse occurs in dry deposits with very low moisture content compared to close to saturation. The collapse potential is significantly influenced by mechanical characteristics, such as yielding response and compression behaviour. Hence, an alternative constitutive

model incorporating collapse behaviour through simple and fewer parameters is needed to predict the mechanical response of different collapsible soils under various initial compaction conditions.

2.5 Influence of Pore-Fluid Chemistry on Kaolin Behaviour

Past studies examined the volume change and shear response of non-active clays such as kaolin under the influence of pore fluid chemistry (Sridharan & Rao, 1973, 1979; Wahid et al., 2011b; Wang & Siu, 2006a, 2006b; Yang et al., 2023).

Sridharan & Rao (1979) studied the influence of electro-chemical forces on the drained shear strength response of kaolin by qualitative prediction inferred from the Mohr-Coulomb failure envelopes produced in shear box apparatus. In the above investigation, the drained shear strength of kaolin is found to decrease with an increase in the di-electric permittivity of the pore fluid. No theoretical estimation for electrostatic forces to be used in the effective stress equation is attempted.

Wang & Siu (2006a, 2006b) and Wahid et al. (2011a, 2011b) showed that the pH of the pore-fluid significantly influences the deformation and shear characteristics of kaolin soils. However, the mechanical response is insignificantly influenced by the pore-fluid salinity. The pH-dependent edge charges affect the inter-particle electrochemical forces and particle arrangement in kaolinite (Wang & Siu, 2006b).

Based on the consolidation tests and microstructural analysis of kaolin samples, Pedrotti & Tarantino (2014, 2018) and Choudhury and Bharat (2018) found that the inter-particle interactive forces and particle associations play a crucial role in controlling elasto-plastic volume change response. Moreover, electro-chemical forces depend on the pore-fluid composition, and these forces influence the net interactions. However, the nature of kaolin particle interaction during shearing is not known.

Yang et al. (2023) performed various experiments such as Liquid limit tests, equilibrium sediment volume tests (ESV), SEM image tests, and oedometer compression tests on slurry samples of kaolinitic clay under physico-chemical influence. It was found that the pore solution concentration and valence have significantly impacted the volume change behaviour of kaolin clay. The variation in pore fluid chemistry caused changes in inter-particle electro-chemical forces, which are responsible for volume change in consolidated slurry samples.

2.6 Large-Strain Shear Behaviour of Clays

Many studies (Skempton 1985; Moore 1991; Mesri et al., 2003; Li et al., 2017; Duong et al., 2018; Yao et al., 2020) reported that the large-strain shear response, including peak and residual strength of clays, is affected by the pore fluid chemistry, rate of shearing, clay content, particle orientation, and mineral composition.

Skempton (1985) observed peak response at small shear deformation under higher normal stress for normally consolidated clay against the torsional loading in drained conditions from ring shear test. It was suggested that the post-peak drop in shear resistance was only due to the particle re-orientation, but there was no experimental and theoretical support for the such statement was given.

Experimental results presented by Moore (1991) indicated that the residual strength of kaolinite and montmorillonite clays was strongly affected by the clay mineralogy and pore-fluid chemistry (salt concentration).

The influence of the shear rate and over-consolidation ratio (OCR) on the drained residual strength of silty sand was investigated by Li et al. (2017) using ring shear tests. A series of ring shear tests were performed to measure the drained residual strength under low to very high shear rates of 0.06 to 30 mm/min and OCR from 1 to 12. The experimental results

revealed that the OCR did not significantly influence the residual shear strengths. The influence of shear rate on residual shear strength was not followed any regular pattern for shear rates between 0.06 – 10 mm/min. Reduction in residual shear strength was seen for higher shear rates. Moreover, peak response was observed for NC soil (OCR = 1) at 50 kPa of consolidation stress under different shear rates. However, no explanation was given for such abnormal behaviour.

To examine the effect of shear rate on residual shear strength of low to high plastic soils, Duaong et al. (2018) conducted several ring shear tests on kaolin and kaolin-bentonite mixtures using a ring shear device. The shear rate was kept from 0.02 to 20 mm/min for individual samples. The test results indicated that the bentonite content significantly influences the rate effect on the residual strength of kaolin-bentonite mixtures. The NC peak behaviour was observed at all shear rates under consolidation pressure of 98 kPa. In addition to that, volumetric contraction during shearing was reported at all shear rates. However, the reason for the occurrence of strain-softening response in NC clays was not discussed.

The influence of pore-fluid chemistry on torsional shear characteristics of NC clays under different consolidation pressures was investigated by Yao et al. (2020). Several ring shear experiments were conducted on two natural soils (expansive and kaolin clays). The influence of pore solution concentration on shear resistance was examined. It was observed that the shear strength of expansive clay was significantly affected by the saline concentrations under all normal stresses. However, the shear strength of kaolin was not significantly influenced by variable salt concentration. Interestingly, at all consolidation pressures, the strain-softening response was observed for NC clays, and the peak was more pronounced at higher normal stresses. However, similar to other studies, no explanation was given for such anomalous behaviour of NC clays.

It was shown from literature studies that pore-fluid chemistry strongly influences the torsional shear strength response of clayey soils. Thus, to interpret the large-strain shear behaviour of clays under the physico-chemical influence, the existing effective stress concept were explored and discussed in the next section.

2.7 Effective Stress Concept Approach for Partially Saturated Soils

A significant influence of electro-chemical attractive and repulsive forces at the particle level can be brought into the modified effective stress concept to analyze the shear strength response of kaolin clays. Terzaghi's effective stress equation is modified by Lambe (1960) to consider the influence of physico-chemical forces into the classical effective stress equation as given by

$$\sigma' = \bar{\sigma} a_m + R - A \qquad [2.5]$$

where, $\bar{\sigma}$ is mineral to mineral contact stress; a_m is the fraction of total inter-particle area that is mineral to mineral contact; R is the effective inter-particle repulsive pressure and equal to total inter-particle electrical repulsion divided by total inter-particle area; and A is the effective inter-particle attractive pressure and equal to total inter-particle electrical attraction divided by total inter-particle area. According to eq. (2.5), the effective stress increases with repulsive pressure and decreases with attractive pressure, which contradicts the physical behaviour of clay soils. Later, Sridharan (1968) modified eq. (2.5) and expressed it as

$$\sigma' = \sigma - u_w - u_a + A - R \qquad [2.6]$$

where, σ' is effective stress that controls the shearing resistance; σ is external applied normal stress on a unit area; u_w is effective pore water pressure; u_a effective pore air pressure; and the term (A-R) represents the net electro-static pressure. This effective stress equation is used to predict and understand the shear strength behaviour of expansive clays

due to physico-chemical effects. To date, no explicit expression is available to estimate the net electro-static pressure (Yao et al., 2020), as no analytical equations for inter-particle electro-chemical attractive forces and formula for effective area of interaction are available. However, when particles are arranged in a face-to-face manner, as shown in Fig. 2.4, the analytical equation for the electrostatic force of repulsion F_{ff} can be written as (Pedrotti and Tarantino 2018)

$$F_{ff} = \frac{\pi\rho^2 a^2}{8\varepsilon_o\varepsilon_r}\left[\frac{z}{\sqrt{a^2+y^2}}-1\right] \qquad [2.7]$$

Where ρ is electrical surface charge density on both plates (C/m^2); a is the radius of particle (m); ε_o is the vacuum permittivity (8.85×10^{-12} F/m); ε_r is the di-electric constant of pore medium; y is the distance between the particles (m).

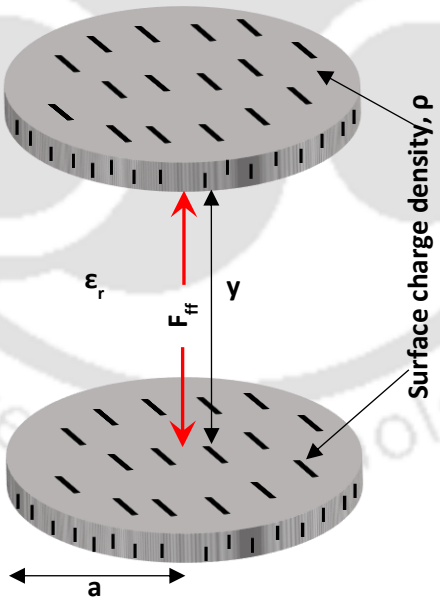

Fig. 2.4. Electrostatic interaction between the kaolin particles: face-to-face configurations when pH > IEP_{edge}: net repulsive interaction.

Because of the unavailability of an explicit formula for (*A*-*R*), it is challenging to implement the modified effective stress eq. (2.6) to predict the shear strength response of clays when the physico-chemical effect comes into play. Due to this reason, Yao et al. (2020) utilized

an explicit effective stress expression equation to estimate average intergranular stress for the shear strength behaviour of both active and non-active clays saturated with different salt solutions based on the previous work of Wei (2014). However, this framework is limited to the ionic strength influence. The influence of pH and di-electric characteristics of pore-fluid cannot be accounted for in this expression. It is clear that this approach is not valid for non-active clays as the shear influence of pH and di-electric on the kaolin behaviour could not be explained. Thus, the development of explicit expression for the term (*A*-*R*) is essential to capture the variation in effective stress from eq. (2.6) caused by alternation in electro-chemical forces during shear.

2.8 Stabilization of Collapsible Soils

Prior to the employment of a ground improvement technique based on geopolymerization at the sites, the proper knowledge of the mechanical characteristics of compacted soil treated with alkali activated materials AAMs is essential under distinct curing periods. Recently, many studies are available on the investigation of the microstructure and mechanical behaviour of kaolin soil treated with varying concentrations of alkali activators (Abdullah et al., 2021; Abdullah & Shahin, 2022; Coudert et al., 2019, 2022; Cristelo et al., 2011; Heah et al., 2013; Wilkinson et al., 2010; Zhang et al., 2016).

The laboratory experiments conducted by Cristelo et al. (2011) reveal that the deformation and mechanical strength significantly improved when soil collected from the site consisted of dominated quartz, kaolinite, and muscovite minerals mixed with fly ash activated by the different concentrations of NaOH. The improvement was more pronounced at larger curing periods of 28 days. The improved mechanical characteristics were also compared with the soil treated with common binders such as Portland cement, however alkaline treated samples showed higher long-term strength. The field technique involved the creation of jet grouting columns of activated fly ash mixture cemented into the deep soft soil deposit. After 28 days,

three months, and one year of curing, the column samples from the site were excavated and tested for unconfined compressive strength (UCS) in the laboratory. The three months UCS strength of alkali grouted columns was found to be higher than that of the cement grout columns.

A case study of the stabilization of soft granitic residual soil, which contained kaolinite and mica minerals and was frequently used in rammed earth construction in northern Portugal, was reported by Silva et al. (2013). Granitic residual soils are not suitable for rammed earth construction until it goes through the stabilization process. The stabilized granitic residual soil specimens with different percentages of fly ash activated by alkali solution indicated that the durability performance was improved considerably. However, improvement in the compressive strengths of the samples was not significant to meet the minimum requirements in the field condition. They concluded that the poor performance related specimens in terms of compressive strength might be related to high fly ash content in the samples and less curing period.

Heah et al. (2013) investigated the influence of NaOH concentration on the unconfined compressive strength of kaolin geopolymers. The alkali concentration significantly affects the compressive strength of geopolymers, while strength is highest at a specific optimum alkali concentration. The concentration of an alkali activator higher than the optimum one did not enhance the compressive strength in treated kaolin samples.

The improvement in mechanical characteristics of speswhite kaolin due to two different alkali activated fly ashes is studied by Vitale et al. (2017). One-dimensional compression tests on the treated kaolin demonstrated mechanical improvement due to alkali activated binders. In significantly less time, a decrease in soil compressibility and an increase in yield stress are reported. The alkali activated fly ashes as an alumino-silicate source exhibited

high reactivity, according to microstructural investigations, to stimulate the deposition of new mineralogical phases and forms chains with cementitious material.

Abdullah et al. (2020) studied the mechanical behaviour of two different alkali treated kaolin soil mixed with either bentonite or clean sand. The geopolymer used in this study was composed of fly ash, granulated blast furnace slag, and sodium-based activators. The mixture of fixed weight ratios of slag to (fly ash + activator) and activator to (fly ash + slag) of 20 % and 40 %, respectively, were selected to synthesize the geopolymer. The effect of geopolymer content on treated soil characteristics such as compaction, plasticity, compressive strength, durability, and pH level are examined. Clays treated with a suitable amount of geopolymer and cured for a longer duration showed reduced plasticity index, increased strength, and improved durability. The pH level of treated clays decreased with increased curing time while their strength increased.

The effect of geopolymer content and curing time on the mechanical response of treated kaolin was studied by Abdullah et al. (2021). It was observed that adding more geopolymer to a material generally increased compressive strength and that this effect intensified as curing time increased. Also, it was found that treated clay with insufficient geopolymer content may have issues with durability performance during wetting-drying conditions. Furthermore, it was discovered that the quantity of activator added to the geopolymer mixture significantly affected both strength and durability performance. Comparing mixes with high and low activator contents for a given geopolymer content, a combination with a high activator content exhibited higher strength gain and durable performance.

The study of mechanical characteristics of compacted kaolin treated with geopolymer binder fly ash which is activated by the NaOH alkaline solution, was reported by Coudert et al. (2022). The stiffness of treated kaolin was checked using one-dimensional oedometer

compression experiments. The treated samples under different curing periods showed increased yield stress. Stiffness was increased against loading up to 700 kPa, and the increase was significant at eight days of curing time. The stiffness increase was associated with the formation of geopolymer bonds at inter-aggregate locations. Because of geopolymers bonding, the clay aggregates configuration was edge-to-face, which provided higher resistance than the untreated sample.

However, existing studies have not explored the wetting-induced collapse deformation in treated clays. The application of existing lab techniques for field application is complex as the alkali concentration is sensitive to equilibrium strength and curing time. Mixing alkali and activators with compacted kaolin deposits in the field is tedious and requires a vast quantity of costly alkali activators. Moreover, mixing cannot be done in field conditions where kaolin deposits are found at higher depths. The field mixing of alkali and maintaining the desired concentration is challenging. Thus, a new cost-effective suitable procedure is required that can be employed in the field.

2.9 Scope for the Research Work

Based on the existing studies reported and the identified research gaps form the scope of the present work as defined below

1. The existing studies revealed that the volume change response of collapsible soils at near saturation state (i.e., optimum moisture condition) is well studied. However, very limited studies are available to investigate the mechanical behaviour of air-dry compacted collapsible soils. Thus, a detailed study is required to understand the effect of initial compaction characteristics, such as moisture content or matric suction, on the mechanical response of collapsible soil.

2. The existing elasto-plastic constitutive models for unsaturated soils are applicable to very specific initial conditions, such as soil compacted to a very high degree of saturation. Moreover, these models involve some complex parameters, and the estimation of such parameters is not simple. Therefore, it is essential to develop a generalized constitutive model which can predict the unsaturated soil behviour in any circumstances, including saturation states, loading stress history, and compaction stress history.
3. The pore fluid chemistry greatly influenced the shear strength and deformation characteristics of non-active clays such as kaolin. Quantitative evaluation of electro-chemical forces on kaolin behaviour is not available. Therefore, exploring the mechanical behaviour of kaolin clay under the influence of overburden pressure and physico-chemical factors with the accommodation of inter-particle forces is essential.
4. Until now, no laboratory study has been reported on the stabilization of kaolin to arrest the collapse potential. In the field, any collapsible soil can undergo massive volumetric collapse under certain overburden pressure due to wetting. The available proposed field stabilization methods cannot be employed in the field due to the associated limitations. Thus, a new viable and simple stabilization procedure based on laboratory study is required to minimize the collapse potential for field applications.

2.10 Objective of the research work

Based on the scope of research, some objectives for the present work are defined below

1. To investigate the influence of initial suction and normal stress on the measured mechanical behaviour of dry compacted unsaturated kaolin soils.
2. To develop a new generic constitutive model applicable to all types of collapsible soils with different saturation conditions, loading stress history, and compaction stress history.

3. To study the effect of normal stress and pore fluid chemistry on the large-strain shear resistance response of saturated compacted kaolin soil and to formulate a theoretical framework for modeling the torsional shear resistance of clayey soils under the physico-chemical influence.

4. To explore the measured mechanical response of dry compacted kaolin treated with alkali activator solution to reduce the collapse potential and to propose a new cost-effective suitable procedure that can be implemented in the field.

Chapter 3

Materials and Testing Procedure

3.1 Materials

In this work, two different kaolin clays, K1 and K2, were selected. The K1 is a naturally occurring kaolin obtained from a hill slope of Barapani, East Khasi Hills, Meghalaya, India, as shown in Fig. 3.1(a) and 3.1(b).

(a)

(b)

Fig. 3.1. (a) Location of Barapani in Meghalaya and **(b)** collection of soil K1 from the hill site.

The soil was oven dried, pulverized to break up the clay lumps, and sieved through a 0.425 mm sieve. The grain size distribution of K1 was shown in Fig. 3.2 based on the hydrometer analysis using the standard test method, D7928-17 (ASTM 2021). The soil comprises of 28% clay size, 66% silt size, and 6% fine sand fraction. The consistency limits of the soil were determined as per the standard D4318-17 (ASTM 2018) and presented in Table 3.1.

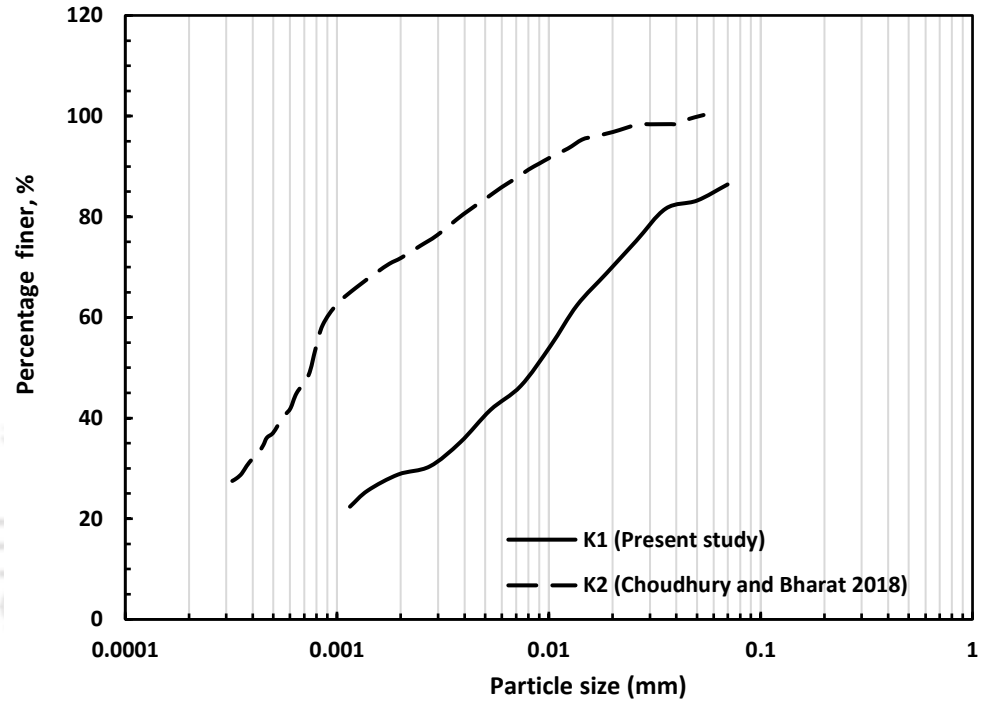

Fig. 3.2. Grain size distribution of the studied kaolin K1 and K2.

The soil was categorized as inorganic clay of low plasticity (CL), as per the USCS classification system D 2488-17e1 (ASTM 2018). The kaolinite mineral was identified by X-ray diffraction (XRD) and based on the standard peak data (Grim 1953), as presented in Fig. 3.3. A few peaks on the XRD plot indicated the presence of illite and quartz minerals. Thus, the K1 was kaolin clay with a predominant kaolinite mineral. The specific gravity was estimated by the density bottle method as per IS 2720: Part III/Sec 1 (IS 1980). Brunauer-Emmett-Teller (BET) was utilized to estimate specific surface area S_s by the N_2 gas adsorption technique. The amount of soil available for testing was limited, thus the mini

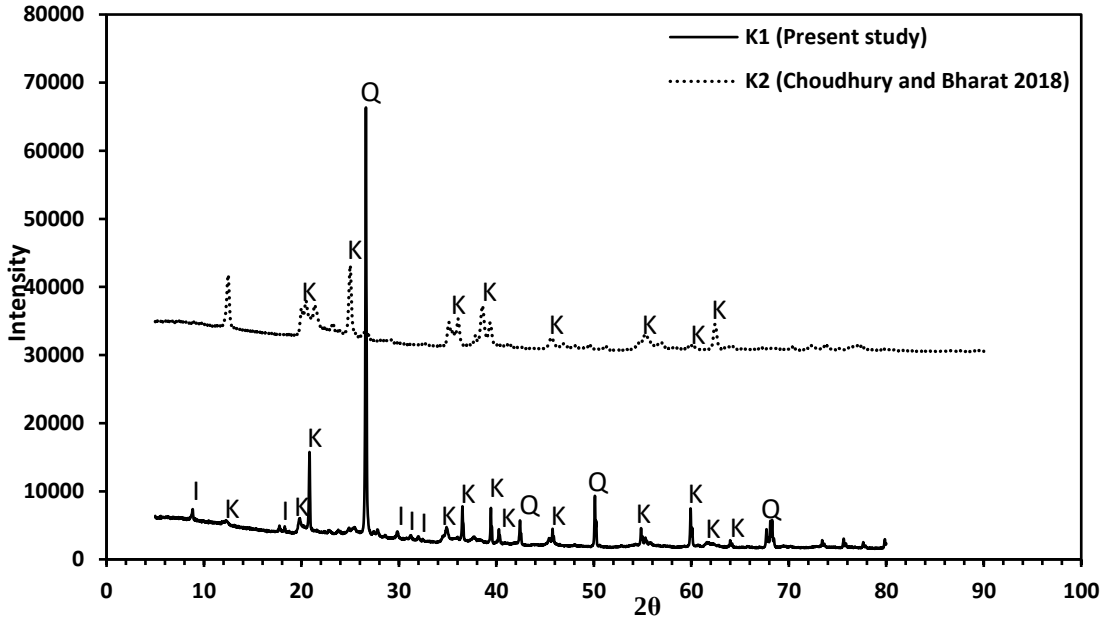

Fig. 3.3. XRD patterns of K1 and K2.

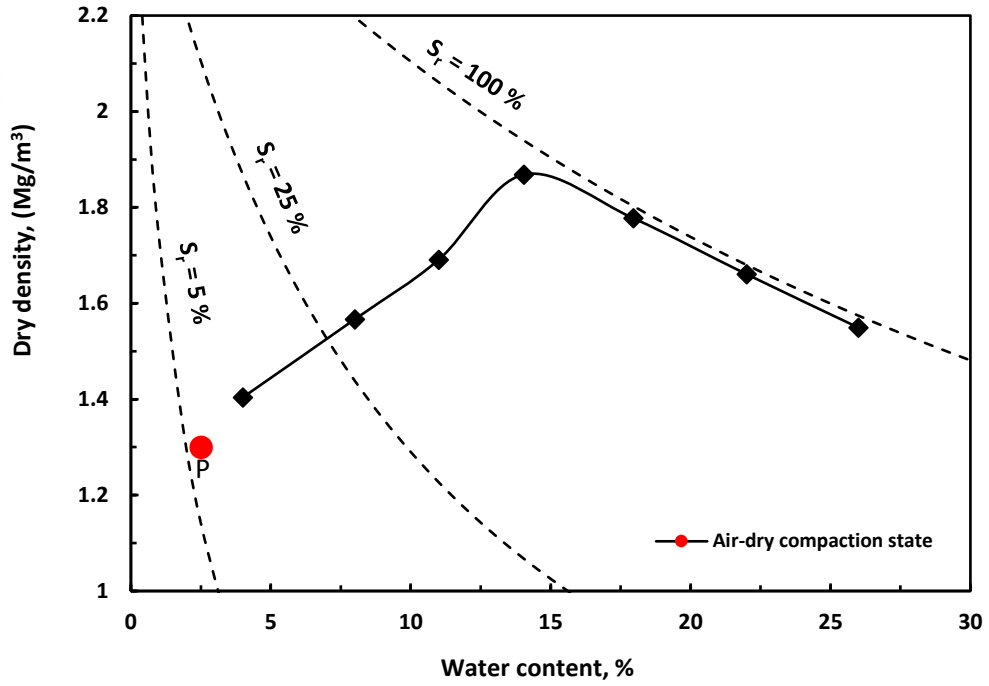

Fig. 3.4. Compaction curve and chosen compaction state for K1.

compaction testing technique (Sridharan & Sivapullaiah, 2005) was adopted. However, the mini compaction test method can slightly overestimate the maximum dry density and optimum moisture content of the soil. This is because the mini compaction mould has a

small diameter and height, which induces bottom and side wall boundary effects. The compaction curve developed using the mini compaction apparatus was shown in Fig. 3.4. The estimated OMC and MDD of the studied soil K1 from the compaction curve were reported in Table 3.1. The conventional method (Chapman, 2016) was used to determine the cation exchange capacity, CEC of K1, which was 3 meq/100 gm. The K2 is commercially procured kaolin, which comprises 72% clay size and 28% silt size fractions. The grain size distribution curve of K2 was shown in Fig. 3.2. The XRD data in Fig. 3.3 shows the presence of the dominant kaolinite mineral in K2, which was reproduced from Choudhury & Bharat (2018). According to the USCS classification system, K2 was categorized as ML. The cation exchange capacity of K2 was 5 meq/100 gm. The basic properties of K2 are given in Table 3.1, as presented by Choudhury & Bharat (2018). The pH-dependent sediment volume

Table 3.1. Basic properties of tested kaolin soils K1 from present study and K2 from Choudhury & Bharat (2018).

Property	**K1**	**K2**
Grain size distribution		
Clay content, % (size<0.002 mm)	28	72
Silt content, % (0.002 mm<size<0.075 mm	66	28
Fine sand, % (0.075 mm<size<0.425 mm)	6	-
Consistency limits (%)		
Liquid limit, w_L	33	40
Plastic limit, w_p	17	32
Specific gravity, G_s	2.67	2.62
Specific surface area, S_a (m^2/g)	17	12
Standard Procter compaction test		
Maximum dry density (g/cc)	1.85	1.65
Optimum water content (%)	14	16
Cation exchange capacity, CEC (meq/100 g)	3	5
IEP_{edge}	3.9	5.3

behaviour of kaolin was analyzed through eight ESV tests performed under electrolyte-free suspensions of aqueous solutions of varying pH range from 1.7 – 8, as depicted in Fig. 3.5. Sedimentation tests were conducted in accordance with the guidelines in (IS. 2720-40: 1977). The IEP_{edge} was estimated from the established ESV curve; accordingly, the zone of

flocculated and dispersed clay fabric interaction was decided on the ESV data. Additionally, four more ESV tests (Fig. 3.6) were conducted to study the effect of di-electric pore

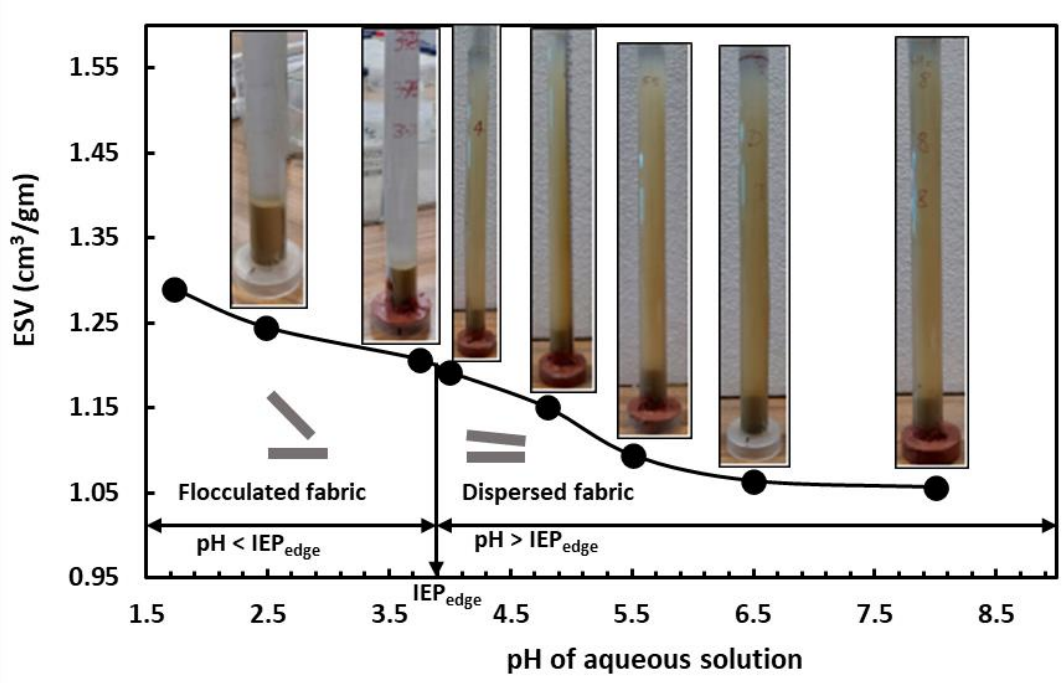

Fig. 3.5. Variation of equilibrium sediment volume with pH of aqueous solution.

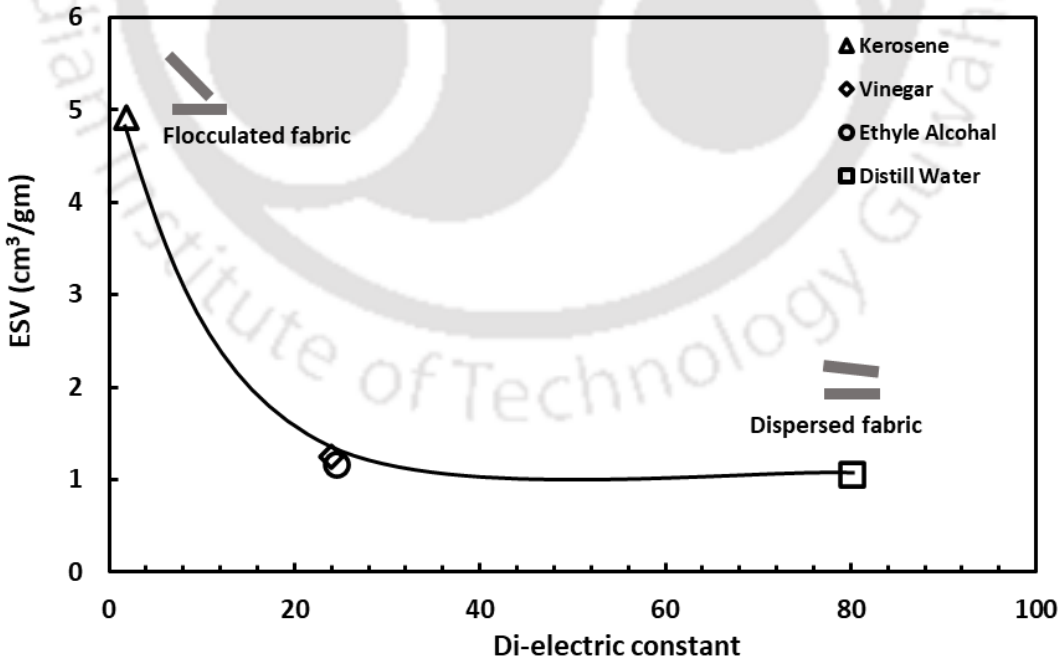

Fig. 3.6. Variation of equilibrium sediment volume with di-electric permittivity of pore fluids.

mediums (distill water, ethyl alcohol, vinegar, and kerosene) on the deposition behaviour of kaolin. The schematic diagram of the sediment volume test was shown in Fig. 3.7.

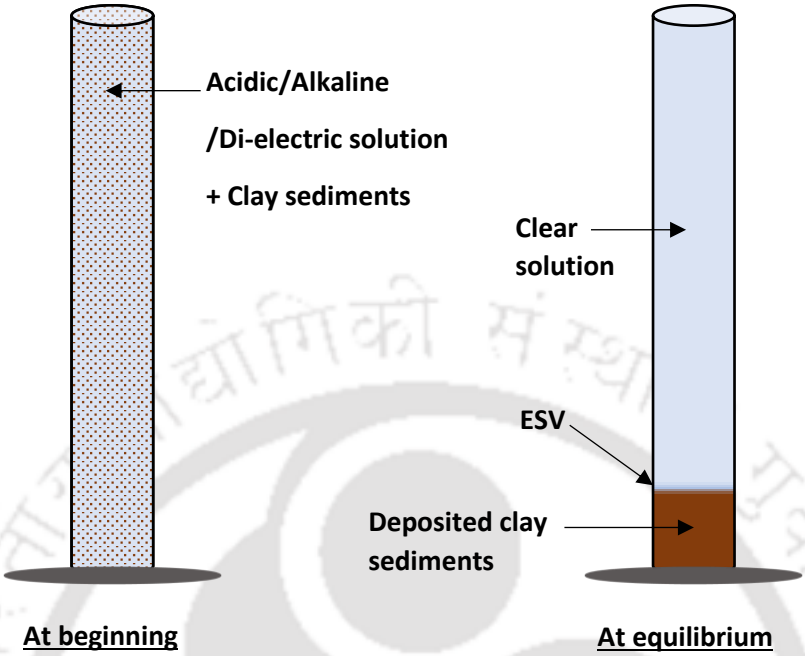

Fig. 3.7. Schematic diagram representing sedimentation behaviour of clay sediments.

3.2.1 *Suction-Controlled Compression Tests*

The influence of the initial compaction state on the volume change and yield response was studied in suction-controlled oedometer tests, as shown in Fig. 3.8. The K1 soil sample from *P* (Fig. 3.4) was loaded under K_o -condition to follow the stress path *PQU* as shown in Fig. 3.9. A duplicate specimen was saturated to follow *QT* stress path and consolidated along *TX*. Further, the suction in these tests was controlled by the osmotic technique (Bharat & Gapak, 2021). A semipermeable membrane was placed between the compacted specimen and porous stone to control the osmotic suction. The osmotic cell was connected to the polyethylene glycol (PEG) solution in a burette. The osmotic flow of water from the PEG solution to the clay chamber took place to equalize the total head across the membrane (Delage et al. 1998). The PEG solution concentration in the burette was monitored frequently by measuring the refractive or brix index using a commercially available optical, handheld Brix refractometer. A constant value of the Brix index indicated an equilibrium

Fig. 3.8. Laboratory oedometer set-up.

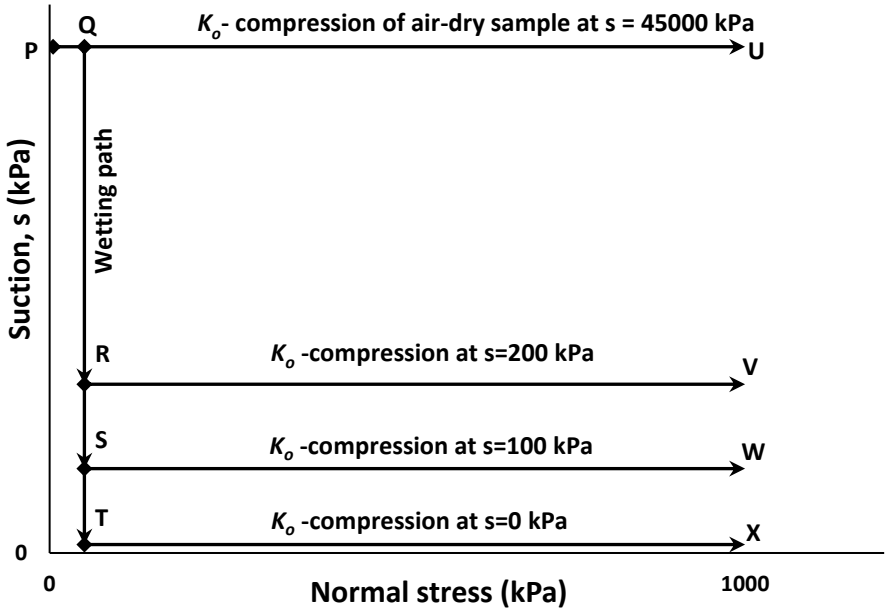

Fig. 3.9. One-dimensional compression and wetting from the air-dry state for K1.

suction across the membrane. The K1 soil samples were partly saturated (wetting load) by following *PQS* and *PQR* to achieve equilibrium suction values of 100 kPa and 200 kPa, respectively, and increased the mechanical load from 5 kPa to 1000 kPa as shown in Fig. 3.9 along *RV* and *SW*. Only the air-dry compression data of K2 were available from Choudhury (2019) and considered in this study.

A compaction state of MDD and OMC represented by *A* in Fig. 3.10 was considered for K1 to study the influence on yielding characteristics. Sample of K1 was statically compacted in an oedometer ring at initial state *A*. The sample was subjected to a mechanical seating load

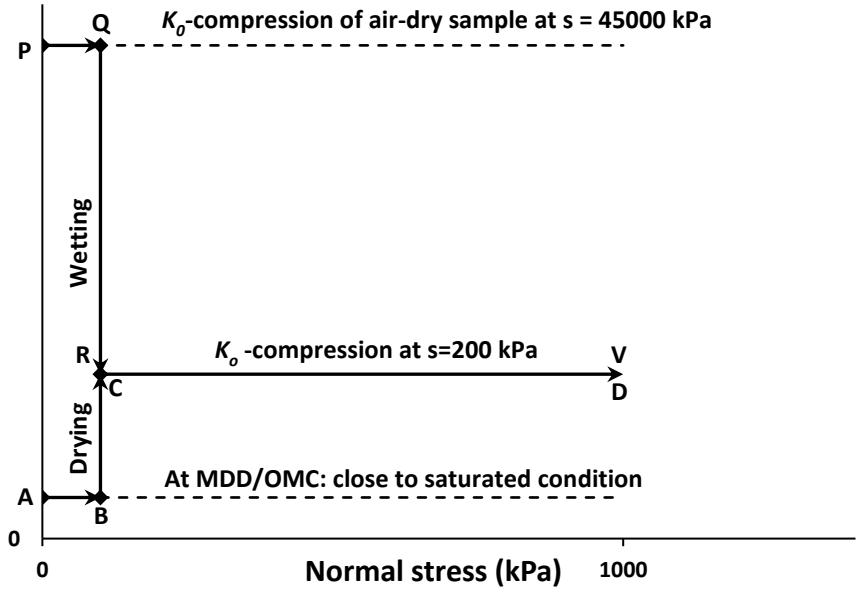

Fig. 3.10. One-dimensional compression followed by suction loading and unloading paths from different initial compaction states of K1.

of 5 kPa represented by *B*, then increased suction to 200 kPa along *BC* and subjected to a mechanical load along *CD*. The influence of the initial fabric of the compacted soil K1 on the yielding behaviour was also studied through field emission scanning electron microscopy (FESEM) image analysis on lyophilized samples (Choudhury & Bharat, 2018) at *Q*, *R* along the wetting path and *B*, *C* along the drying path (Fig. 3.10) by carefully extruding with less disturbance and preserving the fabric.

3.2.2 *Wetting Tests*

Inundation tests were carried out to investigate the influence of initial suction and normal stress on the collapse behaviour by standard procedure (Choudhury & Bharat, 2018, ASTM 2021). Each air-dry compacted sample of K1 in K_o-condition was subjected to normal stress and inundated with distilled water to study the volume change response. Independent one-dimensional compression and inundation tests were conducted in an oedometer at various normal stresses. Test paths for inundation tests were *QC*, *DE*, *FG*, *HI*, *JK*, *LM*, and *NO* after respective air-dry compression paths of *PQ*, *PD*, *PF*, *PH*, *PJ*, *PL*, and *PN*, as shown in Fig. 3.11.

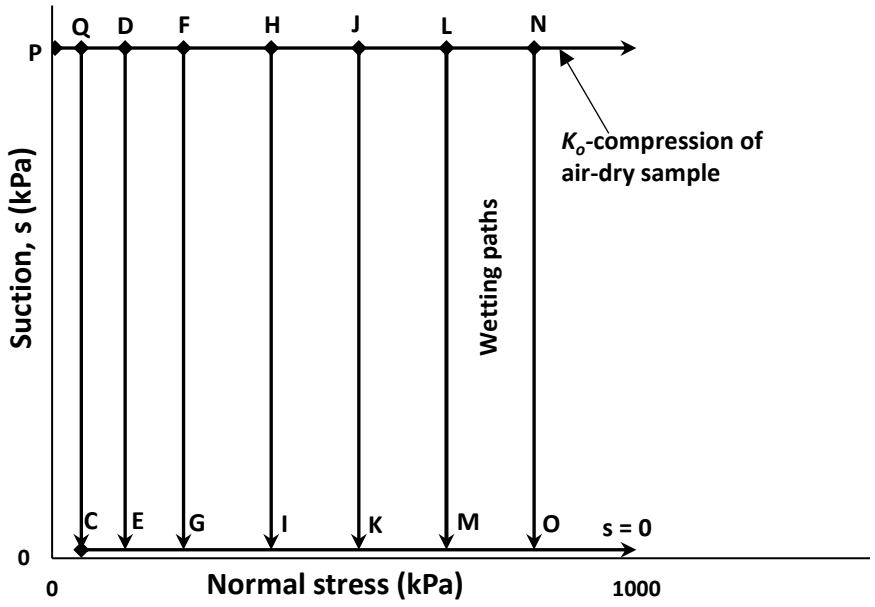

Fig. 3.11. Wetting under multiple inundation pressure from air-dry states for K1.

The results of volume change during collapse for soil K2 due to variation in suction under various normal stresses was considered from Choudhury (2019), and the stress paths were described here. Three independent controlled wetting tests, Test-I, Test-II, and Test-III, were performed under normal stresses of 100, 400, and 800 kPa, respectively, as shown in Fig. 3.12. Initially, compacted soil K2 at state *L* in air-dry conditions was bring to points *M*, *N*, and *O* by load increments in Test-I, Test-II, and Test-III in oedometer set-up. Subsequently,

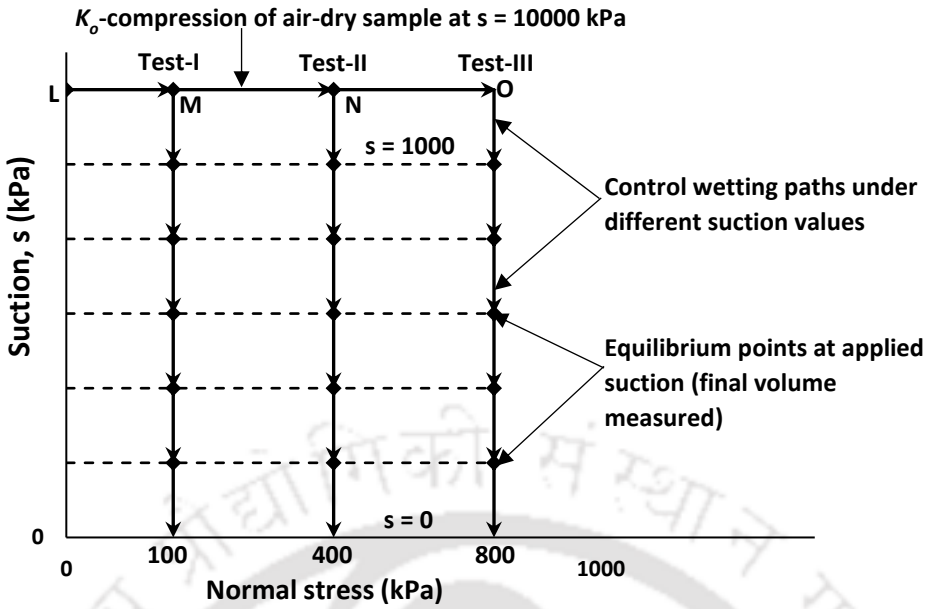

Fig. 3.12. K_o – compression and wetting stress paths for K2.

the samples were inundated in staged-suction unloading similar to K1 soil, as discussed in the previous section. The final deformation at each suction unloading stage under a given normal stress was recorded. The collapse response was captured in the suction range of 10000 to 0 kPa at different normal stresses. The complete stress paths of wetting experiments for soil K2 are presented in Fig. 3.12. The procedure used to generate the wetting response for soils K1 and K2 was similar to the methods described by Jotisankasa et al. (2007) and Mu et al. (2020). The effect of inundation pressure, consolidation pressure, and pore fluid chemistry on the mechanical characteristics of kaolin was investigated using two different tests: equilibrium sediment volume (ESV) and torsional ring shear tests.

Further, the effect of inundation pressure, consolidation pressure, and pore fluid chemistry on the shear strength characteristics of kaolin K1 was investigated using torsional shear experiments.

3.2.3 *Ring Shear Tests*

The torsional or ring shear device used in this study for the experiments is the Bromhead ring shear apparatus manufactured by CONTROLS Group, Italy. The ring shear device has

several advantageous over the standard triaxial and direct shear testing apparatus for clay specimens for studying the shear behaviour. The ring shear test is useful for quickly determining the drained shear strength due to a short drainage path through a very thin soil specimen. The cross-sectional area of the shear surface is constant during shearing, and unlimited rotational deformation in one direction is applied to achieve minimum constant residual strength. As a result, the whole shear resistance profile is established, from which the peak, critical, and residual shear strengths can be evaluated. The laboratory ring shear set-up used in this study and different components details were shown in Fig. 3.13-3.16. The

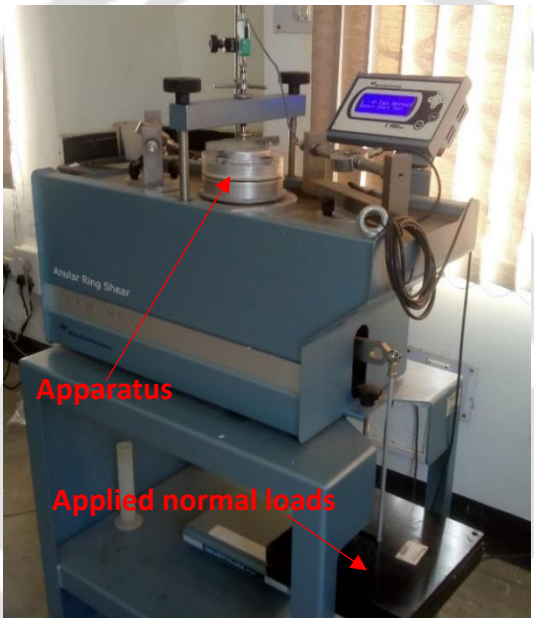

Fig. 3.13. Laboratory ring shear set-up.

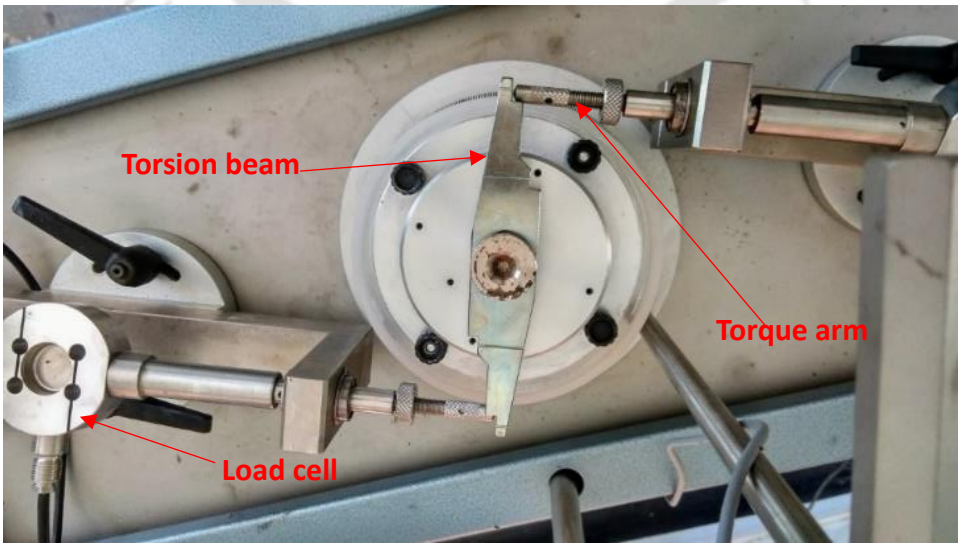

Fig. 3.14. Ring shear apparatus arrangement.

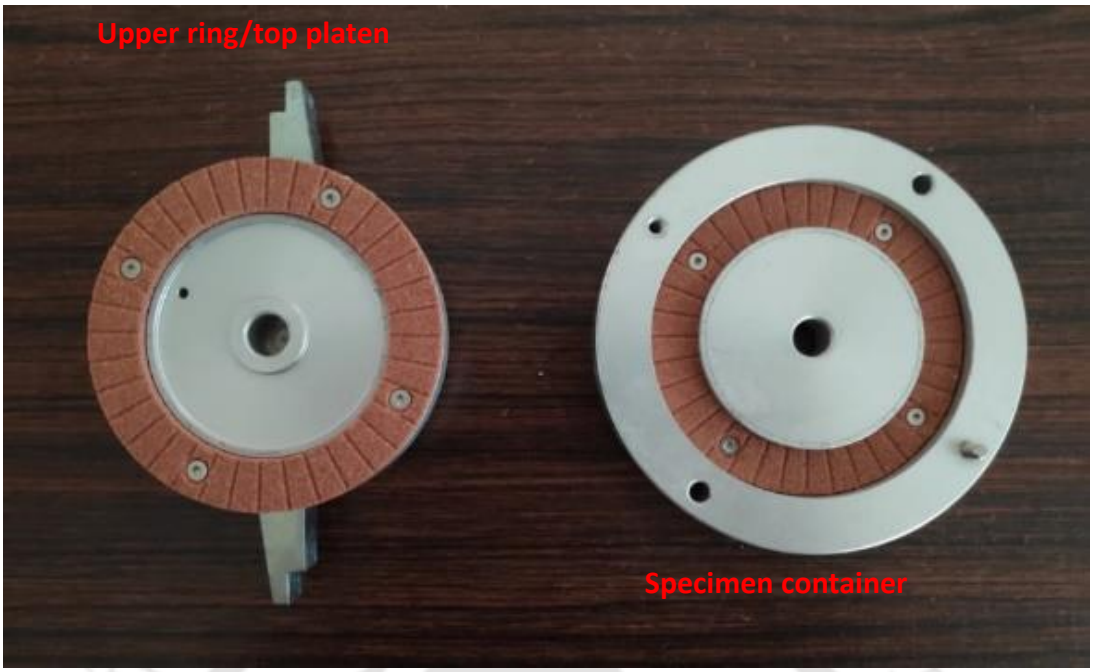

Fig. 3.15. Upper ring and lower ring/specimen container.

soil specimen for the ring shear device was annular with an inner diameter of 70 mm, outer diameter of 100 mm, thickness of 5 mm, and shear surface area of 4000 $mm^{2,}$ as shown in Fig. 3.16. The ring shear specimen is annular so that the variation in shear stress from the inner edge to the outer edge will be uniform, and hence a constant value of shear stress can be measured across the cross-section at a time.

In this test, a lower ring containing specimen is subjected to continuous rotation in one direction at a slow fixed rate against the top upper fixed ring during the shearing. A horizontal shear surface is formed at the interface between the upper and lower rings. The shear force, vertical deformation, and rotational shear deformation were measured at the shear surface until a constant value of drained shear resistance was obtained

The oven-dried soil specimens were statically compacted in the annular space of a lower ring container by utilizing an unconfined compression soil testing device at a dry density of 1.3 Mg/m^3. The experiments were conducted in two phases on the prepared soil specimens in accordance with the standard (ASTM. D6467: 2021). In the first phase, compression, inundation (saturation), and consolidation were carried out under the application of pre-

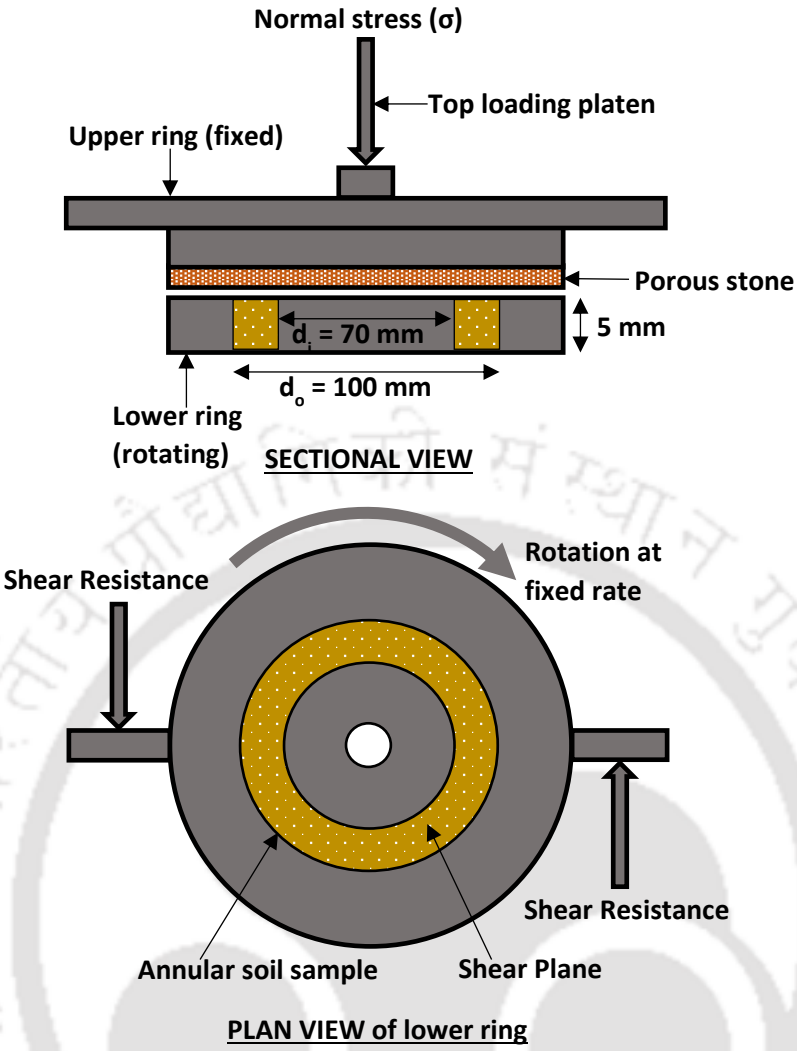

Fig. 3.16. Schematic diagram of torsional ring shear device.

determined normal stresses in stages through the top loading platen (Fig. 3.16). During the second phase, the drained shearing was performed on the inundated/consolidated specimens at a slow displacement rate of 0.037 mm/min (0.05°/min) to avoid excess pore water pressure generation, and hence drained condition was maintained throughout the shearing phase.

Investigation of the influence of inundation pressure on the shear strength and volume change behaviour was made by ring shear test. Four separate compacted specimens in the consecutive independent experiments were initially compressed to normal stresses of 200, 450, 700, and 950 kPa, respectively. The compressed specimens were inundated with distilled water, and the samples were allowed to come to equilibrium. After reaching

equilibrium states, all the specimens were subjected to drained shearing at a constant displacement rate until shear resistance became constant at extensive shear deformation to achieve the residual conditions. Further, to investigate the effect of consolidation pressure on the soil mechanical response, the three duplicate compacted samples were subjected to compression until 200 kPa. All specimens were saturated with distilled water under 200 kPa vertical normal stress. After allowing them to reach their equilibrium states, each sample consolidated to 450, 700, and 950 kPa separately. At the end of the consolidation phase, every specimen was sheared under the drained condition at a constant deformation rate until the residual state was reached.

The physico-chemical effect on kaolin behaviour was investigated by varying the pore-fluid solution instead of distilled water. Six separate ring shear tests were conducted on the compacted kaolin specimens in two phases. In the first phase, all samples were compressed to 450 kPa. Four samples were then saturated with aqueous solutions of varying pH = 2, 3.2, 4.5, and 6. The remaining two specimens were inundated with kerosene and vinegar, respectively. Every sample was allowed to attenuate the equilibrium state, and then shearing was performed at a constant strain rate to attain residual conditions.

Moreover, field emission scanning electron microscopy (FESEM) tests were conducted to examine the clay fabric evolution of saturated samples with different pore fluids (pH and di-electric mediums) and sheared samples under different inundation and consolidation pressures. At the end of each test, samples were carefully extracted from the annular specimen container with minimal disturbance. In order to preserve the soil structure, the extruded samples were lyophilized using freeze and drying approach. The samples were frozen at a very low temperature of -60 C using a sublimation method, then dried for around 4 hours by applying a vacuum at a pressure of -756 kPa. In the end, lyophilized samples

underwent FESEM image analysis to compare and analyse the soil structure associations at selected states.

3.2.4 *Laboratory Study of Chemical Stabilization of Kaolin*

The modern and suitable stabilization technique, such as alkali-stabilization to form geopolymer, was explored to reduce the collapse potential of kaolin soil. A series of compression and wetting tests on compacted geo-polymerized kaolin were conducted in an oedometer.

The sample preparation was done to simulate the field procedure similar to sand drains. Compacted kaolin was treated with a mixture of sodium hydroxide (NaOH) as alkali agent and sodium silicate (Na_2SiO_3) as an activator to synthesize the kaolin geopolymer. The NaOH solution with distilled water and the Na_2SiO_3 solution with distilled water were prepared by stirring for 1 hour (Coudert et al., 2022; Vitale et al., 2017). An alkali activator solution was produced by mixing the prepared sodium hydroxide solution at 4, 10, 12, and 14 mol/L with the sodium silicate solution at a ratio (Na_2SiO_3/NaOH) of 0.25 by the mass for one hour at a temperature of 80° C (Heah et al., 2013; Wang et al., 2005).

The oven-dried kaolin powder was statically compacted for a 10 mm depth by a plunger, and the plunger simultaneously drilled five symmetrical cylindrical columns (pattern *A)* of diameter 7 mm and depth 9 mm in the dry soil mass. The Brahmaputra sand was loosely filled in the drilled columns with the help of a conical funnel, as shown in Fig. 3.17. The prepared alkali activator solution was poured into the sand columns, as shown in Fig. 3.18. The sand columns were intended to distribute the alkali solution uniformly throughout the volume of compacted soil. The prepared soil samples with varying concentrations of alkali activator solution were placed inside oedometer cells and cured for eight days at ambient conditions to initiate the geo-polymerization reactions. The purpose of keeping a curing time

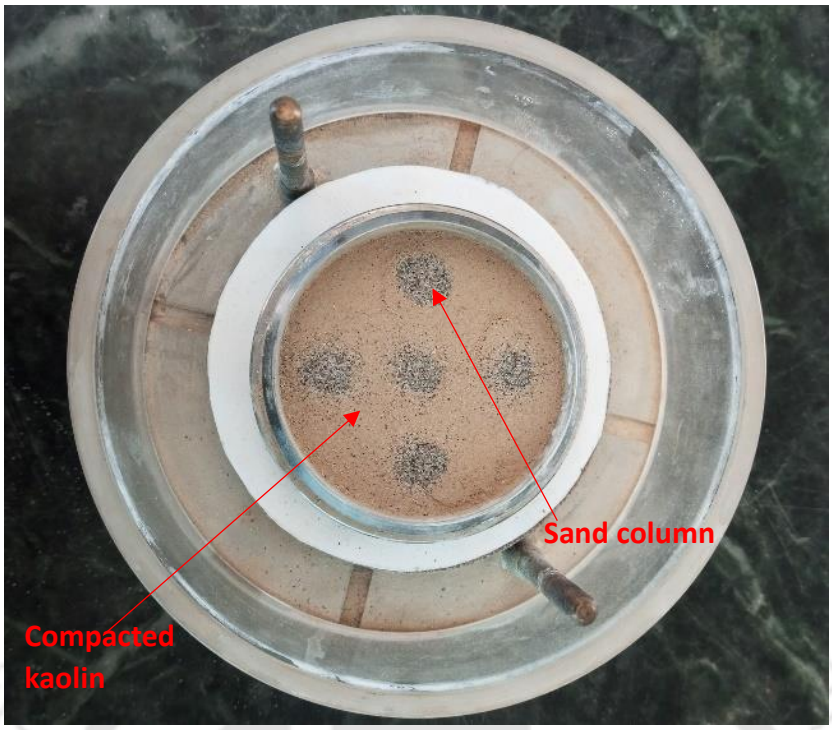

Fig. 3.17. Kaolin samples compacted in **pattern *A*** inside the oedometer ring: Moment before the application of alkali activator solution.

Fig. 3.18. Kaolin samples compacted in **pattern *A*** inside the oedometer ring: Moment just after the application of alkali activator solution.

of 8 days was to gain optimum stiffness (Coudert et al., 2022). Similarly, another pattern *B* of the sand columns group (Fig. 3.19(a) and 3.19(b)) was adopted to investigate the effect of the geometry of the columns group on the mechanical response. Further, one-dimensional compressions and inundation tests at vertical pressures of 50, 100, and 800 kPa were carried out on the two different patterns *A* and *B* of compacted kaolin samples treated with 4, 10, 12, and 14 mol/L concentrations of alkali activator solution (NaOH and Na_2SiO_3). Finally, X-ray diffraction (XRD) tests were carried out on the treated samples extruded from the oedometer ring under given inundation pressures. The XRD analysis was done to investigate the formation of new compounds or minerals due to geopolymerization reactions in kaolin and sand samples.

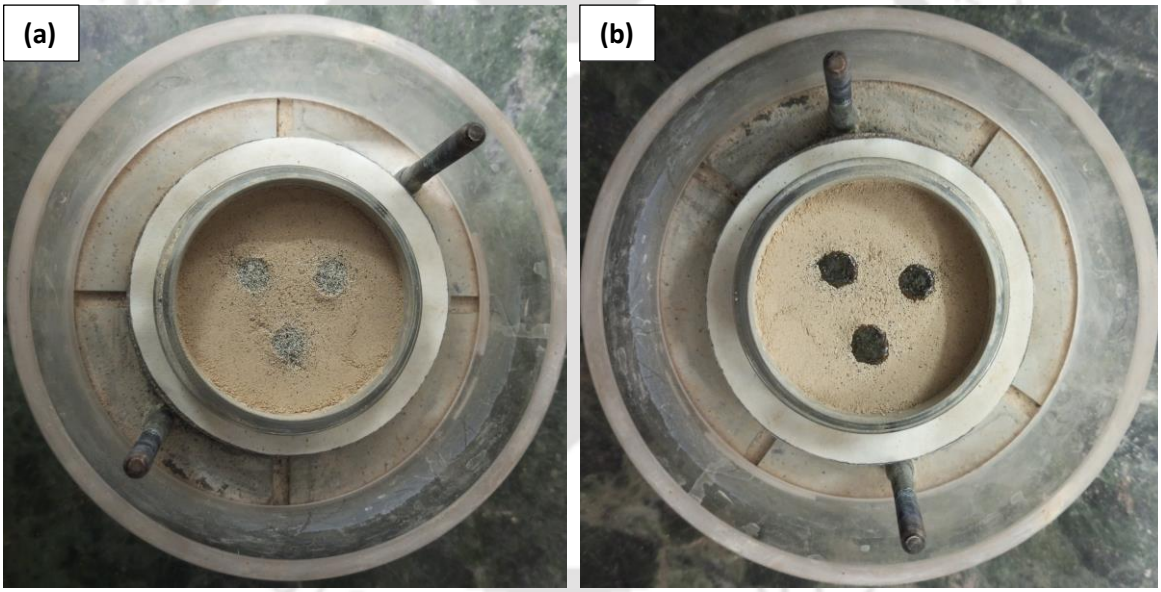

Fig. 3.19. Kaolin samples compacted in **pattern *B*** inside the oedometer ring: (a) Moment before the application of alkali activator solution, and (b) Moment just after the application of alkali activator solution.

Chapter 4

Experimental Study on Influence of Initial Suction and Normal Stress on Mechanical Behaviour of Air-dry Compacted Kaolin Clays

4.1 General

In chapter 2, from the literature analysis, it was observed that the initial compaction characteristics such as suction/moisture content, soil particle arrangements, and density could significantly control the unsaturated mechanical behaviour of compacted collapsible soils. Under the influence of such parameters, the mechanical behaviour of unsaturated air-dry compacted kaolin soils has never been explored. Therefore, in this chapter, the influence of initial conditions, including matric suction, clay fabric, and initial dry density, on the compression, yielding, and collapse behaviour was investigated experimentally.

4.2 Results and Discussion

4.2.1 *Compression and Wetting Response*

The one-dimensional air-dry compression and consolidation data of K1 are shown in Fig. 4.1. The consolidation and air-dry compression curves meet at a specific normal stress designated as a transition point and where corresponding normal stress was referred to as a transition normal stress. The transition point in Fig. 4.1 represents the mechanical load corresponding to no volume change due to wetting. The results of various wetting tests performed were shown in Fig. 4.1 with dark circle legends. The measured wetting-induced volumetric response was in agreement with the past results on compacted kaolin (Sridharan et al., 1973; Josa et al., 1992). The equilibrium void ratio at higher mechanical loads ($\geq$ 400 kPa) was smaller than the consolidation void ratio at the same mechanical loading. The soil samples saturated at normal stress less than transition normal stress exhibited swelling with the final equilibrium void ratio at the consolidation curve. Similar observations were made

for soil K2, as shown in Fig. 4.2. A series of suction-controlled compression tests (Fig. 4.1) were also carried out to investigate the effect of suction on the compression and wetting

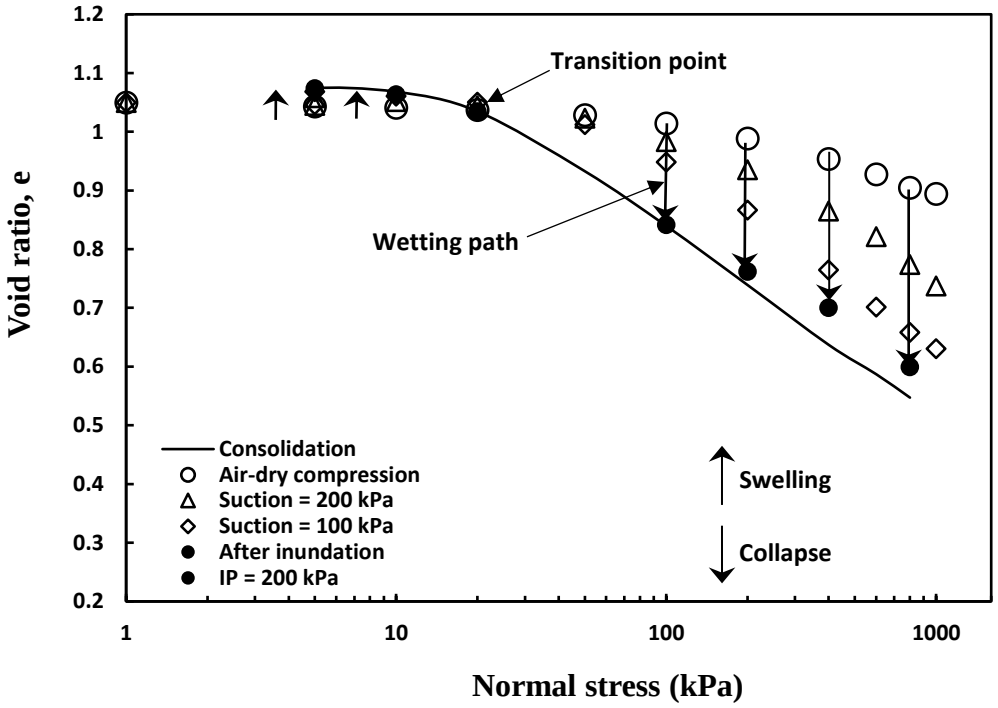

Fig. 4.1. Compression and wetting under different inundation pressures for the soil K1 compacted at state P.

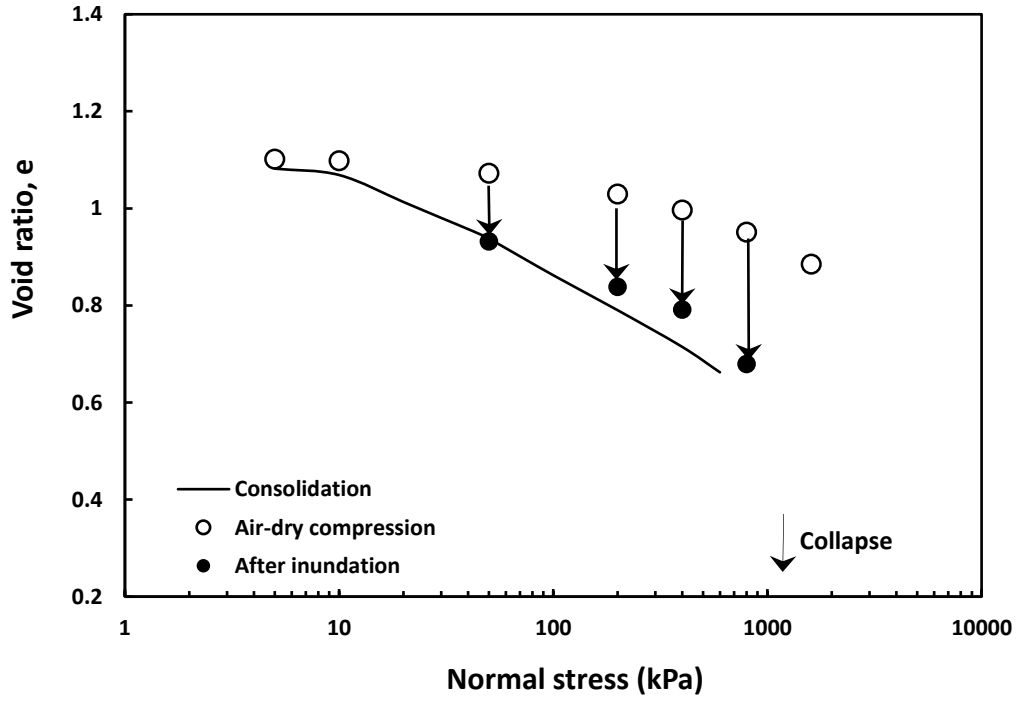

Fig. 4.2. Compression and wetting under different inundation pressures for the soil K2 compacted at dry density 1.25 Mg/m^3 (Choudhury 2019).

characteristics of initially air-dry compacted K1. The influence of initial suction on the wetting-induced collapse response was analyzed under different normal stresses (Fig. 4.1).

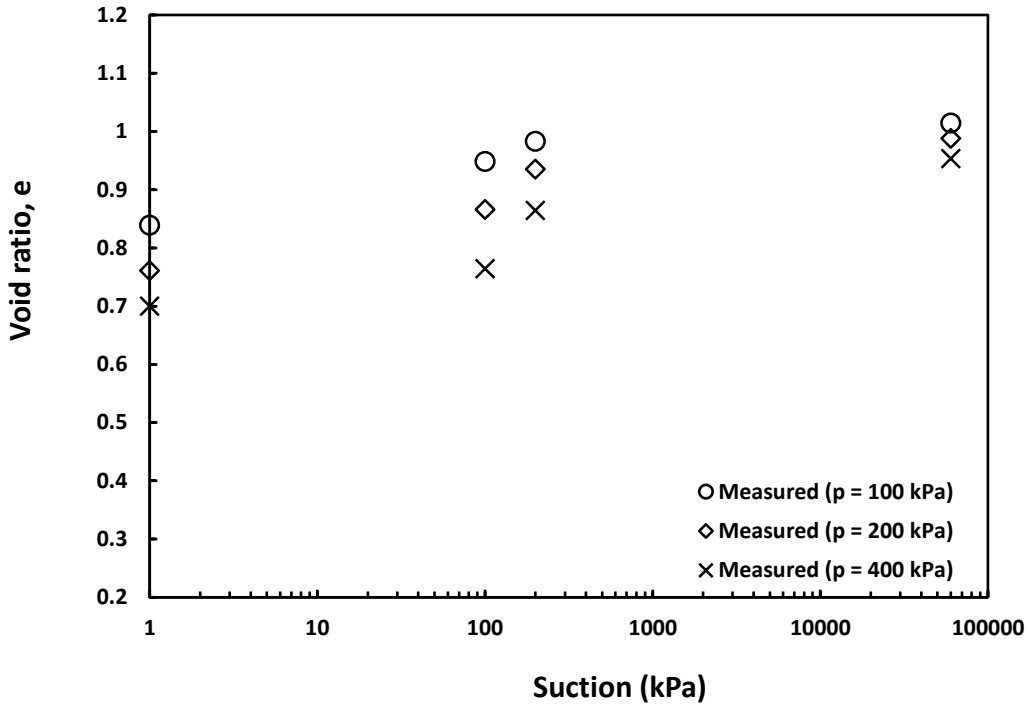

Fig. 4.3. Variation of volume during the wetting process under different inundation pressures for the soil K1 compacted at state P.

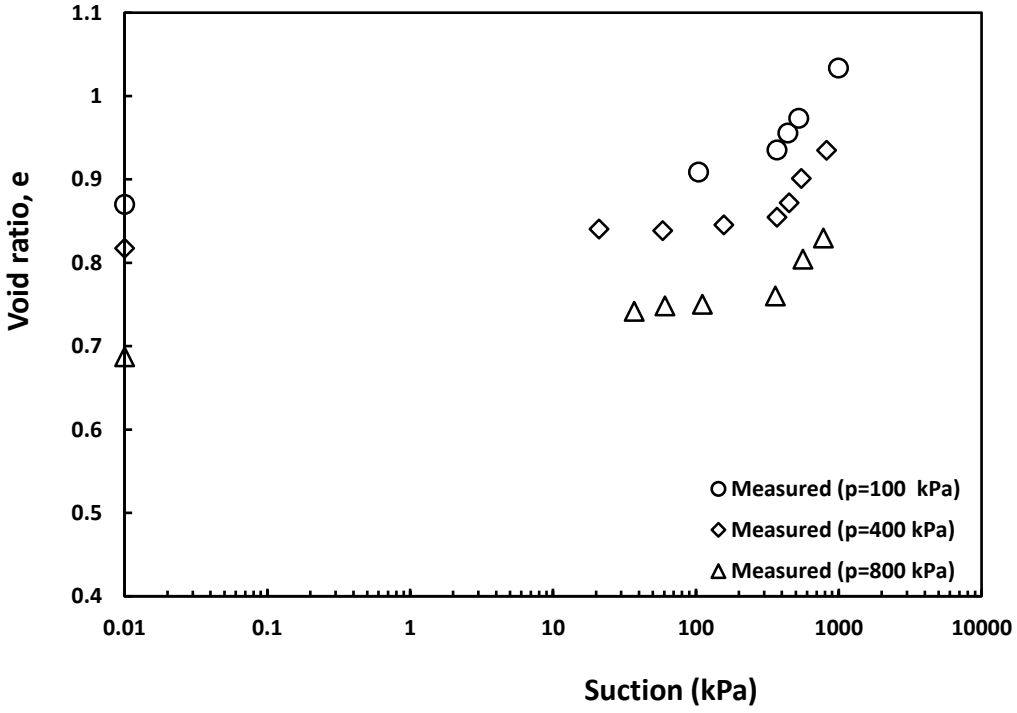

Fig. 4.4. Variation of volume during wetting process under different inundation pressures for the soil K2 compacted at dry density 1.25 Mg/m^3 (Choudhury 2019).

The Fig. 4.3 shows the variation in the measured equilibrium void ratios along the wetting paths under different normal stresses for K1. The wetting-induced volume change response for soil K2 was shown in Fig. 4.4 for the wetting paths discussed in Fig. 3.9. The void ratio decreased significantly due to wetting up to the water-entry value and then achieved a nearly constant void ratio up to full saturation (Choudhury 2019).

4.2.2 *Yield Locus*

The development of a yield curve requires experimental observations of compression behaviour at different constant suctions through wetting and loading stress paths and then identification of yield points on the compression curves. The yield curve illustrates the increase in yield stress associated with increasing suction and the collapse phenomenon observed during the wetting process. This is the reason the yield curve is also called a loading-collapse (LC) curve. Accurate yield stress determination is difficult when compression data changes smoothly with loads, as in the current study. Studies of Jose et al. (1989); Sridharan et al. (1991); Prakash et al. (2014); Prakash & Sridharan (2020) based on experimental validations showed that the Log-Log method is the most accurate technique for the determination of yield stress. The Log-Log method is superior among several methods Casagrande method (Casagrande 1936), Burmister method (Burmister, 1952; Burmister, 1942), Schmertmann method (Schemertmann, 1955), void index method (Burland, 1990), Log-Log method (Jose et al., 1989), Jacobsen's method (Jacobsen, 1992), etc. Apart from the Log-Log method, the Casagrande approach has been the only one used, despite certain inherent disadvantages, including the fact that it relies heavily on judgment calls made by the individual, which leaves room for error. It was discovered that the Casagrande technique overestimates yield stress, resulting in unsafe settlement predictions. However, the Log-Log method is free from scale effects and gives relatively conservative yield stress values. Other proposed methods could not get widespread acceptance since they

required too much time and effort and lacked accuracy and clarity. Therefore, Log-Log method (Jose et al., 1989) was used in the present study (Fig. 4.5) to determine the yield stress accurately.

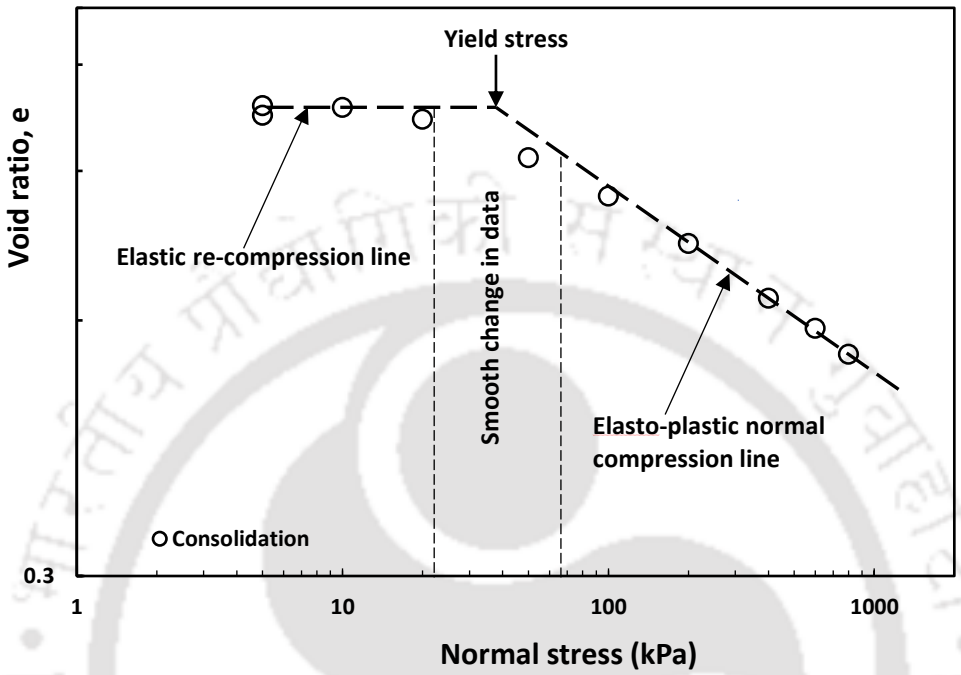

Fig. 4.5. Illustrating the estimation of the yield stress for a typical consolidation curve from the Log-Log technique.

The estimated yield stresses of air-dry compacted soils K1 and K2 for different compression curves were shown in Fig. 4.6 and Fig. 4.7. The Fig. 4.8 shows the plot of the LC curve by BBM, along with the measured data. Table. 4.1 provides the BBM parameters inputted for the prediction. A significant discrepancy in the modeled LC response was found when compared to the measured data. The deviation by BBM was discussed from the microstructural perspective in the following section.

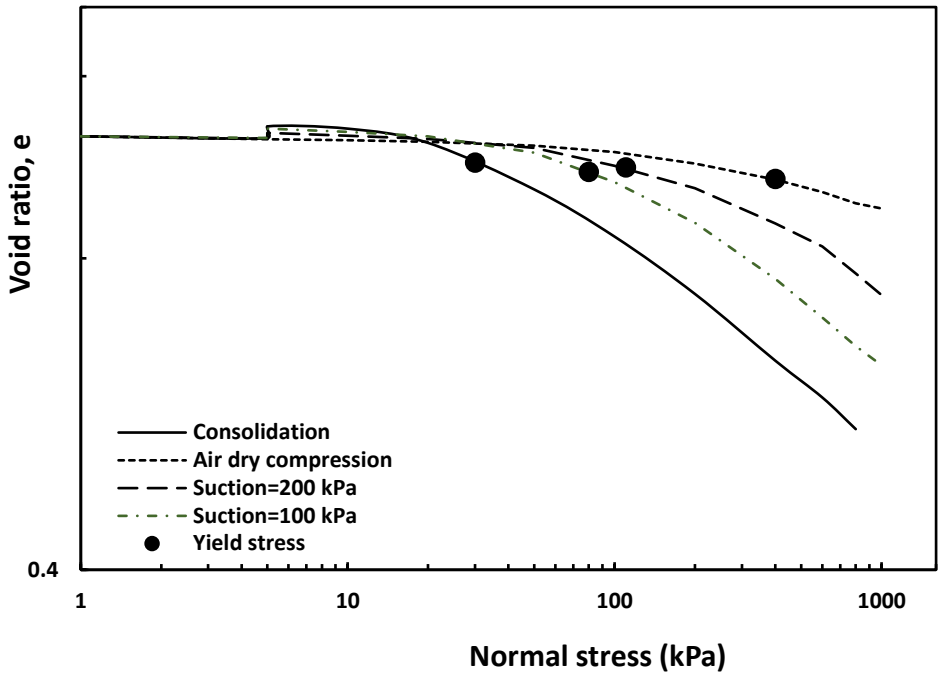

Fig. 4.6. Identification of yield stress for soil K1 compacted at state P.

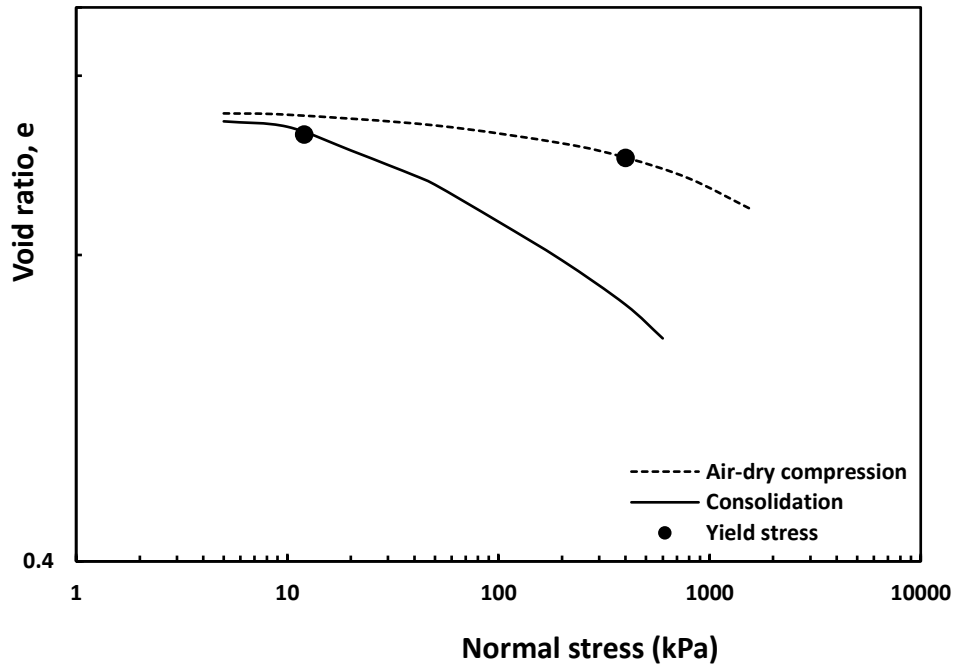

Fig. 4.7. Identification of yield stress for soil K2 compacted at dry density 1.25 Mg/m^3.

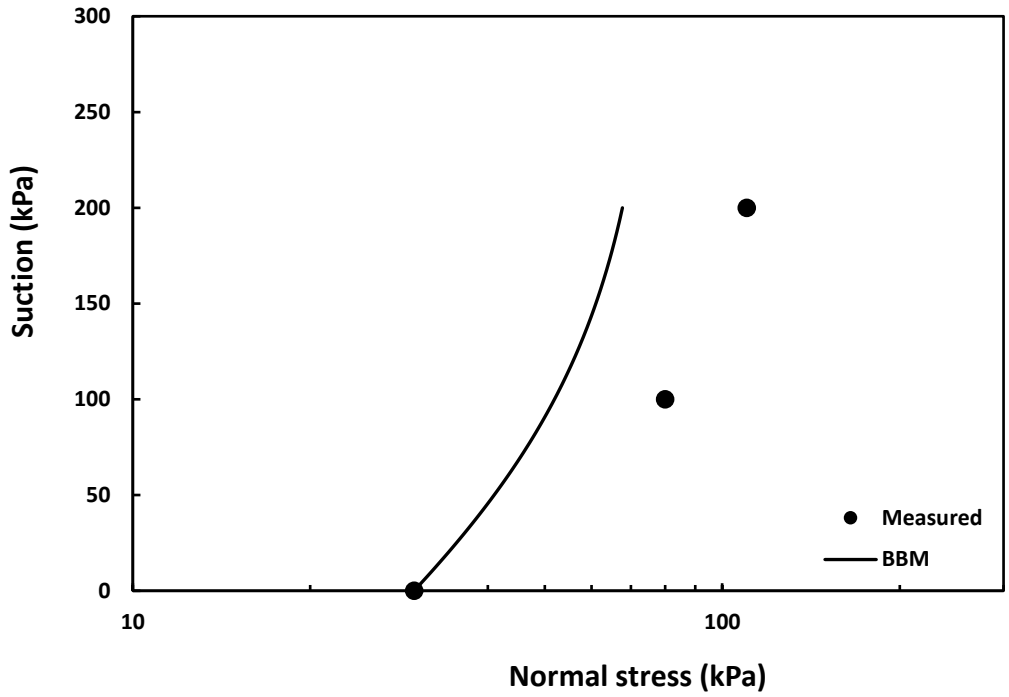

Fig. 4.8. Comparison of experimental loading- collapse yield curve with the predicted BBM for the K1 compacted at air-dry state A.

Table 4.1. Initial conditions and BBM model parameters for the studied kaolin soils.

Soil type	Dry density (Mg/m^3)	Initial degree of saturation, S_r (%)	Initial matric suction, s (kPa)	BBM parameters					
				$\lambda(0)$	$\kappa(0)$	$P_y(0)$	r	β (kPa^{-1})	p^c (kPa)
K1	1.3	6.34	45000	0.138	0.028	30	0.72	0.011	5
K2	1.25	7.17	10000	0.101	0.019	12	-	-	-

4.2.3 *Influence of Fabric Orientation*

Comparison of the measured yield data with the predicted yield curve by BBM (Fig. 4.8) showed a significant underprediction of yield stresses with the increase in the suction values. Some past researchers (Alonso et al., 1987; Sivakumar & Wheeler, 2000; Wheeler et al., 2003) opined that the yielding of collapsible soil compacted on dry of the optimum is affected by the orientation of soil fabric. Thus, tests were conducted by the procedure mentioned in Fig. 3.10 to study the influence of the initial fabric arrangement of K1 at the

following states B, C, Q, and R. The FESEM micrographs were analyzed at the states mentioned above and presented in Fig. 4.9-4.12. Clay fabrics orientation at state B was found

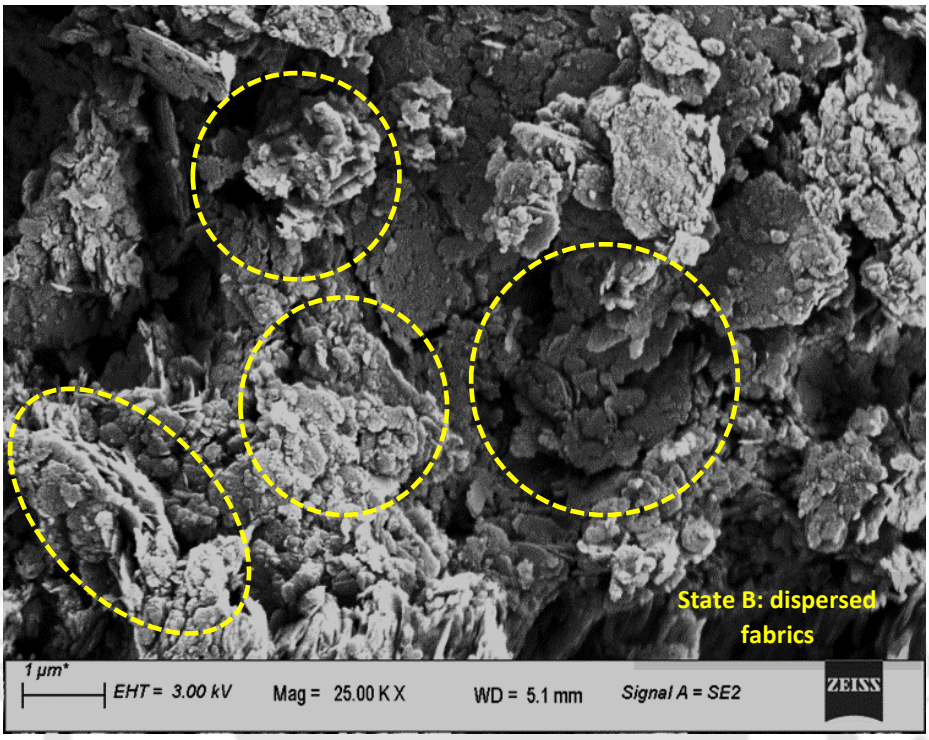

Fig. 4.9. FESEM image analysis of evolution of fabric orientation in the compacted soil K1 for the state at MDD and OMC.

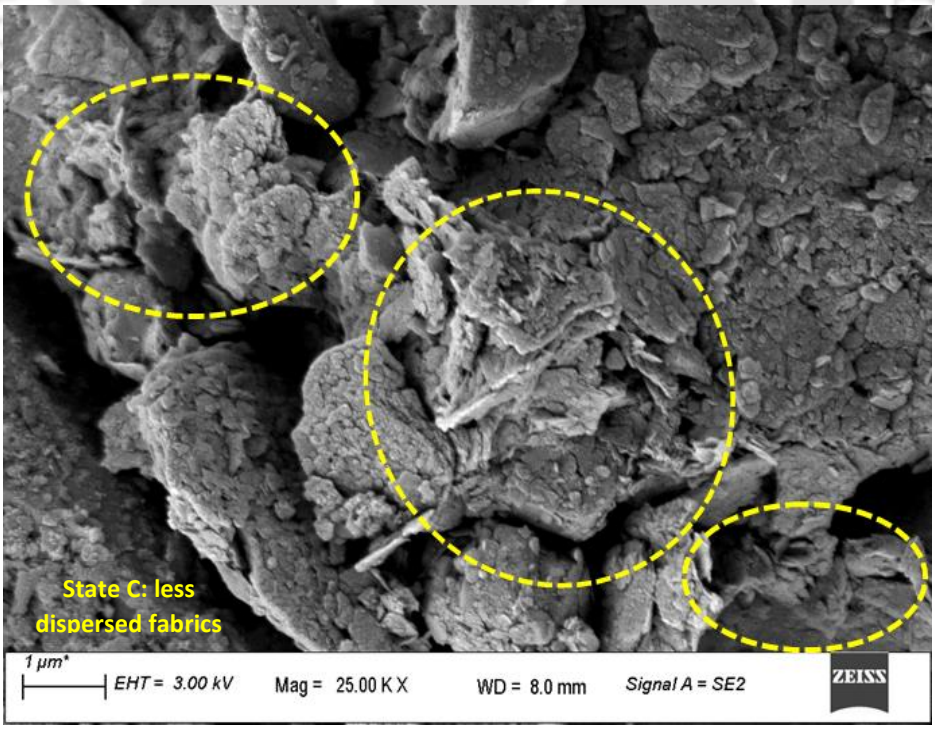

Fig. 4.10. FESEM image analysis of evolution of fabric orientation in the compacted soil K1 for the state at 200 kPa suction dried from MDD and OMC condition.

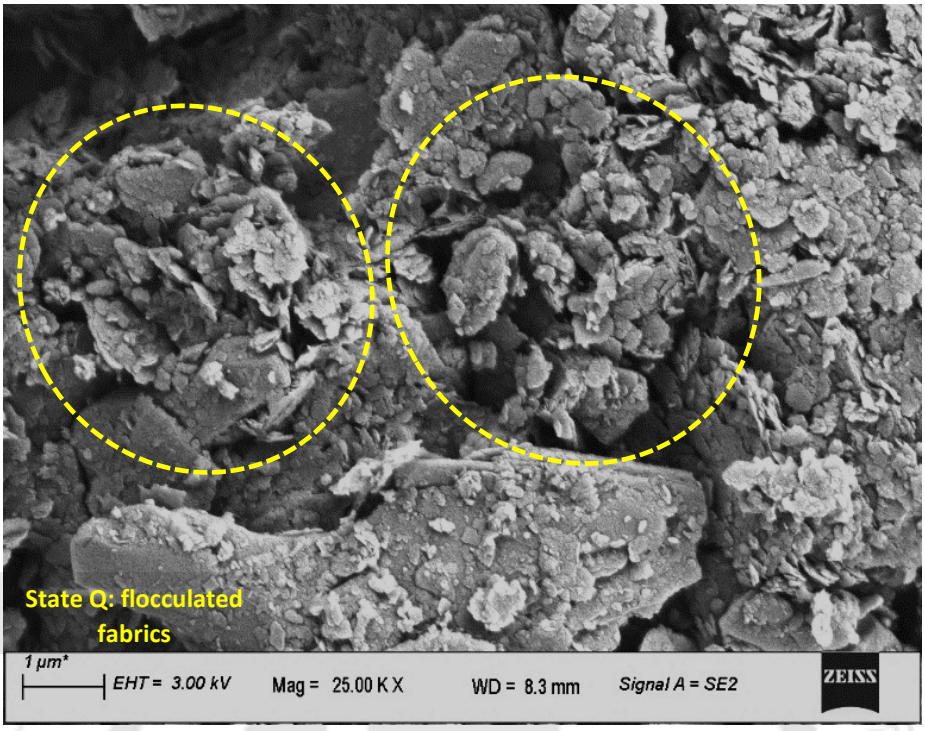

Fig. 4.11. FESEM image analysis of evolution of fabric orientation in the compacted soil K1 for the states at Air-dry state.

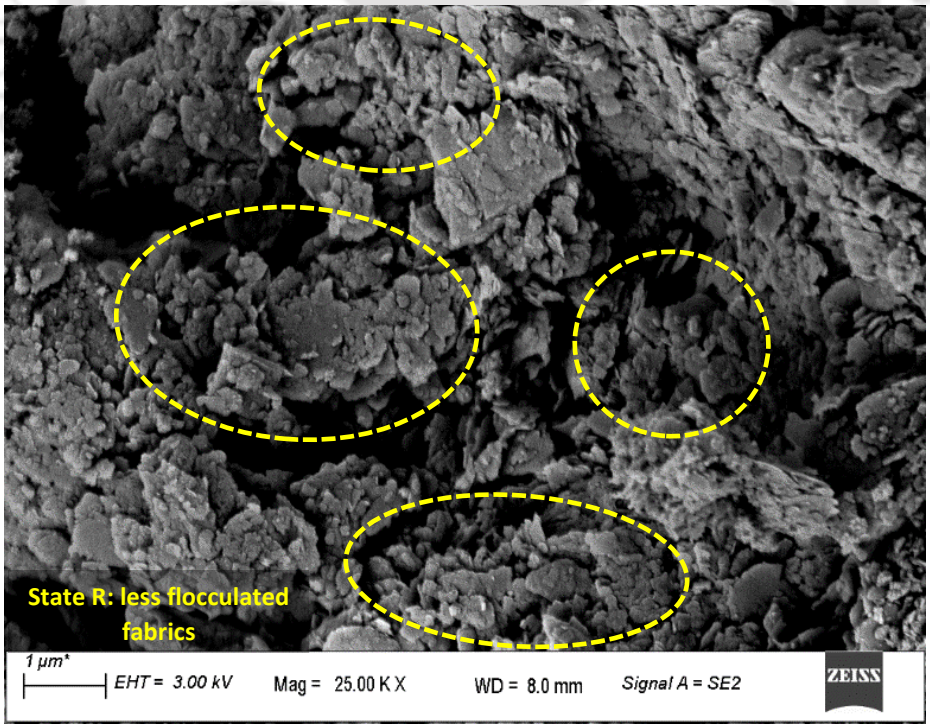

Fig. 4.12. FESEM image analysis of evolution of fabric orientation in the compacted soil K1 for the state at 200 kPa suction wetted from air-dry state condition.

to be dispersed and represented by dash boundaries in Fig. 4.9. On the other hand, the soil particles were less dispersed at state C, as shown in Fig. 4.10. The structure of particles at air-dry state Q was observed to be flocculated or in edge-to-face association (Fig. 4.11). Moreover, the connection of fabrics at the state R was less flocculated, as shown in Fig. 4.12.

The FESEM images confirm that the moisture content/suction affects the soil particle arrangement in compacted kaolin soil. Thus, the kaolin particle arrangement at different compaction and suction states was studied to explain the deviation in the estimated yielding response of the BBM from the measured data and propose a holistic model to account for the initial state of the soil. It is noteworthy to recall that all the available studies (Alonso et al., 1990; Gens & Alonso, 1992; Sivakumar & Wheeler, 2000, Sun et al., 2007b, Farulla et al., 2010; Ge et al., 2021) are at a very high degree of saturation.

A hypothesis was developed based on the evolution of clay fabric along the wetting and drying paths of soil based on the present analysis, as illustrated in Fig. 4.13. The relative change in LC yield response with the initial compaction state will be explained. The inter-

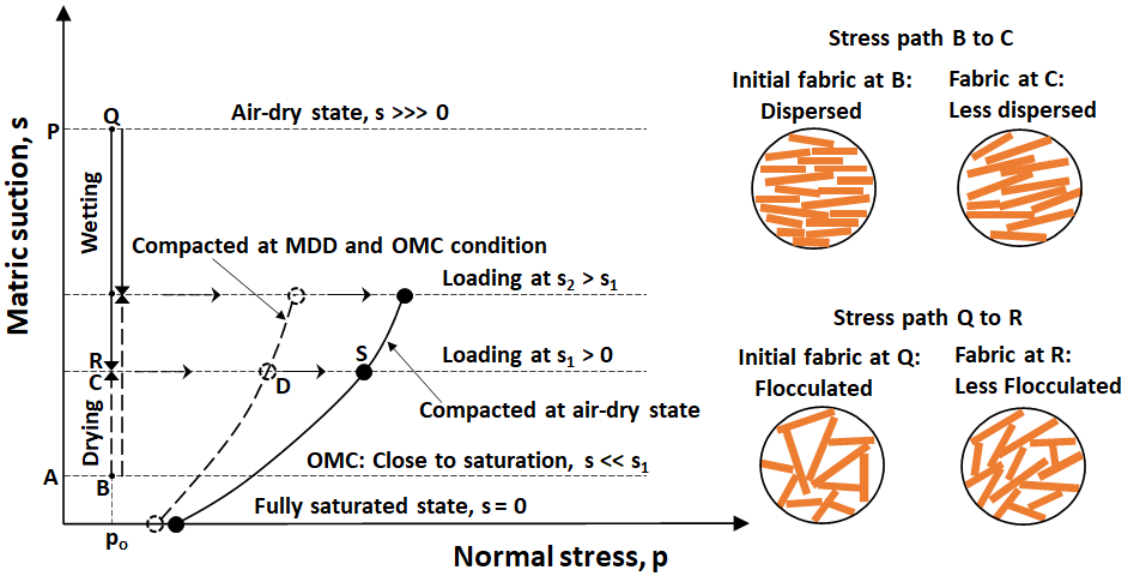

Fig. 4.13. The hypothesis of loading-collapse yield functions under different drying-wetting stress paths for compacted clay.

particle forces, such as Coulomb and Van der Waal forces, control the fabric association and elasto-plastic mechanical response of kaolin (Pedrotti & Tarantino 2014, 2018; Choudhury & Bharat, 2018). The initial state of the sample compacted at OMC was represented by B in Fig. 4.13. Kaolin edges charges turn positive to negative when adding distilled water while bringing the sample to OMC. Thus, the clay particle orientation in state B is a face-to-face configuration due to dominant coulombic repulsion between the negatively charged faces and negatively charged edges. The application of a suction higher than that at OMC (drying path BC) will decrease moisture content and increase Van der Waals's attractive forces. Therefore, particle arrangement at state C is still dominant by face-to-face configuration. Conversely, at air-dry state, Q, the clay fabric arrangement will be edge-to-face due to the existence of huge attractive coulombic forces between negatively charged faces and positively charged edges at a very low moisture content. The wetting from Q to R will cause the fabric to change from flocculated to less-flocculated. Because of pre-existing large attractive forces, particle association is likely to dominate in an edge-to-face manner. The soil sample initially brought to state R will yield at a higher stress point S, as more energy is required to yield the soil mass with edge-to-face fabric. Therefore, the soil sample that was initially compacted at air-dry conditions will have a more shift yield locus than the soil sample that was compacted initially at OMC or higher saturation

Experimental observations were presented here to support the proposed hypothesis. The measured suction-controlled compression response of the soil initially compacted in OMC and MDD was shown in Fig. 4.14. The estimated yield stress from the compression curve was 50 kPa, which is less than the yield stress for the soil initially compacted at air-dry conditions. Therefore, it can be expected that the yield curve for the soil initially compacted at OMC-MDD condition will lie left side of the yield curve for the soil compacted air-dry state, as shown in hypothesis diagram Fig. 4.13.

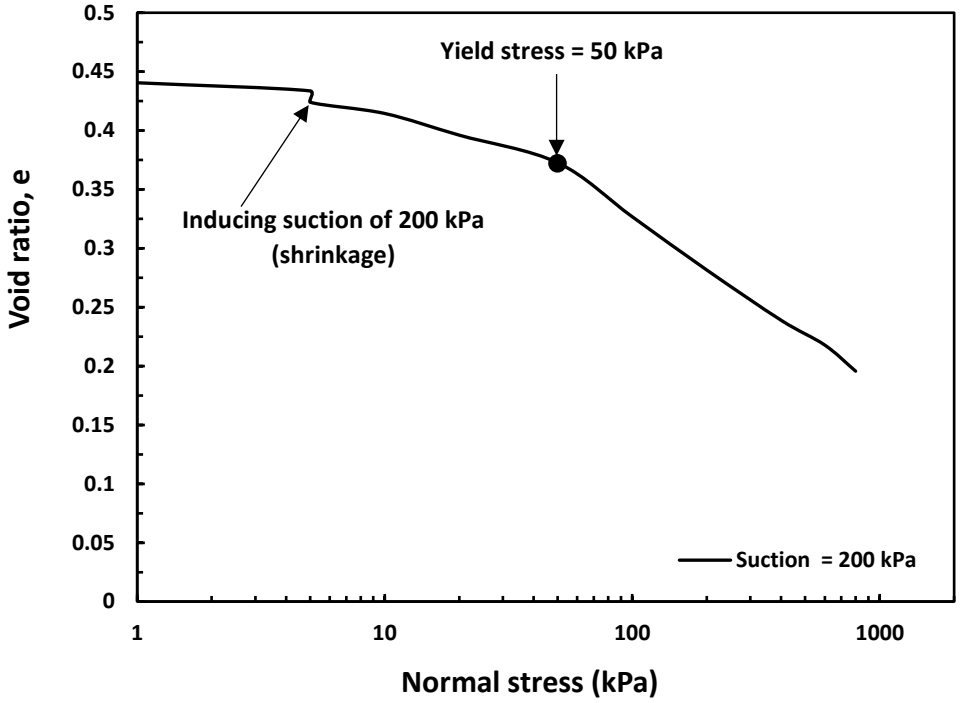

Fig. 4.14. Measured suction-controlled compression response of soil initially compacted at OMC of 14 % and MDD of 1.85 Mg/m^3.

condition will lie left side of the yield curve for the soil compacted air-dry state, as shown in hypothesis diagram Fig. 7(b).

The above discussion qualitatively explains the critical role of surface forces in controlling the mechanical behaviour of collapsible soil compacted at different initial conditions. Therefore, a predictive model that captures inter-particle surface forces is required to predict the mechanical response accurately. In the following chapter, a model framework was proposed which implicitly accommodates the particle surface forces for predicting three key mechanical behaviours of compacted collapsible soils; yielding, compression, and collapse.

4.3 Critical Remarks

This work used suction-controlled compression under K_o -conditions and wetting experiments to study the compression, yielding, and collapse behaviours of the kaolin soil samples initially compacted in air-dry conditions. The following observation were made:

1. The volume change and yielding response were highly affected by the initial moisture conditions/suction.
2. BBM was incompetent in predicting the accurate yielding response of air-dry compacted kaolin.
3. The mechanical behaviour of kaolin was depending on the initial clay fabric.
4. Inter-particle surface forces control the mechanical response of kaolin.
5. A new comprehensive predictive model is required which can model collapsible soil behaviour under different initial saturation conditions, loading stress history, and compaction stress history.

Chapter 5

Collapsible Soil Model (CoSM) for the Prediction of Mechanical Characteristics of Partially-Saturated Collapsible Soils

5.1 General

It was evident in the previous chapter that the predicted yield curve from BBM was significantly deviating from the measured, yielding response of air-dry compacted kaolin soil, as the BBM has not incorporated collapse behaviour and inter-particle electrical forces. Moreover, the applicability of other existing constitutive models was also discussed, and it was observed that most models were an extension of BBM involving additional complex parameters. None of the models incorporated wetting-induced collapse behaviour which is essential for predicting the mechanical characteristics of collapsible soils. Thus, in this chapter, a constitutive model based on a holistic framework was developed for the collapsible soils. A new model that explicitly accounts for the wetting phenomenon with collapse volume change has been formulated in this study. The purpose of the proposed model is to predict the yielding, compression, and collapse response of compacted collapsible soils. The generalized model was useful for predicting the mechanical behaviour of all types of collapsible soils with various initial compaction states and loading stress history. The proposed model showed a very good agreement with the past data on collapsible soils.

5.2 Model Framework

The theoretical development of yield locus can be understood through experimental observations of locating yield points at different suction states through wetting and loading stress paths, as shown in Fig. 5.1. The measured loading-collapse yield path was developed

by wetting various air-dry compacted samples to the desired suction values under suction-controlled environment and then subjected to incremental mechanical loadings to yield the soil samples as shown in Fig. 5.1. Consider soil samples initially compacted in air-dry

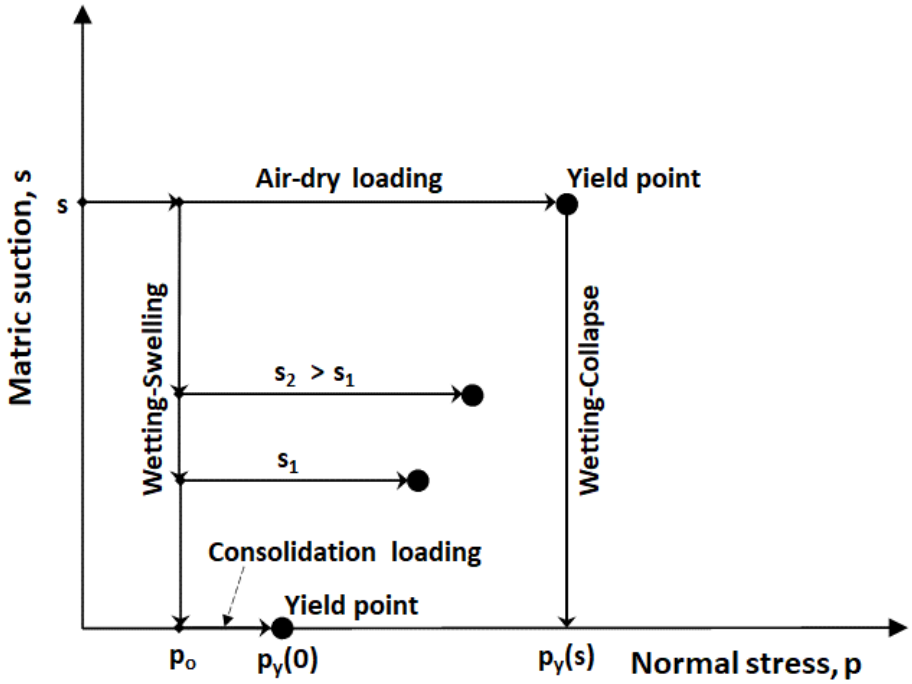

Fig. 5.1. Development of yield locus through suction unloading and mechanical loading stress paths under K_o – conditions.

condition at a very large suction *s*, and then samples are brought down by the wetting process to other smaller suction states s_1 and s_2 as shown in Fig. 5.1. Further, the application of mechanical load increments at a constant suction s_2 will yield the soil sample at higher yield stress than the sample with suction s_1. In this manner, the entire yield path will be traced with the support of wetting and compression experiments.

A mathematical relationship to describe yield function using the constitutive parameters can be developed from the measured yield behaviour. Proposed wetting and loading paths for determining the yield locus are presented in Fig. 5.2. Based on the experimental findings from this work and past observations, the compression behaviour of compacted collapsible

soils can be modeled as a combination of re-compression line *XY*, and normal compression line *YZ* (NCL) connected through yield point *Y*, as shown in Fig. 5.2. Consider the geometry of the wetting and loading stress paths in two extreme soil conditions, such as air-dry and saturated states, for integrating wetting features into the loading collapse yield function. The

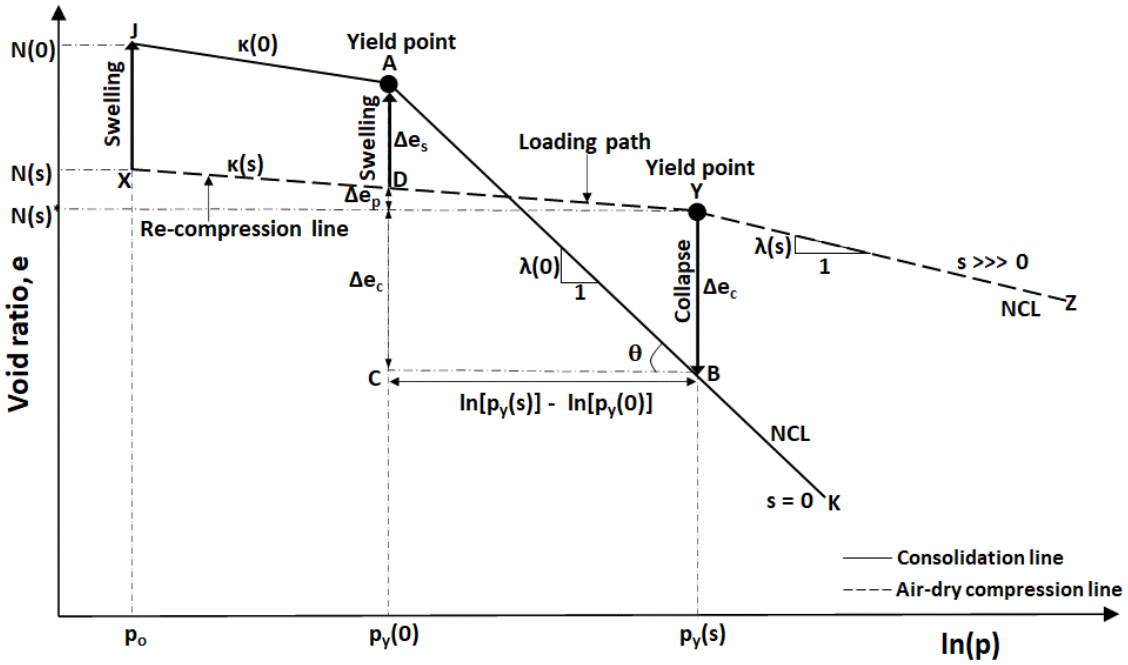

Fig. 5.2. Compression and the yielding response of unsaturated collapsible soils.

extreme conditions are the air-dry state with significantly high suction (s>>>0) *XYZ* and the saturated state with zero suction (s =0) *JAK*.

5.2.1 *Loading-Collapse Yield Function*

A mathematical relationship to describe the yield function using the constitutive parameters was developed from the measured compression behaviour (Fig. 5.2). The evolution of the yield curve will be governed by

$$p_y(s) = p_y(0)\left[\frac{s+1}{1}\right]^{\frac{2k_{sc}}{[\lambda(0)-\kappa(0)]}} \qquad [5.1]$$

The derivation of eq. (5.1) is given in Appendix-A. The above expression represents the yield curve in (*p*, *s*) co-ordinate space for the collapsible soil compacted at a specific density

with initial matric suction, *s*. The yield stress $p_y(s)$ in eq. (5.1) is increasing power function of suction, *s*. This yield function is a four-parameter model. The model parameters $p_y(0)$, $\lambda(0)$, and $\kappa(0)$ can be determined from the consolidation test alone. The procedure for determining the soaking gradient, k_{sc} was proposed in the later part of the manuscript. The proposed yield curve incorporated collapse behaviour through a single parameter, k_{sc}. The main advantage of the new yield function was that the whole normal compression behaviour could be predicted using the derived expression for yield stress, $p_y(s)$ under various controlled suctions. In the following section, the constitutive equation for normal compression line (NCL) was developed by linking with the yield function and wetting behaviour.

5.2.2 *Prediction of NCL Behaviour*

The proposed equation of the family of normal compression lines for various controlled-suction s, in (*e*, *p*) space incorporating wetting behaviour is given by,

$$e = N(0) - k_{sc} \ln\left[\frac{s+1}{1}\right] - \kappa(s) \ln\left[\frac{p_y(s)}{p_o}\right] - \lambda(s) \ln\left[\frac{p}{p_y(s)}\right] \qquad [5.2]$$

where $N(0)$ is an intercept of the consolidation line at normal stress p_o. The derivation of NCL eq. (5.2) is provided in Appendix-A. The deformation state variable void ratio, e in eq. (5.2) is a function of two independent stress state variables, *p* and *s*; it represents the smooth surface in three-dimensional space (*e*, *p*, *s*) by coupling the normal compression curves with the wetting curves. Thus, eq. (5.2) theoretically describes the compression behaviour of compacted collapsible soils under coupled wetting and normal compression phenomena. Further, most suitable empirical expression for the gradient of NCL, $\lambda(s)$ was chosen based on the best fit of the slope of measured post-yield compression data of various collapsible soils from current and literature studies as its performance was superior to eq. (2.4) given by,

$$\lambda(s) = a\exp(bs) \quad [5.3]$$

where a and b are model parameters controlling the stiffness of soil and can be determined by the best fit of experimental data. If the slope of NCL increases with an increase in suction, then $a > 0$ and $b > 0$; if the slope of NCL decreases with an increase in suction, then $a > 0$ and $b < 0$. The slope of the re-compression line $\kappa(s)$ can be selected based on the value of suction; if suction is very large, as in the case of air-dry compression, then $\kappa(s)$ is considered to be zero because the re-compression curve becomes flat at a very high suction, otherwise $\kappa(s) \approx \kappa(0)$. Normal compression lines for different suction values are separately connected with the loading-collapse yield curve. This can be noticed from the expression of NCL (eq. (5.2)), which involves yield stress $p_y(s)$ at suction, s. Therefore, the prediction of adequate NCL behaviour depends on how accurately the theoretical yield function is established.

Total four additional soil parameters $N(0)$, p_o, a, and b, are required to model normal compression behaviour with the proposed constitutive equation. Out of four parameters, $N(0)$ and p_o can be determined from one consolidation test performed on a compacted soil sample in an oedometer set-up. The parameters a and b can be determined by conducting a few suction control compression tests. Moreover, a simple approach is proposed in the following section for estimating the soaking gradient k_{sc}.

5.2.3 *Estimation of Soaking Gradient k_{sc}*

The soaking gradient can be derived by estimating the slope of the wetting line from wetting test results at particular normal stress for the air-dry sample compacted at a known dry density, as shown in Fig. 5.3. Some past researchers (Alonso et al., 1990; Sivakumar et al., 2010) opined that the gradient of the wetting curve might depend on normal stress and compaction density. The estimated magnitude of k_{sc} from the measured wetting-induced collapse data exhibits a constant trend for various dry densities, as shown in Fig. 5.4. The present study shows no significant influence of normal stress on k_{sc}. The soaking data for

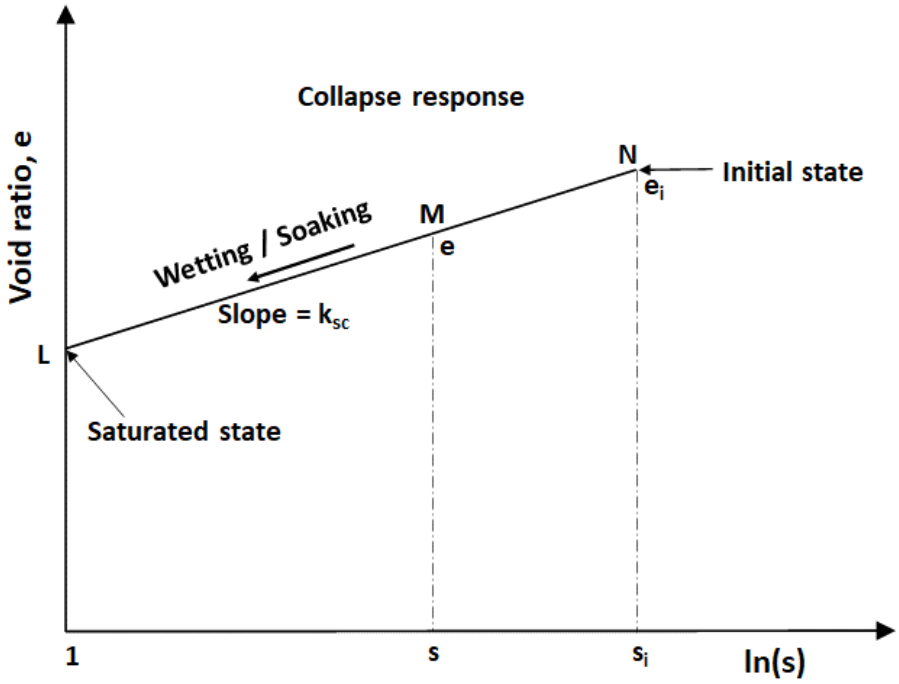

Fig. 5.3. Schematic representation of volume change response due to wetting at constant normal stress.

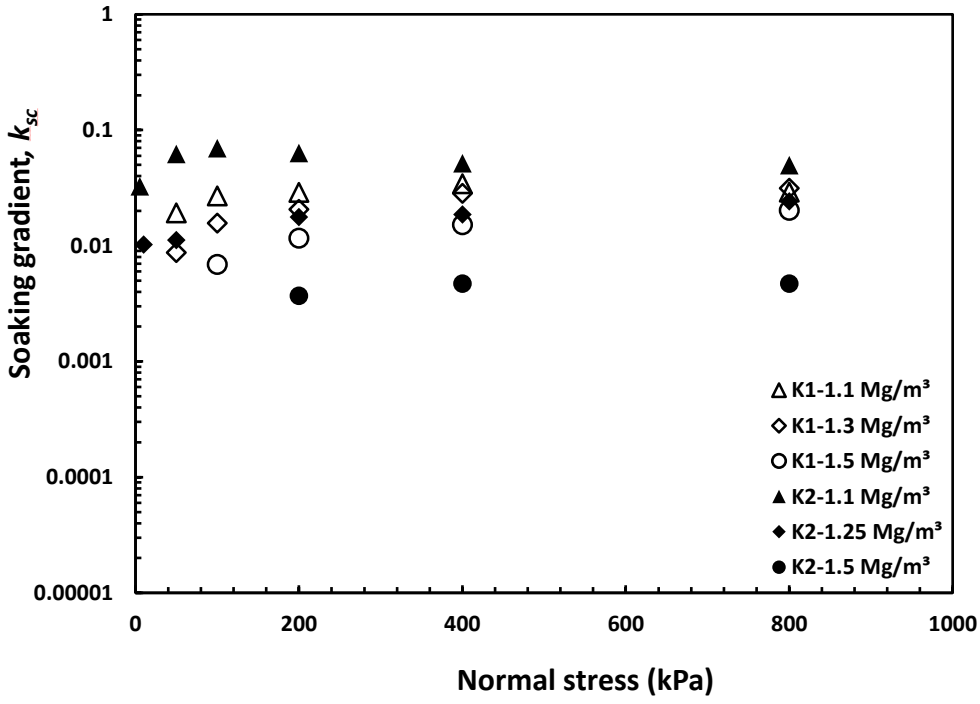

Fig. 5.4. Variation of soaking gradient with normal stress for air-dry soils K1 & K2 compacted at different densities.

the kaolin soil compacted at an in-situ water content of 15% and dry density of 1.73 Mg/m^3 also showed (Farulla et al. 2010) similar trend and supports the present observation. Therefore, based on experimental evidence, the soaking gradient is considered to be constant for a given range of normal stress at one particular density. Finally, k_{sc} will be determined by optimization procedure while fitting eq. (5.2) on the post-yield air-dry compression data, considering $\kappa(s)$ equal to zero. The estimated constant value of k_{sc} was then used for the predictions. The evaluation of the soaking gradient k_{sc} enables the assessment of wetting-induced deformation characteristics, as from the definition k_{sc} represents the ratio of change in volume to the change in suction due to wetting. Therefore, a model is presented in the following section for the prediction of collapse behaviour.

5.2.4 *Collapse Response*

Past studies already showed a similar trend for measured deformation response due to wetting, and the present work also agreed with earlier research. Therefore, the most general behaviour selected for the prediction was shown in Fig. 5.3. The following model was derived from the equation of the line shown in Fig. 5.3 for deformation estimation to represent observed behaviour accurately for one particular density under normal stress p.

$$e = e_i + k_{sc} \ln\left[\frac{s+1}{s_i+1}\right] \qquad [5.4]$$

where e_i is a void ratio known at the initial state; s_i is the known matric suction at the initial state; k_{sc} is the slope of a wetting line. Prediction of volume change response during wetting from eq. (5.4) requires only one unknown input parameter k_{sc}. In the following section, the performance of the proposed models was checked for various compacted collapsible soils.

5.3 Model Validation

The proposed constitutive models were capable of predicting three crucial features of partially saturated soils, viz; yielding behaviour, compression response under controlled-

suction, and volumetric deformation (collapse) characteristics due to wetting. The model requires eight parameters ($N(0)$, k_{sc}, $\kappa(0)$, P_o, $\lambda(0)$, a, b, and $P_y(0)$) to describe all three essential aspects of the compacted collapsible soils at any given compacted state. Out of these three behaviours, the prediction of yield and collapse responses does not require suction-controlled experiments on air-dry compacted soil. However, complete prediction of NCL behaviour requires additionally one or more measured suction-controlled compression data.

The model was validated on various collapsible soils, including two from the present study and seven from the literature studies. Primarily, the soil parameters ($N(0)$, $\kappa(0)$, P_o, $\lambda(0)$, and $P_y(0)$) for soil K1 and K2 were determined from the measured compression responses shown in Fig. 4.1 and 4.2 and reported in Table 5.1. The measured compression data in the air-dry conditions of these soils were best fitted with the proposed NCL (eq. (5.2)) in the post-yield range of normal stress using a curve-fitting tool (MATLAB 2019), and presented in Fig. 5.5 and 5.6. The optimized values of parameters k_{sc} were reported in Table 5.1 with the coefficient of determination, R^2, and root mean square error (RMSE). The parameters a and b were estimated by fitting eq. (5.3) to the slopes of post-yield measured suction-controlled compression data and given in Table 5.1. The fittings with experimental data were adequate. Subsequently, the yield function was predicted for K1 from eq. (5.1) using computed parameters, as shown in Fig. 5.7 along with measured data. The prediction was in good agreement with measured data. Moreover, the predicted NCL response of K1 shown in Fig. 5.5 were also in good agreement with the measured data. The predicted collapse behaviour from eq. (5.4) for K1 & K2 were validated with measured results, as shown in Fig. 5.8 and 5.9. Some deviation was noticed for collapse response near the saturation for K1. The overall predicted collapse response for soil was in good agreement with the experimental data.

Table 5.1. Model Parameters utilised for the validation of the proposed model with the soils from current study and literatures.

Data description	Dry density (Mg/m^3)	$N(0)$	P_o (kPa)	$\lambda(0)$	$\kappa(0)$	$p_y(0)$ (kPa)	Optimized parameters						
							k_{sc}	R^2	*RMSE*	a	b (kPa^{-1})	R^2	*RMSE*
K1	1.3	1.1	5	0.138	0.028	30	0.014	0.985	0.0032	0.138	-0.000493	0.99	0.0005
K2	1.25	1.1	5	0.101	0.019	12	0.0117	0.97	0.0095	-	-	-	-
Ge et al. (2021)	1.47	0.84	13.5	0.1	0.02	100	0.00937	0.9	0.012	0.101	-0.00275	0.97	0.0046
Mu et al. (2020)	1.3	1.09	10	0.123	0.054	16.2	0.0137	0.88	0.0219	0.124	-0.00227	0.88	0.0045
Mu et al. (2022)	1.5	0.78	1	0.095	0.00884	65	0.00693	0.99	0.0016	0.0946	0.0014	0.98	0.002
Alonso et al. (1990)	1.4	0.915	43	0.14	0.015	55	0.00775	0.985	0.0017	0.14	-0.011	0.99	0.0039
Sivakumar et al. (2010)	1.22	1.278	13.5	0.155	0.015	65	0.013	0.975	0.0042	0.152	0.0009	0.89	0.0051
Villar and Rodrigues (2011)	1.471	0.84	6	0.09	0.029	26	0.0084	0.984	0.0132	0.1	0.00033	0.8	0.0013
Rao & Revanasiddappa (2002)	1.55	0.78	6.5	0.134	0.015	110	0.0031	0.973	0.014	-	-	-	-

Note: K1 and K2 are the soils used in the present study; e.g., Ge et al. (2021) is literature from which soil was considered for validating the proposed model.

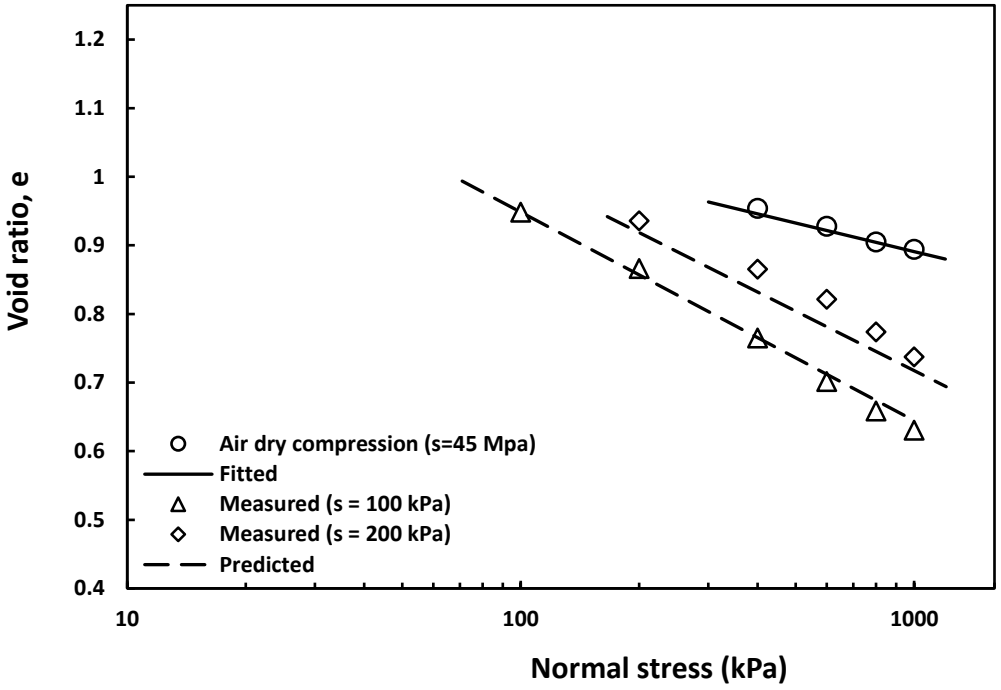

Fig. 5.5. Performance of proposed model for K1 compacted at state P: NCL behaviour.

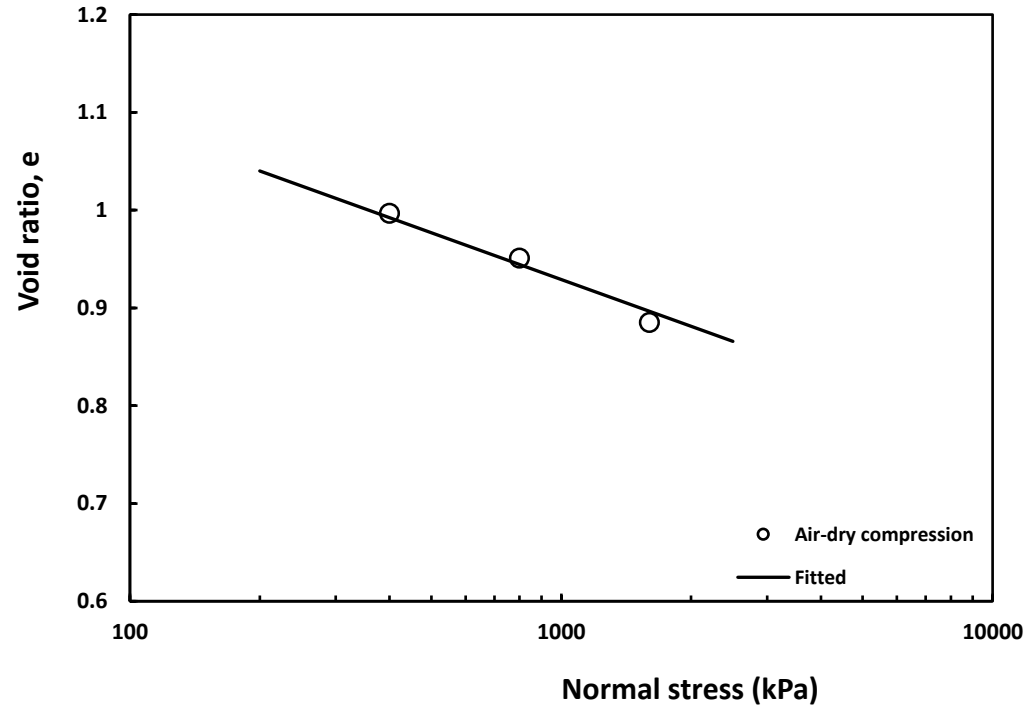

Fig. 5.6. Performance of proposed model for K2 compacted at 1.25 Mg/m^3: NCL behaviour.

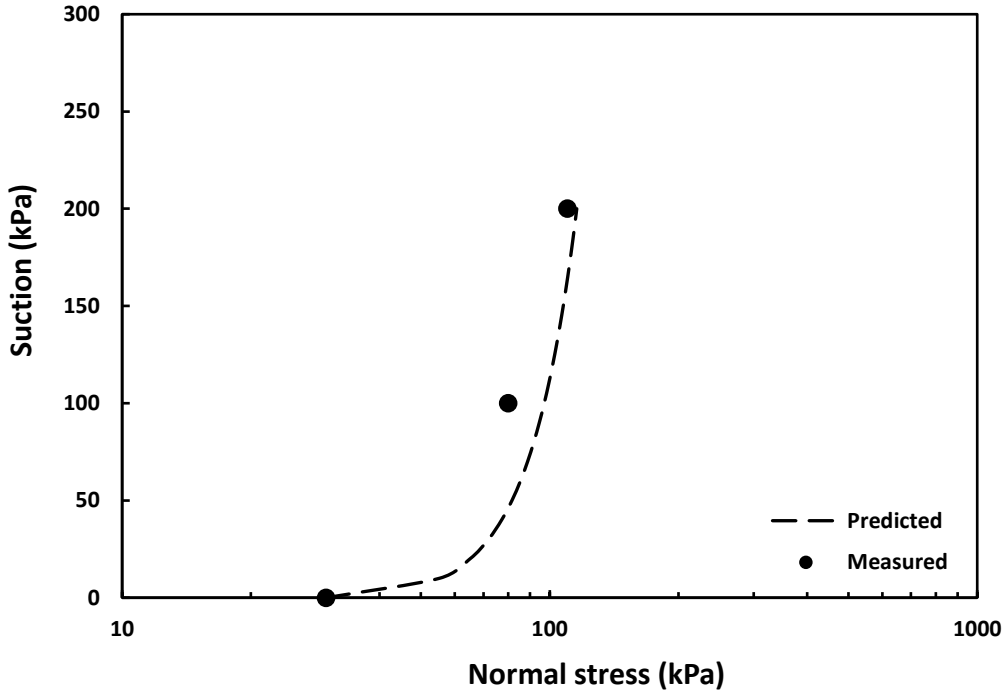

Fig. 5.7. Performance of proposed model for K1 compacted at state P: Yielding behaviour.

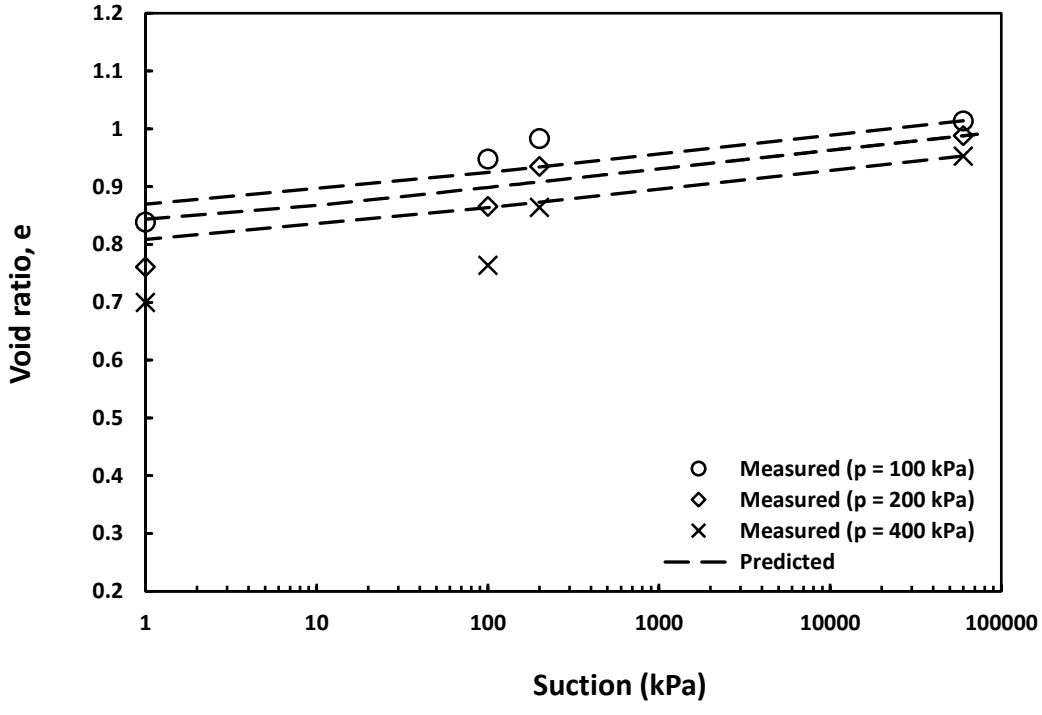

Fig. 5.8. Performance of proposed model for K1 compacted at state P: Wetting response at different normal stresses.

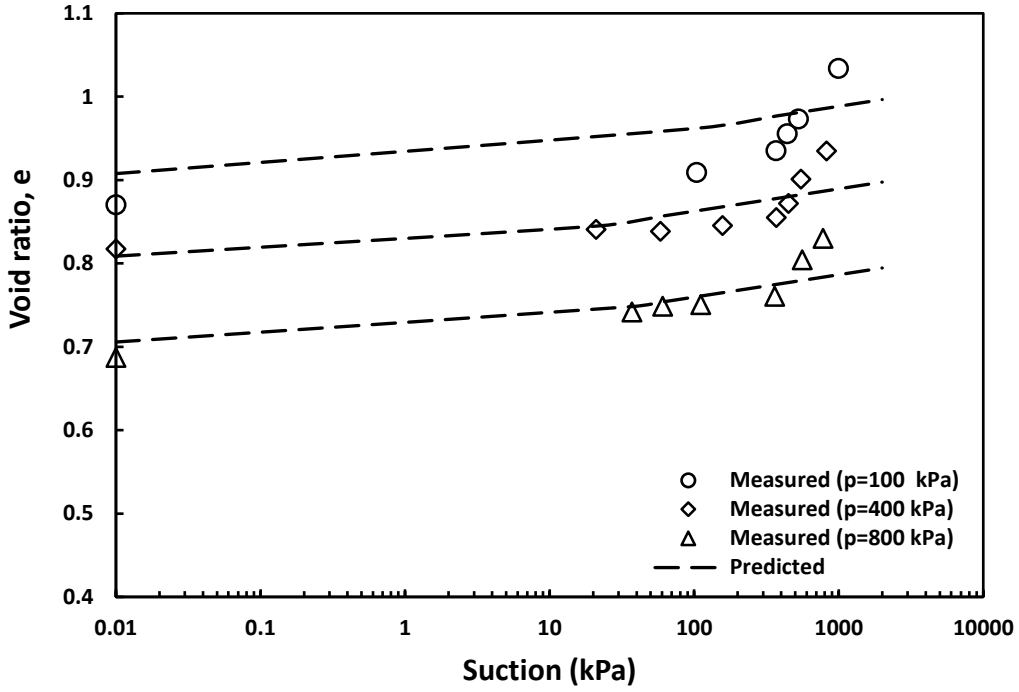

Fig. 5.9. Performance of proposed model for K2 compacted at 1.25 Mg/m^3: Wetting response at different normal stresses.

In addition, extensively investigated collapsible soils from the literature were also validated with the proposed constitutive model. Only those data from literature studies were selected for which at least suction-controlled compression and consolidation data were reported. However, as almost all the existing studies used initial saturation conditions close to OMC and did not report compression data at an air-dry state, only selected studies with required data were chosen. It is interesting to note that the proposed model is very general and useful for the behaviour of loess, kaolin, and laterite soils under the different initial degrees of saturation and compaction conditions.

Loess soil compacted at a dry density of 1.47 Mg/m^3 and close to optimum moisture content was chosen from Ge et al. (2021) for the validation of the proposed model. Suction-controlled compression and consolidation data in K_o-condition were used. Further, yield stresses were estimated from different compression curves to establish measured yield response. Post-yield compression data with the highest suction of 276 kPa was fitted with

eq. (5.2), as shown in Fig. 5.10. The model parameters used for fitting and predictions were given in Table 5.1. The predicted compression (Fig. 5.10), yielding (Fig. 5.11), and collapse response (Fig. 5.12) with the measured data were compared. All the predicted responses

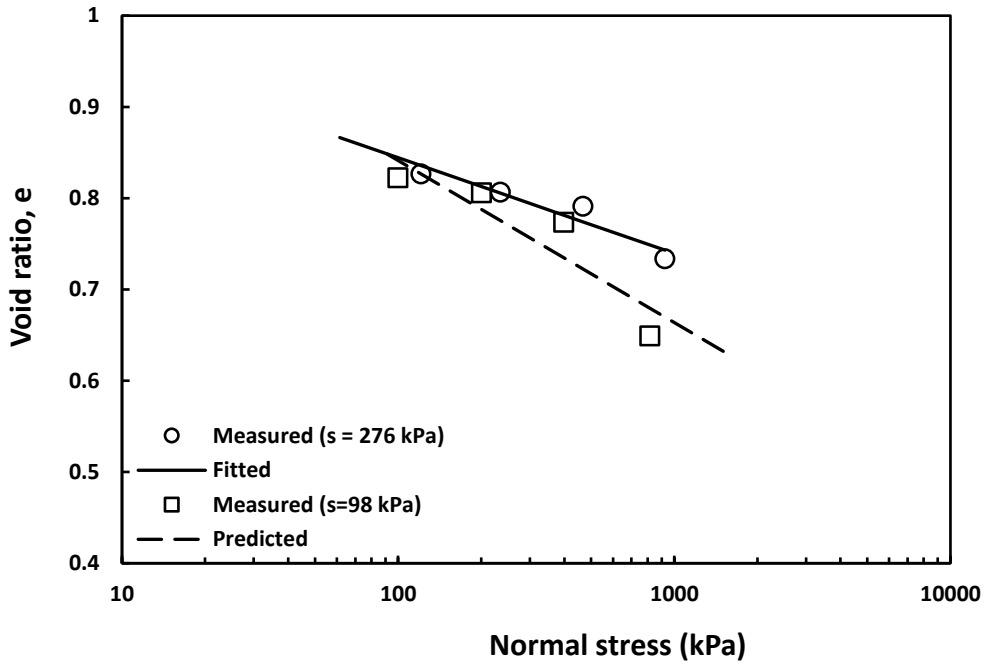

Fig. 5.10. Predicted behaviour for the loess soil compacted at dry density 1.47 Mg/m^3 near optimum moisture content (Ge et al., 2021): NCL response.

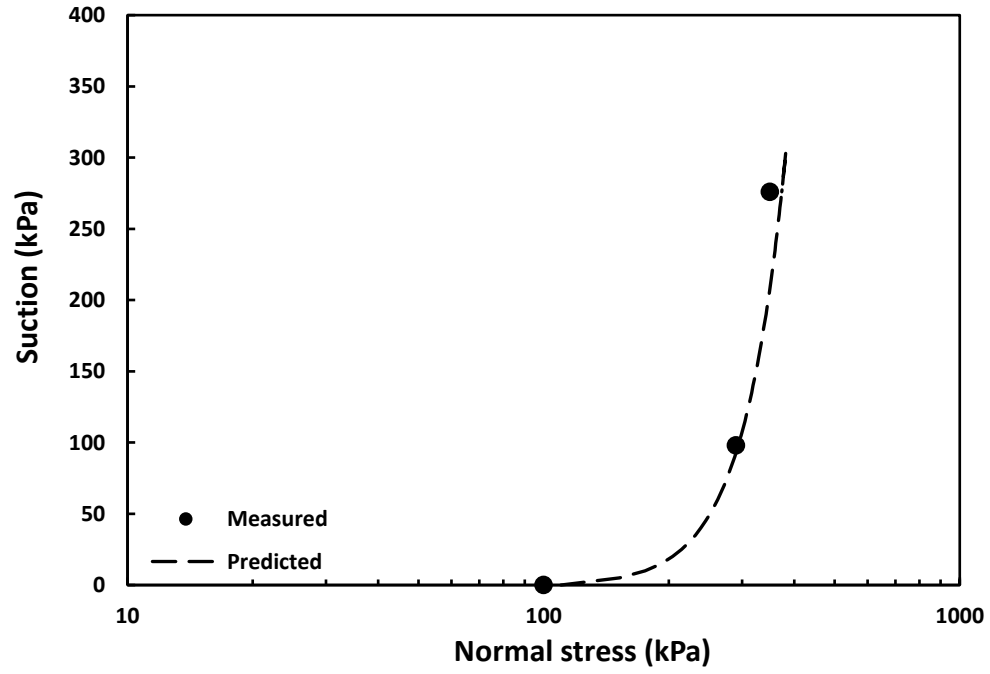

Fig. 5.11. Predicted behaviour for the loess soil compacted at dry density 1.47 Mg/m^3 near optimum moisture content (Ge et al., 2021): Yielding response.

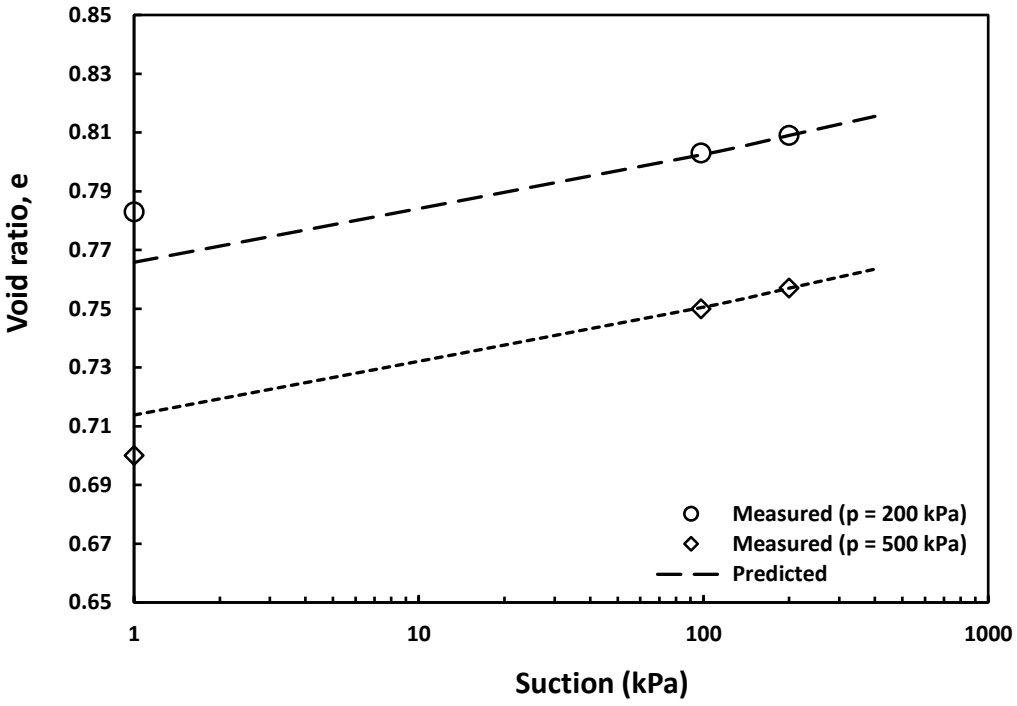

Fig. 5.12. Predicted behaviour for the loess soil compacted at dry density 1.47 Mg/m^3 near optimum moisture content (Ge et al., 2021): Collapse response upon wetting.

showed a very good agreement with experimental data, except for a slight deviation in the collapse response near saturation.

The experimental compression, yielding, and wetting-induced collapse data of loess soil were selected from Mu et al. (2020). The soil was initially compacted at the dry density of 1.3 Mg/m^3 and an in-situ moisture content of 6.31%, with a degree of saturation of 16%. Predictions were made using measured suction controlled-compression and consolidation data under isotropic loading conditions. The computed parameters used for fitting and validations are given in Table 5.1. The predicted compression behaviour and yield response shown in Fig. 5.13 and Fig. 5.14 were very close to the measured data. Also, a good agreement of predicted collapse behaviour (Fig. 5.15) was found with a measured response.

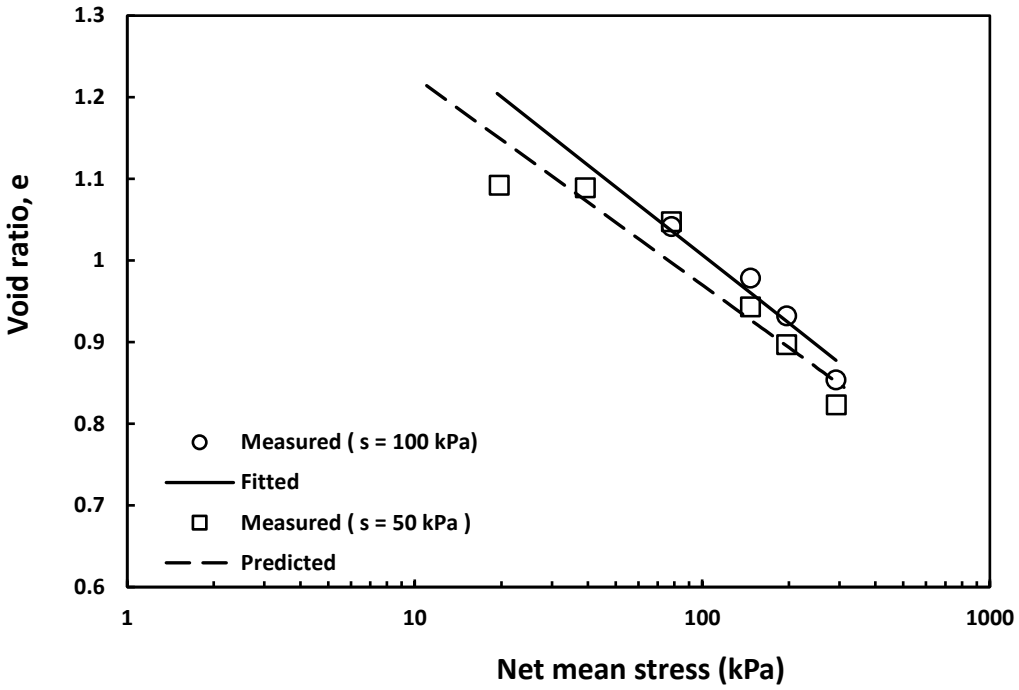

Fig. 5.13. Predicted behaviour for the loess soil compacted at in-situ initial water content 6.31 % and dry density 1.3 Mg/m^3 (Mu et al., 2020): NCL response.

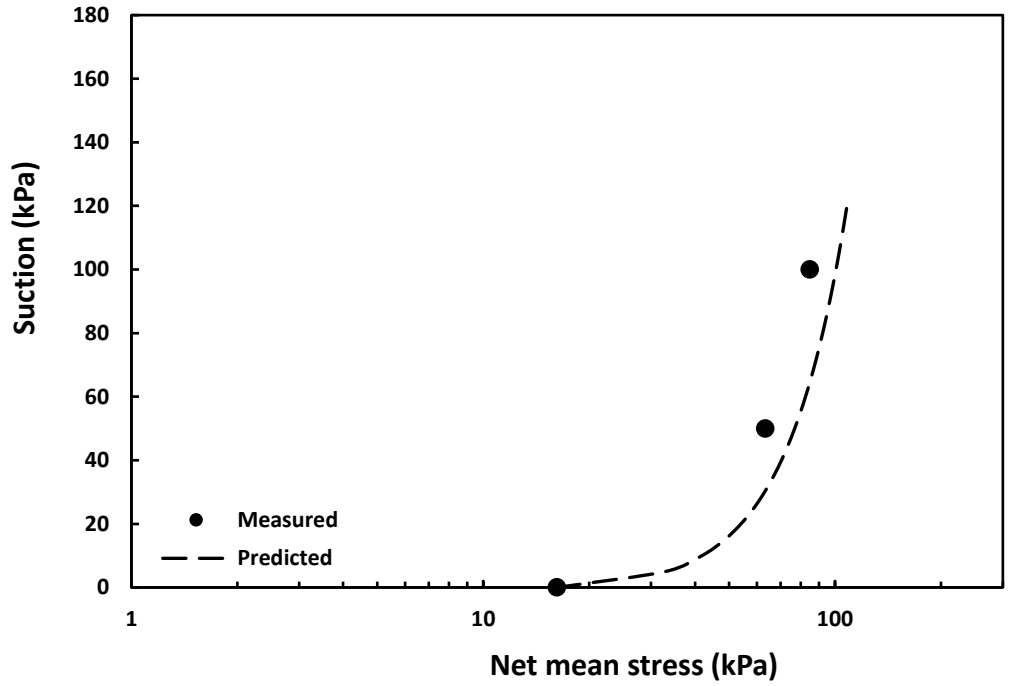

Fig. 5.14. Predicted behaviour for the loess soil compacted at in-situ initial water content 6.31 % and dry density 1.3 Mg/m^3 (Mu et al., 2020): LC yield curve.

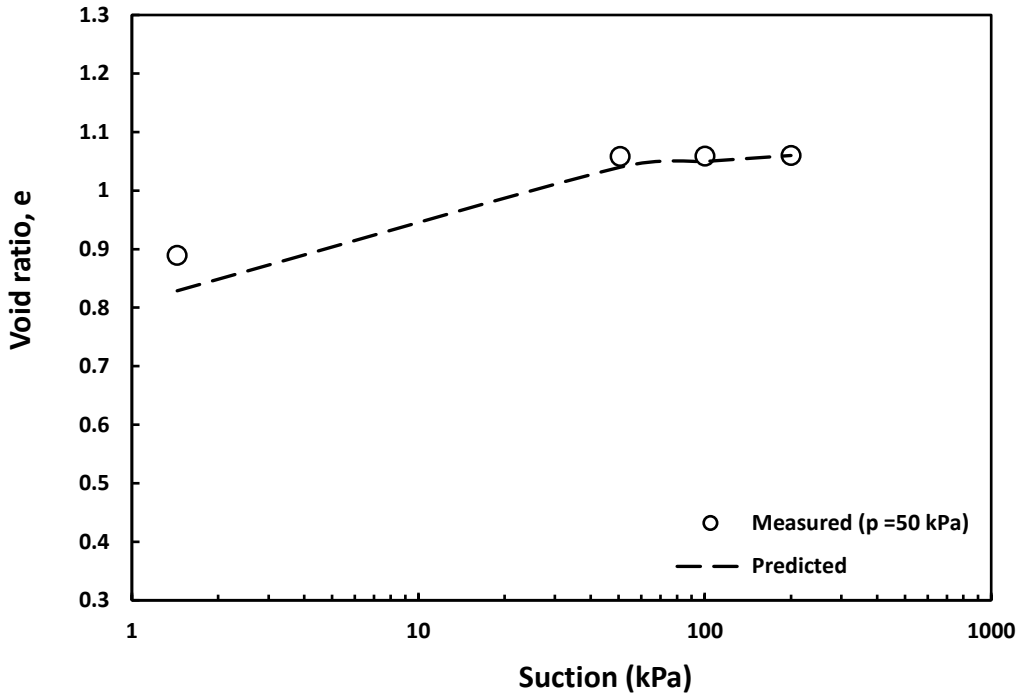

Fig. 5.15. Predicted behaviour for the loess soil compacted at in-situ initial water content 6.31 % and dry density 1.3 Mg/m3 (Mu et al., 2020): Collapse response upon wetting at net mean stress of 50 kPa.

Another literature, Mu et al. (2022), was chosen to examine the proposed model performance. The in-situ dry density, moisture content, and degree of saturation of the loess soil used for the laboratory studies were 1.5 Mg/m^3, 12.74%, and 43.38%, respectively. The compression data under saturated and suction-controlled conditions were chosen from K_o-compression experiments. The measured loading-collapse data of the tested specimen was extracted from the given literature. The desired parameters determined from the measured compression data and utilized for fitting and predictions were presented in Table 5.1. The predicted NCL response (Fig. 5.16) was very close to the measured data. The predicted LC curve (Fig. 5.17) and wetting behaviour (Fig. 5.18) were matched well.

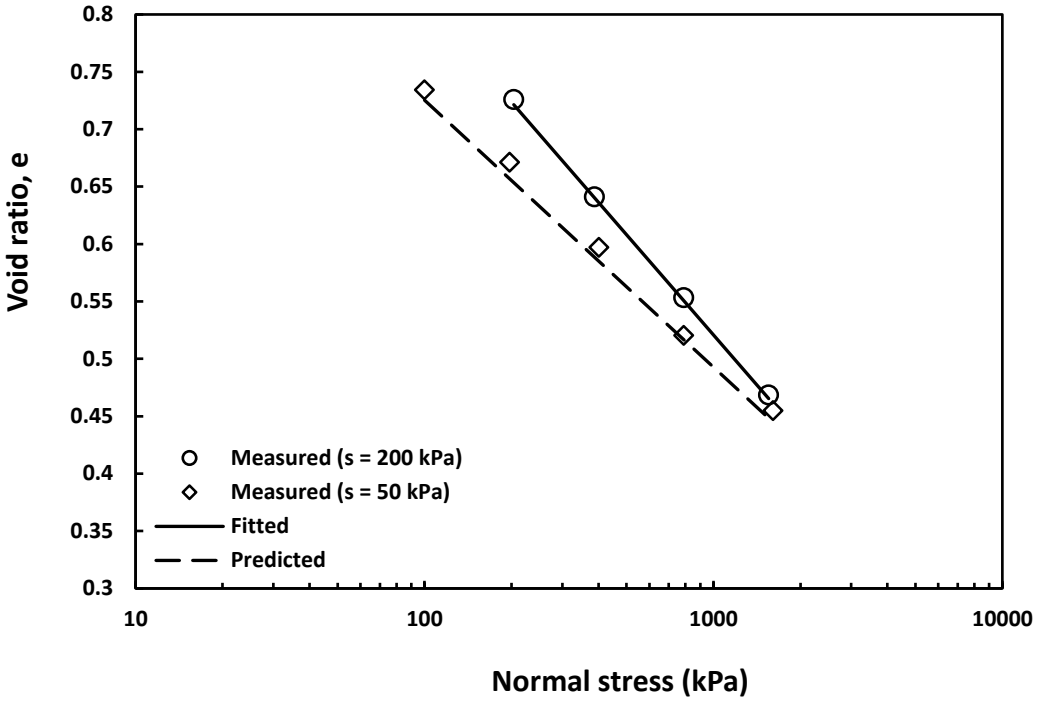

Fig. 5.16. Predicted behaviour for the loess soil compacted initially at dry density of 1.5 Mg/m^3 and in-situ moisture content of 12.74% (Mu et al., 2022): NCL response.

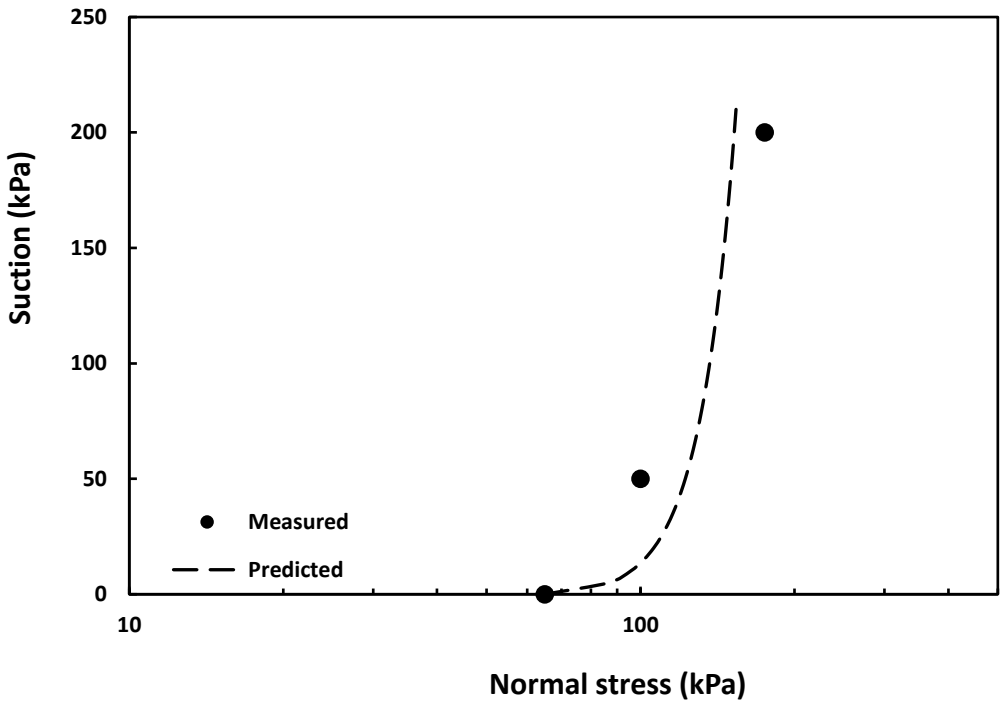

Fig. 5.17. Predicted behaviour for the loess soil compacted initially at dry density of 1.5 Mg/m^3 and in-situ moisture content of 12.74% (Mu et al., 2022): LC yield curve.

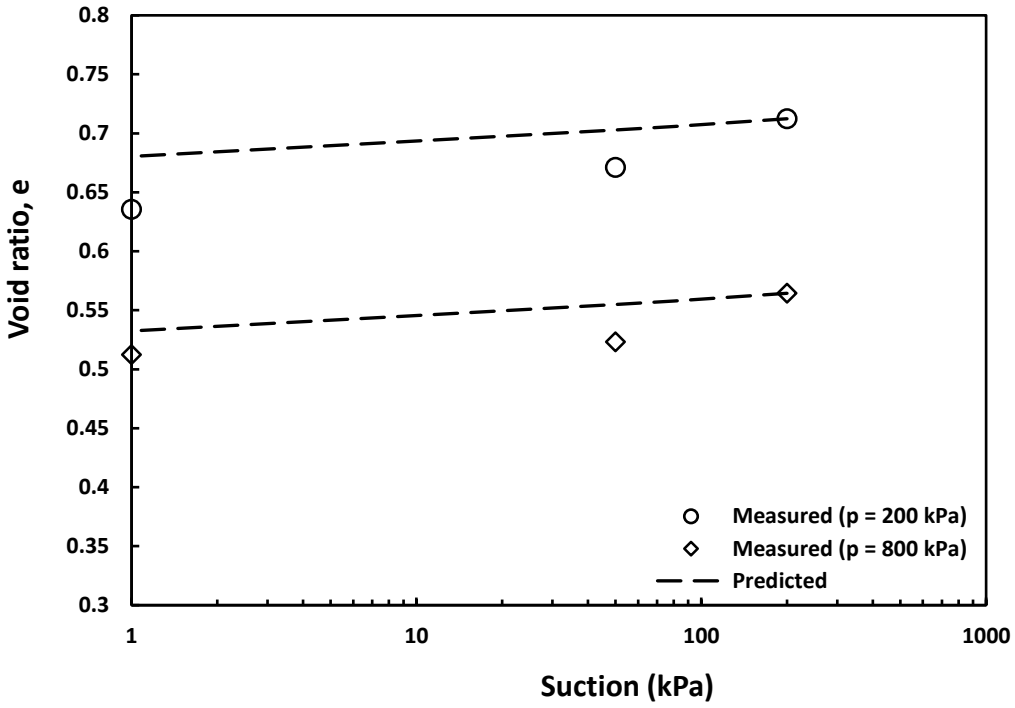

Fig. 5.18. Predicted behaviour for the loess soil compacted initially at dry density of 1.5 Mg/m^3 and in-situ moisture content of 12.74% (Mu et al., 2022): Collapse response upon wetting.

Suction-controlled oedometer compression data of collapsible clayey sand was obtained from Vilar & Rodrigues (2011). The in-situ site collected soil samples were used for the laboratory experiments with a dry density of 1.471 Mg/m^3, moisture content of 6.95%, and degree of saturation of 22.8%. Saturated consolidation data with suction-controlled K_o-compression data produced by the axis-translation technique were considered for model validation. The parameters used for fitting and predictions are provided in Table 5.1. The predicted compression behaviour (Fig. 5.19) for the suction of 75 and 25 kPa shows good agreement with the measured data. Yield curve prediction (Fig. 5.20) was satisfactory. However, some departure can be seen for the few data points near saturation, marked in the red circle. The wetting-induced collapse data at the initial suction of 200 kPa was validated, and very good agreement was noticed for all the net vertical stresses, as shown in Fig. 5.21.

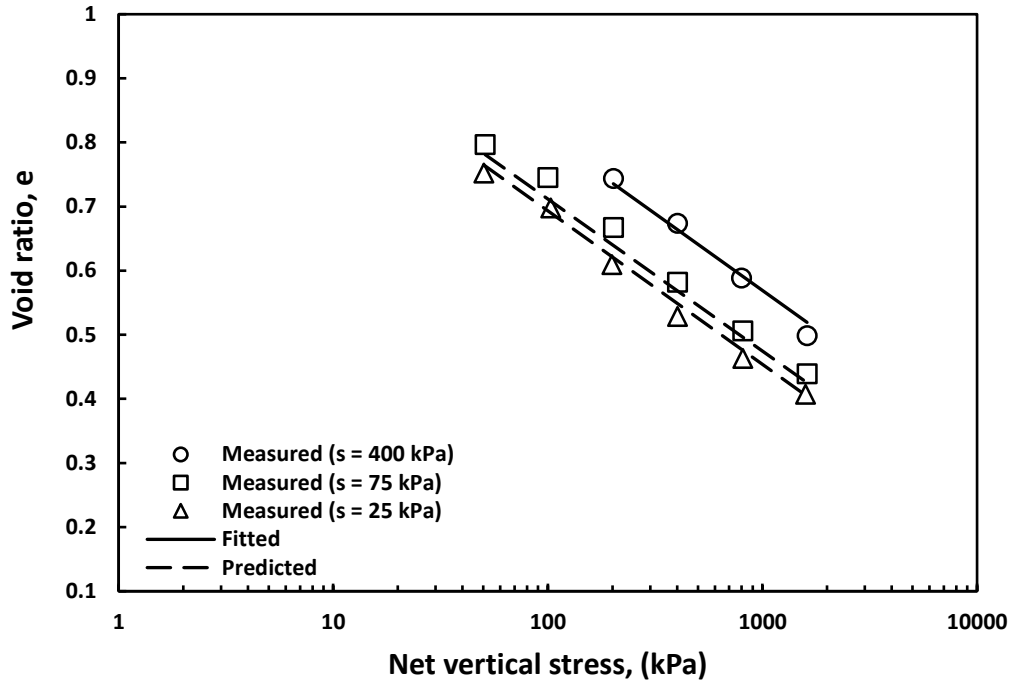

Fig. 5.19. Predicted behaviour for the clayey sand compacted at dry density 1.471 Mg/m^3 and at in-situ water content of 6.95% (Vilar & Rodrigues, 2011): NCL response.

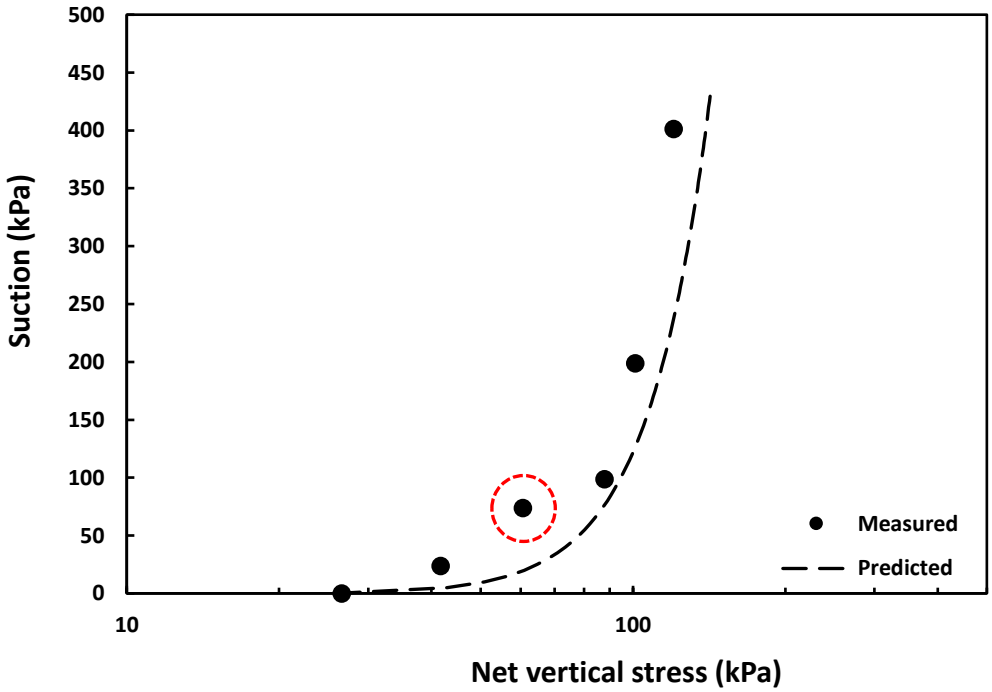

Fig. 5.20. Predicted behaviour for the clayey sand compacted at dry density 1.471 Mg/m^3 and at in-situ water content of 6.95% (Vilar & Rodrigues, 2011): LC yield locus.

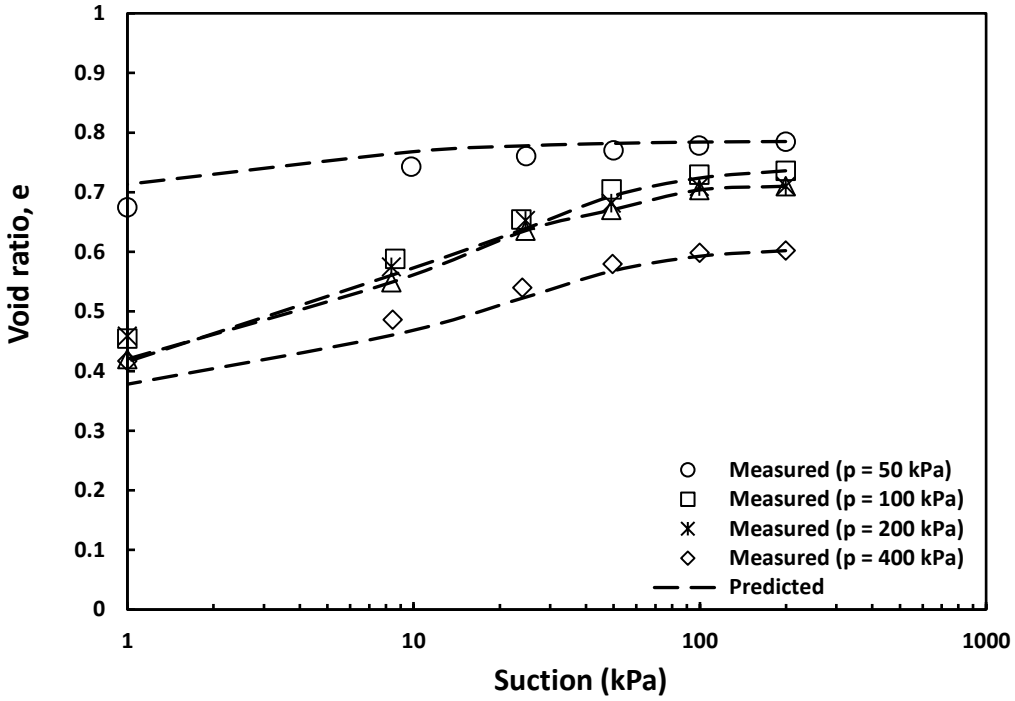

Fig. 5.21. Predicted behaviour for the clayey sand compacted at dry density 1.471 Mg/m^3 and at in-situ water content of 6.95% (Vilar & Rodrigues, 2011): Collapse response under various normal stresses.

The measured data of kaolin was taken from Alonso et al. (1990). The soil was initially compacted at a dry density of 1.4 Mg/m^3, moisture content of 30%, and degree of saturation of 87.5%. Suction-controlled isotropic compression and consolidation data produced in a modified triaxial set-up are considered for validation. Yield stresses were determined from measured compression curves to establish measured loading-collapse behaviour. The parameters required for fitting and predictions were assessed from the measured data provided in Table 5.1. The predicted compression behaviour (Fig. 5.22) for the suction of 60 kPa shows good agreement with the experimental data. The predicted yield curve (Fig. 5.23) was close to the measured response. There were no reports of wetting-induced collapse data in the chosen literature.

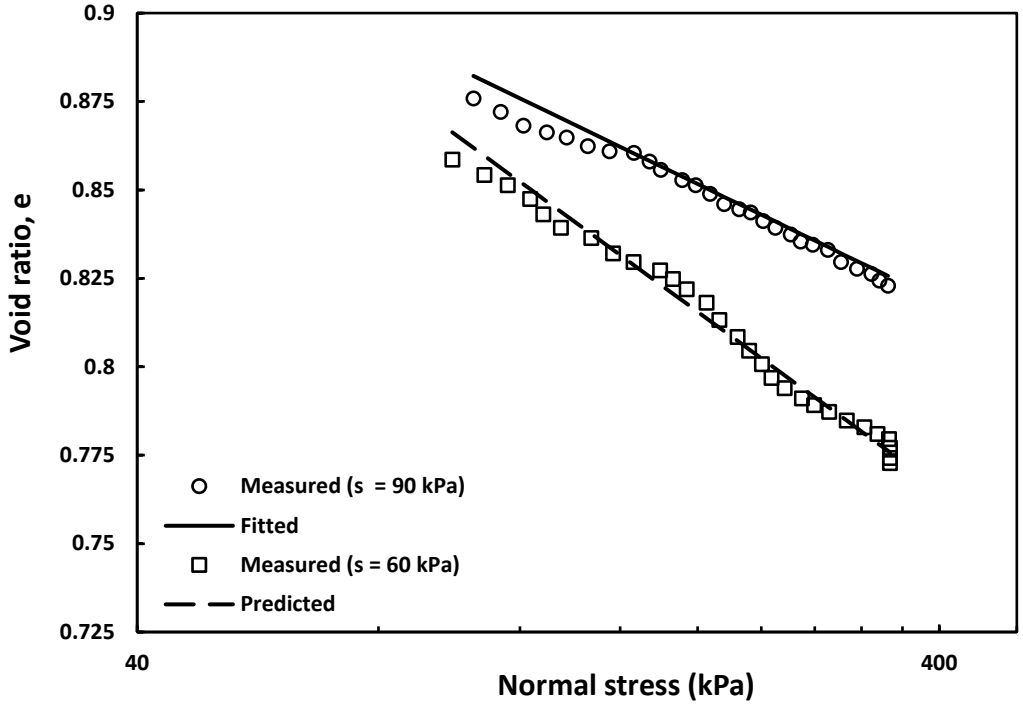

Fig. 5.22. Predicted behaviour for the kaolin soil compacted at dry density of 1.4 Mg/m^3 and moisture content of 30 % (Alonso et al., 1990): NCL response.

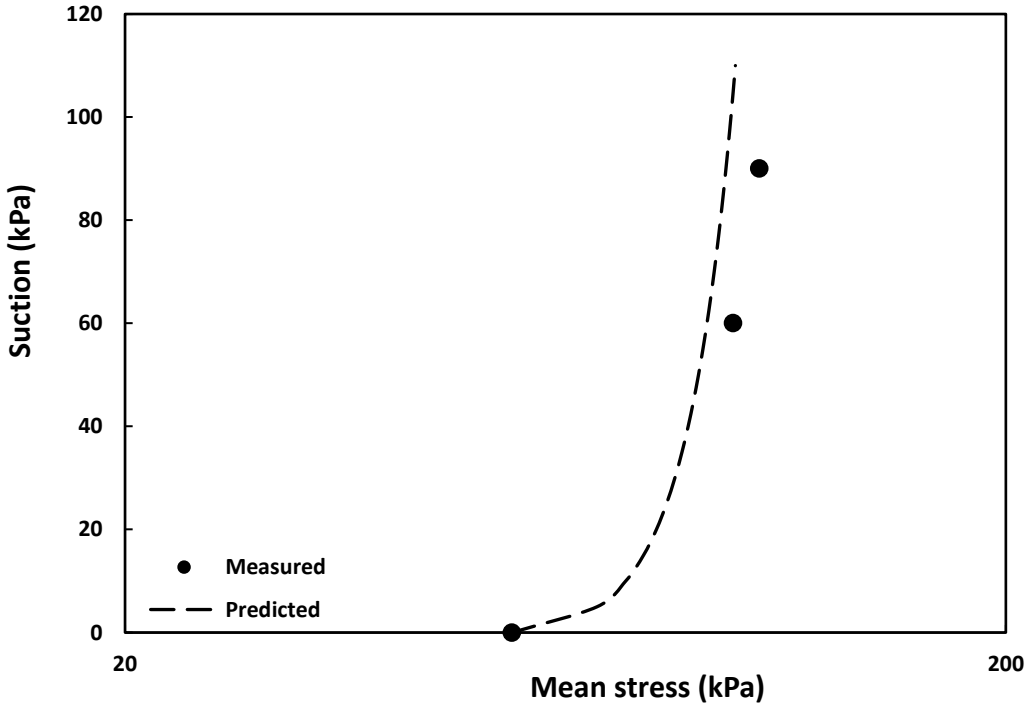

Fig. 5.23. Predicted behaviour for the kaolin soil compacted at dry density of 1.4 Mg/m^3 and moisture content of 30 % (Alonso et al., 1990): LC yield locus.

The experimental data on kaolin soil was obtained from Sivakumar et al. (2010). The soil sample was prepared using isotropic compression at a compaction density of 1.22 Mg/m^3 and a moisture content of 25%, which was 4% dryer than the optimum moisture content. Suction-controlled isotropic compression data generated by the axis-translation technique were used for fitting and validations. Measured LC yield locus was retrieved and utilized to validate the proposed yield function. The necessary parameters for fitting and predictions were estimated and reported in Table 5.1. The predicted compression behaviour (Fig. 5.24) for the suction of 200 and 100 kPa shows good agreement with the measured results. The predicted yield curve Fig. 5.25 passed close to the measured behaviour, although some deviation was observed for the data point indicated by the red circle close to saturation. Only compression and loading-collapse observed data were validated because there were no reports of volumetric collapse data in the selected literature.

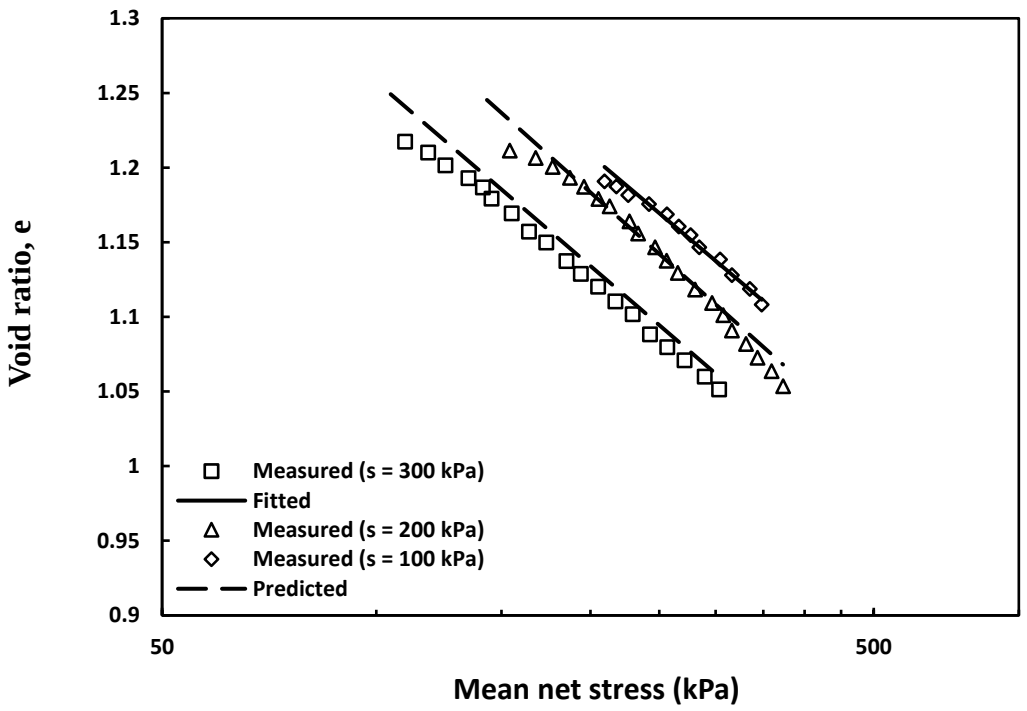

Fig. 5.24. Predicted behaviour for the kaolin soil compacted at dry density 1.22 Mg/m^3 and at water content of 25 % close to OMC (Sivakumar et al., 2010): (a) NCL.

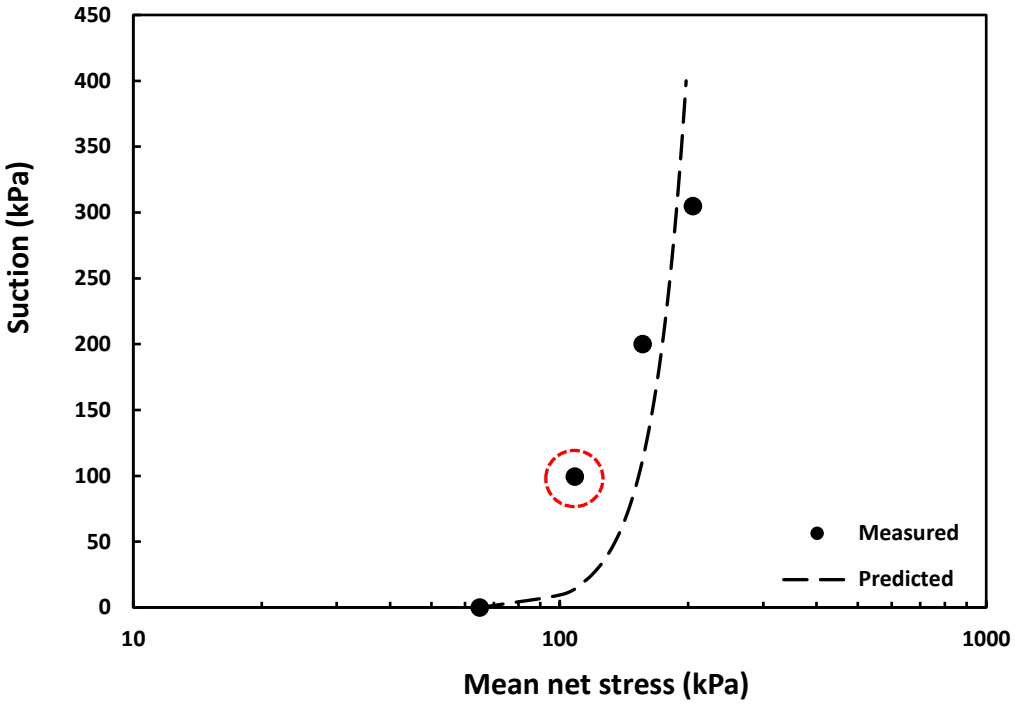

Fig. 5.25. Predicted behaviour for the kaolin soil compacted at dry density 1.22 Mg/m^3 and at water content of 25 % close to OMC (Sivakumar et al., 2010): LC yield locus.

In addition, Rao & Revanasiddappa (2002) was considered for the validation of proposed constitutive laws with red soil. The initial compaction conditions were: dry density of 1.55 Mg/m^3, water content of 15.7%, and a degree of saturation of 53.8%. The measured suction-controlled compression and consolidation data were considered for fitting and validation. The model parameters computed from measured data are reported in Table 5.1. The fitted NCL is shown in Fig. 5.26, and the predicted yield curve (Fig. 5.27) was close to the measured data. There were no reports of additional suction-controlled compression results and measured wetting-induced collapse data in the selected literature.

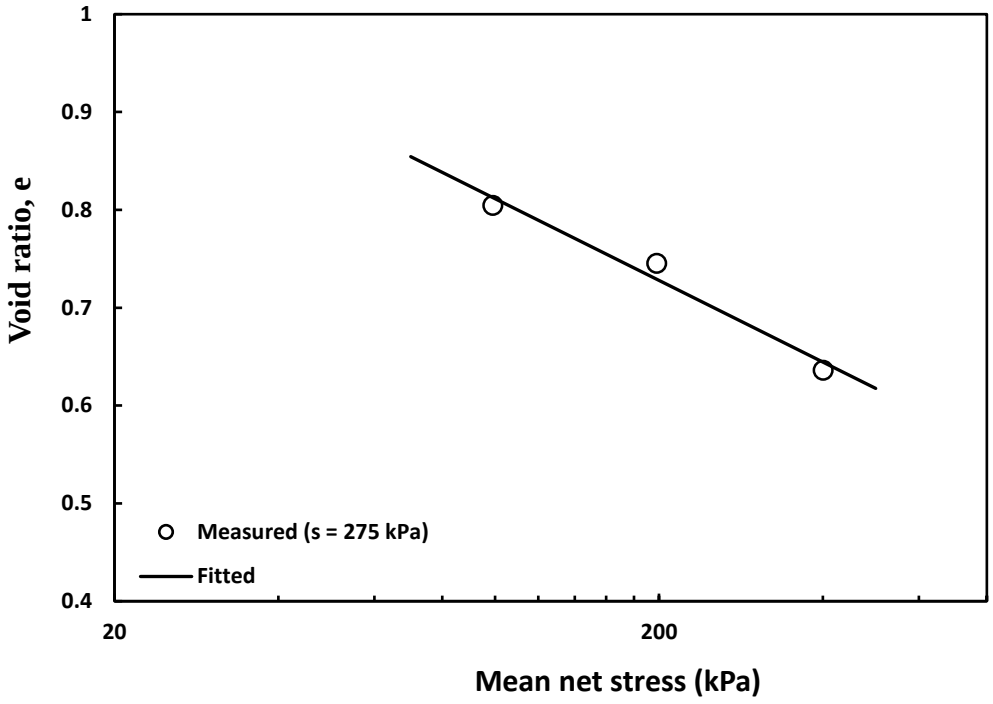

Fig. 5.26. Predicted behaviour for the red soil compacted at dry density 1.55 Mg/m^3 and at in-situ moisture content of 15.7 % (Rao & Revanasiddappa, 2002): NCL response.

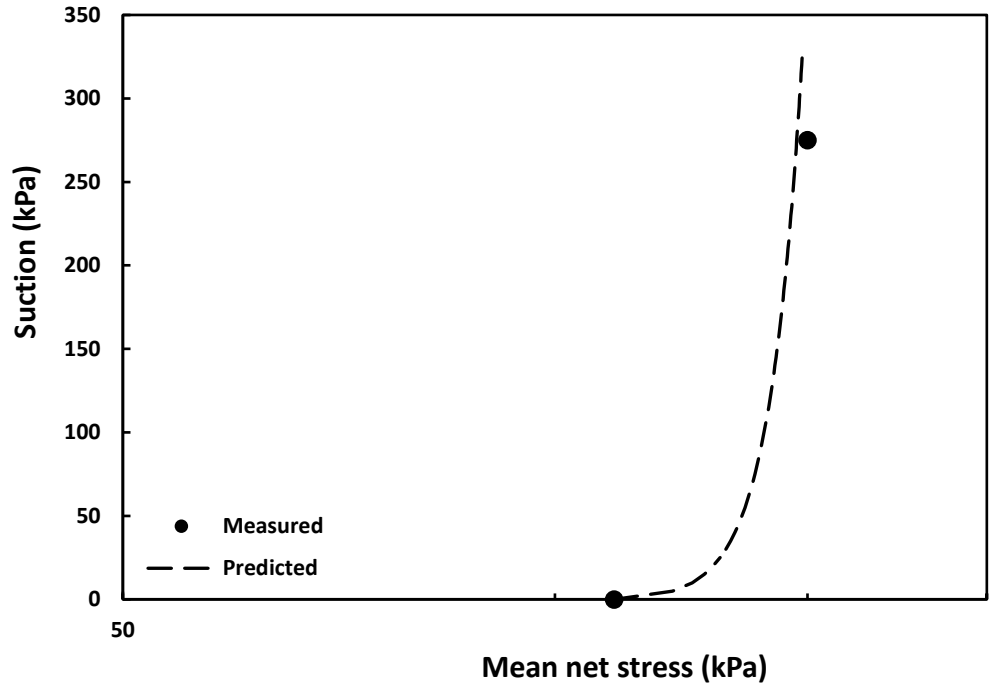

Fig. 5.27. Predicted behaviour for the red soil compacted at dry density 1.55 Mg/m^3 and at in-situ moisture content of 15.7 % (Rao & Revanasiddappa, 2002): LC yield locus.

5.4 Critical Remarks

The effect of wetting on the mechanical behaviour of compacted collapsible soils was incorporated explicitly into the proposed model. Three major mechanical characteristics of compacted collapsible soil, yielding, compression, and collapse were predicted and validated using measured data. The following observation were derived from the complete evaluation:

1. The newly developed model framework requires the minimal number of parameters. Determination of model parameters is easier and can be estimated from the few basic one-dimensional compression test results performed on compacted soil samples. The prediction of the loading-collapse yield curve and collapse response does not require suction-controlled compression experiments; however, for predicting compression behaviour, one or more suction-controlled compression tests are needed in addition to air-dry compression and compression in a saturated condition.
2. The theoretical study of surface forces in the evolution of fabric orientation of kaolinite mineral due to wetting satisfactorily explained the deviation of measured yield response from BBM for yield loci. The proposed constitutive model was able to capture the particle surface forces such as coulumbic attraction due to the inclusion of data at fully saturated and at the air-dry or suction-controlled state through the model parameter soaking gradient.
3. The proposed model has the advantage of predicting wetting or collapse behaviour by just using one parameter soaking modulus, k_{sc} estimated from air-dry compression data. However, existing constitutive models required water retention parameters estimated from the measured soil water retention curve. As a result, the proposed approach is simple and does not demand tedious, complex laboratory experiments to generate a measured soil water characteristic curve (SWCC) to evaluate water retention parameters.

4. The constitutive model was developed based on the experimental observation of unsaturated K_o-compression and the yielding behaviour of compacted collapsible soils. However, the model can also predict accurate soil behaviour under isotropic loading conditions. The proposed approach can effectively predict the mechanical behaviour of soil samples with anisotropic and isotropic compaction stress histories. The model is generic and can predict soil responses for all varieties of unsaturated collapsible soils under various initial compaction conditions, mechanical loading stress history, and compaction stress history.

Chapter 6

Theoretical Framework for Large-Strain (Torsional) Shear Resistance of Kaolin Clays under Chemo-Mechanical Loadings

6.1 General

The importance of inter-particle electro-chemical forces and physico-chemical influence on the mechanical behaviour of kaolin clay was illustrated in chapter 2. The effect of inter-particle forces, including coulomb and van der Waals forces, on volume change and yielding behaviour were explored through experimental observations in chapter 4. The theoretical study of inter-particle forces in the kaolinite clay fabric changes due to wetting well elucidated the deviation of measured yield response from the predicted yield curve from BBM. This aspect led to a new model formulation in chapter 5, which includes inter-particle forces implicitly. Moreover, under the physico-chemical influence, how soil responds to mechanical loading and wetting needs in-depth insight into the experimental and theoretical study.

This chapter proposes a theoretical framework for explaining and predicting the large-strain shear response of kaolin clay using a modified effective stress approach and the Mohr-Coulomb criterion. This model was able to explain the peak behaviour under NC conditions during the shear. The proposed approach developed the novel explicit expressions of net electrostatic pressures for NC kaolin clays. The present study showed ring shear experiment results for the kaolin soil (K1) under different inundation and consolidation pressures with varying pH of aqueous solution and di-electric mediums to accommodate physico-chemical effects. On the basis of the microstructural study and changes in the electrostatic forces between the kaolinite particles, the process of kaolinite fabric evolution during shear was described. Further, effective stress during the shear was quantitatively estimated. The shear strength behaviour, including effective stress paths, peak, and residual envelopes for NC

kaolin under drained shearing conditions were predicted in the two-dimensional space of shear stress versus effective stress.

6.2 Results

6.2.1 *Effect of Inundation and Consolidation Pressure*

The results of inundation tests at different mechanical pressures of 200 kPa, 450 kPa, 700 kPa, and 950 kPa for oven-dried compacted kaolin samples in the separate ring shear tests were shown in Fig. 6.1. The wetting of the samples induced collapse (volume reduction) in

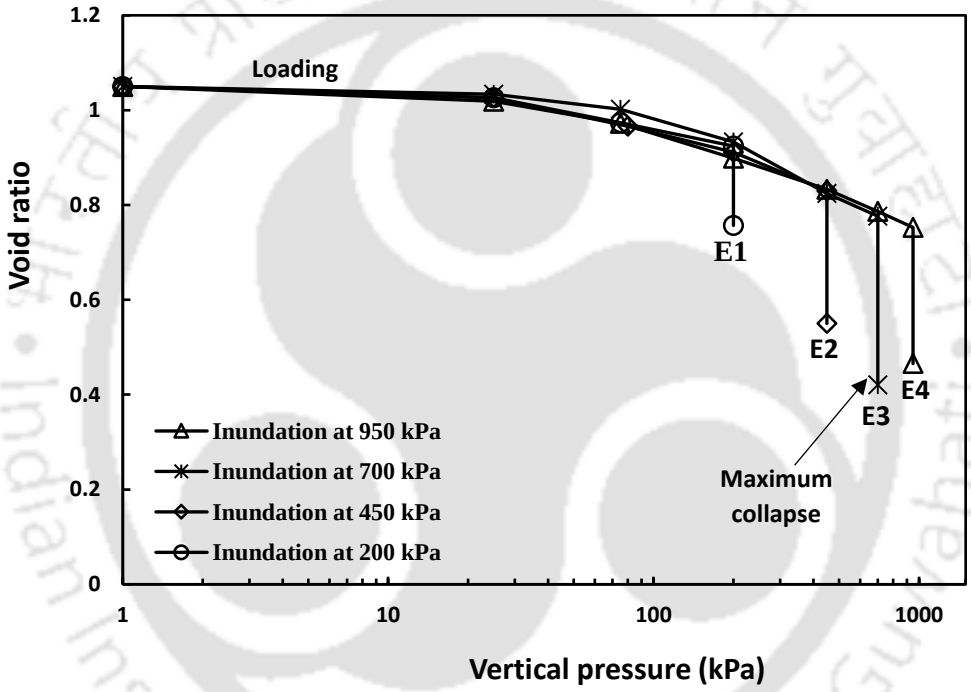

Fig. 6.1. Compression and collapse response of the kaolin compacted at 1.3 Mg/m^3 under different inundation pressures.

the soil mass. The samples achieved the equilibrium states indicated by *E1*, *E2*, *E3*, and *E4* (Fig. 6.1) at the end of the collapse. The void ratio due to collapse reached a minimum value of 0.42 at 700 kPa inundation pressure, and the collapse decreased with further pressure. From the equilibrium states, the samples were sheared until residual conditions were achieved. The variation in shear stress against shear deformation at different inundation pressures were shown in Fig. 6.2. The peak was observed at small shear deformations of around 4 mm and 5.5 mm at inundation pressures of 450 kPa and 950 kPa, respectively.

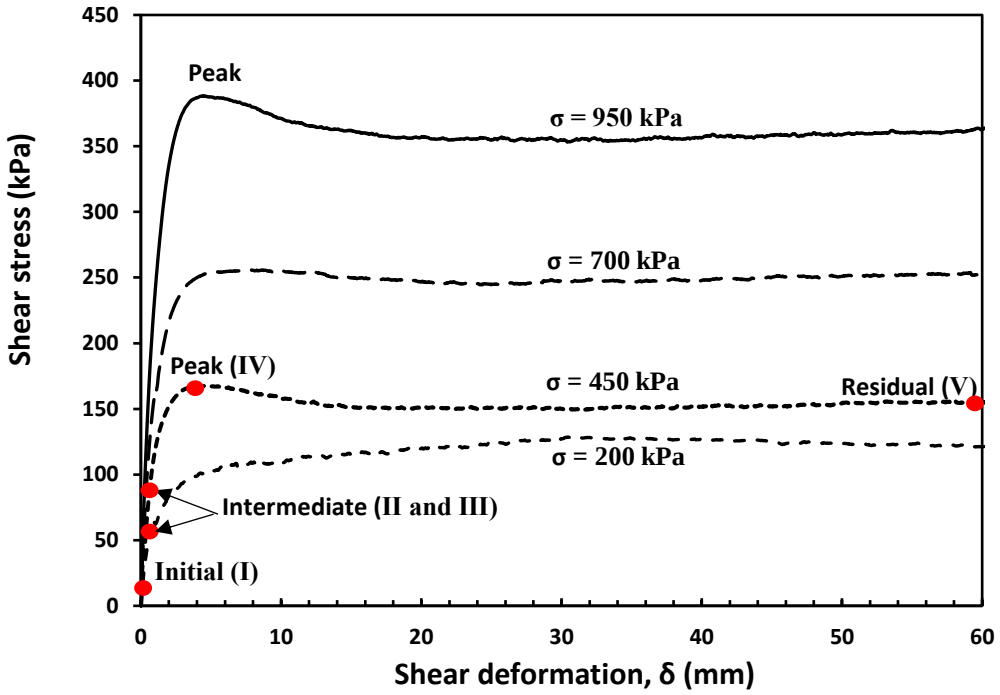

Fig. 6.2. Shear resistance offered by the duplicate soil specimens under various inundation pressures.

However, no peak strength was mobilized at the lowest pressure of 200 kPa and at the intermediate pressure of 700 kPa, where collapse was maximum. The shear stress then decreased with a further increase in shear deformation, which was a strain-softening response in NC conditions. The measured peak followed by strain softening response in NC conditions was in agreement with the previous results on kaolin (Skempton 1985, Duong et al. 2018, Yao et al. 2020). All the samples attained residual conditions at shear deformation of approximately 60 mm. The higher the inundation pressure, the greater were peak and residual shear strengths. The shearing caused a volumetric contraction in the samples at different inundation pressure, as shown in Fig. 6.3. The sample sheared at the lowest pressure of 200 kPa, underwent the least volume change during shearing. The highest deformation due to shearing was experienced at 700 kPa, where the maximum collapse occurred.

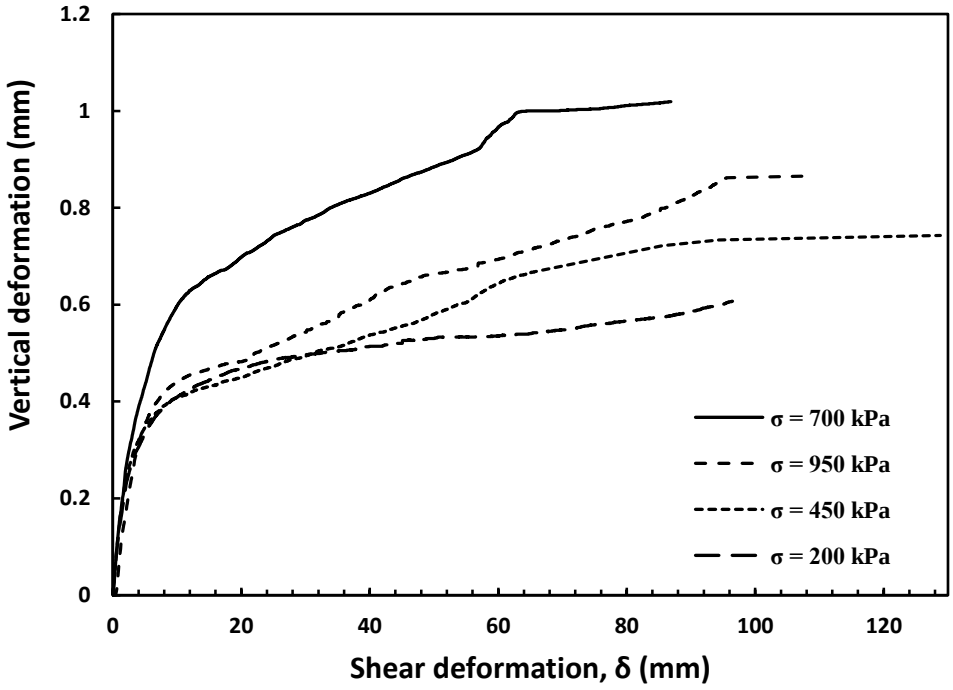

Fig. 6.3. Deformation profiles at different inundation pressure during shear.

The Fig 6.4, 6.5, and 6.6 shows consolidation test results at different consolidation pressures 450, 700, and 900 kPa pressures for NC kaolin samples in the separate ring shear tests. The inundation test results at pressures of 450, 700, and 950 kPa were also shown in the same figures. The void ratios at the end of the consolidation were 0.6, 0.459, and 0.4, which were found to be close to the void ratios of 0.55, 0.42, and 0.46 at the end of the inundation tests at the pressure of 450, 700, and 950 kPa, respectively. Further, shearing was performed on NC samples, and the measured shear stress versus shear deformation profiles at different consolidation pressures were depicted in Fig. 6.7. The peak shear strength was mobilized at small shear deformation of 6.8 mm and 9.5 mm at the pressure of 700 kPa and 950 kPa, respectively. However, no peak behaviour was observed at lowest pressure of 450 kPa. Further, strain softening response was observed with an increase in shear deformation. The residual shear strength was achieved at shear deformation of around 80 mm for all the samples. The peak and residual shear strengths were increased with an increase in inundation pressure. Moreover, the shear strength of consolidated samples was higher than that of the

inundated samples, and the effect is more pronounced at higher pressures, as shown in Fig. 6.8.

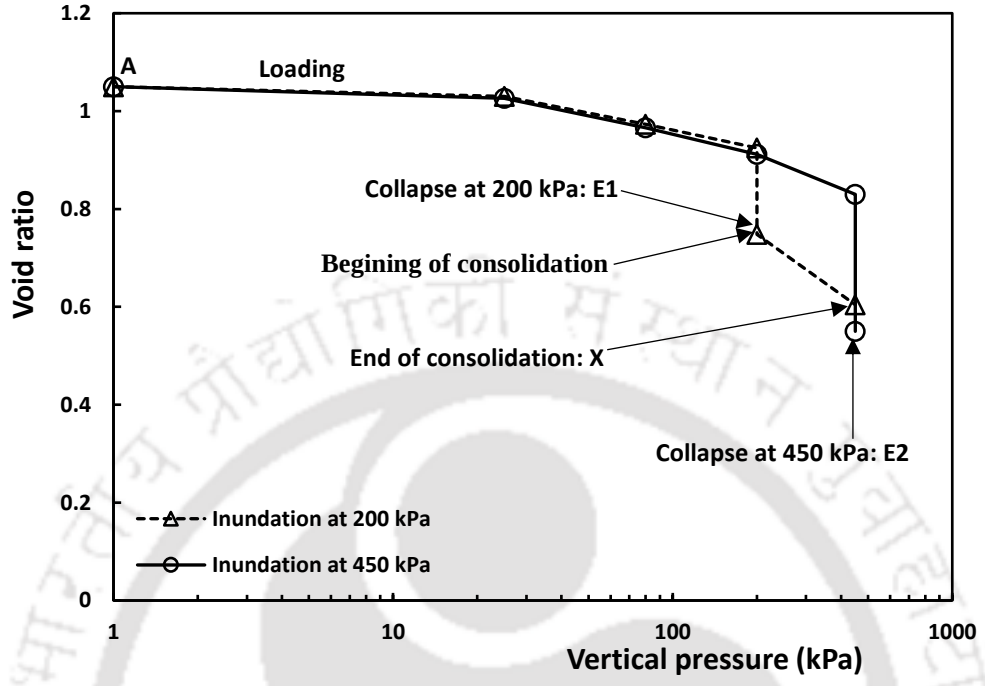

Fig. 6.4. Deformation response at consolidation and inundation pressure of 450 kPa.

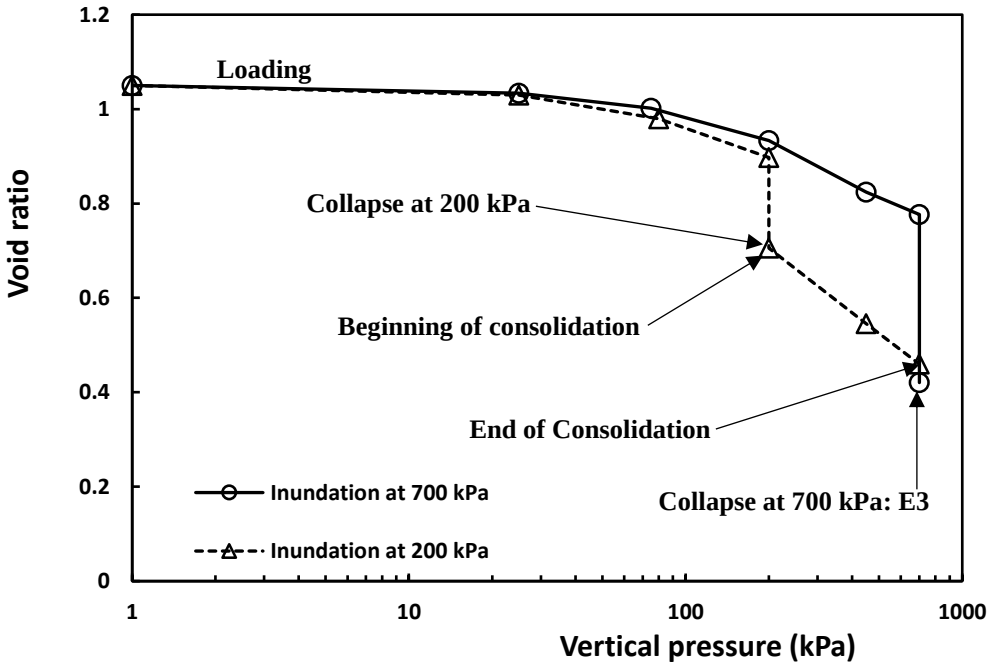

Fig. 6.5. Deformation response at consolidation and inundation pressure of 700 kPa.

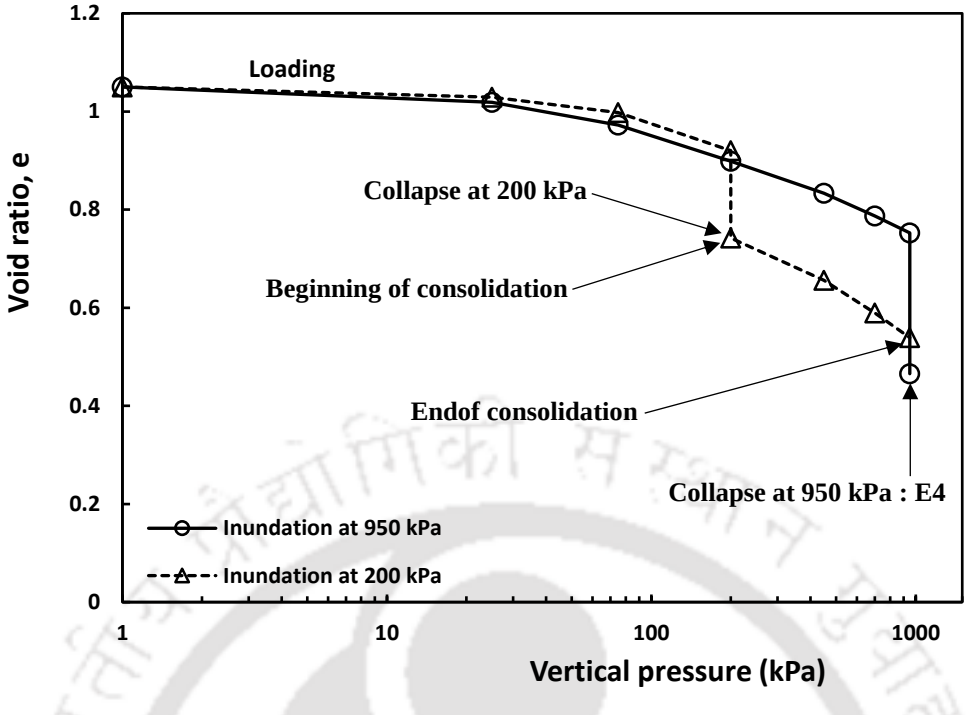

Fig. 6.6. Deformation response at consolidation and inundation pressure of 950 kPa.

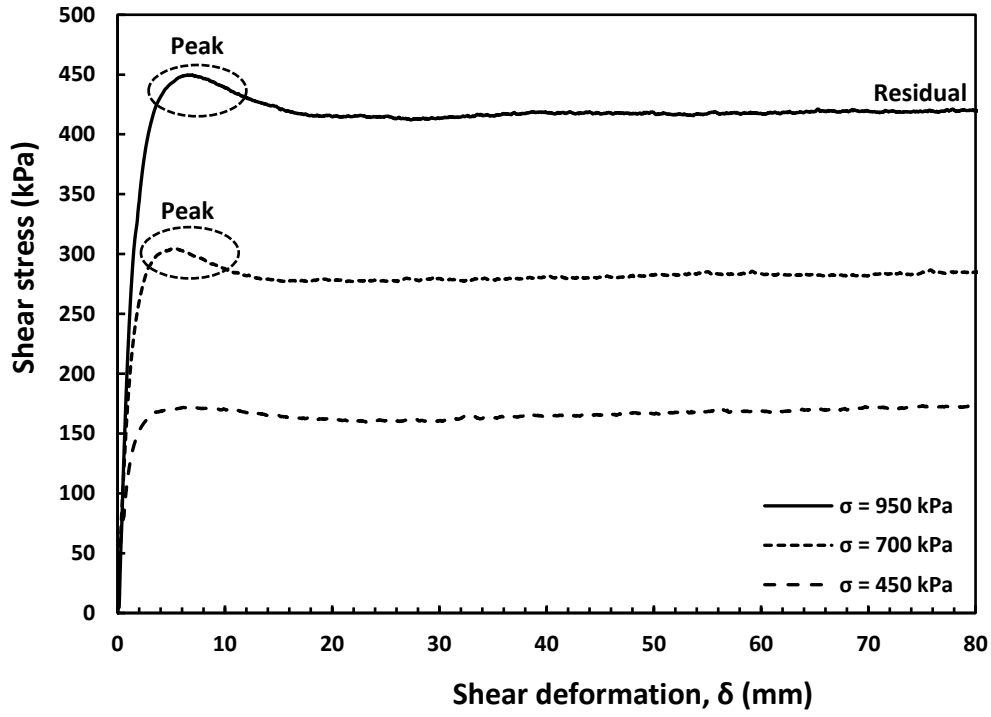

Fig. 6.7. Shear stress variation with shear deformation at different inundation pressures.

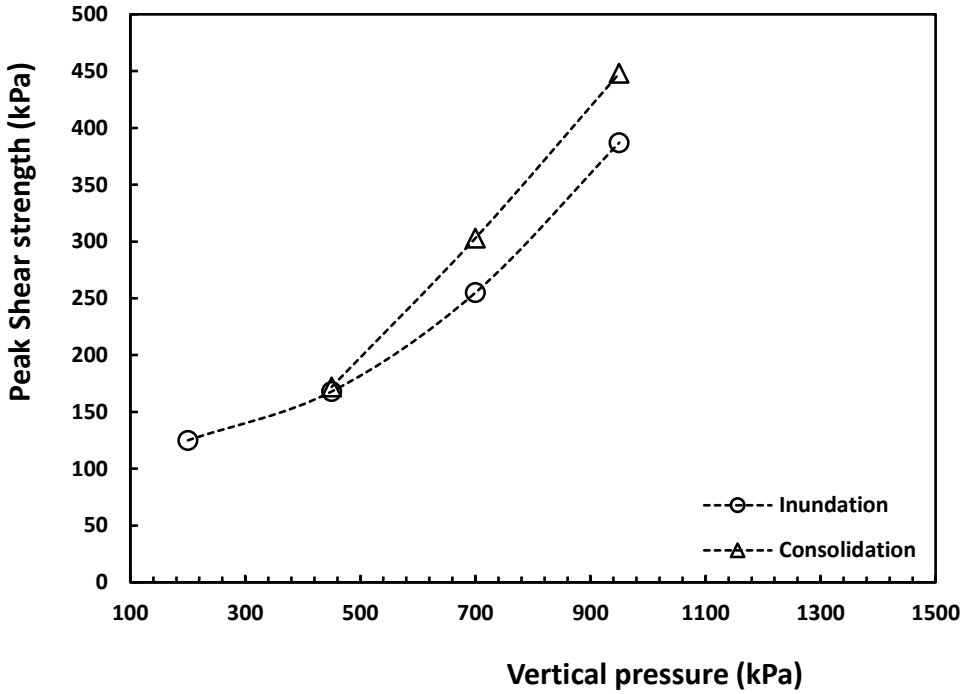

Fig. 6.8. Comparison of peak strength against applied inundation and consolidation pressure.

6.2.2 *Influence of Pore Fluid Chemistry*

Fig. 6.9 shows the volume change response for the four oven-dry compacted samples of kaolin inundated with different pH solutions at a constant mechanical pressure of 450 kPa in separate ring shear tests. The final states at the end of collapse were indicated by *B*, *C*, *D*, and *E2* for the pH of 2, 3.2, 4.5, and 6, respectively. The collapse was maximum at the highest pH = 6 for distilled water, with a change in the void ratio of 0.279. The collapse decreased with a reduction in the pH of the solution. Subsequently, from the final states, the samples were subjected to shearing until residual conditions were reached. The measured shear stress versus shear deformation response at different pH was shown in Fig. 6.10. The less pronounced peak followed by strain softening behaviour in NC conditions was observed at pH of 2, 3.2, and 6; however, peak strength was not mobilized at pH of 4.5. The lowest peak and residual shear strengths of 172 and 151 kPa were observed at the highest pH of 6, where collapse was maximum. Moreover, the smaller the pH of pore fluid, the higher were

peak and residual shear strengths. The residual conditions at different pH were achieved at shear deformation of approximately 50 mm.

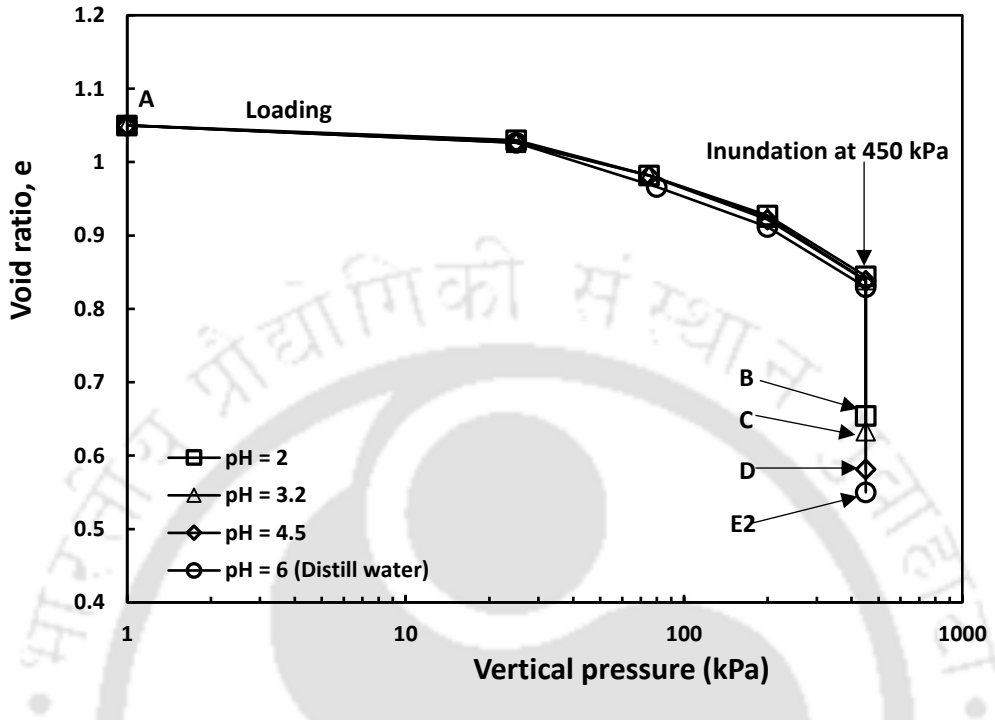

Fig. 6.9. Deformation response under various pH solutions.

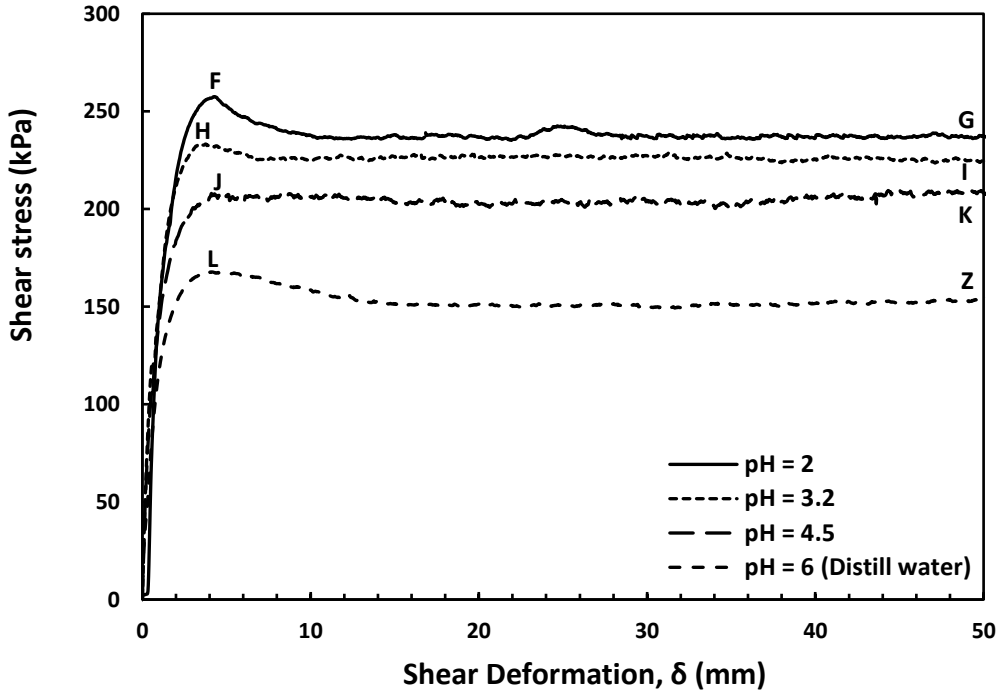

Fig. 6.10. Shear strength behaviour under different pH of aqueous solutions at constant inundation pressure of 450 kPa.

The inundation test results for oven-dry compacted kaolin samples saturated with different di-electric pore-fluids at a constant mechanical pressure of 200 kPa and 450 kPa in separate ring shear tests were shown in Fig. 6.11. The samples showed collapse due to wetting, and the deformation ceased at equilibrium states indicated by *M* for kerosene, *N* and *N'* for vinegar, and *E2* for distilled water. The sample saturated with the lowest di-electric constant (ε_r = 1.8) pore fluid kerosene experienced the smallest collapse with a marginal change in the void of 0.021. The collapse increased with an increase in the di-electric constant of pore-fluid. Subsequently, shearing was carried out from the equilibrium states until the residual condition was achieved. The measured shear stress versus shear deformation response under different di-electric pore mediums were shown in Fig. 6.12. The peak strength was mobilized

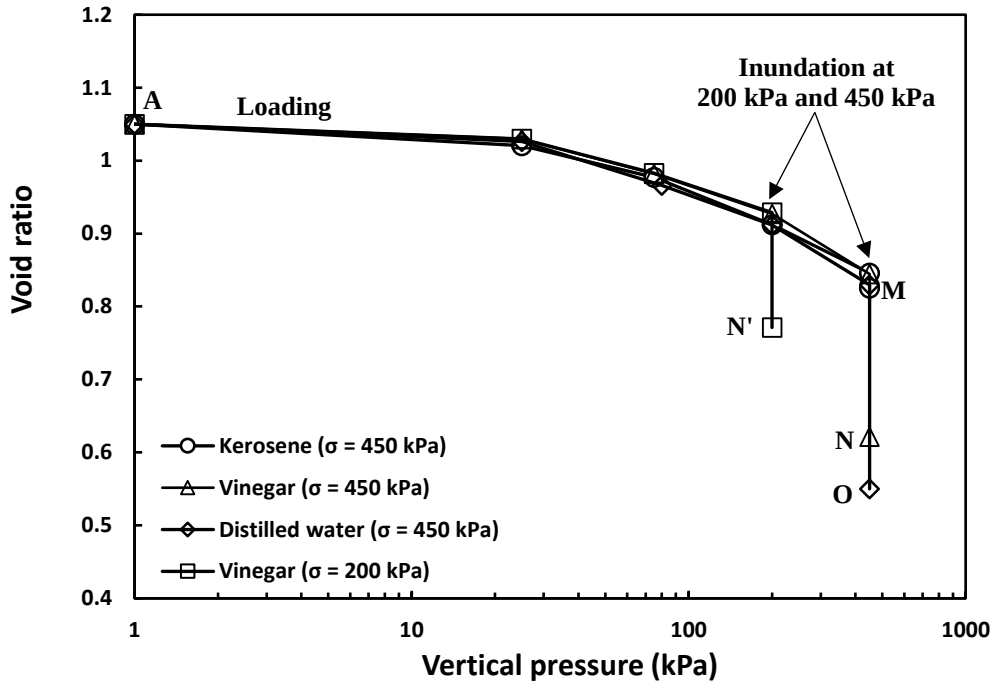

Fig. 6.11. Deformation response under various di-electric pore fluids and inundation pressures.

for all the samples. The peak and residual shear strength were highest for the lowest di-electric constant pore-fluid kerosene, which showed minimal collapse. The residual strengths for different samples at a pressure of 450 kPa were reached at shear deformation

of approximately 60 mm. However, for vinegar at a pressure of 200 kPa, the residual condition was achieved at higher deformation of 100 mm.

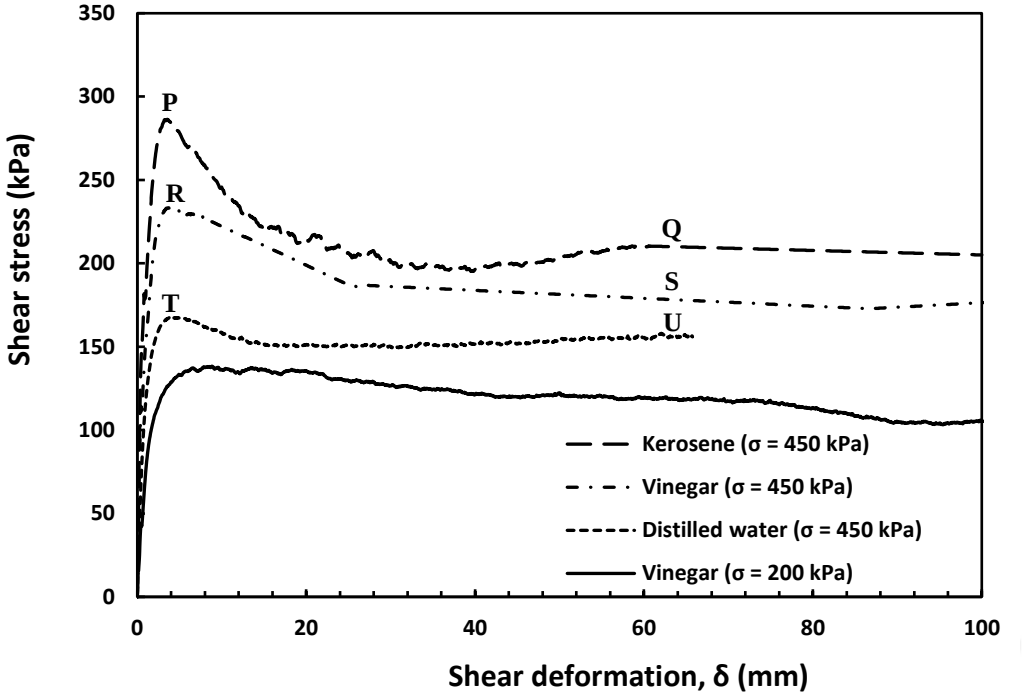

Fig. 6.12. Shear strength behaviour under different di-electric pore fluids and inundation pressures.

Further, the investigation of clay fabric at the peak and residual conditions was carried out using microstructural analysis. The micro-graphs of tested soil samples at different shearing stages under distinct pore-fluid conditions were presented in Fig. 6.13(a) – 6.13(h). At the initial oven-dry compacted condition, A (Fig. 6.4), the edge-to-face association can be seen, as shown in Fig. 6.13(a). The clay particle orientation after inundation at state *B* (Fig. 6.9) was slightly flocculated under the lowest pH = 2, as depicted in Fig. 6.13(b). The clay micro-structure at peak state *F* (Fig. 6.10) appears to be edge-to-face at pH = 2, as shown in Fig. 6.13(c). The less dispersed particle association was observed at residual condition *G* (Fig. 6.10 under pH = 2, as shown in Fig. 6.13(d). The FESEM images of the duplicate kaolin samples after inundation (Point *E2*) with distilled water at 450 kPa (Fig. 6.1) and at the peak shearing stage (Fig. 6.2) were depicted in Fig. 6.13(e) and 6.13(f), respectively. The soil

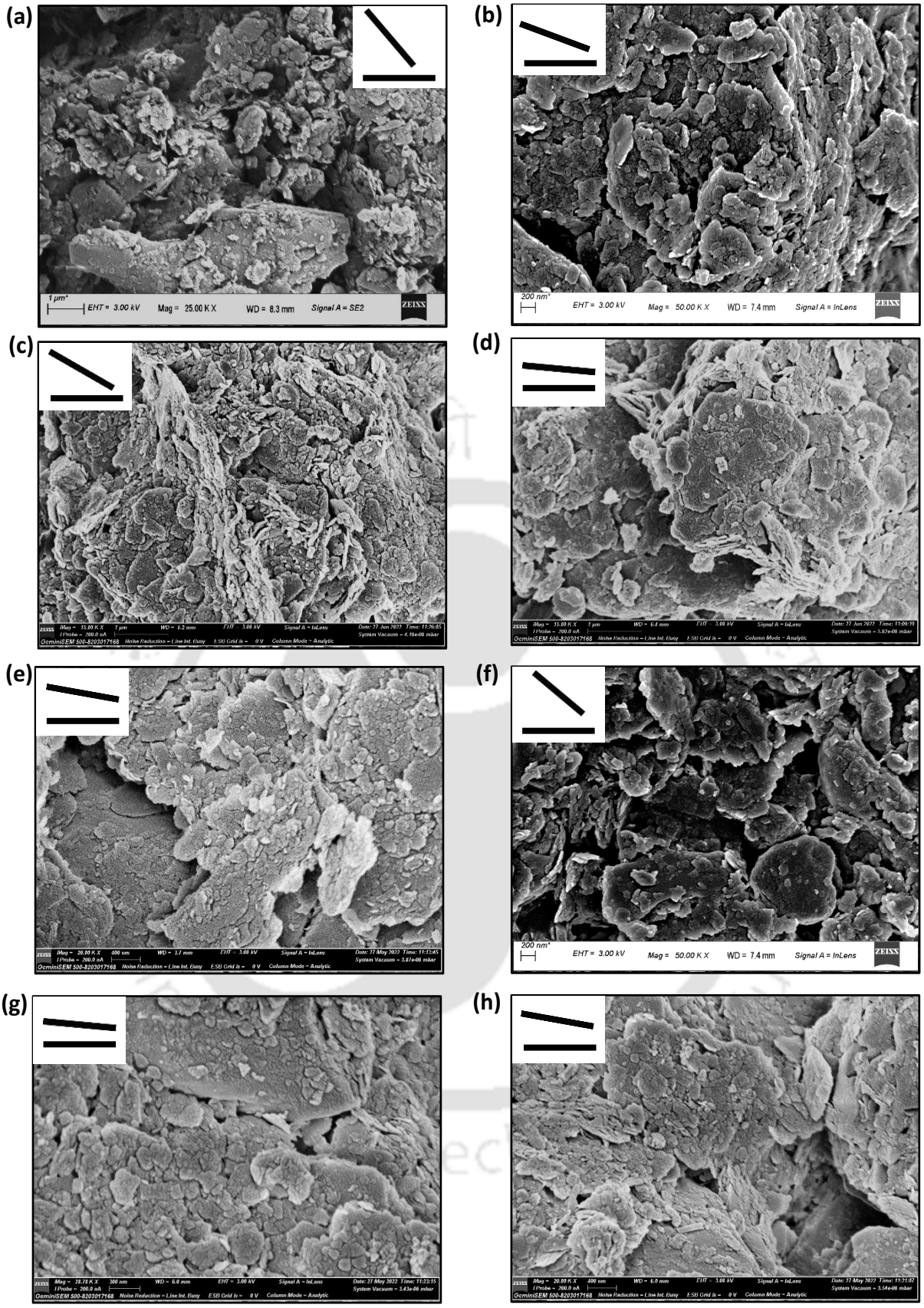

Fig. 6.13. FESEM micrographs of the kaolin samples at different stages of shearing: **(a)** At initial oven dry compacted state ***A*** (Fig. 6(a)), **(b)** After inundation at state ***B*** (Fig. 7(a)) with aqueous solution of **pH = 2**, **(c)** At peak shearing state ***F*** (Fig. 7(b)) under aqueous solution of **pH = 2**, **(d)** At residual shearing state ***G*** (Fig. 7(b)) under aqueous solution of **pH = 2**. **(e)** After inundation at point ***E2*** (Fig. 5(a)) with distilled water, **(f)** At peak shearing state (Fig. 5(b)), **(g)** At residual shearing state ***Z*** (Fig. 7(b)), and **(h)** At the end of consolidation at state ***X*** (Fig. 6(a)).

structure changed from slightly flocculated after inundation to flocculated at the peak stage. Almost parallel particle configuration can be seen in Fig. 6.13(g) at residual state (Fig. 6.2). This observation was consistent with the theoretical explanation; the residual state is formed by large shear displacement in a particular direction due to the parallel alignment of clay particles in a shear direction (Mesri and Shahien 2003, Toyota et al. 2009, Mesri and Huvaj-Sarihan 2012). At the end of consolidation (Point *X*) under 450 kPa pressure (Fig. 6.4), the particle's arrangement was slightly flocculated, as shown in Fig. 6.13(h). The micro-mechanism of change in particle configuration due to shearing was proposed in the following section.

6.3 Micro-Mechanism of Clay Fabric Evolution During Shear

The mechanisms of kaolin fabric evolution during shear were identified from the experimental findings of ring shear tests and FESEM micrographs for the conditions of pH < IEP_{edge} and pH > IEP_{edge}, as illustrated in Fig. 6.14(a) and 6.14(b), respectively. The re-orientation of particles at different stages of shearing can be understood by the kinematics of the particles with alterations associated with inter-particle electrostatic forces under chemo-mechanical loading conditions. Microstructural study at the initial oven-dried compacted state showed edge-to-face particle configuration (Fig. 6.4). An ideal situation was initially considered in which particles interaction was perpendicular to each other (Fig. 6.14(a)). The saturation of oven-dried samples by the pore fluid with pH < IEP_{edge} induced collapse resulting in a change in the magnitude of attractive electrostatic forces as di-electric medium changed and particle orientation angle, α, increased from zero to α_1. In this case, the α is measured from the vertical. The particles reached the equilibrium condition by translation in the y-direction and clockwise rotation about the z-axis. This results in a slightly flocculated structure at the start of the shearing (Stage-*I*) due to the dominant attractive electrostatic forces. The shear stress at the inter-particle level imparted compression in the

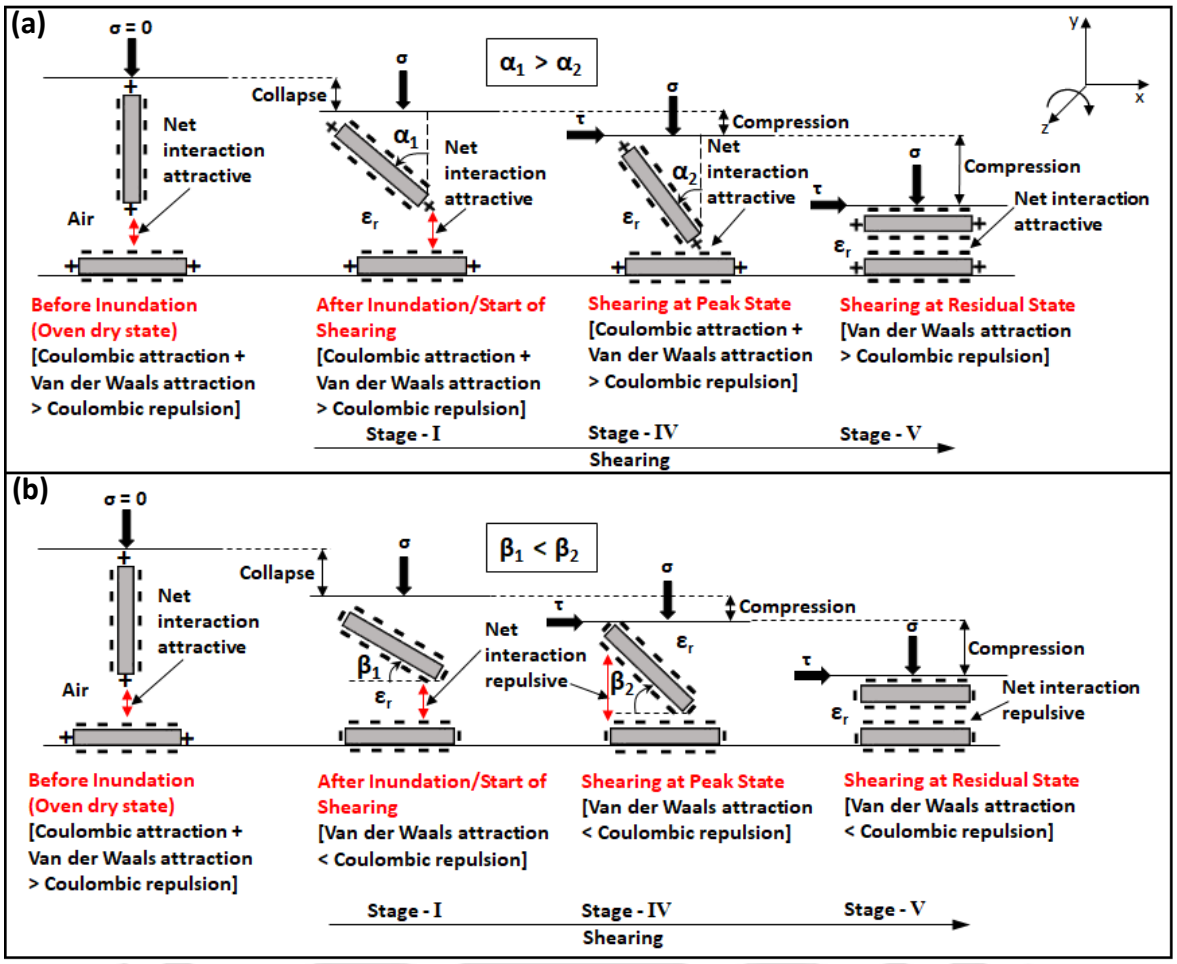

Fig. 6.14. Micro-mechanism describing kaolinite fabric evolution during shear for conditions: **(a)** pH < IEP_{edge} and **(b)** pH > IEP_{edge}.

y-direction and clockwise rotation about the z-axis in the direction of applied shear. The shearing induced edge-to-face particle association at peak (Stage-*IV*) and changed the magnitude of attractive electrostatic forces because of a reduction in particle orientation angle, α from α_1 to α_2 ((Fig. 6.14(a)). Further, the continuous shearing to the residual state brought the soil particles very close to each other in an almost parallel configuration (Stage-*V*). It is noted that the shearing stages (*I*, *IV*, and *V*) have already been marked for the condition as shown in Fig. 6.2. The face-to-face coulombic repulsion can be seen in parallel alignment. According to the effective stress principle, the effective stress should increase when compression occurs. Thus, the van der Waals forces might have dominated at residual condition, which made overall interaction attractive. This indicated that the particles were

very close to each other at the residual state. However, this claim was verified later while estimating the separation distance and net electrostatic pressures from the test results.

The oven-dried sample, when inundated by the aqueous solution with pH > IEP_{edge}, the edge charges were transformed from positive to negative, as shown in Fig. 6.14(b). As a result, electrostatic repulsion prevailed at the microscopic locations between the soil particles. The wetting-induced collapse for pH > IEP_{edge} was higher than in the case of pH < IEP_{edge}, due to the exertion of substantial repulsive electrostatic forces at the inter-particle level. The particle moved towards the less dispersed state (equilibrium condition) through translation and rotation (Stage - *I*). The shearing caused the increment in angle, β in the direction of shear from β_1 (Stage - *I*) to β_2 at the peak (Stage - *IV*), which resulted in a change in the magnitude of repulsive electrostatic forces. Here, β is measured from the horizontal. Further shearing to large shear deformation brought the clay particles in parallel association at the residual condition (Stage - *V*). The edge-to-face and face-to-face coulomb repulsion might have caused large particle separation distances. Thus, van der Waals forces might not appear at the residual state. This assertion was later confirmed when determining the separation distance and net electrostatic pressures from experimental data.

6.4 Framework for Large-Strain Shear Resistance

The electrostatic interactive forces between clay particles can be estimated for different modes of particle arrangement using the concept of electrostatics. For the condition shown in Fig. B1 (Appendix-B), the electrostatic force of attraction F_{ef} between the edge and the face of particles in a pore fluid with pH < IEP_{edge} is given by

$$F_{ef} = \frac{\pi\rho\rho_e ta}{\varepsilon_o\varepsilon_r}\left[1-\frac{y}{\sqrt{a^2+y^2}}\right] \qquad [6.1]$$

The derivation of eq. (6.1) was provided in Appendix-B. In deriving the above expression,

the particles were assumed to be uniformly charged discs. Where ρ_e is electrical edge charge density (C/m^2); t is the particle thickness (m), and the rest of the terms are the same as defined in eq. (2.7). The inter-particle attractive and repulsive coulomb forces (eq. (6.1) and (2.7)) are controlled by physico-chemical factors, including particle dimensions, particle-to-particle distance, surface charge density, and di-electric medium. As discussed earlier that the electrostatic forces also depend on the pore fluid pH and particle orientation angle. The effect of particle orientation was included by considering the inclination factors, $a\,\mathrm{Cos}\,\alpha$ and $a\,\mathrm{Cos}\,\beta$ while deriving eq. (6.1) and (2.7). Thus, both eq. (6.1) and (2.7) were modified and given by

$$F_{ef} = \frac{\pi\rho\rho_e t a Cos\alpha}{\varepsilon_o\varepsilon_r}\left[1-\frac{y}{\sqrt{a^2+y^2}}\right] \quad (\text{for pH} < \text{IEP}_{\text{edge}}) \qquad [6.2]$$

$$F_{ff} = \frac{\pi\rho^2 a^2 Cos\beta}{8\varepsilon_o\varepsilon_r}\left[\frac{y}{\sqrt{a^2+y^2}}-1\right] \quad (\text{for pH} > \text{IEP}_{\text{edge}}) \qquad [6.3]$$

where α is particle orientation angle ($0° \le \alpha < 90°$) measured with respect to vertical for pH < IEP$_{\text{edge}}$, and β is particle orientation angle ($0° \le \beta < 90°$) measured with respect to horizontal for pH > IEP$_{\text{edge}}$, as shown in Fig. 6.14(a) and 6.14(b); ρ is the surface charge density (C/m^2) and was calculated by the well-known equation (Kaya and Fang 2000)

$$\rho = F\frac{CEC}{S_a} \qquad [6.4]$$

where F is Faraday constant (0.965 C/gm); CEC is cation exchange capacity of clay (meq/100gm); S_a is specific surface area of clay (m^2/gm). Van der Waals attractive pressure F_w between two parallel semi-infinite plates with separation distance, y, immersed in a particular fluid is written as (Anandarajahi and Chenii 1997, Kaya and Fang 2000)

$$F_w = \frac{A_H}{6\pi y^3} \qquad [6.5]$$

where F_w is in dyne/cm^2; A_H is Hamaker's coefficient (ergs) varies with the di-electric constant and refractive index of the medium (Sridharan and Rao 1979, Israelachvili 1991); y is the distance between plates (cm). The net-electrostatic attractive pressure in case of edge-to-face association (Fig. B1) when pH < IEP$_{edge}$ is given by

$$A - R = \left[\frac{F_{ef}}{a_{eff}} + F_w \right]$$

It must be noted that effective inter-particle repulsive pressure, R is zero for the condition pH < IEP$_{edge}$, as the interaction between the particles is fully attractive. Where A is effective inter-particle attractive pressure, $A=F_{ef}/a_{eff}$.; a_{eff} is the effective area of interaction, it is equal to the area of the periphery, $2\pi at$. Inserting the F_{ef} from eq. (6.2) and F_w from eq. (6.5) into the above expression for A-R,

$$A - R = \left[\frac{\rho \rho_e Cos\alpha}{2\varepsilon_o \varepsilon_r} \left(1 - \frac{y}{\sqrt{a^2 + y^2}} \right) + \frac{A_H}{60\pi y^3} \right] \qquad [6.6]$$

The net interaction was repulsive for the face-to-face association when pH > IEP$_{edge}$, as shown in Fig. 2.4. The term A will be governed by van der Waals attractive pressure, F_w, since no columbic attraction exist. The net-electrostatic repulsive pressure is written as

$$A - R = \left[F_w - \frac{F_{ff}}{a_{eff}} \right]$$

Where $R=F_{ff}/a_{eff}$.; the effective area of interaction, a_{eff} is πa^2 (Fig. 2.4). Putting the F_{ff} from eq. (6.3) and F_w from eq. (6.5) into the above expression for A-R,

$$A - R = \left[\frac{A_H}{60\pi y^3} - \frac{\rho^2 Cos\beta}{8\varepsilon_o \varepsilon_r} \left| \left(\frac{y}{\sqrt{a^2 + y^2}} - 1 \right) \right| \right] \qquad [6.7]$$

The proposed analytical explicit expressions eq. (6.6) and (6.7) enabled the theoretical determination of net-electrostatic pressure, *A*-*R*, and thus, effective stress can be estimated from eq. (2.6). It is now possible to describe the shear strength behaviour of kaolin under chemo-mechanical loading conditions using the Mohr-Coulomb law in the plane of shear stress versus effective stress, i.e.,

$$\tau = \mathrm{c}' + \sigma' \tan\phi' \qquad [6.8]$$

where, τ is shear stress in kPa; σ' is inter-particle effective stress estimated from eq. (1); ϕ' is effective friction angle; c' is effective cohesion. Finally, the expression for σ' (eq. (2.6)) with the inclusion of eq. (6.6) and (6.7) were inserted into the eq. (6.8), which gives the following general expressions for the shear stress incorporating physico-chemical effects in a saturated soil-fluid system having pH < IEP_{edge} and pH > $\mathrm{IEP}_{edge,}$ respectively,

$$\tau = c' + \left[\sigma - \mathrm{u}_w + \frac{\rho\rho_e Cos\alpha}{2\varepsilon_o\varepsilon_r}\left(1 - \frac{y}{\sqrt{a^2+y^2}}\right) + \frac{A_H}{60\pi y^3}\right]\tan\phi' \qquad [6.9]$$

$$\tau = c' + \left[\sigma - \mathrm{u}_w - \frac{\rho^2 Cos\beta}{8\varepsilon_o\varepsilon_r}\left|\left(\frac{y}{\sqrt{a^2+y^2}} - 1\right)\right| + \frac{A_H}{60\pi y^3}\right]\tan\phi' \qquad [6.10]$$

The eq. (6.9) and (6.10) describe the variation of shear stress with physico-chemical and mechanical factors, including strength parameters, *c'*, ϕ*'*, particle orientations (α and β), the distance between the particles (*y*), pH, di-electric permittivity (ε_r), soil quality ($\rho = 0.965\,CEC/SSA$), and normal stress (σ). Irrespective of drainage conditions and stress history, the above expressions could apply to normally consolidated/overconsolidated kaolin soils under drained/undrained shearing.

Moreover, the pair of models (eq. (6.9) and (6.10)) defined the constitutive relationships between state variables shear stress, τ and normal stress, σ. These two state variables are interlinked by two groups of model parameters, such as strength parameters (c' and ϕ') and physico-chemical parameters (α, β, y, a, t, ε_r, ρ, ρ_e, and A_H). In the next section, the mechanism of fabric evolution (Fig. 6.14) and eq. (6.2-6.7) were utilized at different stages of shearing to compute the inter-particle electrostatic forces and net electrostatic pressures.

6.5 Quantification of Inter-Particle Forces and Pressures

Some of the physico-chemical parameters required in the determination of electrostatic forces and pressures were estimated by utilizing basic geotechnical test results and stated here. Particle size, a: the radius of the particles, cannot be constant, as size varies in the soil specimen. The normal distribution of particle sizes from the particle size distribution curve was assumed, and a corresponding mean value of 0.01μm was considered and given in Table 6.1. Particle thickness, t: the thickness was considered as one-tenth of the mean particle radius. Surface charge density, ρ: the magnitude of surface charge density (C/m^2), was estimated using eq. (6) and reported in Table 6.1. Edge charge density, ρ_e: this was taken as one-tenth of the surface charge density. Hamaker's coefficient, A_H: the A_H for different di-electric fluids were selected from the literature (Sridharan and Rao 1979), and their values were given in Table 6.2.

In the proposed framework, the estimation of inter-particle electrostatic forces at different stages of shearing requires information on the governing mechanism of particle re-orientation. The mechanism of clay fabric changes due to the shearing under different pH conditions was already illustrated (Fig. 6.14). However, the mechanism was unknown for other di-electric pore fluids used in the present study. The sample saturated with pore fluid kerosene showed marginal collapse (Fig. 6.11). This showed little interaction between the

kerosene and kaolin particles, presumably because kerosene is non-polar. Thus, edge charges on kaolin particles did not alter in the presence of kerosene from the initial oven-dry state. Accordingly, the mechanism of clay fabric changes during shearing was similar to the case of pH < IEP_{edge} (Fig. 6.14(a)). However, the sample showed considerable collapse under the inundating fluid vinegar (Fig. 6.11). The vinegar used in this study was made up of acetic acid and water. This showed the soil particles interacted with vinegar due to its acidic nature. The measured pH of vinegar was 2.5 < IEP_{edge}; thus, Fig. 6.14(a) was governing mechanism of particle re-orientation during shearing.

Identification of the shearing mechanism underpinned the quantification of electro-chemical forces and pressures. Fig. 6.15 shows the variation of van der Waals forces with distance estimated using eq. (6.5) for four different di-electric mediums, including distilled water, vinegar, kerosene, and air. As the die-electric permittivity of pore fluid increased, the van der Waals forces decreased and were lowest for distilled water (ε_r = 80). The attractive and repulsive coulomb forces shown in Fig. 6.16, 6.17, and 6.18 were estimated from the eq. (6.2) and eq. (6.3) for solutions having pH < IEP_{edge} and pH > IEP_{edge} by varying particle orientation angles at different stages of shearing (inset Fig. 6.17 and 6.18). It is to be noted that in the case of pH < IEP_{edge}, the attractive and repulsive coulomb forces were plotted (Fig. 6.17) on the primary and secondary axis, respectively. The attractive coulomb forces (Fig. 6.17) were highest between the particles which were oriented at the smallest angle, α = 15°. The repulsive coulomb interaction was observed when particles aligned parallelly (β = 0°), even though pH < $IEP_{edge.}$ However, their net interaction, in this case, was discussed later. The repulsive coulomb interaction can be seen when pH > IEP_{edge} and the magnitude of coulomb forces (Fig. 6.18) was lowest for the largest particle orientation angle, α = 60°.

After estimating electro-chemical forces at different shearing stages, the variation of net-electrostatic pressures, *A-R* with separation distance, y, were determined using the proposed

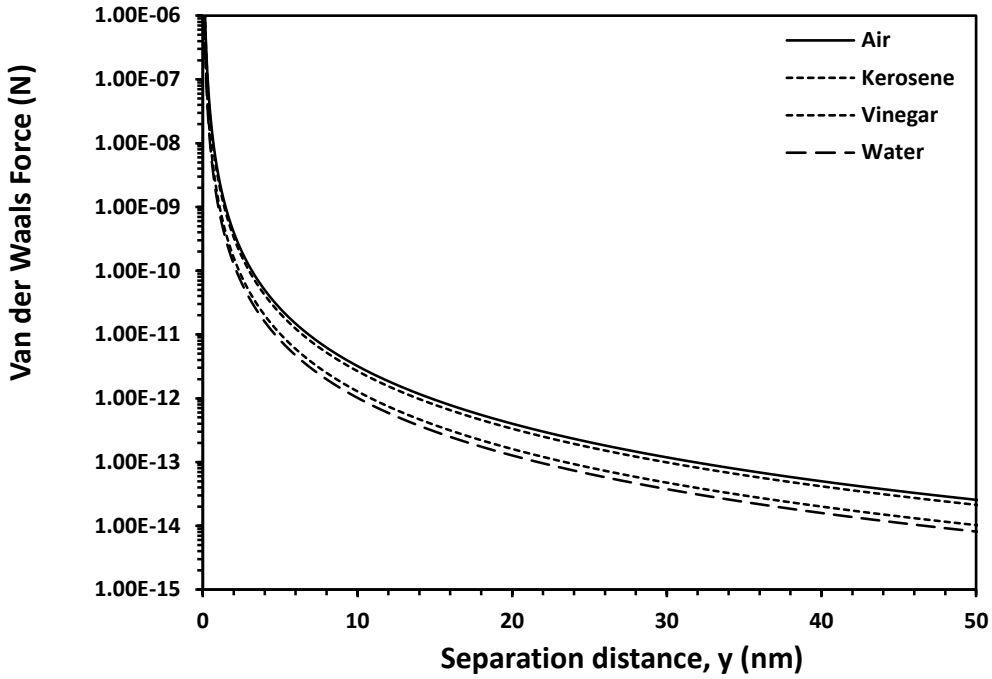

Fig. 6.15. Estimated van der Walls force variation between particles distance for different pore fluids.

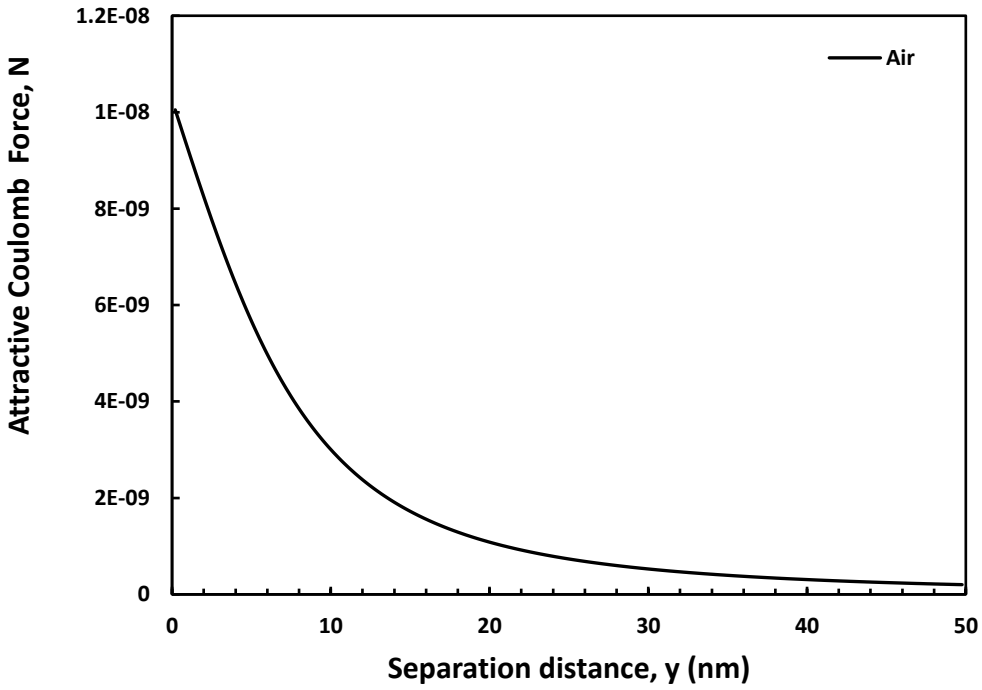

Fig. 6.16. Estimated coulomb force at oven-dry compacted state A (Fig. 6.4).

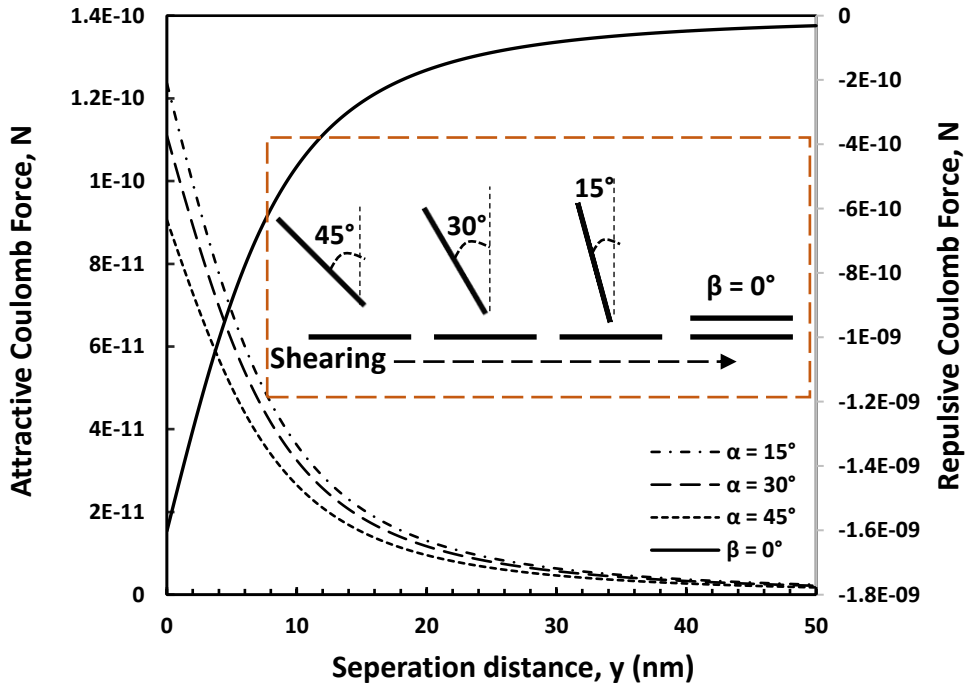

Fig. 6.17. Estimated coulomb forces for different particle orientations under pH < IEP_{edge}.

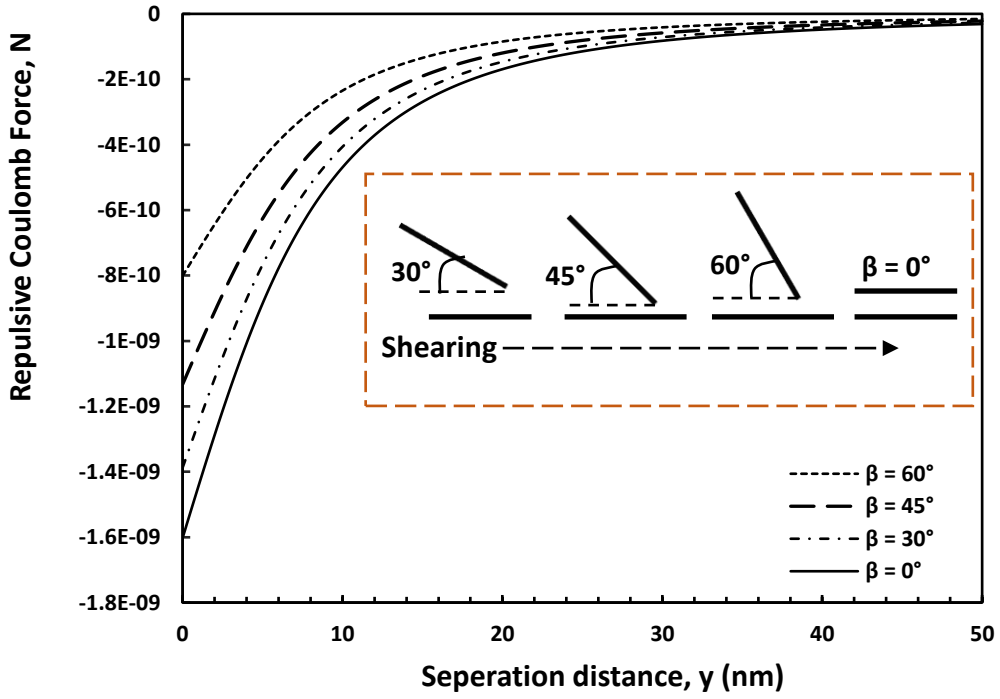

Fig. 6.18. Estimated coulomb forces for different particle orientations at pH > IEP_{edge}.

eq. (6.6) and (6.7). The net interaction was attractive for pH < IEP_{edge} and estimated *A-R* found to be highest for the smallest particle orientation angle, α = 15°, as shown in Fig. 6.19,

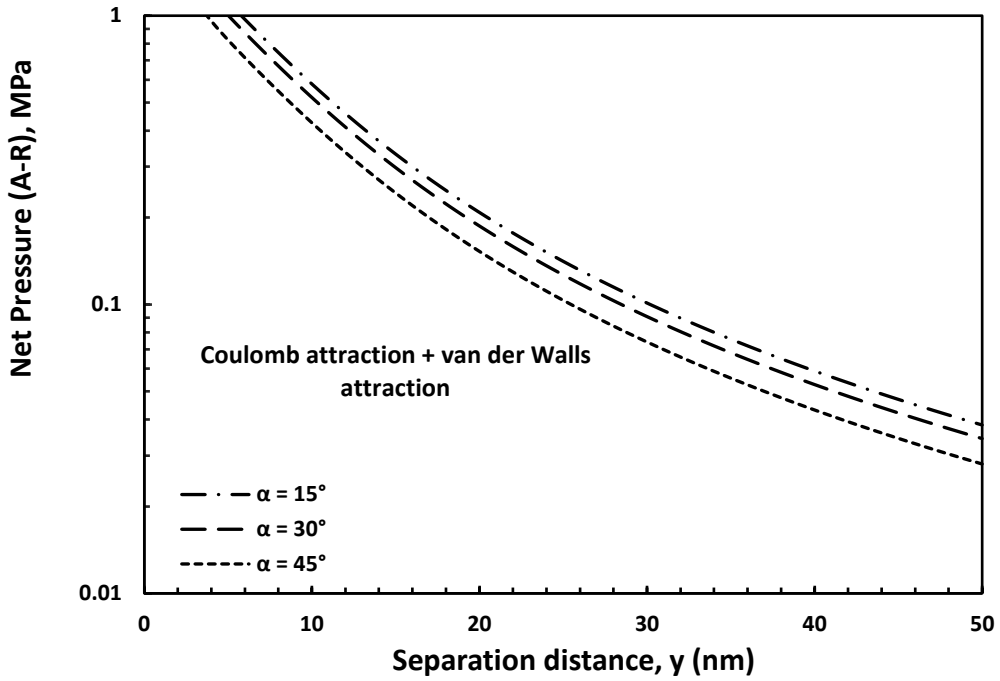

Fig. 6.19. Estimated net electrostatic pressure for different particle orientations at pH < IEP_{edge}.

and *A-R* varied significantly in a domain, 0 nm < y ≤ 50 nm. Interestingly, as the particles achieved face-to-face association, the net inter-particle interaction became attractive in the smaller domain, 0.1 < y ≤ 1 nm, as shown in Fig. 6.20, although there was repulsive coulomb

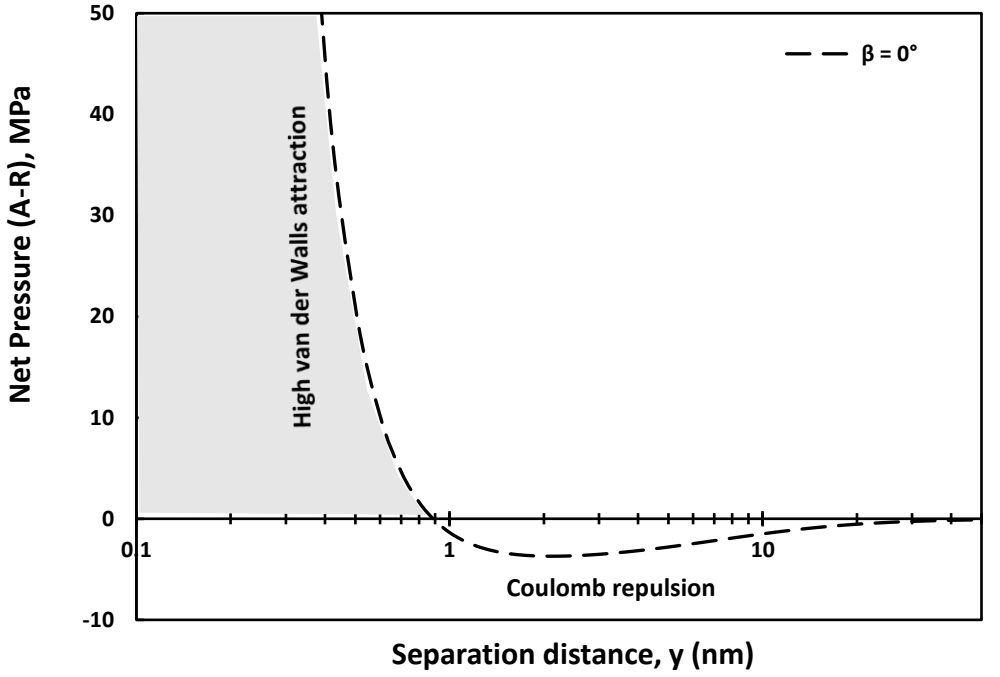

Fig. 6.20. Estimated net electrostatic pressure for different particle orientations at pH < IEP_{edge}.

interaction as well, since β = 0°. This was due to the high magnitudes of van der Waals forces in short distances in the dark segment (Fig. 6.20). It signified that the net interaction could also be attractive at the residual stage when pH < IEP_{edge}. The net-repulsive pressure, *A-R*, under the condition of pH > IEP_{edge} was significant in the domain of 1 nm < y ≤ 50 nm, as shown in Fig. 6.21. Moreover, its magnitudes were highest for the lowest orientation

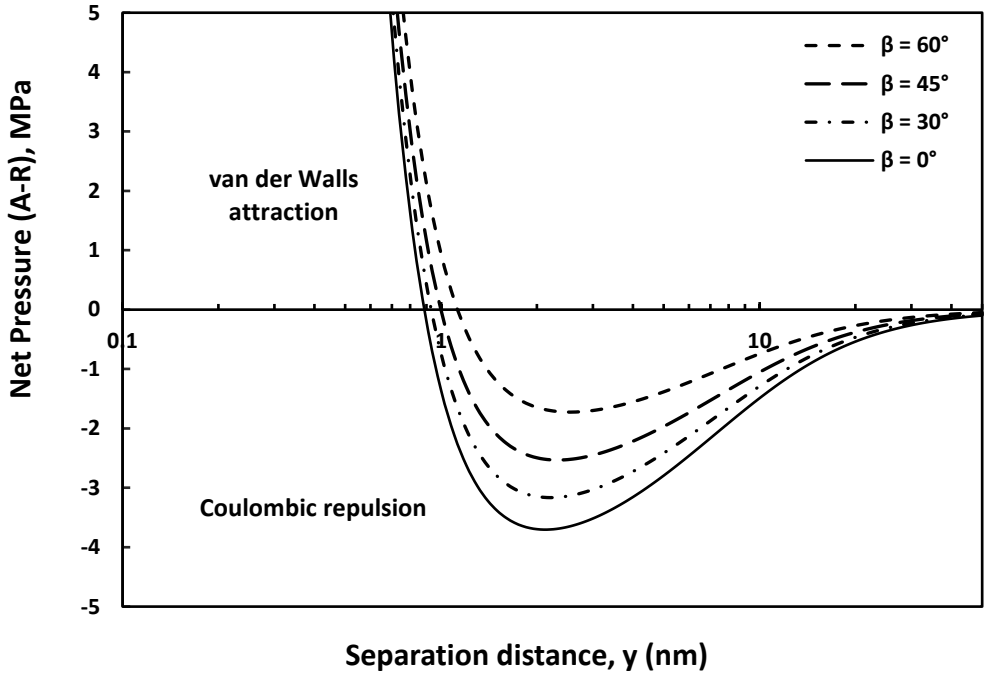

Fig. 6.21. Estimated net electrostatic pressure for different particle orientations at pH > IEP_{edge}.

angle, β = 0°. Therefore, if particle orientation angle at different shearing stages (i.e., initial, intermediate, peak, and residual) is known, then the variation of net-electrostatic pressure, *A-R*, with distance can be estimated. However, the value of *A-R* at a given shearing stage from the estimated variation can only be chosen if the particle separation distance, y, is known. Further, the effective stress at different shearing stages can be computed using the eq. (2.6) and prediction of shear stress can be done by eq. (6.9) and (6.10). The following section discussed a procedure to estimate the effective stress and to predict shear stress in the ring shear stress conditions.

6.6 Predictions

6.6.1 *Model Parameters Estimation*

A simple procedure was explained here to estimate unknown model parameters if the shear test data under one particular pressure with FESEM images at distinct shearing stages are known. Five subsequent shearing stages (*I*, *II*, *III*, *IV*, and *V*) were chosen on the measured profiles of shear stress versus shear deformation, however, indicated only for one profile at inundation pressure of 450 kPa as shown in Fig. 6.2. These stages included the start of shearing (*I*), intermediate stages (*II* and *III*), peak (*IV*), and residual (*V*). The initial and intermediate stages were chosen at specified shear deformations, δ of 0.037 mm, 0.333 mm, and 0.666 mm, respectively. At the initial, peak, and residual stages, the average separation distance, *y*, was determined from FESEM images (Fig. 6.13(e), 6.13(f), and 6.13(g)) using the Image J software tool and reported in Table 6.2. However, for intermediate stages, the distances were assumed to be between those for the initial and peak phases. For any other pressures, i.e., 200 kPa, 700 kPa, and 950 kPa, the distances were assumed to be the same as at 450 kPa pressure. The estimated average distances were found to be lies in the nanometres range. The extracted shear stress data at five different pre-specified shearing stages (*I*, *II*, *III*, *IV*, and *V*) were plotted in the space of shear stress versus normal stress, as shown in Fig. 6.22. The shearing test data at the pressure of 450 kPa was utilized to estimate the parameters for the predictions at other pressures. The ϕ' was calculated using proposed eq. (6.10) by trial and error process by setting the different values of β and known parameters, τ, ρ, y, ε_r, and A_H. The β was found to be 78° at the peak stage, and for other shearing stages, angle β was provided in Table 6.2. The estimated ϕ' from the above procedure was close to the observed ϕ' assessed from measured data sets (Fig. 6.22) and reported in Table 6.2. It is noted that the observed ϕ' were determined by fitting Mohr's Coulomb lines having zero intercepts, i.e., c'=0 with measured data for different stages of

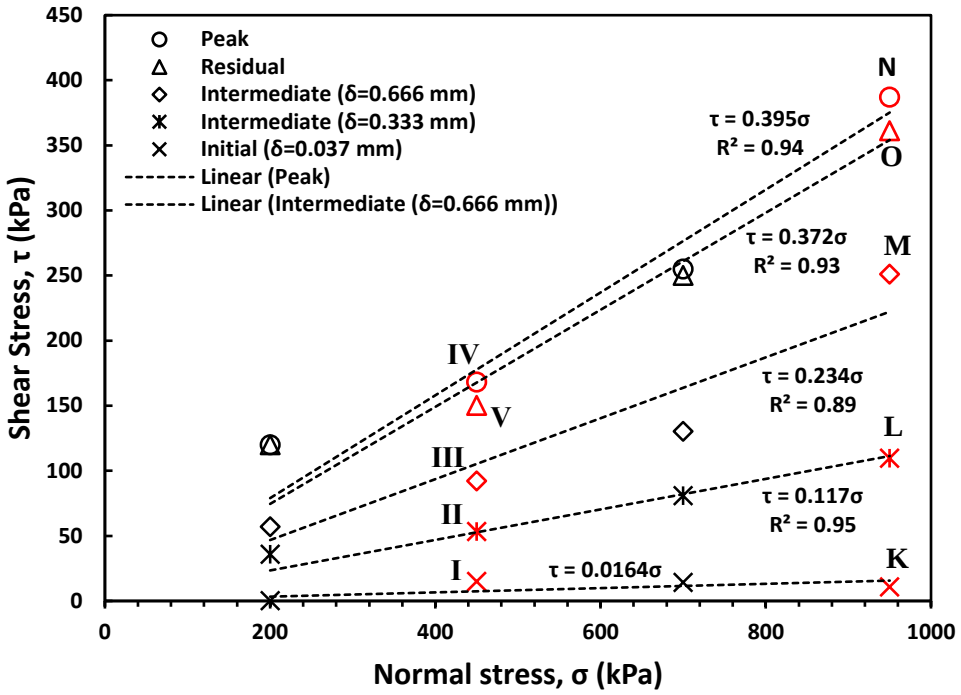

Fig. 6.22. Measured shear strength data under distinct inundation pressures fitted with Mohr-Coulomb envelope for different stages of shearing.

shearing (Fig. 6.22). Cohesion refers to inter-particle attractive forces between the soil particles contributing to the shear strength. It is reasonable to consider the intercept, *c'*=0, for the proposed framework, as proposed eq. (6.9) and (6.10) already accounted for cohesion through attractive electrostatic forces. Further, using the estimated model parameters, effective stress paths (ESPs) were predicted at different pressures for the kaolin soils from the present study and literature studies, which were discussed in the following section.

6.6.2 *Validations*

After determining model parameters for the studied kaolin at an inundation pressure of 450 kPa, as discussed earlier, net electrostatic pressure, *A-R*, was estimated by eq. (6.7) at different shearing stages and given in Table 6.2. The effective stress was determined from eq. (2.6) using estimated *A-R* values at different shearing stages under 450 kPa pressure. Further, assessed *A-R* values under 450 kPa pressure was also utilized at other inundation pressures. Thus, effective stress and shear stress were predicted using eq. (2.6) and eq. (6.10)

at different shearing stages under higher inundation pressures, 700 kPa and 950 kPa. The measured total stress path (TSP) and effective stress path (ESP) at different inundation pressure were plotted along with predicted ESPs in the plane of shear stress versus effective stress, as shown in Fig. 6.23. The measured ESP in Fig. 6.23 represents the experimental

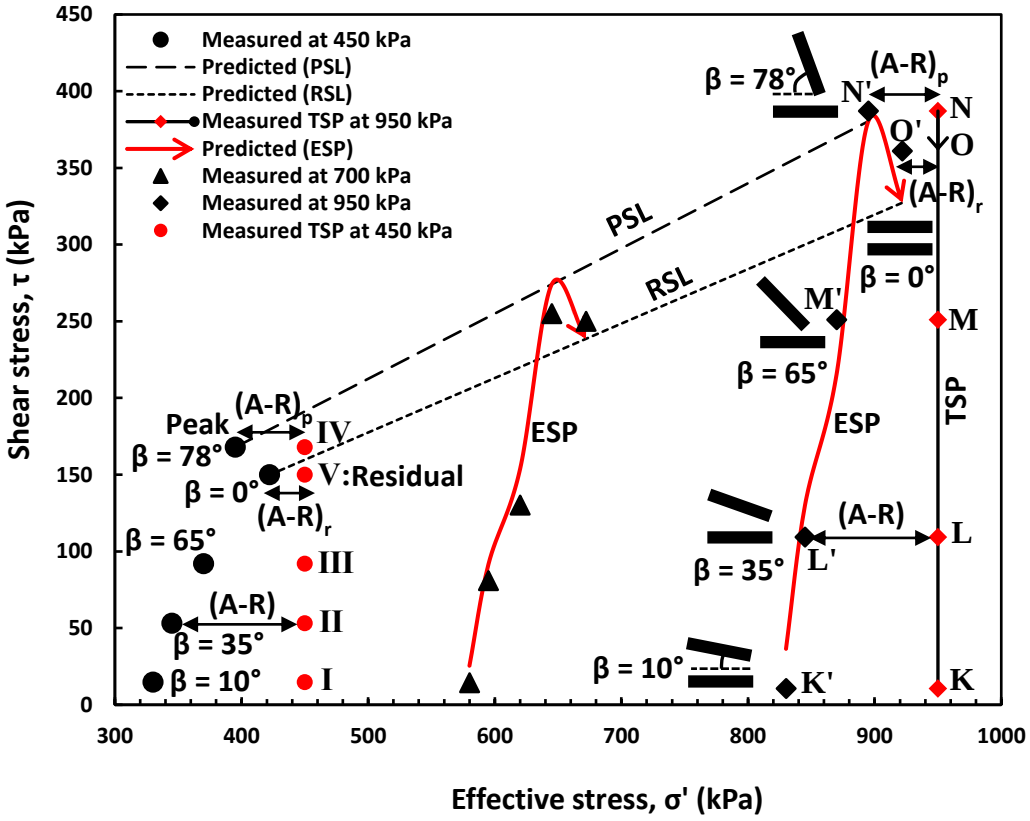

Fig. 6.23. Comparison of Predicted and measured effective stress paths at different inundation pressure - pore fluid: distilled water.

shear stress variation with the estimated or predicted effective stress. The effective stress was common for both measured and predicted ESPs. The measured ESP reached peak condition followed by residual state with increased effective stress during shear. The variations in β and *A-R* during shear were shown at the pressures of 450 kPa and 950 kPa (Fig. 6.23). The net electrostatic pressure, *A-R*, values horizontally reduced the TSP (*KLMNO*) to ESP (*K'L'M'NO'*) at any shearing stage. The overall predictions were satisfactory; however, some over-prediction was observed near the peak at an inundation pressure of 700 kPa, and underprediction was seen near the residual condition at 950 kPa.

Additionally, predicted Mohr-Coulomb peak and residual envelopes, i.e., peak state line (PSL) and residual state line (RSL) were established by joining predicted peak and residual shear stress at different pressures. The predicted envelopes were close to the measured data.

Fig. 6.24 shows the measured ESP data from ring shear tests and predicted ESP response at different consolidation pressures. The measured shear stress data at different stages of shearing from shear stress versus shear deformation response under 450 kPa were utilized to estimate the model parameters reported in Table 6.2. The estimated ϕ' values were close to the observed ϕ' computed from measured shear data. The predicted ESPs were matched well with the measured locus of ESPs at higher consolidation pressures, 700 kPa and 950 kPa. However, at 950 kPa pressure, the peak and residual shear stress were underpredicted. The predicted PSL and RSL were also matched satisfactorily to measured data points. The

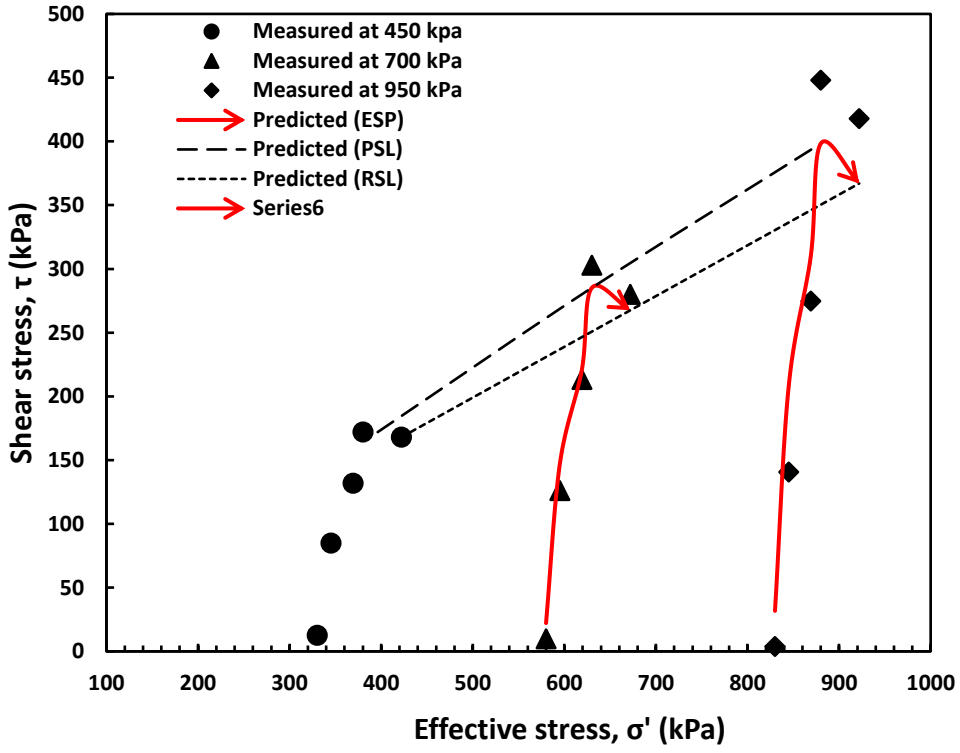

Fig. 6.24. Comparison of Predicted and measured effective stress paths at different consolidation pressure - pore fluid: **distilled water**.

measured shear stress data during shear under pH = 2 at inundation pressure of 450 kPa were used to determine the parameters, as shown in Fig. 6.25. The estimated model parameters are given in Table 6.2. The predicted ESPs using eq. (6.9) at different inundation pressures, i.e., 200 kPa, 700 kPa, and 950 kPa were plotted in the same Figure. The predicted ESP at 200 kPa was close to the measured data. Measured shear stress data at inundation pressure

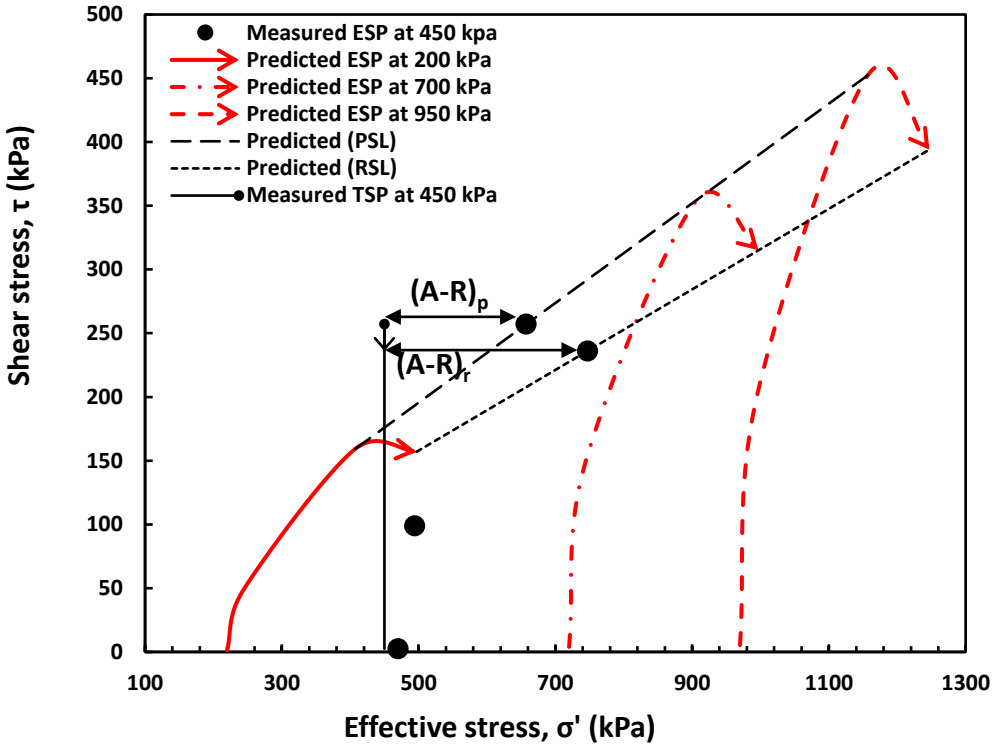

Fig. 6.25. Comparison of Predicted and measured effective stress paths at inundation different pressure - pore fluid: aqueous solution of **pH =2**.

of 450 kPa under inundating fluid vinegar (pH = 2.5), as shown in Fig. 6.26 were used to determine model parameters and given in Table 6.2. Predicted ESP by eq. (6.9) at 200 kPa was close to the measured data points. Moreover, ESP prediction at higher pressures was also shown. The measured shear stresses during shearing at an inundation pressure of 450 kPa for the pore fluid kerosene, as shown in Fig. 6.27, were used to estimate the model parameters provided in Table 6.2. The predictions of ESP at different inundation pressures were presented along with predicted PSL and RSL.

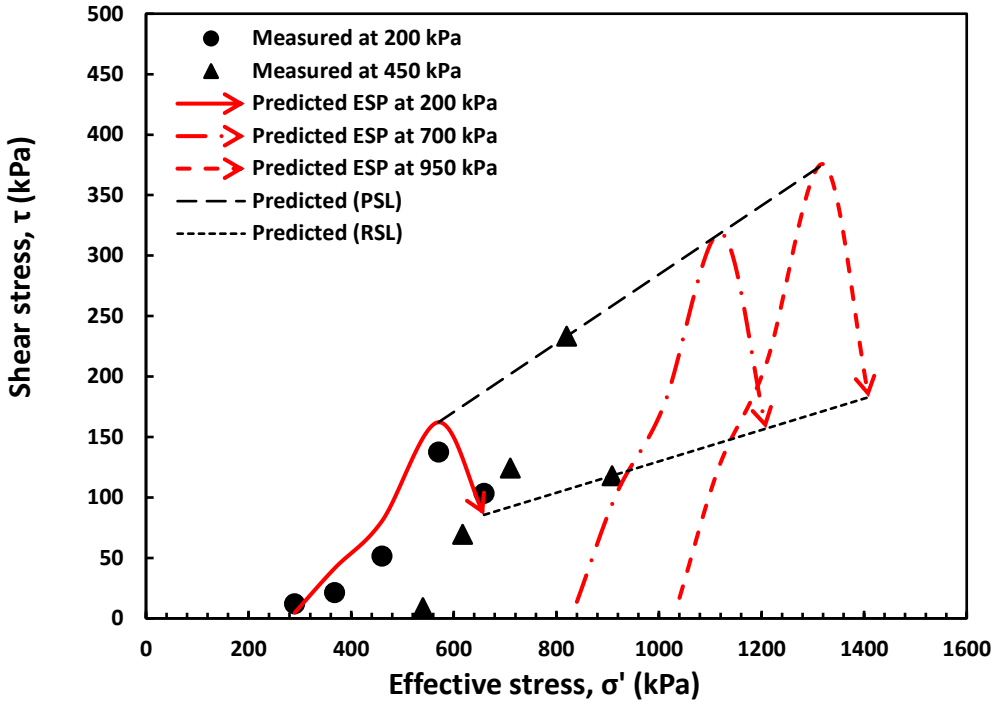

Fig. 6.26. Comparison of Predicted and measured effective stress paths at different inundation pressure - pore fluid: **Vinegar**.

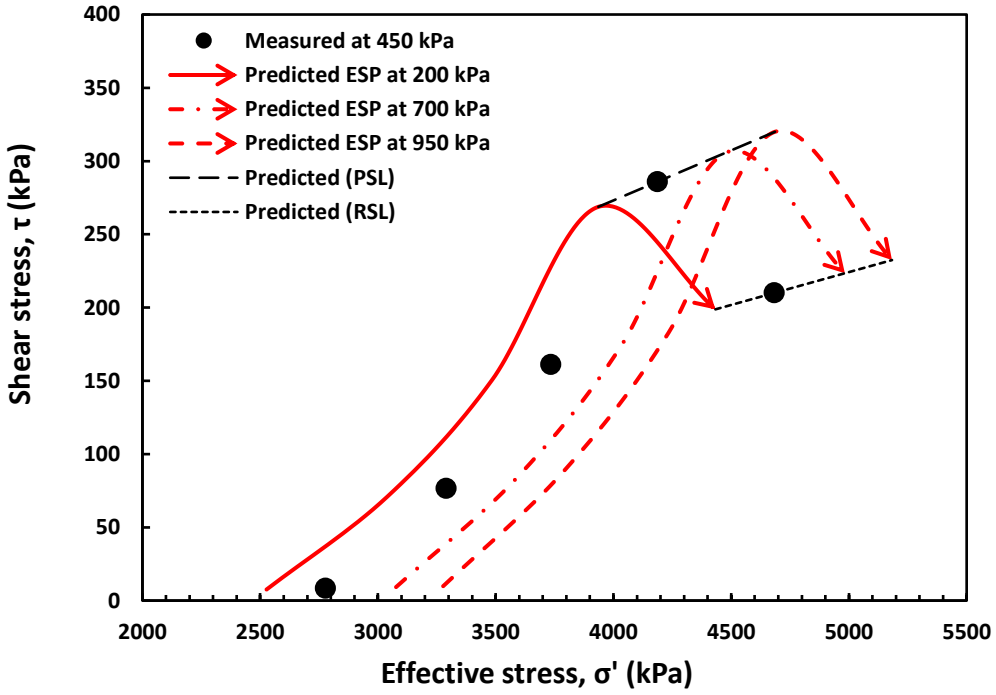

Fig. 6.27. Comparison of Predicted and measured effective stress paths at different inundation pressure - pore fluid: **Kerosene**.

Apart from the validations of studied kaolin, the model performance was examined for the kaolin soils from the different literature studies. Ring shear test data of kaolin soil was considered from the literature study (Suzuki et al. 2017) for validation. In this work, the kaolin slurry samples were initially consolidated to 98 kPa, 196 kPa, and 392 kPa and subsequently sheared under NC conditions until residual conditions were achieved. The pore fluid used to make the slurry was distilled water. Three sets of measured ring shear stress data were extracted from shear stress versus shear deformation profiles at consolidation pressures of 98 kPa, 196 kPa, and 392 kPa. Each data set consists of shear stress at initial, intermediate, peak, and residual stages corresponding to specified shear deformation, δ given in Table 6.2. The shear stress data at a pressure of 392 kPa was used to determine the model parameters given in Table 6.2. Effective stresses at different shearing stages under each consolidation pressure were estimated using eq. (2.6), then measured data sets were plotted as shown in Fig. 6.28. Further, the predictions of shear stresses during

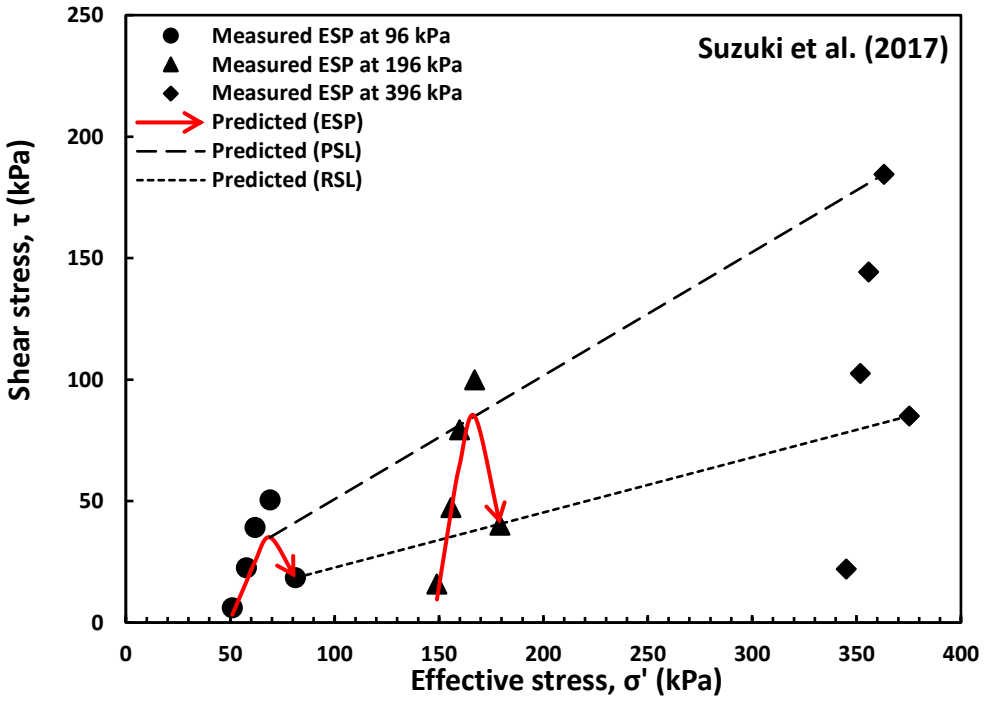

Fig. 6.28. Comparison of Predicted and measured effective stress paths at different consolidation pressure - pore fluid: distilled water (Suzuki et al. (2017).

shearing were made using eq. (6.10) at 96 kPa and 198 kPa; predicted ESPs were illustrated in Fig. 6.28. The predicted ESPs were close to measured data; however, some underprediction was observed at the peak.

Another ring shear test data was chosen from the recent study of Yao et al. (2020) for validation. This study explored the large-strain shear behaviour of slurry kaolin samples at consolidation pressures of 100 kPa, 200 kPa, and 400 kPa under NC conditions. The measured shear stress data at each consolidation pressure during shearing were extracted at initial, intermediate, peak, and residual stages corresponding to specified shear deformation, δ provided in Table 6.2. The shear stress data at 400 kPa was utilized to estimate model parameters, given in Table 3. Consequently, Effective stresses during shear at each consolidation pressure were calculated using eq. (2.6) and measured shear response was plotted, as shown in Fig. 6.29. Further, shear stresses were predicted using eq. (6.10) during

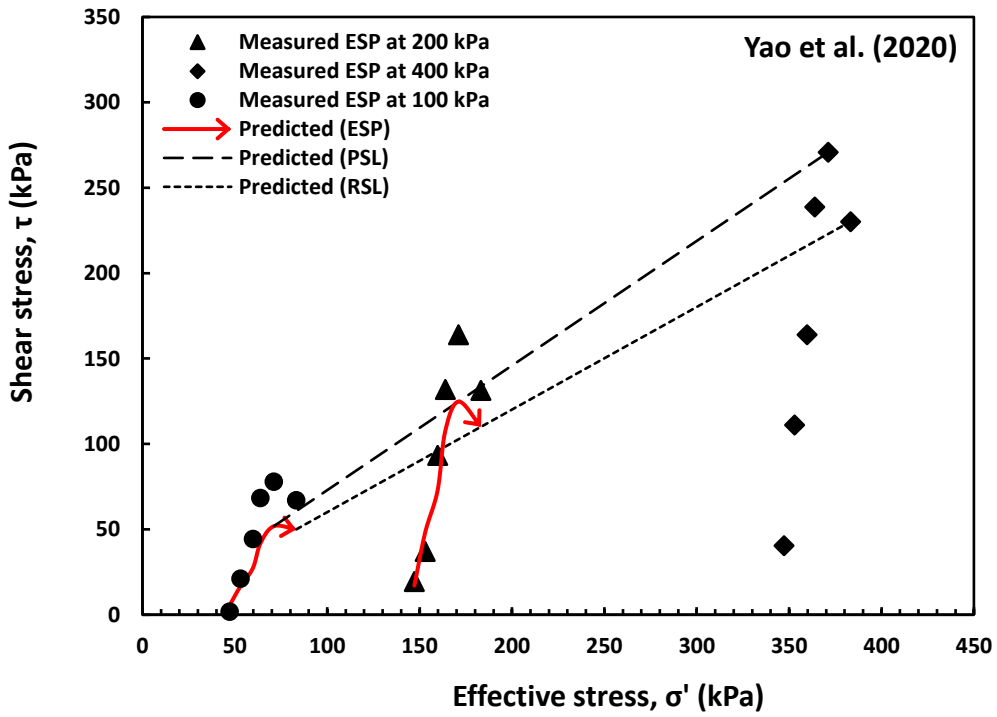

Fig. 6.29. Comparison of Predicted and measured effective stress paths at different consolidation pressure - pore fluid: distilled water (Yao et al. (2020).

shear at the pressure of 100 kPa and 200 kPa; therefore, predicted ESPs were shown in Fig. 6.29. The predicted ESPs well described the measured shear stress versus effective stress response. However, underprediction was observed near peak and residual data points.

The proposed framework demonstrated excellent performance in capturing the measured shear stress versus effective stress data for studied kaolin and kaolin soils from different literature. Moreover, the model was able to capture peak response in NC conditions, which was in agreement with the experimental data. However, underprediction near peak shear strength for the literature soils was possibly due to the scarcity of required data sets, such as FESEM images at different shearing stages for estimating distance (y), *CEC*, and *SSA*. It is to be noted that the unavailable data were assumed to be identical or close to the data of studied soil under given conditions.

Table 6.1. Physico-chemical properties of tested kaolin soil.

Mean particle size, a (μm)	Particle thickness, t (μm)	Specific surface area (BET), S_a (m^2/gm)	Surface charge density, ρ × 10^{-13} (C/μm^2)	Edge charge density, ρ_{edge} × 10^{-13} (C/μm^2)	Cation exchange capacity, CEC (meq/100 gm)	Isoelectric point, IEP_{edge}
0.01	0.001	17	1.7	0.17	3	3.9

Table 6.2. Parameters used for the estimation of net-electrostatic pressure in various pore fluid conditions.

Soil description and testing condition	Shearing stage under given normal stress	Particle orientation angle, α or β (degree)	Particle's separation, d (nm)	Net electrostatic pressure, A-R (kPa)	Estimated friction angle, ϕ' (degree)	Observed friction angle, ϕ' (degree)
Studied kaolin Inundation/consolidation* pressure (kPa): 200/450/700/950 Pore fluid: Distilled water (pH = 6; ε_r = 80) Hamaker's coefficient, A_H = 0.61 × 10^{-19} J	Initial (δ = 0.037 mm)	10	45	-120	2.51/2.19*	0.94/0.57*
	Intermediate (δ = 0.333 mm)	35	43.7	-105	8.75/13.8*	6.67/9.25*
	Intermediate (δ = 0.666 mm)	65	35.4	-80	13.93/19.64*	13.16/16.38*
	Peak	78	30/26*	-53.8/-70*	23/24.3*	21.55/24.13*
	Residual	0	95	-28	19.54/21.7*	20.4/22.73

Aqueous solution (ε_r = 80; pH = 2)	Initial (δ = 0.037 mm)	70	40.7	20	0.33	-
	Intermediate (δ = 0.666 mm)	60	32.73	44	11.31	-
	Peak	30	18.8	207	21.35	-
	Residual	0	0.867	297	17.53	-
Vinegar (pH = 2.5; ε_r = 24), Hamaker's coefficient, A_H = 0.77×10^{-19} J	Initial (δ = 0.037 mm)	75	30	90	0.93	-
	Intermediate (δ = 0.222 mm)	65	28	167.44	6.39	-
	Intermediate (δ = 0.666 mm)	55	26	260	9.87	-
	Peak	45	24	370.28	15.85	-
	Residual	0	1.275	458.93	7.35	-
Kerosene (ε_r = 1.8), Hamaker's coefficient, A_H = 1.6×10^{-19} J	Initial (δ = 0.037 mm)	60	30	2327	0.17	-
	Intermediate (δ = 0.222 mm)	55	29	2839	1.33	-
	Intermediate (δ = 0.666 mm)	50	28.5	3284	2.462	-
	Peak	45	28	3736	3.9	-
	Residual	0	1.05	4233	2.52	-
Kaolin from **Suzuki et al. (2017)**	Initial (δ = 0.43 mm)	65	34	-47	3.67	3.52
Pore fluid: Distilled water	Intermediate (δ = 0.87 mm)	70	33	-40.26	16.17	14.36
Normal stress (kPa): 98/196/392	Intermediate (δ = 2.19 mm)	75	32	-36.14	22	20.6
Surface charge density, $\rho \times 10^{-13}$ ($C/\mu m^2$) = 0.125	Peak	78	30	-28.92	26.93	25.64
	Residual	0	95	-16.78	12.73	12

Kaolin from **Yao et al. (2020)**	Initial (δ = 0.08 mm)	60	35	-52.83	6.61	5.5
Pore fluid: Distilled water	Intermediate (δ = 0.15 mm)	65	34	-47	17.43	14.36
Normal stress (kPa): 100/200/400	Intermediate (δ = 0.32 mm)	70	33	-40.26	24.46	22.88
Surface charge density, $\rho \times 10^{-13}$ ($C/\mu m^2$) = 0.125	Intermediate (δ = 0.94 mm)	75	32	-36.14	33.22	31.46
	Peak	78	30	-28.92	36	35.33
	Residual	0	95	-16.78	30.96	30.75

6.7 Discussion

The physico-chemical and micro-structural study of NC kaolin revealed that the strain softening response was related to particle re-orientation caused by the shearing. The experimental results have shown that the shearing converted the less flocculated fabric after inundation/consolidation to flocculated/edge-to-face structure at peak and produced face-to-face alignment at larger shear displacements. It is clear from the proposed eq. (6.9) and (6.10) that shear resistance not only depends on effective stress but also varies with friction angle. The proposed framework showed that the inter-particle effective stress continuously increased from the start of the shear to the residual condition. However, the observed friction angle, ϕ', first increases to a maximum value at a shear displacement corresponding to the peak. Further, shearing caused a reduction in friction, resulting in less ϕ' at the residual stage. This could be possible because the friction angle depends upon the arrangement of the particles during consolidation and shear (Mesri and Huvaj-Sarihan 2012). The coefficient of friction, $tan\phi'$, controls the slippage at the edge-to-face contact (Pedrotti and Tarantino 2018). These indicated that the particles configured in edge-to-face or flocculated association at peak provided maximum shear resistance because of the large number of particle contacts or maximum ϕ'. Further, the edge-to-face connections started to disappear in the direction of shearing due to the onset of sliding after the peak. Consequently, due to enormous sliding or less ϕ', the parallel or dispersed clay fabric at the residual state generated less shear resistance than the peak. However, the effective stress was higher at the residual stage than at the peak because re-orientation caused the reduction in the magnitude of net electrostatic pressure, A-R, when pH > IEP_{edge}, or increment in A-R when pH < IEP_{edge}. Thus, the inter-particle friction and electrostatic interactions governed the peak and residual shear resistance during shear.

The analysis of the ring shear test results demonstrates a considerable influence of pH and di-electric permittivity on the peak and residual shear strength of kaolin. The higher shear resistance under lower pH solutions at constant inundation pressure (Fig. 6.10) appears to be mainly associated with initial inter-particle effective stress at the start of shearing or after inundation. The initial inter-particle effective stress at pH = 2 estimated from the proposed framework was 470 kPa (Fig. 6.25), while at pH = 6, it was 330 kPa (Fig. 6.23). The attractive electrostatic forces at the particle level contributed to the higher initial effective stress under lower pH = 2 < IEP $_{edge}$, as *A-R* was estimated to be 20 kPa. In contrast, at pH = 6, inter-particle repulsive coulomb forces caused a reduction in net electrostatic pressure, *A-R*, which was -120 kPa. The kaolin samples inundated by different di-electric pore-fluids, i.e., kerosene (ε_r=1.8), vinegar (ε_r=24), and distilled water (ε_r=80), showed a decrease in shear resistance towards higher di-electric constants under constant inundation pressure (Fig. 6.12). The initial effective stress determined from the proposed model for kerosene under 450 kPa inundation pressure was 2777 kPa (Fig. 6.27), which was significantly higher than that for vinegar (σ' = 540 kPa) and distilled water (σ' = 330 kPa). In this case, di-electric permittivity played a significant role in controlling the initial inter-particle effective stress, as the di-electric permittivity of kerosene was 1.8, near to 1 as of air. Moreover, the experiments showed the marginal kerosene interaction with soil particles, indicating that the sample was almost dry. Thus, strong, attractive inter-particle electrostatic forces at the start of the shear contributed to higher shear resistance. The above discussion highlighted the potential of the novel conceptual framework to explain the experimental shear strength behaviour of kaolin under chemo-mechanical loading conditions.

6.8 Critical Remarks

1. The inundation and consolidation pressures affected both peak and residual shear strengths. The peak and residual shear strengths under different consolidation pressures

were greater than those of inundation pressures, and their difference was more pronounced at higher normal stresses.

2. The pH of the aqueous solutions significantly influenced the peak and residual shear strength, which were increased with a decrease in pH values. The effect of di-electric permittivity (distilled water, vinegar, kerosene) was significant on peak shear strength, whereas residual shear strength was less affected. Peak and residual shear strength were increased as the di-electric constant of the medium decreased.
3. The effective stress estimated using the proposed framework increased during shear under chemo-mechanical loading conditions. This was consistent with the effective stress principle, which states that effective stress increases when soil undergoes compression.
4. The proposed framework provided a satisfactory explanation for the anomalous peak response under NC conditions. The peak was due to the variation in inter-particle friction caused by the fabric change during shear. Moreover, the framework could also describe the experimental shear resistance under different pH and di-electric pore fluid conditions.
5. The proposed approach uses simple model parameters that can be easily determined using experimental data from a few ring shear tests, FESEM images at distinct shearing stages, and basic soil classification laboratory tests. The key benefit of the proposed model is that the shear strength characteristics at different pressures can be predicted, provided the shear stress versus shear deformation data at one pressure is known. The validation of the proposed model for shear strength characteristics of NC kaolin soils from the current work and literatures showed that the model adequately described the shear strength behaviour.

Chapter 7

Chemical Stabilization of Kaolin to Prevent Collapse

7.1 General

It was seen in chapters 4 and 6 that the unsaturated compacted kaolin, when subjected to wetting, undergoes significant collapse. The collapse volume change increased with an increase in applied inundation pressure. This collapse settlement in the soil mass is detrimental for the development of engineering infrastructure. Thus, minimizing such destructive collapse volume changes in the collapsible soils, such as kaolin clay deposits, in the practical field scenario is essential. This chapter presents an experimental investigation of the volume change behaviour of compacted kaolin clay (K1) treated with an alkali activator solution of sodium hydroxide (NaOH) and sodium silicate (Na_2SiO_3). One-dimensional compression and inundation tests were conducted to investigate the compressibility and collapse potential of the compacted kaolin samples with two different patterns of group of sand columns treated with different concentrations of alkali activators. The treated samples were cured for eight days before applying mechanical load. After completion of the curing period, the treated samples were compressed to different normal stresses and subsequently inundated. At the end of tests, X-ray diffraction (XRD) tests were also carried out on extruded samples to explore the formation of the mineral in samples prepared with different concentrations of solution. In the end, a field technique was demonstrated to minimize the collapse potential in underground kaolin deposits.

7.2 Results and Discussion

7.2.1 *Effect of Concentration of Alkali Activator and Inundation Pressure*

Fig. 7.1, 7.2, and 7.3 show the inundation test results under different mechanical loads for raw kaolin and kaolin samples *(pattern 'A')* treated with alkali activator solution of 4 M NaOH and 1 M Na_2SiO_3. The treated samples, after inundation, shows a final void ratio

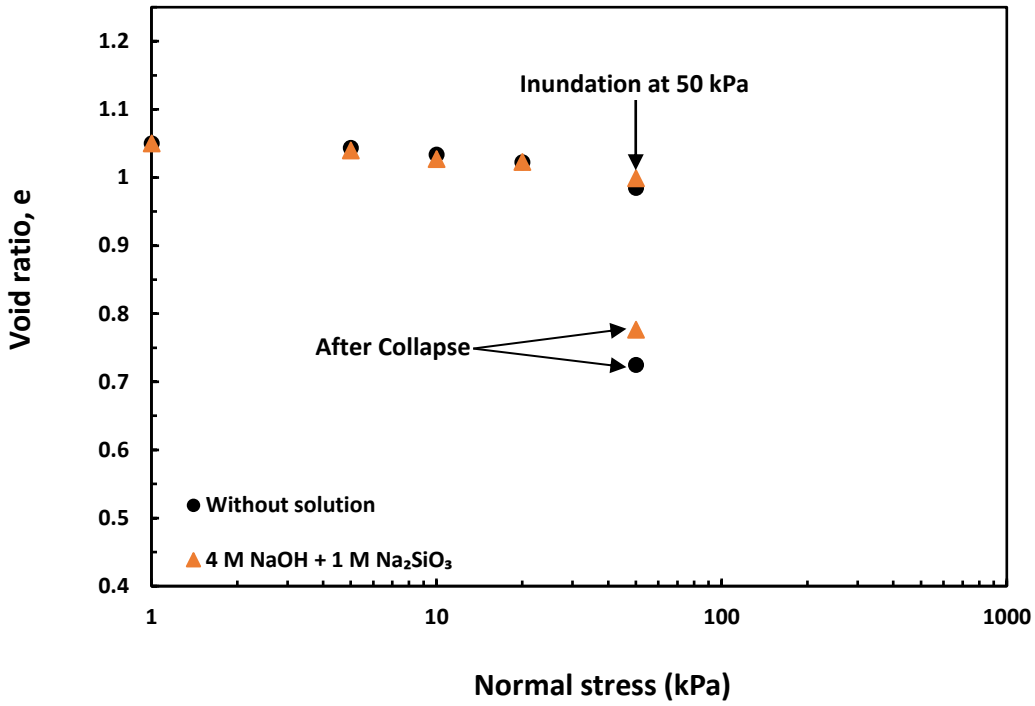

Fig. 7.1. Compression and collapse response at 50 kPa inundation pressure for raw kaolin and kaolin treated with 4 M NaOH and 1 M Na_2SiO_3 solution for pattern '*A*'.

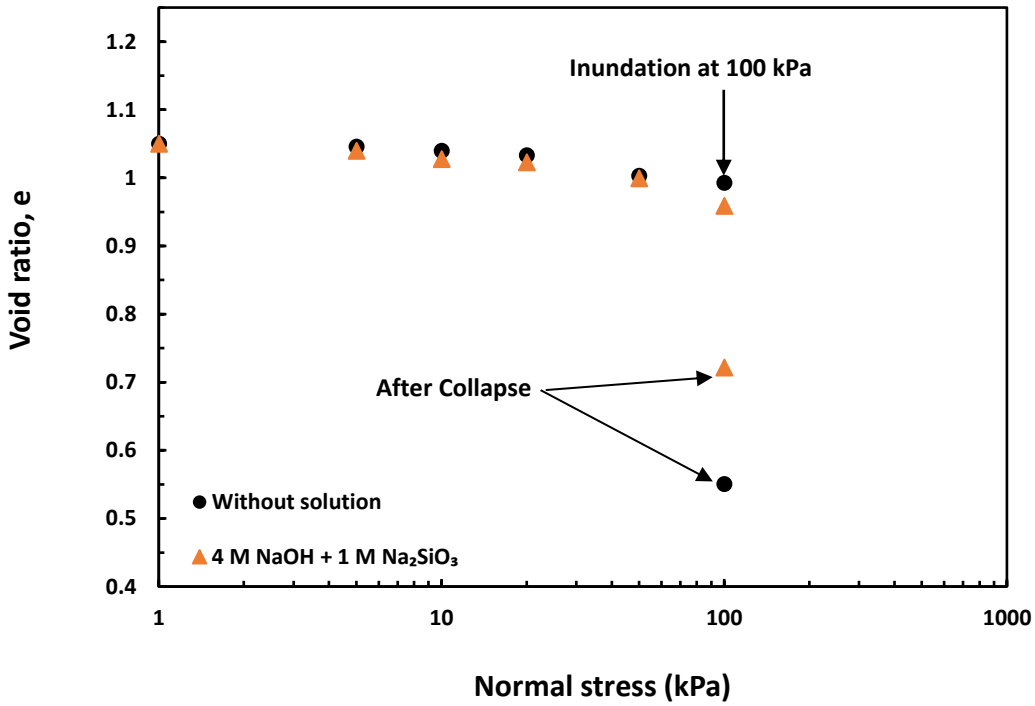

Fig. 7.2. Compression and collapse response at 100 kPa inundation pressure for raw kaolin and kaolin treated with 4 M NaOH and 1 M Na_2SiO_3 solution for pattern '*A*'.

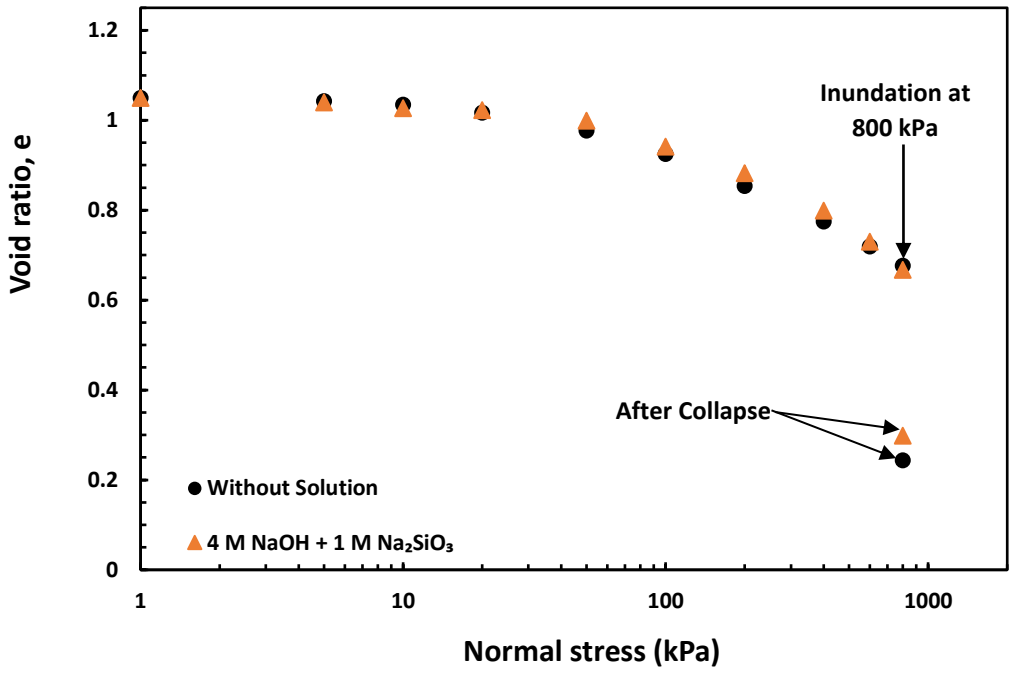

Fig. 7.3. Compression and collapse response at 800 kPa inundation pressure for raw kaolin and kaolin treated with 4 M NaOH and 1 M Na_2SiO_3 solution for pattern '*A*'.

slightly lesser than the raw kaolin for 50 and 800 kPa inundation pressures. In the case of 100 kPa inundation pressure, the void ratio was somewhat lower than other inundation pressures. These observations indicate that the geopolymerization was not effective at the studied lower alkali concentrations. Thus, the soil stiffness was not increased, and volume change due to collapse was also not reduced to an appreciable value. Duplicate experiments were performed on the samples treated with higher concentrations of alkali activator.

The compressibility and collapse response under different mechanical loads for untreated kaolin samples and kaolin samples treated with 10 M NaOH and 2.5 M Na_2SiO_3 solution were presented in Fig. 7.4, 7.5, and 7.6, respectively. The samples initially showed swelling from point *X* to *Y* after the treatment with an alkali solution. On loading, the treated samples show higher void ratios than those of raw kaolin samples with a slightly flatter profile than that of untreated kaolin. The collapse volume change due to saturation at all inundation

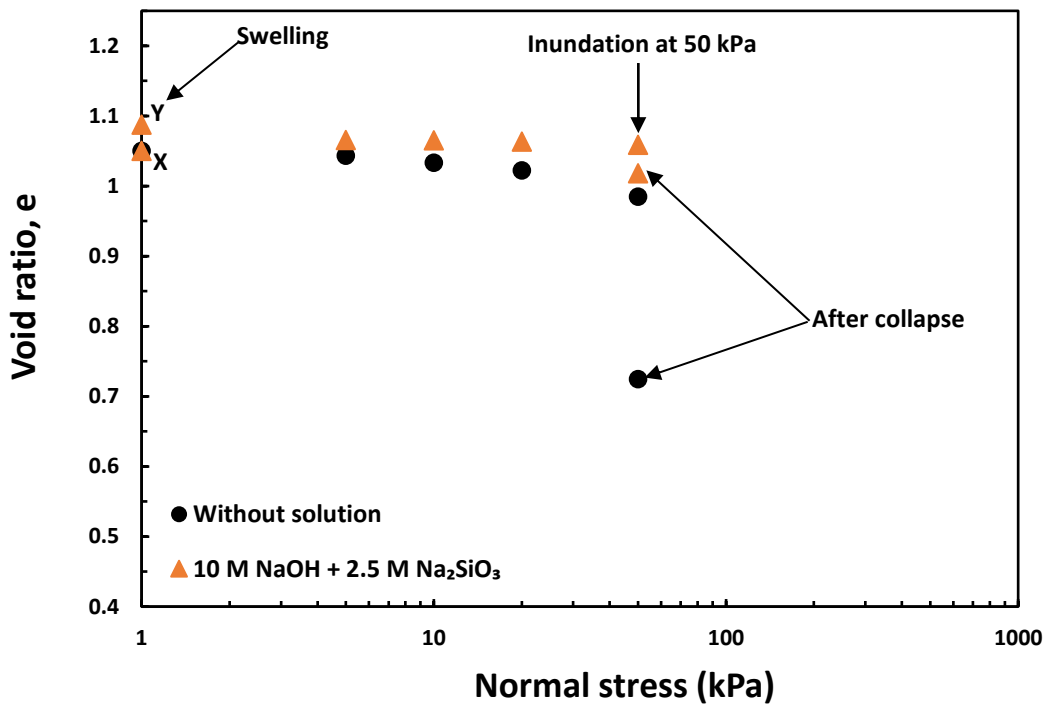

Fig. 7.4. Compression and collapse response at 50 kPa inundation pressure for raw kaolin and kaolin treated with 10 M NaOH and 2.5 M Na_2SiO_3 solution for pattern '*A*'.

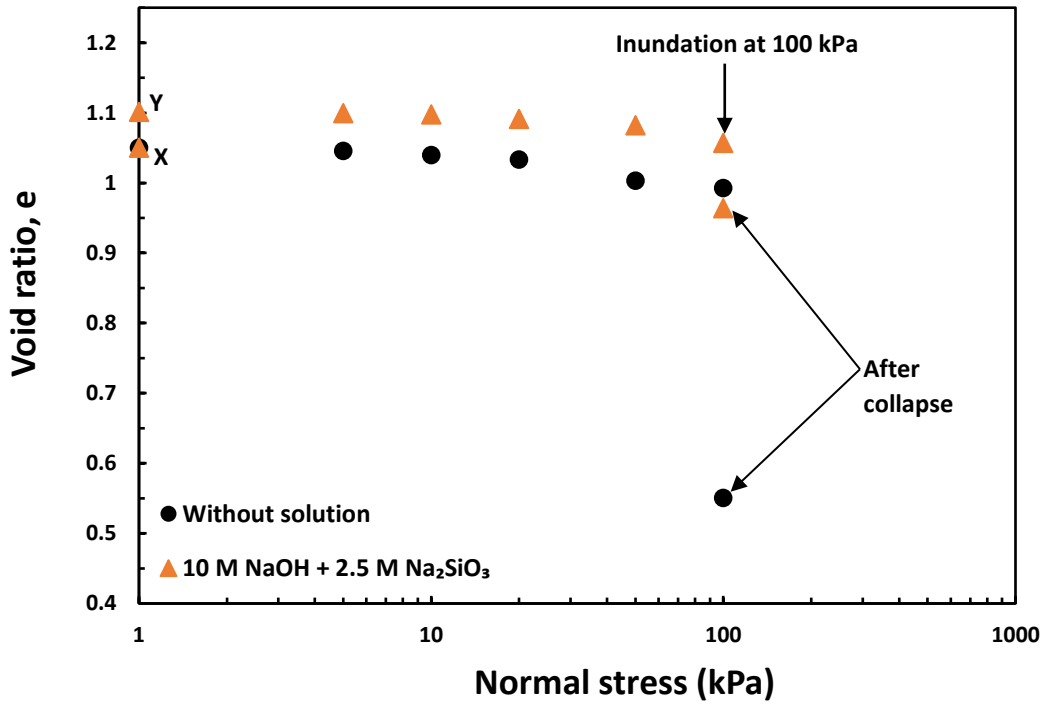

Fig. 7.5. Compression and collapse response at 100 kPa inundation pressure for raw kaolin and kaolin treated with 10 M NaOH and 2.5 M Na_2SiO_3 solution for pattern '*A*'.

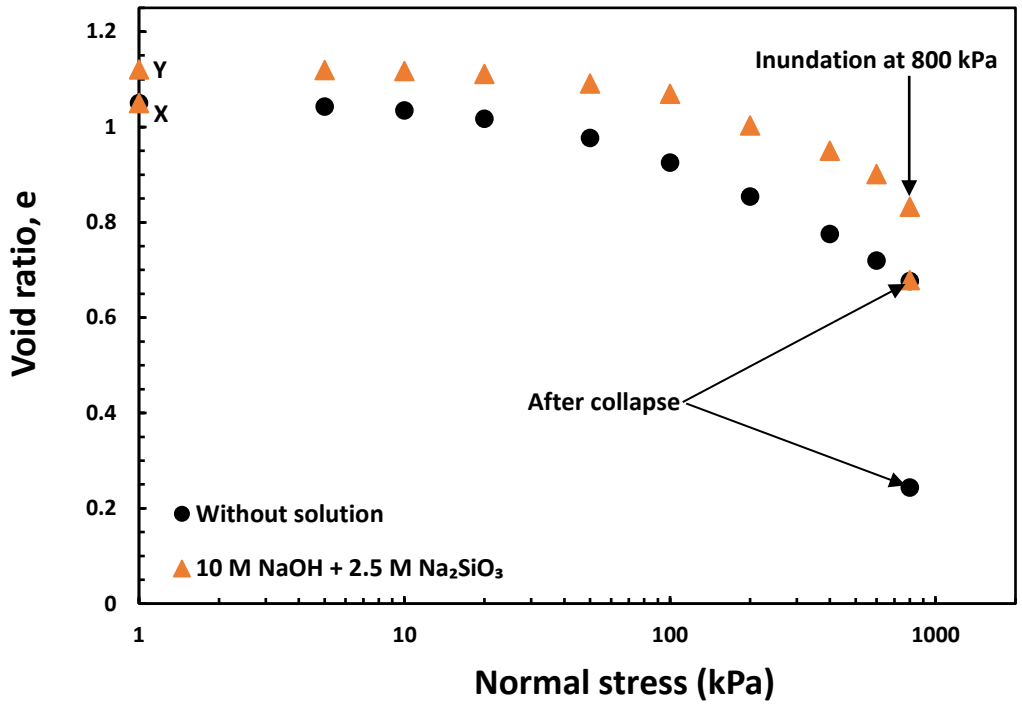

Fig. 7.6. Compression and collapse response at 800 kPa inundation pressure for raw kaolin and kaolin treated with 10 M NaOH and 2.5 M Na_2SiO_3 solution for pattern '*A*'.

pressures were reduced significantly and was smallest at the lowest inundation pressure of 50 kPa.

The compressibility and volume change response under different mechanical loads for untreated samples and samples treated with 12 M NaOH and 3 M Na_2SiO_3 solution were presented in Fig. 7.7, 7.8, and 7.9, respectively. The sample initially showed swelling from point A to B when treated with an alkali solution. On loading, the treated samples show higher void ratios than those of the raw kaolin sample with a slightly flatter profile than that of untreated kaolin. The collapse volume change due to saturation at all inundation pressures were reduced significantly and was smallest at the lowest inundation pressure of 50 kPa. The gain in stiffness and reduction in collapse potential might be related to the kaolin particle associations at the beginning of the test at point A and at the end of the seven days of curing at point B, as shown in Fig. 7.7. The clay particle's orientation at oven-dry state A was edge-to-face, as already seen in chapter 4. Coudert et al. (2022) found that geopolymer bonds exist between the aggregates with the edge-to-face arrangement in the treated kaolin samples at

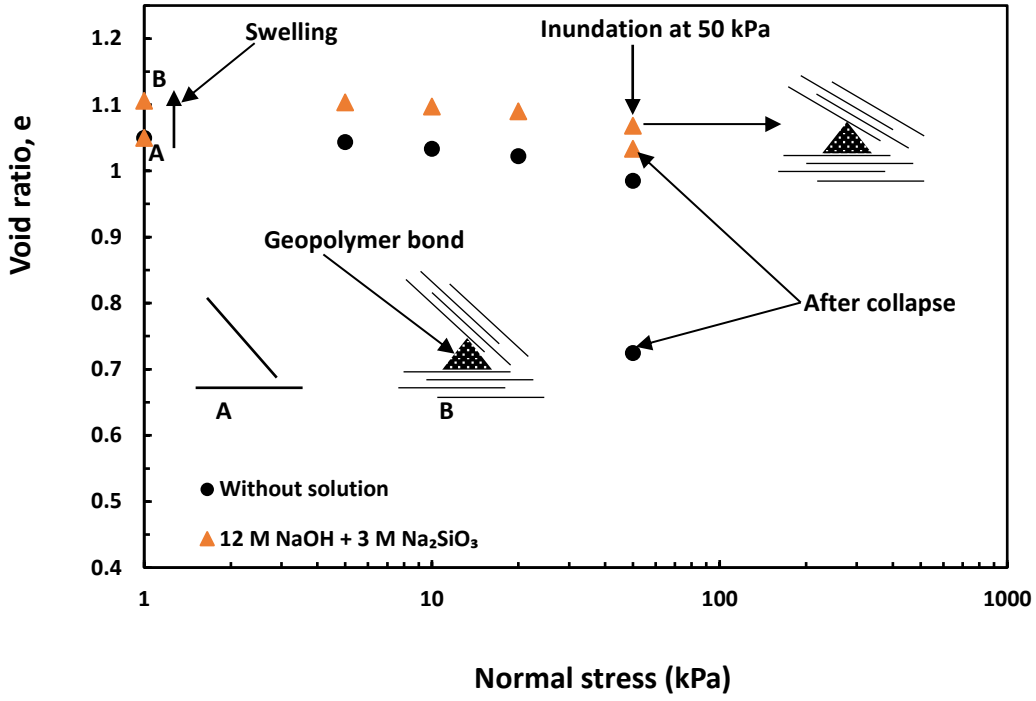

Fig. 7.7. Compression and collapse response at 50 kPa inundation pressure for raw kaolin and kaolin treated with 12 M NaOH and 3 M Na_2SiO_3 solution for pattern '*A*'.

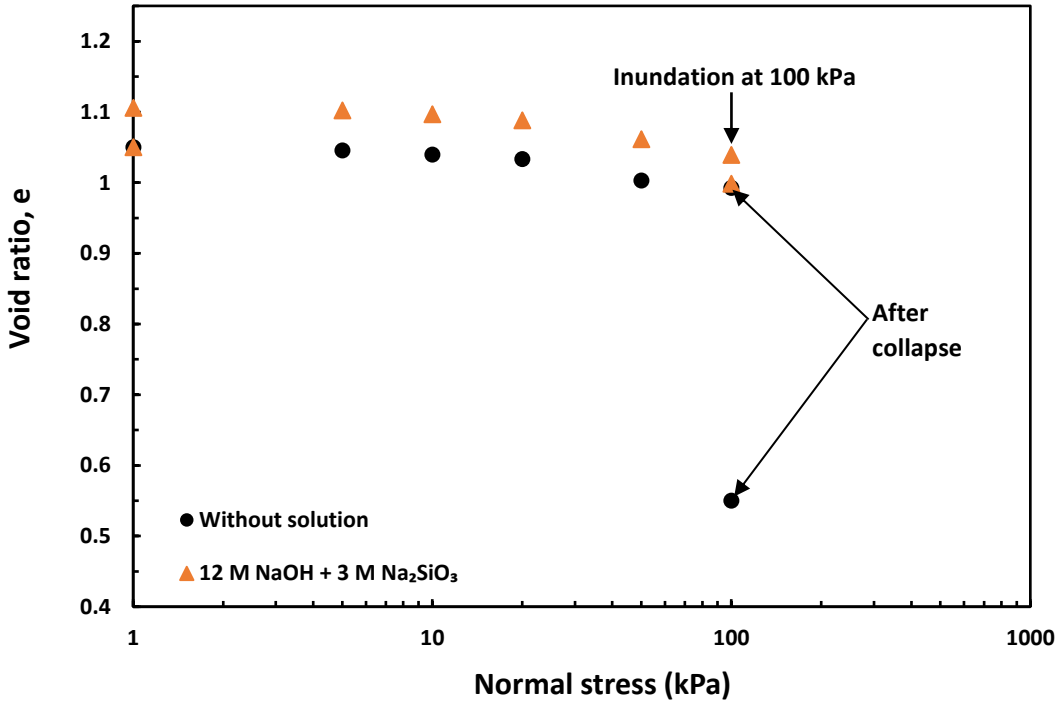

Fig. 7.8. Compression and collapse response at 100 kPa inundation pressure for raw kaolin and kaolin treated with 12 M NaOH and 3 M Na_2SiO_3 solution for pattern '*A*'.

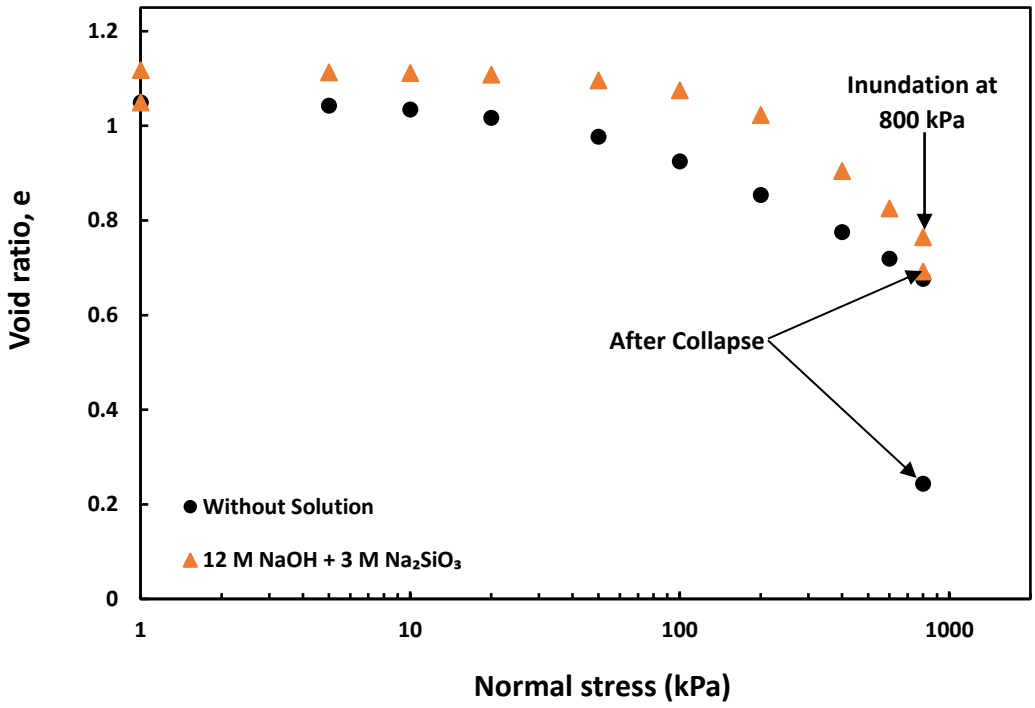

Fig. 7.9. Compression and collapse response at 800 kPa inundation pressure for raw kaolin and kaolin treated with 12 M NaOH and 3 M Na_2SiO_3 solution for pattern '*A*'.

state B, as shown in Fig. 7.7. Thus, existing geopolymer bonds imparted extra stiffness and strength to the sample against loading and saturation. Further, a higher concentration of alkali soultion of 14 M was chosen.

The Fig. 7.10, 7.11, and 7.12 show the compressibility and collapse response at different mechanical loads for kaolin samples treated with 14 M NaOH and 3.5 M Na_2SiO_3 solution and untreated kaolin samples. Initially, slight swelling was observed after the treatment of kaolin samples. Upon loading, the void ratios of treated samples were similar to those of raw samples until 100 kPa pressure. After 100 kPa, void ratios were higher until 800 kPa pressure. The volume changes due to collapse were reduced significantly because of geopolymerization. The reduction was highest at the lowest inundation pressure of 50 kPa and reduced with further pressure. The wetting-induced collapse at different inundation pressures was smaller than the samples treated with lower concentration solutions (i.e., 4M NaOH and 1 M Na_2SiO_3 and 10 M NaOH and 2.5 M Na_2SiO_3). However, the collapse

deformations were higher than those of samples treated with 12 M NaOH and 3 M Na_2SiO_3 solution.

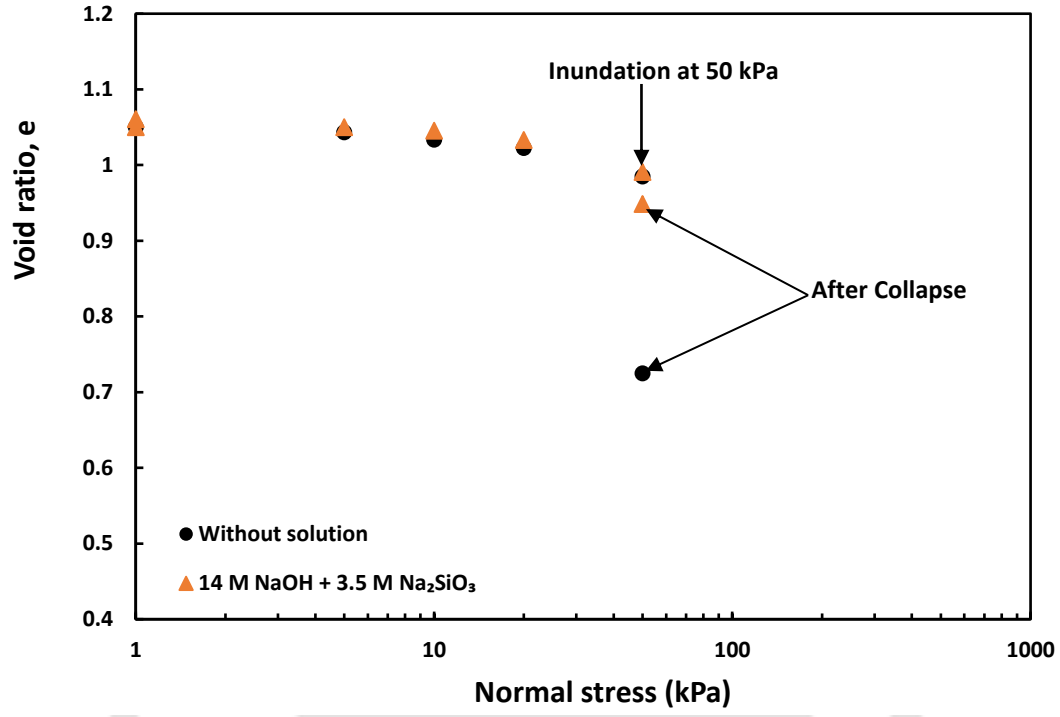

Fig. 7.10. Compression and collapse response at 50 kPa inundation pressure for raw kaolin and kaolin treated with 14 M NaOH and 3.5 M Na_2SiO_3 solution for pattern '*A*'.

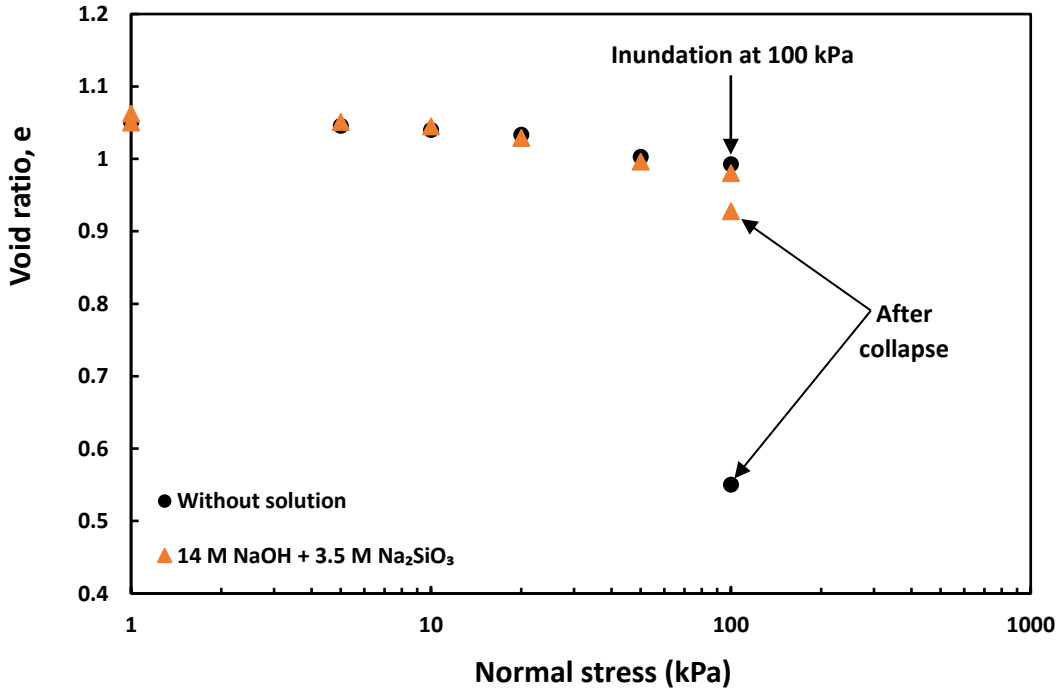

Fig. 7.11. Compression and collapse response at 100 kPa inundation pressure for raw kaolin and kaolin treated with 14 M NaOH and 3.5 M Na_2SiO_3 solution for pattern '*A*'.

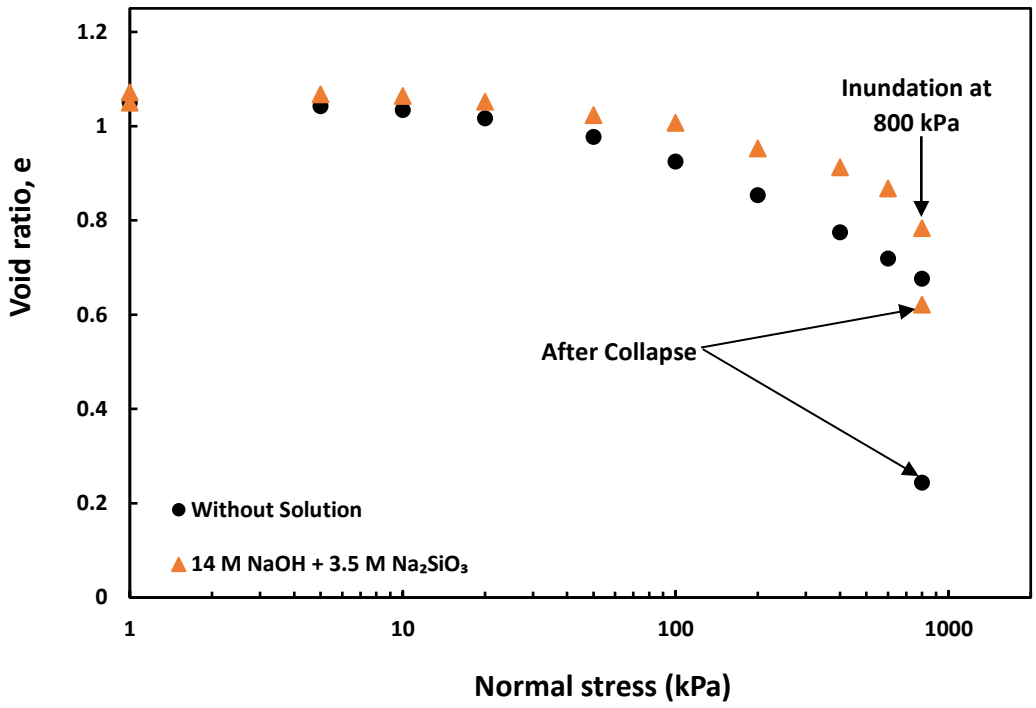

Fig. 7.12. Compression and collapse response at 800 kPa inundation pressure for raw kaolin and kaolin treated with 14 M NaOH and 3.5 M Na_2SiO_3 solution for pattern '*A*'.

The compressibility and collapse response under different mechanical loads for untreated kaolin samples and kaolin samples (pattern '*B*') treated with 10 M NaOH and 2.5 M Na_2SiO_3 solution were presented in Fig. 7.13, 7.14, and 7.15, respectively. The samples initially

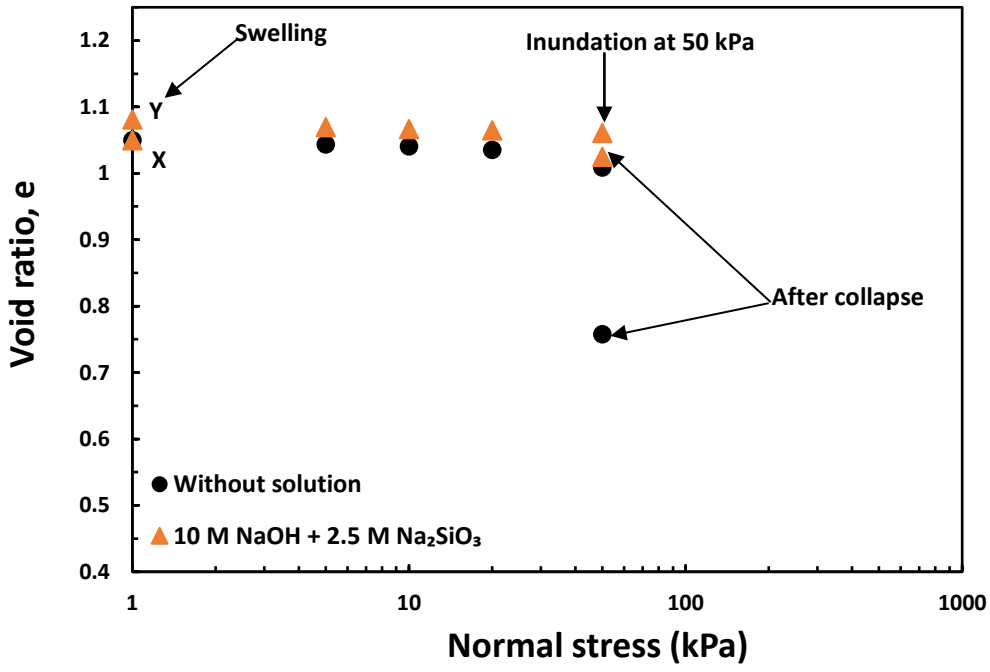

Fig. 7.13. Compression and collapse response at 50 kPa inundation pressure for raw kaolin and kaolin treated with 10 M NaOH and 2.5 M Na_2SiO_3 solution for pattern 'B'.

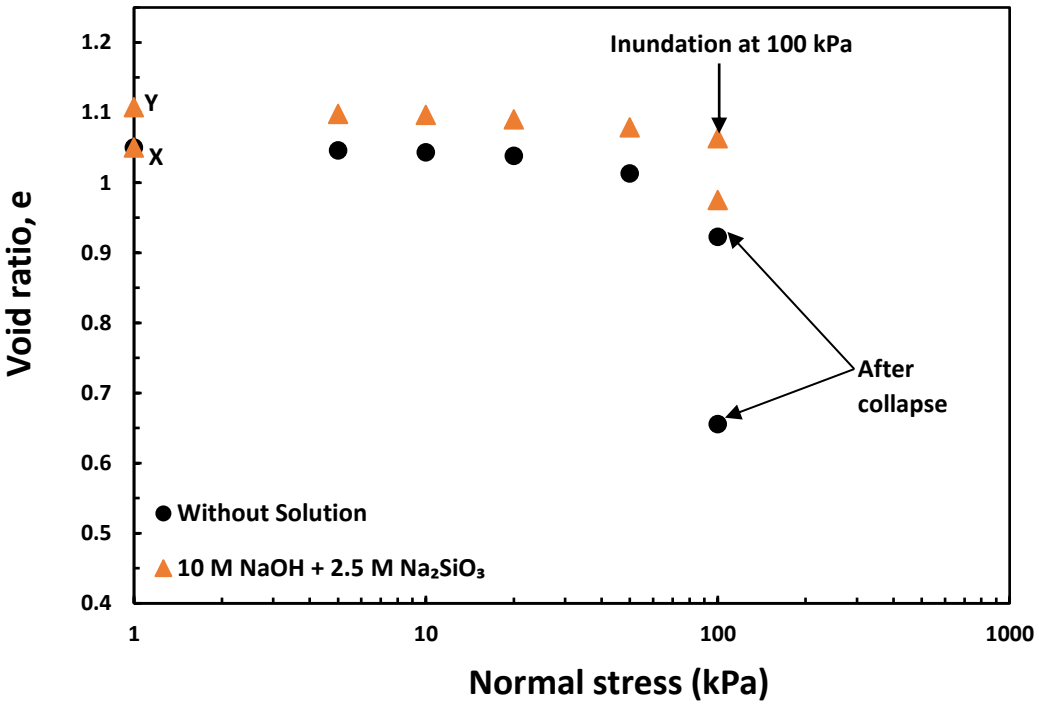

Fig. 7.14. Compression and collapse response at 100 kPa inundation pressure for raw kaolin and kaolin treated with 10 M NaOH and 2.5 M Na_2SiO_3 solution for pattern 'B'.

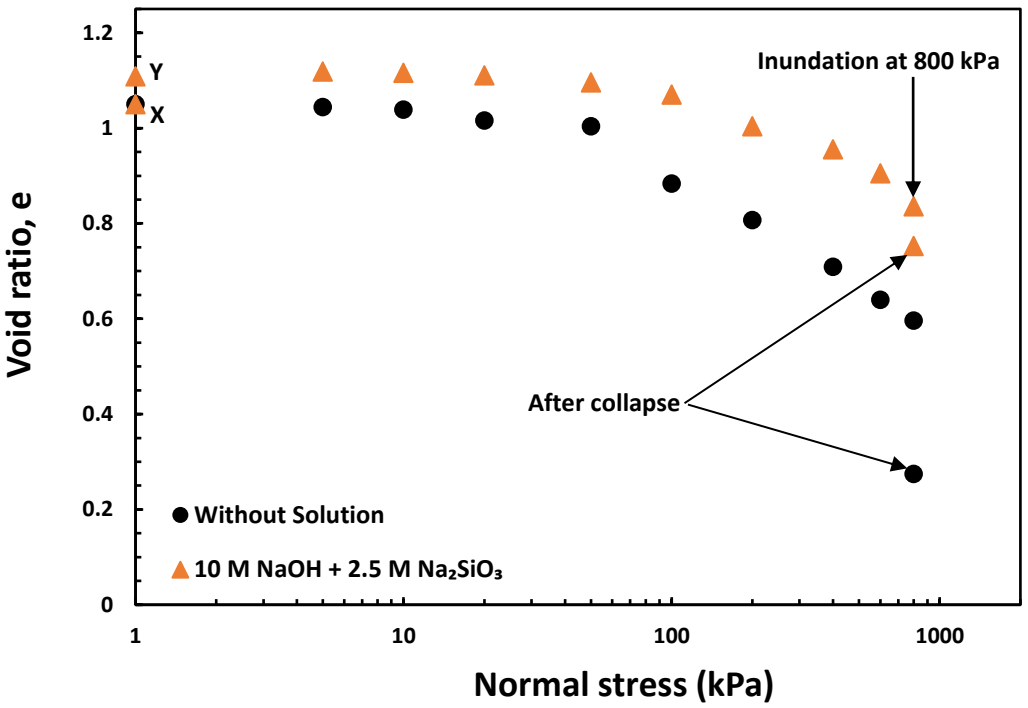

Fig. 7.15. Compression and collapse response at 800 kPa inundation pressure for raw kaolin and kaolin treated with 10 M NaOH and 2.5 M Na_2SiO_3 solution for pattern 'B'.

showed swelling from point *X* to *Y* after the treatment with an alkali solution. On loading, the treated samples show higher void ratios than those of raw kaolin samples than that of untreated kaolin. The collapse volume change due to saturation at all inundation pressures was reduced significantly and was smallest at the lowest inundation pressure of 50 kPa.

The compressibility and volume change response under different mechanical loads for untreated samples and samples treated with 12 M NaOH and 3 M Na_2SiO_3 solution were presented in Fig. 7.16, 7.17, and 7.18, respectively. The sample initially showed swelling when treated with an alkali solution. On loading, the treated samples show higher void ratios than those of the raw kaolin sample, with a slightly flatter profile than that of untreated kaolin. The collapse volume change due to saturation at all inundation pressures was reduced significantly and was smallest at the lowest inundation pressure of 50 kPa. Further, a higher concentration of alkali solution of 14 M was selected.

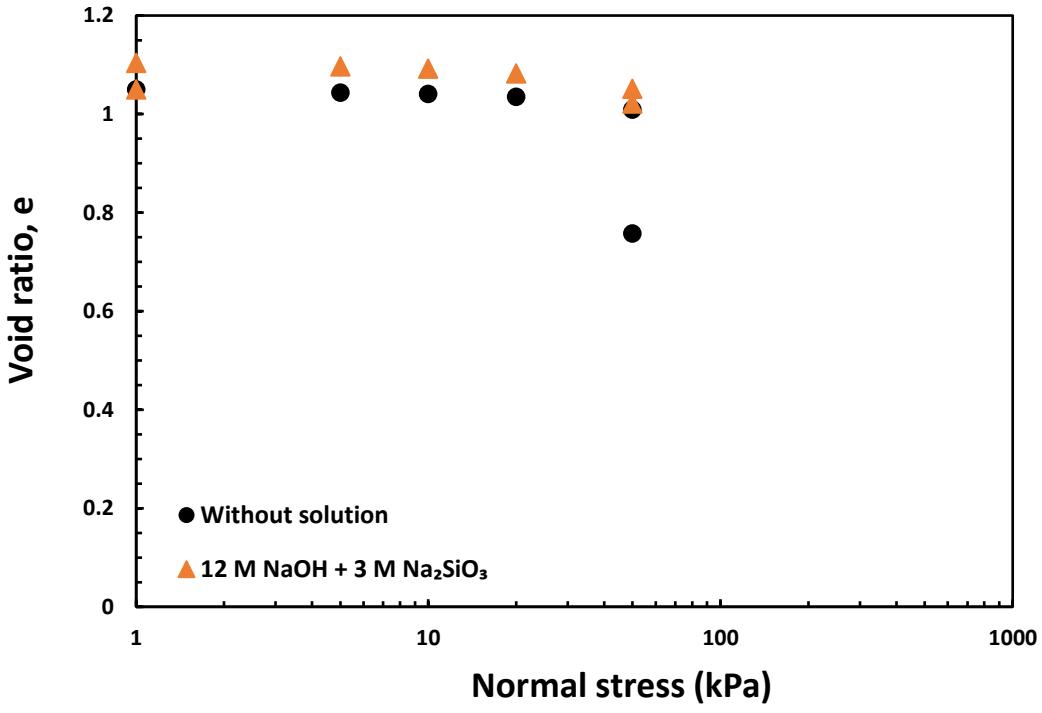

Fig. 7.16. Compression and collapse response at 50 kPa inundation pressure for raw kaolin and kaolin treated with 12 M NaOH and 3 M Na_2SiO_3 solution for pattern 'B'.

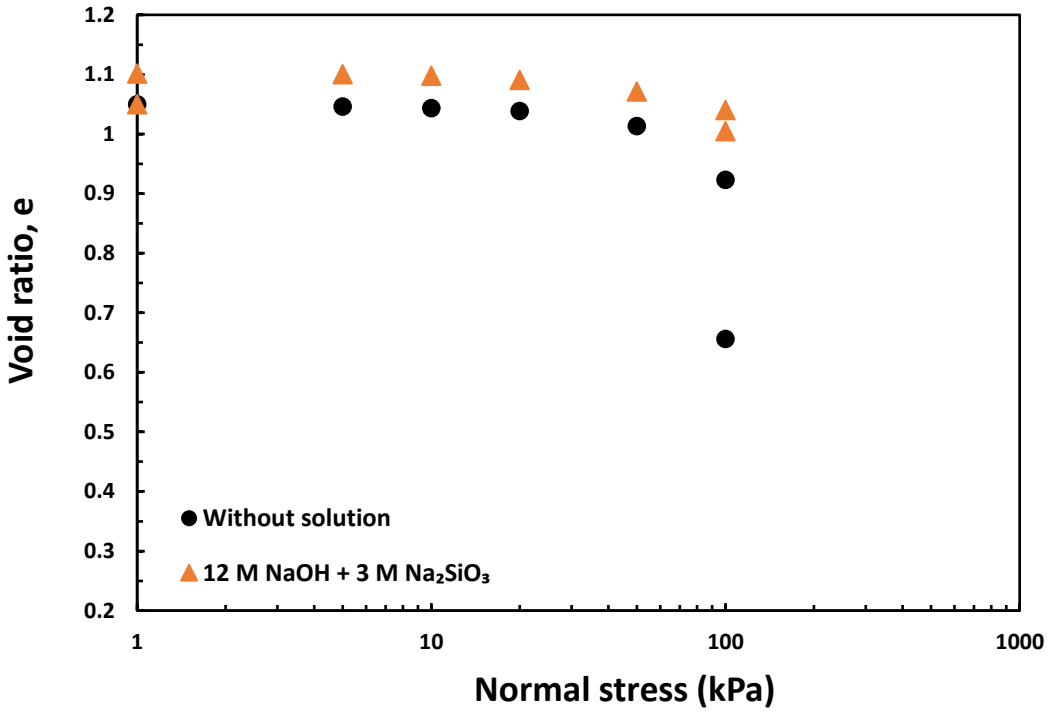

Fig. 7.17. Compression and collapse response at 100 kPa inundation pressure for raw kaolin and kaolin treated with 12 M NaOH and 3 M Na_2SiO_3 solution for pattern 'B'.

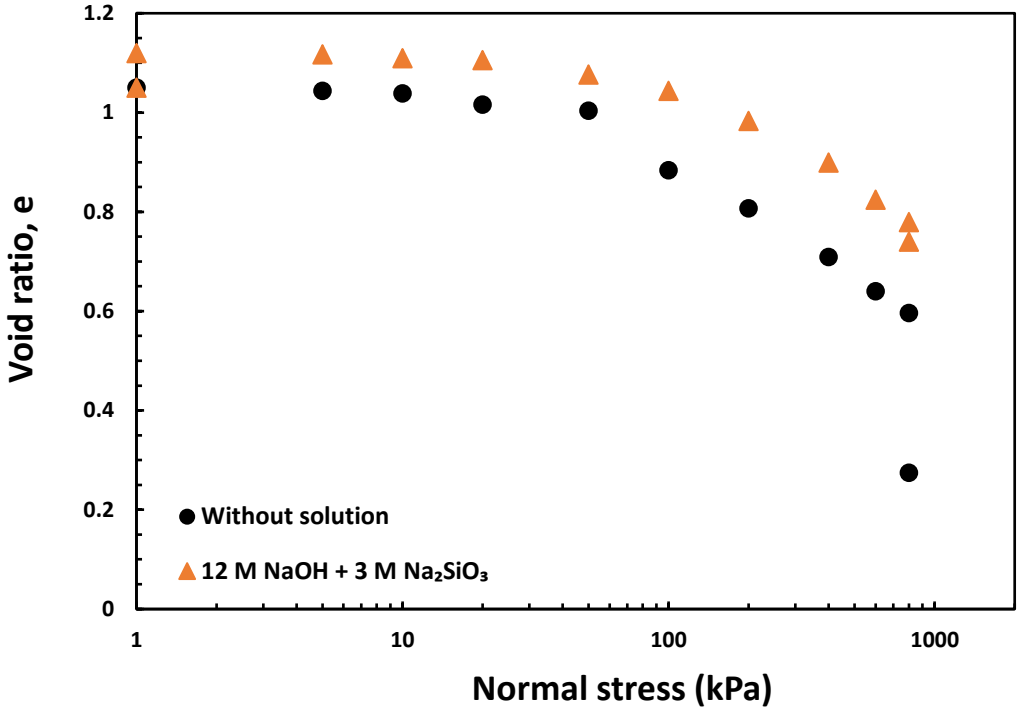

Fig. 7.18. Compression and collapse response at 800 kPa inundation pressure for raw kaolin and kaolin treated with 12 M NaOH and 3 M Na_2SiO_3 solution for pattern 'B'.

The Fig. 7.19, 7.20, and 7.21 show the compressibility and collapse response at different mechanical loads for kaolin samples treated with 14 M NaOH and 3.5 M Na_2SiO_3 solution and untreated kaolin samples. Initially, slight swelling was observed after the treatment of kaolin samples. Upon loading, the void ratios of treated samples were similar to those of raw samples until 50 kPa pressure. The void ratios after 50 kPa, were higher till the end of loading. The volume changes due to collapse were reduced significantly because of geopolymerization. The reduction was highest at the lowest inundation pressure of 50 kPa and reduced with further pressure.

Interestingly, a significant drop in wetting-induced deformation was observed at 800 kPa for pattern 'B' samples at all concentrations of alkali activator solutions. Moreover, the volume changes due to collapse deceased at all inundation pressures for pattern '*B*' samples compared to that of pattern '*A*' samples.

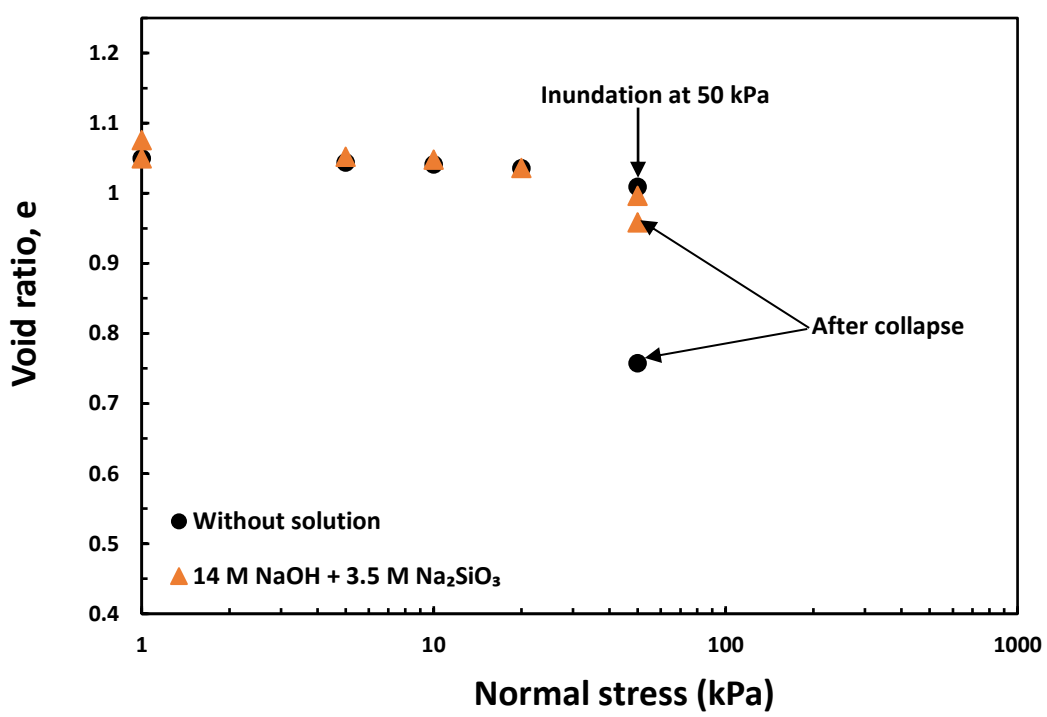

Fig. 7.19. Compression and collapse response at 50 kPa inundation pressure for raw kaolin and kaolin treated with 14 M NaOH and 3.5 M Na_2SiO_3 solution for pattern 'B'.

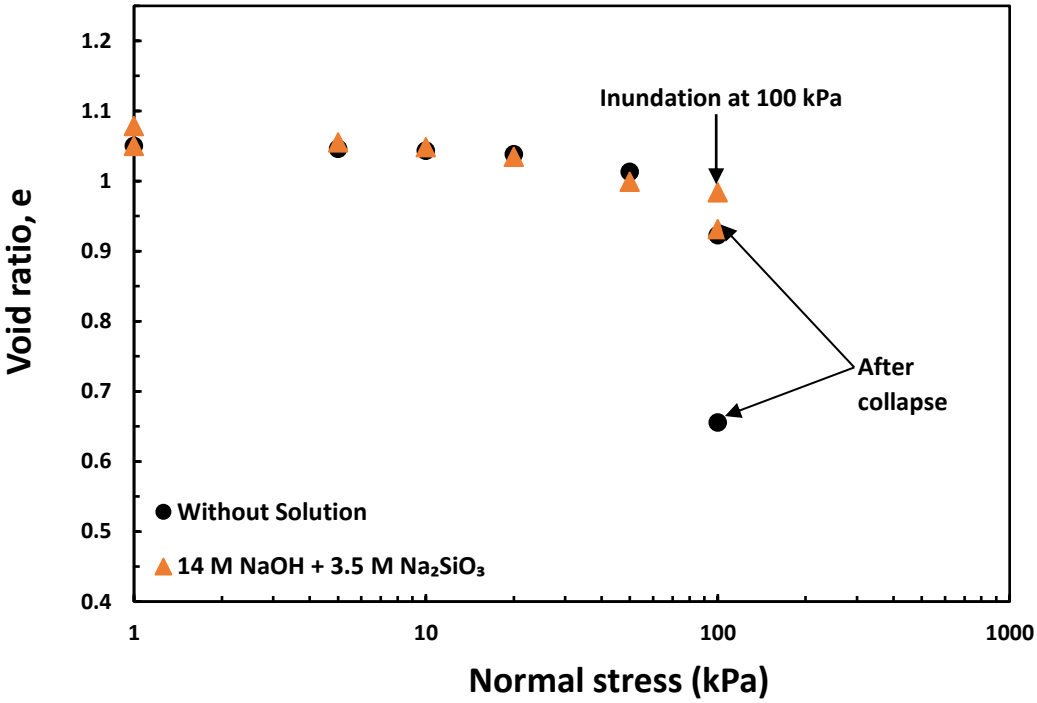

Fig. 7.20. Compression and collapse response at 100 kPa inundation pressure for raw kaolin and kaolin treated with 14 M NaOH and 3.5 M Na_2SiO_3 solution for pattern 'B'.

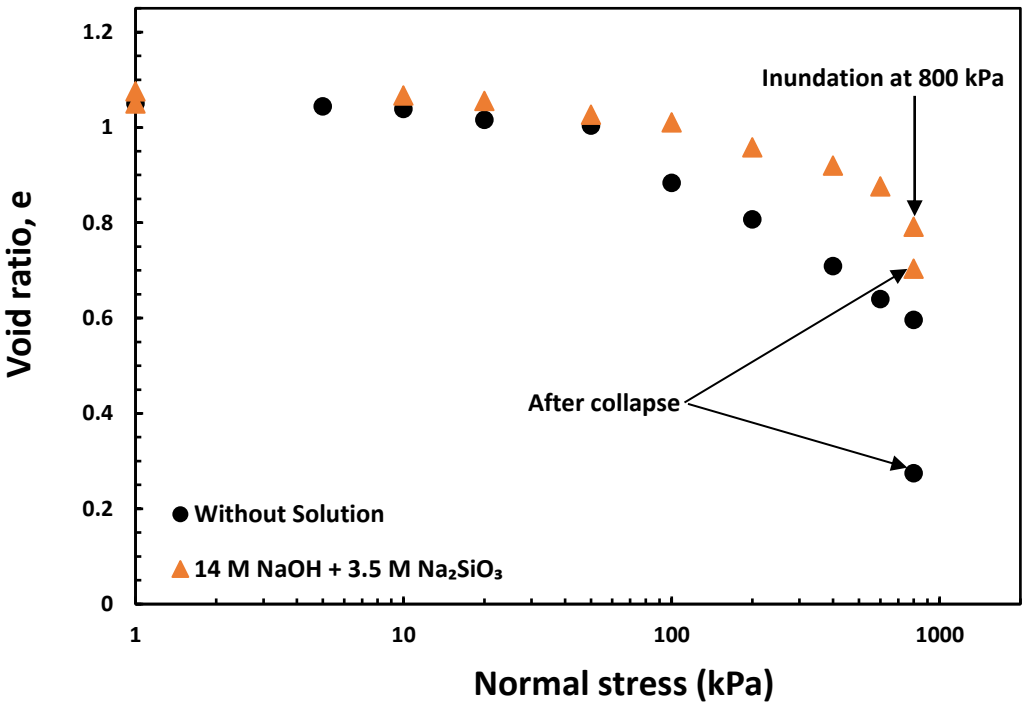

Fig. 7.21. Compression and collapse response at 800 kPa inundation pressure for raw kaolin and kaolin treated with 14 M NaOH and 3.5 M Na_2SiO_3 solution for pattern 'B'.

7.2.3 *Collapse Potential Severity*

The laboratory test procedure described in (ASTM. 2021. D4546-21) was used to estimate the collapse potential of soil. The wetting-induced collapse in dry collapsible soils is defined as the reduction in the soil volume or densification caused by the addition of water at constant vertical normal stress, σ (Lawton et al., 1992), as shown in Fig. 7.22. Mathematically, the collapse was defined by Jennings & Burland (1962) in terms of collapse potential, *CP* in % under a given inundation pressure, σ as

$$CP = \frac{\Delta e}{(1+e_o)} \times 100 \qquad [7.1]$$

where e_o is the initial void ratio before inundation; Δe is a change in void ratio caused by the wetting at constant inundation pressure, σ. The collapsible soils can impose damage to the engineering structure due to settlement issues caused by the wetting of underlying soil mass. The degree of damage can be qualitatively understood from the range of collapse potential suggested by Jennings & Burland (1962) and given in Table 7.1.

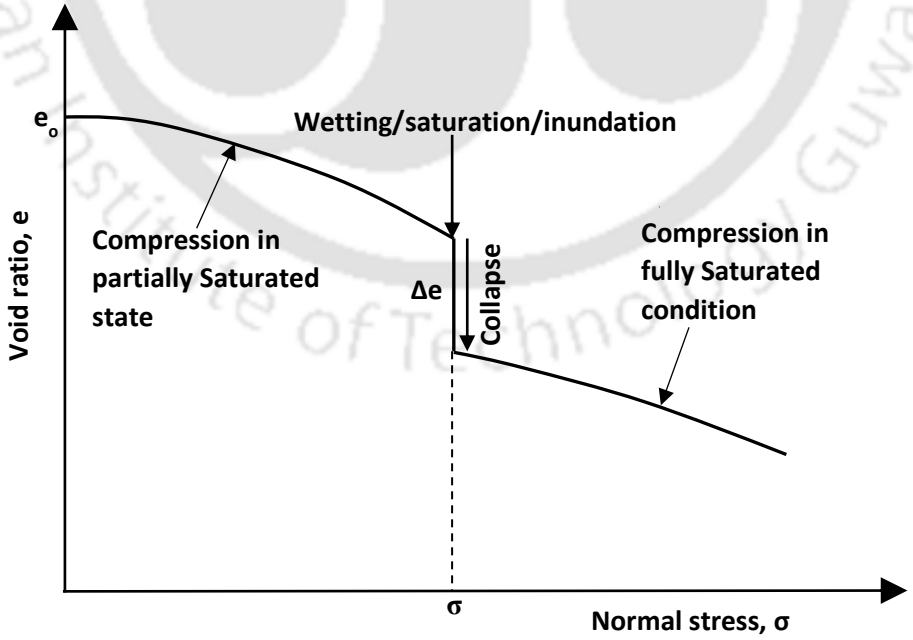

Fig. 7.22. Schematic diagram of volume change response of compacted collapsible soil produced from laboratory experiment.

Table 7.1. Potential severity of collapse (Jennings & Burland, 1962).

Collapse potential, %	Severity of Problem
0-1	No Problem
1-5	Moderate Trouble
5-10	Trouble
10-20	Severe Trouble
> 20	Very Severe Trouble

The Fig. 7.23 shows the variation of estimated collapse potential (eq. 7.1) with inundation pressures as a function of the concentration of the alkali activator solution pattern '*A*'. It can be seen that the collapse potential was increasing with inundation pressure for all the concentrations. The collapse potential was lowest under all different inundation pressures for the kaolin sample treated with 12 M NaOH and 3 M Na_2SiO_3 solution. The column chart diagram, as shown in Fig. 7.24, indicates the untreated and treated samples (4 M NaOH and 1 M Na_2SiO_3) have collapse potential in the range of 10-30 % and can cause very severe

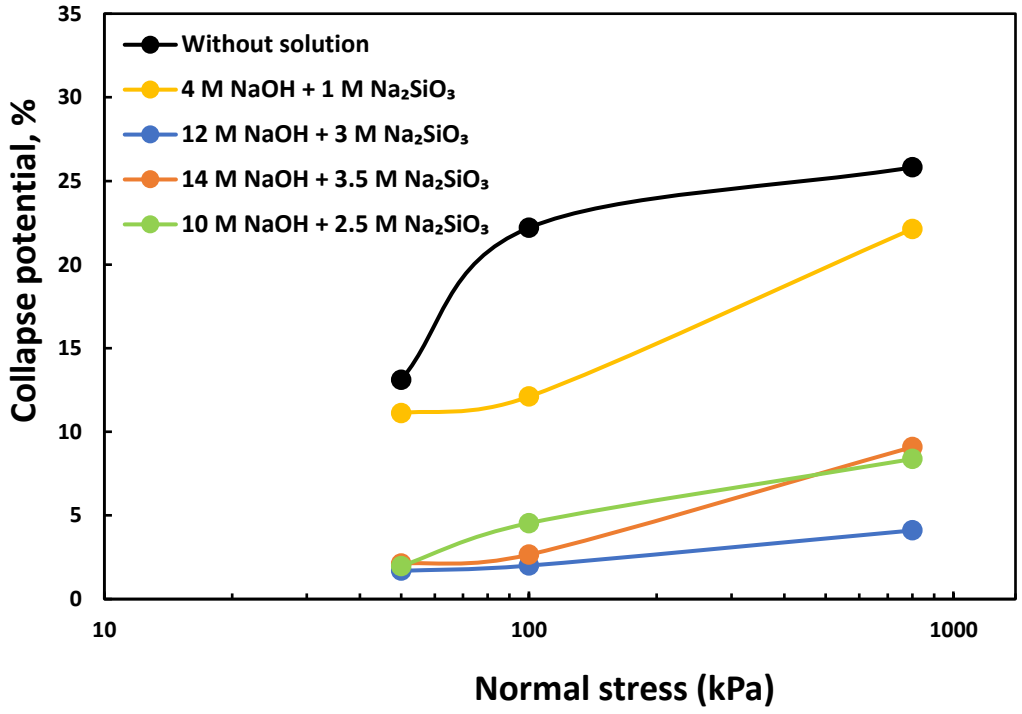

Fig. 7.23. Variation of collapse potential with inundation pressure at different solution concentrations for pattern 'A' samples.

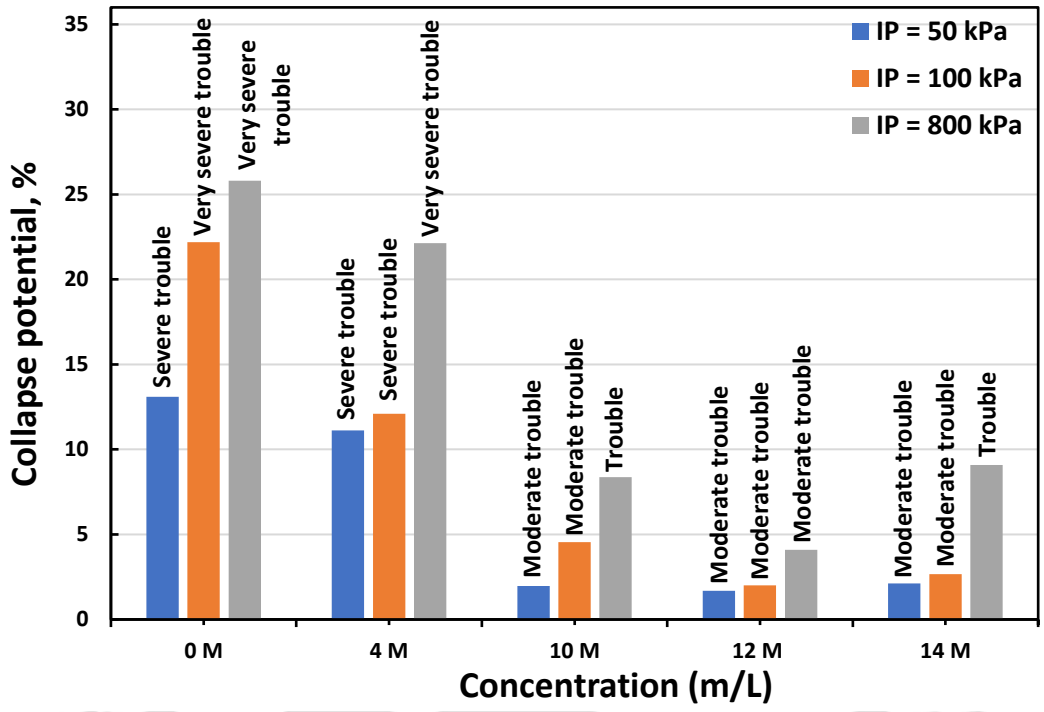

Fig. 7.24. Variation of collapse potential with alkali activator solution concentration under different inundation pressures for pattern 'A' samples.

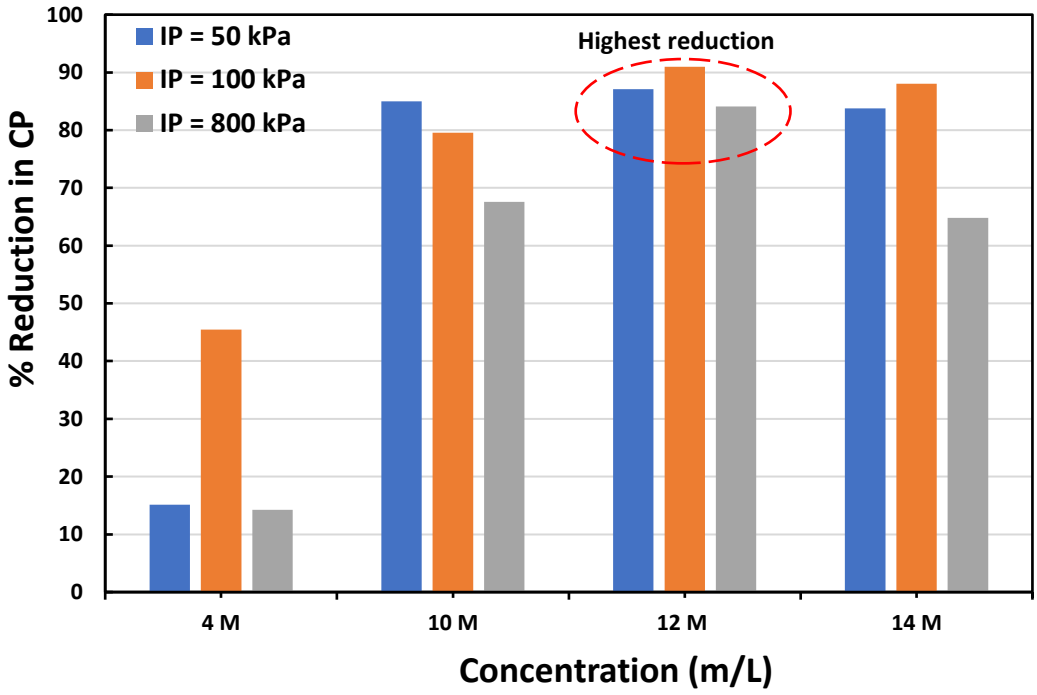

Fig. 7.25. Variation of reduction in collapse potential with alkali activator solution concentration under different inundation pressures for pattern 'A' samples.

trouble to the engineering structure. However, the samples treated with 12 M NaOH and 3 M Na_2SiO_3 solution can result in moderate or minor trouble among all the cases, as the collapse potential was 1-5 %. The highest reduction in collapse potential was found to be approximately 91 % for the samples treated with 12 M NaOH and 3 M Na_2SiO_3 solution, as shown in Fig. 7.25 (column charts). Thus, 12 M NaOH and 3 M Na_2SiO_3 solution act as an optimum concentration at which maximum reduction in collapse potential was achieved.

The Fig. 7.26 shows the variation of estimated collapse potential (eq. 7.1) with inundation pressures as a function of the concentration of the alkali activator solution for pattern '*B*' samples. It was observed that the collapse potential increased with inundation pressure for all the concentrations. The collapse potential was lowest under all different inundation pressures for the kaolin sample treated with 12 M NaOH and 3 M Na_2SiO_3 solution. The column chart diagram, as shown in Fig. 7.27, indicated the untreated samples have collapse potential in the range of 10-30 % and can cause severe to very severe trouble to the engineering structure. However, the samples treated with other concentrations solution can result in moderate or minor trouble among all the cases, as the collapse potential was 1-5 %. The highest reduction in collapse potential was found to be approximately 92 % for the samples treated with 12 M NaOH and 3 M Na_2SiO_3 solution, as shown in Fig. 7.28 (column charts). Thus, 12 M NaOH and 3 M Na_2SiO_3 solution act as an optimum concentration at which maximum reduction in collapse potential was achieved for pattern '*B*' samples similar to pattern '*A*' samples. However, the decrease in Collapse potential at all concentrations was more significant for pattern '*B*' samples compared to pattern '*A*' samples. These might be related to the number of sand columns in a group, as only three sand columns were used in pattern' B' samples. Thus, during saturation, the sand might collapse, resulting in less collapse.

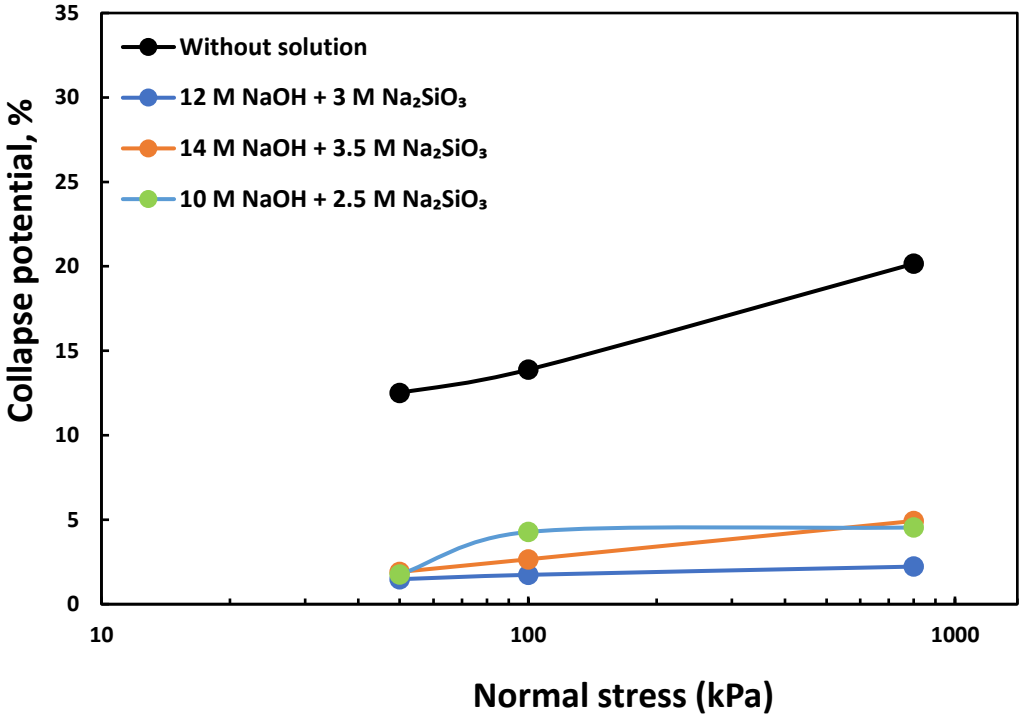

Fig. 7.26. Variation of collapse potential with inundation pressure at different solution concentrations for pattern 'B' samples.

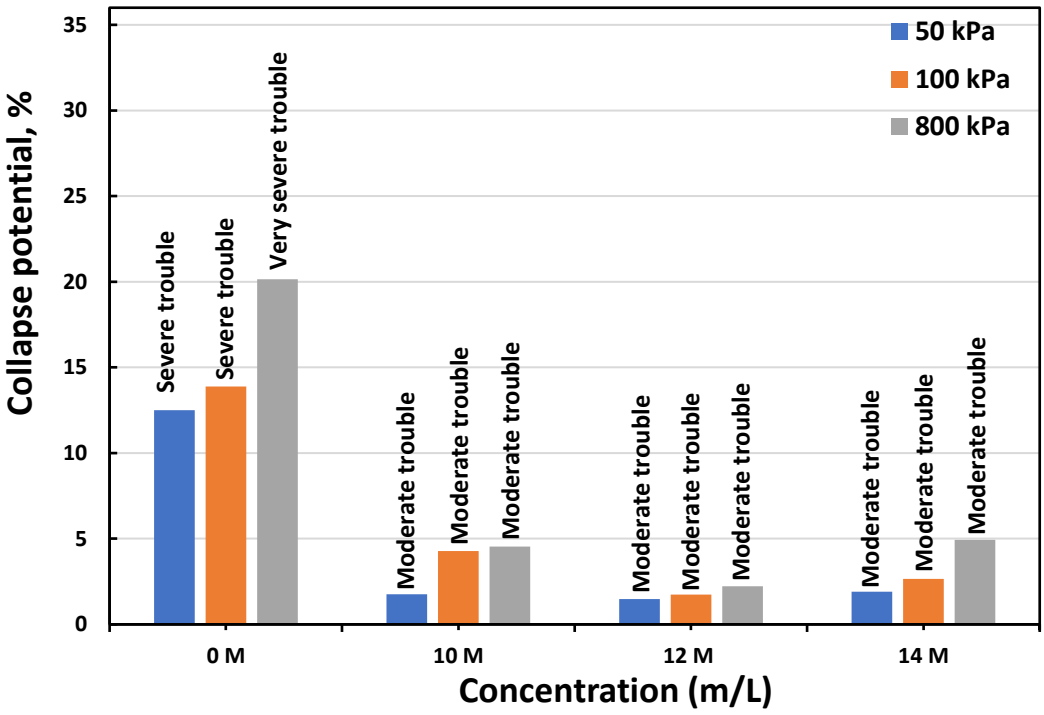

Fig. 7.27. Variation of collapse potential with alkali activator solution concentration under different inundation pressures for pattern 'B' samples.

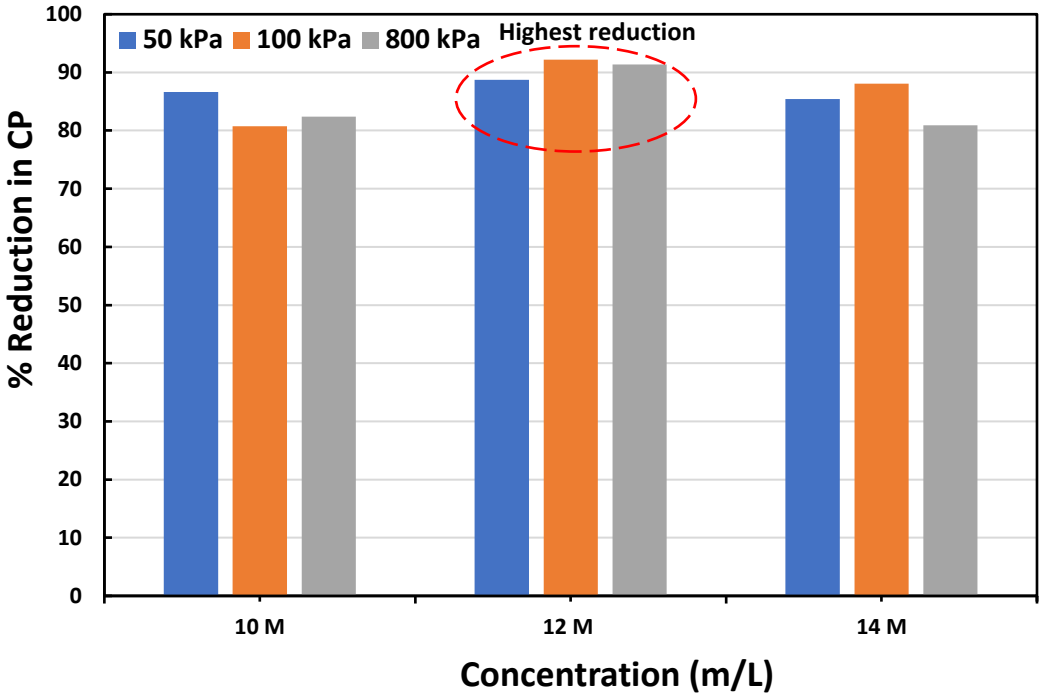

Fig. 7.28. Variation of reduction in collapse potential with alkali activator solution concentration under different inundation pressures for pattern 'B' samples.

7.2.2 *XRD Spectra Analysis*

Fig. 7.29 shows the XRD results for untreated kaolin and treated kaolin for pattern '*A*' samples at different concentrations of alkali activator solution at eight days of curing. XRD pattern of untreated kaolin indicated the presence of kaolinite (K) as a major mineral and also contained siliceous mineral quartz (Q); however, illite (I) was found in trace amounts. The XRD results of treated samples showed that some parts of unreacted minerals, such as kaolinite and quartz, remained with reduced intensities. Small intensities or absent kaolinite peaks in the XRD spectrums indicated that the treated kaolin samples have an amorphous structure. The geopolymerization reaction resulted in the formation of zeolite (Z) mineral as a major constituent of treated samples under 12 M NaOH and 3 M Na_2SiO_3 solution. However, only a trace amount of zeolite formation takes place under 14 M NaOH and 3.5 M Na_2SiO_3 solution. Kamarudin et al., (2011) and Heah et al., (2013) reported similar observations for treated kaolin at different concentrations of alkali activator solution. Thus,

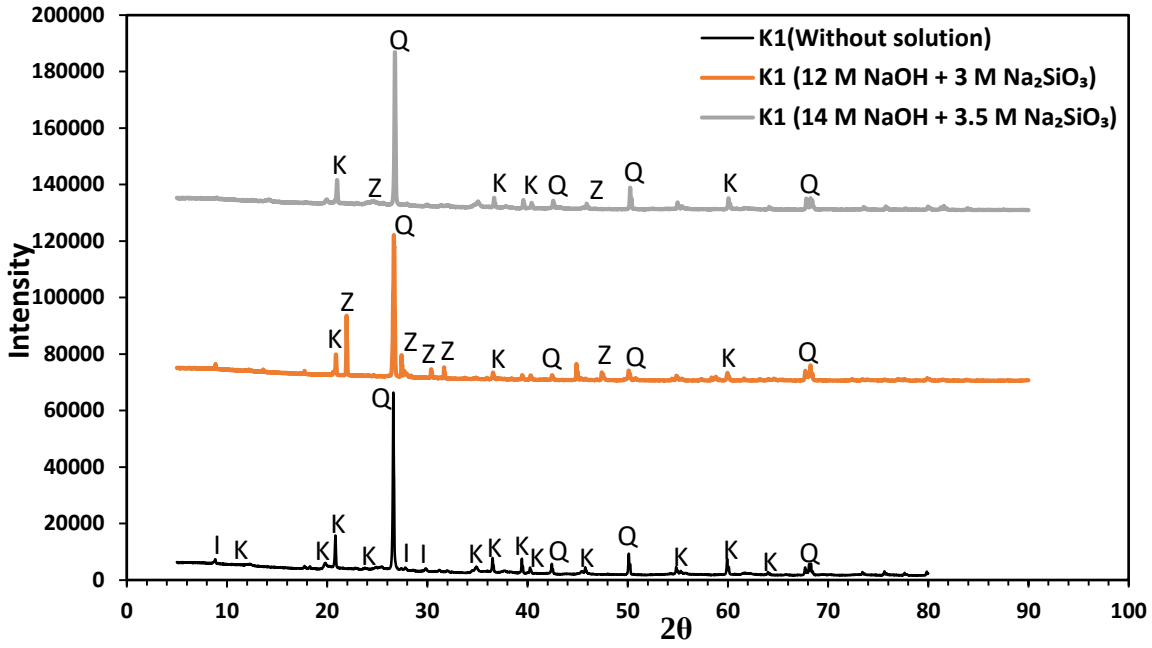

Fig. 7.29. XRD patterns of kaolin treated with different solution concentrations.

12 M NaOH and 3 M Na_2SiO_3 solution showed higher amorphous content of treated samples, which comply with its lowest collapse potential. The slight drop in quartz intensities was observed at 12 M NaOH and 3 M Na_2SiO_3 solution, indicating the siliceous quartz also participated in the geopolymerization reaction. However, the drop-in quartz intensities were due to the dilution effect (Lecomte et al., 2003).

It is to be noted that zeolite possesses pozzolanic reactivity by virtue of it can form cementing/chemical bonds with alumino-silicate materials and thereby imparts mechanical strength (Yousef et al., 2009, Perraki et al., 2010, Mola-Abasi and Shooshpasha 2016, Kaya et al., 2022). Thus, it can be interpreted that the cementing bonds between the kaolin particles (Fig. 7.7) were due to zeolite formation, which significantly reduced wetting-induced collapse deformation.

Fig. 7.30 shows the XRD results of untreated sand and treated sand samples extracted from the sand columns for different concentrations of alkali activator solution at eight days of curing. New geopolymer products or minerals with new peaks were observed in treated sand

samples. This suggested the sand was also taken part in the geopolymerization process along with compacted kaolin samples and thus complied with improved mechanical behaviour.

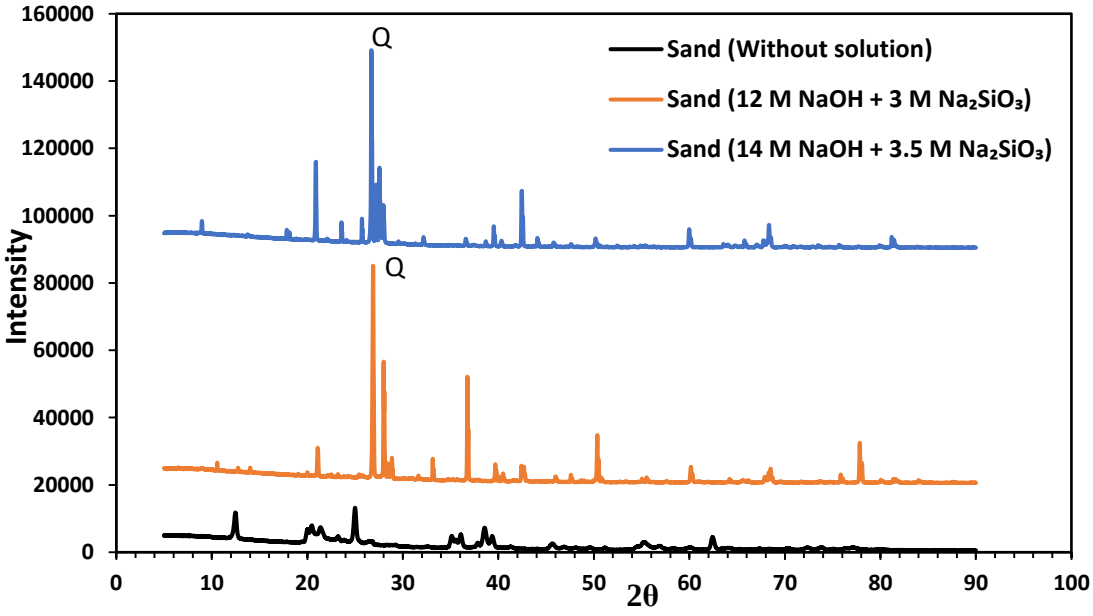

Fig. 7.30. XRD patterns of sand treated with different solution concentrations.

7.3 Methodology for Field Implementation

In the natural conditions of slopes, the rainwater infiltration limits to a shallow depth of the soil mass, as shown in Fig. 7.31. However, owing to the built environment, rainwater infiltrates into a deeper depth (Fig. 31), and changes the stress state of the soil. The altering stress state of the underlying collapsible soils brings instability at the particle level and appears as subsidence at the macro level. Therefore, it is essential to minimize the collapse potential of sub-surface kaolin deposits to avoid infrastructure losses. Presently, no ground improvement method has been proposed to reduce the collapse potential of natural kaolin deposits in field conditions. A new technique was proposed to minimize the collapse volume change caused due to wetting of underground kaolin deposits.

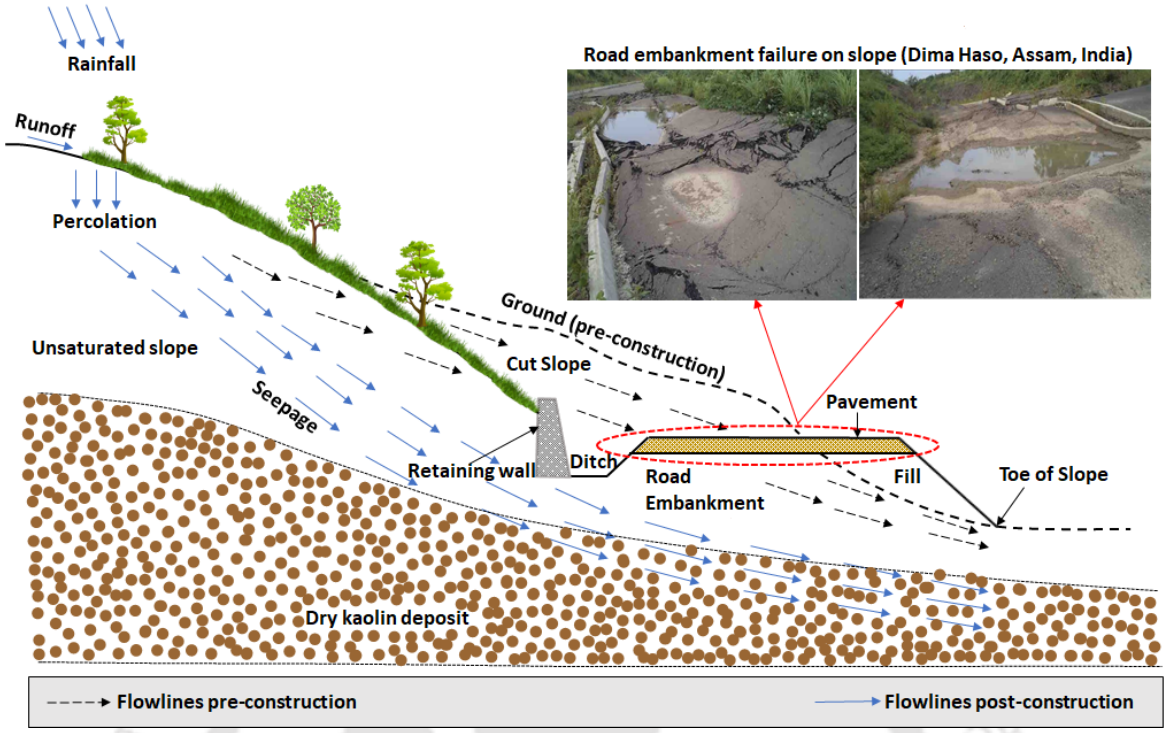

Fig. 7.31. Wetting of slope and embankment in the actual field situation.

Fig. 7.32 shows the schematic diagram of the procedure which can be adopted in field situations to control the deformation caused by saturation in the kaolin deposits. The same laboratory test procedure can be mimicked to solve the field issue. Initially, cylindrical holes are drilled into the entire depth of the kaolin deposit. The casing of non-corrosive material on peripheral walls of cylindrical columns can be provided in the other soil deposits to avoid loss of solution during infiltration. Subsequently, the dry sand is loosely poured inside the drilled columns to create a group of sand columns for uniform distribution of the alkali activator solution in desired soil volume. Further, an alkali solution of optimum concentration is sprinkled from the top of the sand columns. Finally, the curing time of eight days under ambient conditions should be allowed to form geopolymer bonds between the soil particles to gain optimum stiffness or mechanical strength.

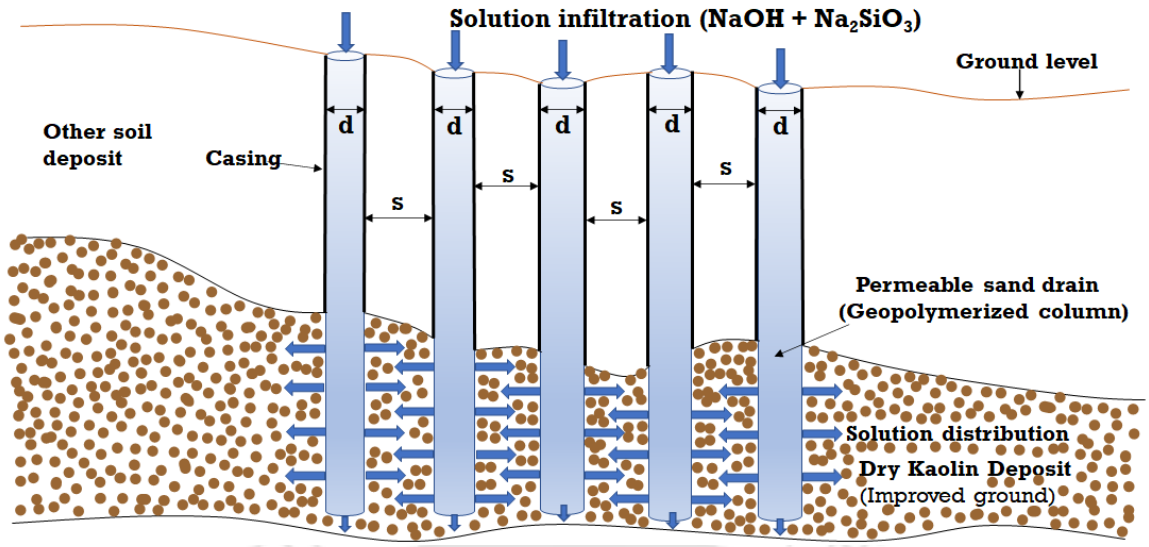

Fig. 7.32. Schematic representation of ground improvement by the proposed technique.

7.3.1 *Design of Group of Stabilized Sand Columns*

The bearing capacity of reinforced soil deposit with the sand column is directly related to the load-carrying capacity of a group of sand columns. Since the load from the top has to be transferred through the surrounding soil as well as through the sand column. Thus, the overall safety of the super-structure or sub-structure that has to be built on top will also depend on the stability of reinforced sand columns. The design of the group of sand columns can be done by considering the bearing capacity of the footing that has to be rested on soil reinforced with several sand columns. Bouassida et al. (1995) derived an analytical expression for the ultimate bearing capacity, q_{ult}, of a group of columns reinforced in the soil regardless of the geometrical arrangement of columns and shape of footing and given by

$$q_{ult} = 4c + 2A_s\left[c(K_p - 2) + c_s\sqrt{K_p}\right] \geq Q/A \qquad [7.1]$$

where Q is vertical applied load (kN); c is the cohesion of soil (kPa); K_p is passive earth pressure coefficient; c_s is the cohesion of column material (kPa); A_s is the total cross-sectional area of columns ($A_s = N_s\,\pi d^2/A$) (m^2), as shown in Fig. 7.33; N_s is a number of

columns; *d* is the diameter of the column (m); *A* is footing area (m^2) (. Indian Road Congress (IRC: SP:109, 2015) recommended a minimum spacing of 3*d* or a distance equal to the pile diameter for the friction piles.

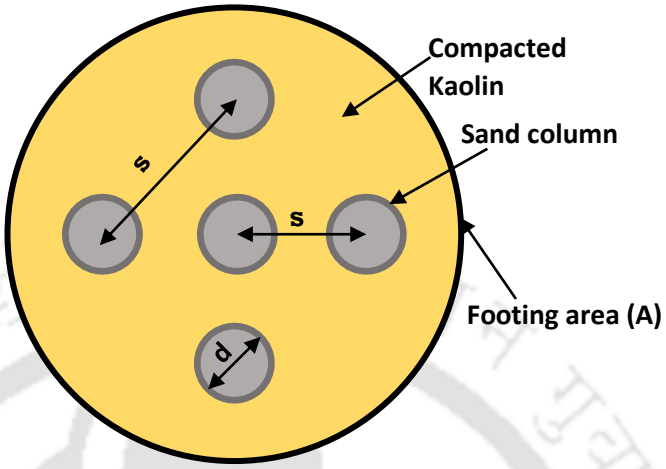

Fig. 7.33. Model for the design of group of sand columns.

7.4 Critical Remarks

1. Synthesis of kaolin geopolymer was more effective at higher concentrations.
2. Kaolin geopolymers showed strong stability against wetting with distilled water with the least collapse potential at 12 M alkali concentration.
3. XRD patterns indicated that more synthesis of cementing agent zeolite occurred under 12 M NaOH + 3 Na_2SiO_3 solution, because of which geopolymerization was more effective at this optimum concentration.
4. The collapse potential in treated kaolin samples was reduced significantly at different inundation pressures under higher concentrations of alkali activator solution. However, the reduction in collapse potential was more pronounced for pattern '*B*' samples. Moreover, the highest reduction in collapse potential of approximately 92 % was noticed under 12 M NaOH + 3 Na_2SiO_3 solution.
5. The proposed laboratory technique can be implemented in the field to reduce excessive wetting-induced collapse settlements in soils.

Chapter 8

Conclusions and Future Scope

8.1 Conclusions

1. The volume change and yielding response of compacted unsaturated kaolin were highly affected by the initial suction conditions and the clay fabric. The BBM was unable to predict the accurate yielding response of air-dry compacted kaolin, as the inter-particle surface forces, which control the particle configuration, are not incorporated.
2. For the first time, a generalized model was formulated that explicitly accommodated the collapse behaviour and implicitly incorporated surface forces through a single parameter soaking modulus, k_{sc}. The full description of the wetting-induced collapse behaviour of soil would require many parameters. The model incorporates only one parameter soaking gradient, k_{sc} to quantify volumetric collapse behaviour, which makes the model very simple. The model involves simple parameters whose determination is easy compared to the parameters in existing models, which require complex and tedious laboratory tests such as the measurement of SWCC data.
3. A new theoretical framework based on effective stress approach was developed to interpret the large-strain shear behaviour, including anomalous peak response of NC clays. The modified effective stress concept was employed using proposed equations for inter-particle electro-chemical forces to describe the drained shear response of kaolin. The proposed conceptual framework provided satisfactory explanation for experimental large-strain shear response under different chemo-mechanical loadings. The predicted large-strain shear response by the proposed models could adequately capture the kaolin behaviour in ring shear stress conditions.

4. The mechanical response, i.e., the collapse potential of kaolin under different mechanical loads, was considerably reduced by the treatment of compacted dry kaolin samples with an optimal concentration of alkali sodium hydroxide and activator sodium silicate solution. The proposed technique based on geopolymerization for minimizing collapse potential is suitable for kaolin soils located at shallow or deeper depths. The proposed method is simple and may not involve costly procedures and equipment's.

8.2 Future Scope

1. The volume change and shear strength behaviour of the dry compacted kaolin can be explored under different compaction densities. The soil density may have a significant influence due to the distinct resultant clay particle association under different initial compaction densities, as it was observed that clay fabric had a substantial impact on the mechanical characteristics of kaolin.
2. In this study, it was found that the volume change and yielding behaviour depended on the initial suction of the dry compacted kaolin. It can be expected that the shear strength behaviour, including peak and residual strength of compacted kaolin, may also be a strong function of suction. Therefore, more studies need to be conducted for the investigation of the suction-controlled shear strength response of initially dry compacted kaolin.
3. The mechanical strength tests on alkali treated kaolin samples can be conducted to understand its stability and improvement in the shear strength behaviour. Moreover, long-term leaching characteristics in treated kaolin can also be explored.
4. The proposed theoretical approach based on effective stress concept for the interpretation and prediction of large-strain shear resistance can be extended for volume change response.

List of Publications

Journal Publications

1. **Srivastava, A**., Bharat, T.V. Collapsible Soil Model (CoSM) for the Prediction of Mechanical Characteristics of Partially-Saturated Compacted Collapsible Soils. (*Under Review* in International Journal of Geomechanics, *ASCE*)
2. **Srivastava, A**., Bharat, T.V. Theoretical Framework for Modelling the Shear strength Characteristics of Kaolin soil Under Physico-chemical Influence. (*Under review* in Canadian Geotechnical Journal).
3. **Srivastava, A**., Bharat, T.V. Chemical Stabilization of Kaolin to Prevent Collapse. (*Manuscript Preparation*)
4. Bharat, T. V., **Srivastava, A**., & Gapak, Y. (2021). Prediction of wetting hydraulic characteristics of compacted bentonites in isochoric conditions. *Journal of Geotechnical and Geoenvironmental Engineering*, *147*(8), 04021067.

Conferences / Book Chapters

1. **Srivastava, A** & Bharat, T.V. Shearing Behaviour of Calcined Kaolin Clays in Ring Shear Apparatus. Geo-Congress 2024 (Under Review).
2. **Srivastava, A** & Bharat, T.V. Experimental Study on Volumetric Shrinkage Behaviour of Indian clays. Proceedings of Indian Geotehnical Conference 2021. *Springer Nature.*
3. Bharat, T.V., Das, P., **Srivastava, A**. (2019). Insights into Contaminant Transport Modeling Through Compacted Bentonites. In: Latha G., M. (eds) Frontiers in Geotechnical Engineering. Developments in Geotechnical Engineering. Springer, Singapore.

References

Abdullah, H. H., & Shahin, M. A. (2022). Geomechanical Behaviour of Clay Stabilised with Fly-Ash-Based Geopolymer for Deep Mixing. *Geosciences (Switzerland)*, *12*(5). https://doi.org/10.3390/geosciences12050207

Abdullah, H. H., Shahin, M. A., Walske, M. L., & Karrech, A. (2020). Systematic approach to assessing the applicability of fly-ash-based geopolymer for clay stabilization. *Canadian Geotechnical Journal*, *57*(9), 1356–1368. https://doi.org/10.1139/cgj-2019-0215

Abdullah, H. H., Shahin, M. A., Walske, M. L., & Karrech, A. (2021). Cyclic behaviour of clay stabilised with fly-ash based geopolymer incorporating ground granulated slag. *Transportation Geotechnics*, *26*. https://doi.org/10.1016/j.trgeo.2020.100430

Alonso, E. E., Gens, A., & Hight, D. W. (1987). General report. In Groundwater effects in geotechnical engineering. *Proc. 9th European Conf. SMFE*, *3*, 1087–1146. https://cir.nii.ac.jp/crid/1570572699177951744.bib?lang=en

Alonso, E. E., Gens, A., & Josa, A. (1990). A constitutive model for partially saturated soils. *Géotechnique*, *40*(3), 405–430. https://doi.org/10.1680/geot.1990.40.3.405

Alonso, E. E., Pinyol, N. M., & Gens, A. (2013). Compacted soil behaviour: initial state, structure and constitutive modelling. *Géotechnique*, *63*(6), 463–478. https://doi.org/10.1680/geot.11.P.134

Anandarajahi, A., & Chenii, J. (1997). VANDER WAALS ATTRACTIVE FORCE BETWEEN CLAY PARTICLES IN WATER AND CONTAMINANTS. In *SOILS AND FOUNDATIONS* (Vol. 37, Issue 2). Japanese Geotechnical Society.

ASTM. D2488: (2018). *Standard Practice for Description and Identification of Soils (Visual-Manual Procedures)*. https://doi.org/10.1520/D2488-17E01

ASTM. D4318: (2018). *Standard Test Methods for Liquid Limit, Plastic Limit, and Plasticity Index of Soils*. https://doi.org/10.1520/D4318-17

ASTM. D4546: (2021). *Standard Test Methods for One-Dimensional Swell or Collapse of Soils*. https://doi.org/10.1520/D4546-21

ASTM. D6467: (2021). *Standard Test Method for Torsional Ring Shear Test to Determine Drained Residual Shear Strength of Fine-Grained Soils 1*. https://doi.org/10.1520/D6467-21E01

ASTM. D7928: (2021). *Standard Test Method for Particle-Size Distribution (Gradation) of Fine-Grained Soils Using the Sedimentation (Hydrometer) Analysis*. https://doi.org/10.1520/D7928-17

Bharat, T. V., & Das, D. S. (2017). Physicochemical approach for analyzing equilibrium volume of clay sediments in salt solutions. *Applied Clay Science*, *136*, 164–175. https://doi.org/10.1016/j.clay.2016.11.021

Bharat, T. V., & Gapak, Y. (2021). Soil-water characteristic curves of bentonites in isochoric conditions during wetting: measurement and prediction. *Canadian Geotechnical Journal*, *58*(5), 711–721. https://doi.org/10.1139/cgj-2019-0818

Bishop, A. W., Green, G. E., Garga, V. K., Andresen, A., & Brown, J. D. (1971). A New Ring Shear Apparatus and Its Application to the Measurement of Residual Strength. *Géotechnique*, *21*(4), 273–328. https://doi.org/10.1680/geot.1971.21.4.273

Blinova, I., Bityukova, L., Kasemets, K., Ivask, A., Käkinen, A., Kurvet, I., Bondarenko, O., Kanarbik, L., Sihtmäe, M., Aruoja, V., Schvede, H., & Kahru, A. (2012). Environmental hazard of oil shale combustion fly ash. *Journal of Hazardous Materials*, *229–230*, 192–200. https://doi.org/10.1016/j.jhazmat.2012.05.095

Bouassida, M., De Buban, P., & Donnieux, L. (1995). *Bearing capacity of a foundation resting on a soil reinforced by a group of columns* (Vol. 45, Issue 1).

Braggs, B. (1994). The Effect of Surface Modification by an Organosilane on the Electrochemical Properties of Kaolinite. *Clays and Clay Minerals*, *42*(2), 123–136. https://doi.org/10.1346/CCMN.1994.0420203

Burland, J. B. (1990). On the compressibility and shear strength of natural clays. *Géotechnique*, *40*(3), 329–378. https://doi.org/10.1680/geot.1990.40.3.329

Burmister, D. D. M. (1952). The Application of Controlled test Methods in Consolidation Testing. *ASTM International*, 83–98. https://doi.org/10.1520/STP48299S

Burmister, D. M. (1942). Laboratory Investigations of Soils at Flushing Meadow Park. *Transactions of the American Society of Civil Engineers*, *107*(1), 187–204. https://doi.org/10.1061/TACEAT.0005453

CASAGRANDE, A. (1936). The determination of pre-consolidation load and it's practical significance. *Proc. Int. Conf. Soil Mech. Found. Eng. Cambridge, Mass., 1936*, *3*, 60. https://cir.nii.ac.jp/crid/1571135650387167744.bib?lang=en

Chapman, H. D. (2016). *Cation-Exchange Capacity* (pp. 891–901). https://doi.org/10.2134/agronmonogr9.2.c6

Choudhury, C. (2019). *Effective stress development in kaolin and bentonite clays during the hydro-mechanical loading*. http://gyan.iitg.ernet.in/handle/123456789/1816

Choudhury, C., & Bharat, T. V. (2018). Wetting-induced collapse behavior of kaolinite: Influence of fabric and inundation pressure. *Canadian Geotechnical Journal*, *55*(7), 956–967. https://doi.org/10.1139/cgj-2017-0297

Corrêa-Silva, M., Araújo, N., Cristelo, N., Miranda, T., Gomes, A. T., & Coelho, J. (2019). Improvement of a clayey soil with alkali activated low-calcium fly ash for transport infrastructures applications. *Road Materials and Pavement Design*, *20*(8), 1912–1926. https://doi.org/10.1080/14680629.2018.1473286

Coudert, E., Paris, M., Deneele, D., Russo, G., & Tarantino, A. (2019). Use of alkali activated high-calcium fly ash binder for kaolin clay soil stabilisation: Physicochemical evolution. *Construction and Building Materials*, *201*, 539–552. https://doi.org/10.1016/j.conbuildmat.2018.12.188

Coudert, E., Russo, G., Deneele, D., & Tarantino, A. (2022). Mechanical behaviour of compacted kaolin clay stabilised via alkali activated calcium-rich fly ash binder. *Geomechanics for Energy and the Environment*, *32*. https://doi.org/10.1016/j.gete.2022.100404

Cristelo, N., Glendinning, S., & Pinto, A. T. (2011). Deep soft soil improvement by alkaline activation. *Proceedings of the Institution of Civil Engineers: Ground Improvement*, *164*(2), 73–82. https://doi.org/10.1680/grim.900032

Das, A. P., & Thyagaraj, T. (2018). Collapse behaviour of compacted red soil. *International Journal of Geotechnical Engineering*, *12*(1), 20–27. https://doi.org/10.1080/19386362.2016.1243506

Derbyshire, E. (2001). Geological hazards in loess terrain, with particular reference to the loess regions of China. In *Earth-Science Reviews* (Vol. 54). www.elsevier.comrlocaterearscirev

Duong, N. T., Suzuki, M., & van Hai, N. (2018). Rate and acceleration effects on residual strength of kaolin and kaolin–bentonite mixtures in ring shearing. *Soils and Foundations*, *58*(5), 1153–1172. https://doi.org/10.1016/j.sandf.2018.05.011

Farulla, C. A., Ferrari, A., & Romero, E. (2010). Volume change behaviour of a compacted scaly clay during cyclic suction changes. *Canadian Geotechnical Journal*, *47*(6), 688–703. https://doi.org/10.1139/T09-138

Gan, J. K. M., Fredlund A N, D. G., & Rahardjo, D. H. (1988). *Determination of the shear strength parameters of an unsaturated soil using the direct shear test*.

Ge, M., Pineda, J. A., Sheng, D., Burton, G. J., & Li, N. (2021). Microstructural effects on the wetting-induced collapse in compacted loess. *Computers and Geotechnics*, *138*. https://doi.org/10.1016/j.compgeo.2021.104359

Gibo, S., Egashira, K., & Ohtsubo, M. (1987). Residual strength of smectite-dominated soils from the Kamenose landslide in Japan. *Canadian Geotechnical Journal*, *24*(3), 456–462. https://doi.org/10.1139/t87-057

Grim, R. E., York, N., & London, T. (1953). *CLAY MINERALOGY*.

Heah, C. Y., Kamarudin, H., Mustafa Al Bakri, A. M., Binhussain, M., Luqman, M., Khairul Nizar, I., Ruzaidi, C. M., & Liew, Y. M. (2011). Effect of curing profile on kaolin-based geopolymers. *Physics Procedia*, *22*, 305–311. https://doi.org/10.1016/j.phpro.2011.11.048

Heah, C. Y., Kamarudin, H., Mustafa Al Bakri, A. M., Bnhussain, M., Luqman, M., Khairul Nizar, I., Ruzaidi, C. M., & Liew, Y. M. (2013). Kaolin-based geopolymers with various NaOH concentrations. *International Journal of*

Minerals, Metallurgy and Materials, *20*(3), 313–322. https://doi.org/10.1007/s12613-013-0729-0

Hounsi, A. D., Lecomte-Nana, G., Djétéli, G., Blanchart, P., Alowanou, D., Kpelou, P., Napo, K., Tchangbédji, G., & Praisler, M. (2014). How does Na, K alkali metal concentration change the early age structural characteristic of kaolin-based geopolymers. In *Ceramics International* (Vol. 40, Issue 7 PART A, pp. 8953–8962). Elsevier Ltd. https://doi.org/10.1016/j.ceramint.2014.02.052

IRC:SP:109-2015. (2015). *Guidelines for design and construction of small diameter piles for road bridges*.

IS. 2720-40: (1977). *IS 2720-40 (1977): Methods of test for soils, Part 40: Determination of free swell index of soils*.

Israelachvili. (1991). *Intermolecular and surface forces. Academic Press, London.*

Jacobsen, H. (1992). Bestemmelse af forbelastningstryk i laboratoriet. I NGM-92 : Proceedings fra 11. In *Nordiske Geoteknikermøde* (Vol. 16).

Jambhulkar, H. P., Shaikh, S. M. S., & Kumar, M. S. (2018). Fly ash toxicity, emerging issues and possible implications for its exploitation in agriculture; Indian scenario: A review. In *Chemosphere* (Vol. 213, pp. 333–344). Elsevier Ltd. https://doi.org/10.1016/j.chemosphere.2018.09.045

Jennings, J. E. B., & Burland, J. B. (1962). Limitations to the Use of Effective Stresses in Partly Saturated Soils. *Géotechnique*, *12*(2), 125–144. https://doi.org/10.1680/geot.1962.12.2.125

Jiang, M., Hu, H., & Liu, F. (2012). Summary of collapsible behaviour of artificially structured loess in oedometer and triaxial wetting tests. *Canadian Geotechnical Journal*, *49*(10), 1147–1157. https://doi.org/10.1139/T2012-075

Josa, A., Balmaceda, A., Gens, A., & Alonso, E. E. (1992). An elastoplastic model for partially saturated soils exhibiting a maximum of collapse. *Proceedings of the 3rd International Conference on Computational Plasticity, Barcelona (Vol. 1, Pp. 815-826)*. https://scholar.google.com/scholar?hl=en&as_sdt=0%2C5&q=An+elastoplastic+model+for+partially+saturated+soils+exhibiting+a+maximum+of+collapse&btnG=

Jose, B. T., Sridharan, A., Mathews, B., Jose, R. :, Sridharan, A., & Abraham, B. M. (1989). Log-log Method for Determination of Preconsolldation Pressure. In *Geotechni-cal Testing Journal, GTJODJ* (Vol. 12, Issue 3).

Jotisankasa, A., Ridley, ; Andrew, & Coop, M. (2007). *Collapse behavior of compacted silty clay in suction-monitored oedometer apparatus Cite this paper Collapse Behavior of Compacted Silty Clay in Suction-Monitored Oedometer Apparatus*. https://doi.org/10.1061/ASCE1090-02412007133:7867

Kaya, A., & Fang, H.-Y. (2000). *The effects of organic fluids on physicochemical parameters of fine-grained soils*.

Kodikara, J., Jayasundara, C., & Zhou, A. N. (2020). A generalised constitutive model for unsaturated compacted soils considering wetting/drying cycles and environmentally-stabilised line. *Computers and Geotechnics*, *118*. https://doi.org/10.1016/j.compgeo.2019.103332

Lambe. (1960). A mechanistic picture of shear strength in clay. *Conf. on Shear Strength of Cohesive Soils, 1960, 1960 - Cir.Nii.Ac.Jp*.

Lawton, E. C., Fragaszy, R. J., & Hetherington, M. D. (1992). REVIEW OF WETTING-INDUCED COLLAPSE IN COMPACTED SOIL. *Journal of Geotechnical Engineering* , *118*(9), 1–19. https://doi.org/https://doi.org/10.1061/(ASCE)0733-9410(1992)118:9(1376)

Lecomte, I., Liégeois, M., Rulmont, A., Cloots, R., & Maseri, F. (2003). Synthesis and characterization of new inorganic polymeric composites based on kaolin or white clay and on ground-granulated blast furnace slag. *Journal of Materials Research*, *18*(11), 2571–2579. https://doi.org/10.1557/JMR.2003.0360

Lehmann, P., Leshchinsky, B., Gupta, S., Mirus, B. B., Bickel, S., Lu, N., & Or, D. (2021). Clays Are Not Created Equal: How Clay Mineral Type Affects Soil Parameterization. *Geophysical Research Letters*, *48*(20). https://doi.org/10.1029/2021GL095311

Li, D., Yin, K., Glade, T., & Leo, C. (2017). Effect of over-consolidation and shear rate on the residual strength of soils of silty sand in the Three Gorges Reservoir. *Scientific Reports*, *7*(1). https://doi.org/10.1038/s41598-017-05749-4

Li, P., Vanapalli, S., & Li, T. (2016). Review of collapse triggering mechanism of collapsible soils due to wetting. *Journal of Rock Mechanics and Geotechnical Engineering*, *8*(2), 256–274. https://doi.org/10.1016/j.jrmge.2015.12.002

Mahur, A. K., Kumar, R., Sengupta, D., & Prasad, R. (2008). Estimation of radon exhalation rate, natural radioactivity and radiation doses in fly ash samples from Durgapur thermal power plant, West Bengal, India. *Journal of Environmental Radioactivity*, *99*(8), 1289–1293. https://doi.org/10.1016/j.jenvrad.2008.03.010

Matalkah, F., Aqel, R., & Ababneh, A. (2020). Enhancement of the Mechanical Properties of Kaolin Geopolymer Using Sodium Hydroxide and Calcium Oxide. *Procedia Manufacturing*, *44*, 164–171. https://doi.org/10.1016/j.promfg.2020.02.218

Mesri, G., Asce, M., Shahien, M., & Asce, A. M. (2003). *Residual Shear Strength Mobilized in First-Time Slope Failures*. https://doi.org/10.1061/ASCE1090-02412003129:112

Mitchell and Soga. (2005). *Fundamentals of Soil Behavior* (Third Edition).

Moore, R. (1991). *The chemical and mineralogical controls upon the residual strength of pure and natural clays* (Vol. 41, Issue 1).

Mu, Q. Y., Dong, H., Liao, H. J., Zhou, C., Li, S. B., & Zhang, J. W. (2022). Effects of in situ wetting–drying cycles on the mechanical behaviour of an intact loess.

Canadian Geotechnical Journal, *59*(7), 1281–1284. https://doi.org/10.1139/cgj-2020-0696

Mu, Q. Y., Zhou, C., & Ng, C. W. W. (2020a). Compression and wetting induced volumetric behavior of loess: Macro- and micro-investigations. *Transportation Geotechnics*, *23*. https://doi.org/10.1016/j.trgeo.2020.100345

Olphen, H. (1977). *An introduction to clay colloid chemistry, for clay technologists, geologists, and soil scientists.* (No.2nd edition).

Opukumo, A. W., Davie, C. T., Glendinning, S., & Oborie, E. (2022). A review of the identification methods and types of collapsible soils. In *Journal of Engineering and Applied Science* (Vol. 69, Issue 1). Springer Science and Business Media B.V. https://doi.org/10.1186/s44147-021-00064-2

Pedrotti, M., & Tarantino, A. (2014). Microstructural interpretation of compression behaviour of compacted kaolin clay. *Unsaturated Soils: Research and Applications - Proceedings of the 6th International Conference on Unsaturated Soils, UNSAT 2014*, *1*, 739–745. https://doi.org/10.1201/b17034-104

Pedrotti, M., & Tarantino, A. (2018). An experimental investigation into the micromechanics of non-active clays. *Geotechnique*, *68*(8), 666–683. https://doi.org/10.1680/jgeot.16.P.245

Phetchuay, C., Horpibulsuk, S., Arulrajah, A., Suksiripattanapong, C., & Udomchai, A. (2016). Strength development in soft marine clay stabilized by fly ash and calcium carbide residue based geopolymer. *Applied Clay Science*, *127–128*, 134–142. https://doi.org/10.1016/j.clay.2016.04.005

Prakash, K., & Sridharan, A. (2020). Log–Log Method of Pre-consolidation/Yield Stress Determination: An Appraisal. *Geotechnical and Geological Engineering*, *38*(1), 947–959. https://doi.org/10.1007/s10706-019-01030-9

Prakash, K., Sridharan, A., & Prasanna, H. S. (2014). Compaction Induced Yield Stress. *Geotechnical and Geological Engineering*, *32*(2), 311–319. https://doi.org/10.1007/s10706-013-9715-6

Provis, J. L. (2018). Alkali-activated materials. In *Cement and Concrete Research* (Vol. 114, pp. 40–48). Elsevier Ltd. https://doi.org/10.1016/j.cemconres.2017.02.009

Rahardjo, H., Lim, T. T., Chang, M. F., & Fredlund, D. G. (1995). Shear-strength characteristics of a residual soil. *Canadian Geotechnical Journal*, *32*(1), 60–77. https://doi.org/10.1139/t95-005

Rand, B., & Melton, I. E. (1977). *Particle Interactions in Aqueous Kaolinite Suspensions I. Effect of pH and Electrolyte upon the Mode of Particle Interaction in Homoionic Sodium Kaolinite Suspensions*.

Rao, S. M., & Revanasiddappa, K. (2002). Collapse behaviour of a residual soil. *Géotechnique*, *52*(4), 259–268. https://doi.org/10.1680/geot.2002.52.4.259

Rao, S. M., & Revanasiddappa, K. (2006). Influence of cyclic wetting drying on collapse behaviour of compacted residual soil. *Geotechnical and Geological Engineering*, *24*(3), 725–734. https://doi.org/10.1007/s10706-004-5077-4

Rios, S., Cristelo, N., Viana da Fonseca, A., & Ferreira, C. (2016). Structural Performance of Alkali-Activated Soil Ash versus Soil Cement. *Journal of Materials in Civil Engineering*, *28*(2). https://doi.org/10.1061/(asce)mt.1943-5533.0001398

Rojas, E., Pérez-Rea, M. L., López-Lara, T., Hernández, J. B., & Horta, J. (2015). Use of Effective Stresses to Model the Collapse upon Wetting in Unsaturated Soils. *Journal of Geotechnical and Geoenvironmental Engineering*, *141*(5). https://doi.org/10.1061/(asce)gt.1943-5606.0001251

Roscoe, K. H., Mech, A. M. I. E., Schofield, A. N., & Thurairajah, A. (1963). *YIELDING OF CLAYS IN STATES WETTER THAN CRITICAL*.

Roscoe, K. H., Schofield, A. N., & Wroth, C. P. (1958). *ON THE YIELDING OF SOILS*.

Sasitharan, S., Robertson, D. P. K., Sego, D. C., & Morgenstern, N. R. (1994). *State-boundary surface for very loose sand and its practical' implications*.

Schemertmann, J. (1955). The undisturbed consolidation of clay. *Tran. ASCE*. https://cir.nii.ac.jp/crid/1570854175723384832.bib?lang=en

Scrivener, K. L., & Kirkpatrick, R. J. (2008). Innovation in use and research on cementitious material. *Cement and Concrete Research*, *38*(2), 128–136. https://doi.org/10.1016/j.cemconres.2007.09.025

Shi, X. S., Herle, I., & Yin, J. (2018). Laboratory Study of the Shear Strength and State Boundary Surface of a Natural Lumpy Soil. *Journal of Geotechnical and Geoenvironmental Engineering*, *144*(12). https://doi.org/10.1061/(asce)gt.1943-5606.0001987

Silva, R. A., Oliveira, D. V., Miranda, T., Cristelo, N., Escobar, M. C., & Soares, E. (2013). Rammed earth construction with granitic residual soils: The case study of northern Portugal. *Construction and Building Materials*, *47*, 181–191. https://doi.org/10.1016/j.conbuildmat.2013.05.047

Silveira, I. A., & Rodrigues, R. A. (2020). Collapsible Behavior of Lateritic Soil Due to Compacting Conditions. *International Journal of Civil Engineering*, *18*(10), 1157–1166. https://doi.org/10.1007/s40999-020-00523-6

Singhi, B., Laskar, A. I., & Ahmed, M. A. (2016). Investigation on Soil–Geopolymer with Slag, Fly Ash and Their Blending. *Arabian Journal for Science and Engineering*, *41*(2), 393–400. https://doi.org/10.1007/s13369-015-1677-y

Sivakumar, V., Sivakumar, R., Murray, E. J., Mackinnon, P., & Boyd, J. (2010). Mechanical behaviour of unsaturated kaolin (with isotropic and anisotropic stress history). part 1: Wetting and compression behaviour. *Geotechnique*, *60*(8), 581–594. https://doi.org/10.1680/geot.8.P.007

Sivakumar, V., Tan, W. C., Murray, E. J., & Mckinley, J. D. (2006). *Wetting, drying and compression characteristics of compacted clay* (Vol. 56, Issue 1).

Sivakumar, V., & Wheeler, S. J. (2000). Influence of compaction procedure on the mechanical behaviour of an unsaturated compacted clay. Part 1: Wetting and isotropic compression. *Géotechnique*, *50*(4), 359–368. https://doi.org/10.1680/geot.2000.50.4.359

Skempton, A. W. (1964). *LONG-TERM STABILITY OF CLAY SLOPES*.

Skempton, A. W. (1985). *Residual strength of clays in landslides, folded strata and the laboratory**. https://doi.org/https://doi.org/10.1680/geot.1985.35.1.3

Songpiriyakij, S., Kubprasit, T., Jaturapitakkul, C., & Chindaprasirt, P. (2010). Compressive strength and degree of reaction of biomass- and fly ash-based geopolymer. *Construction and Building Materials*, *24*(3), 236–240. https://doi.org/10.1016/j.conbuildmat.2009.09.002

Sridharan. (1968). *Some studies on the strength of partially saturated clays.* [PhD Thesis].

Sridharan, A., Abraham, B. M., & Jose, B. T. (1991). *Improved technique for estimation of preconsolidation pressure* (Vol. 41, Issue 2).

Sridharan, A., & Prakash, K. (1999). *Influence of clay mineralogy and pore-medium chemistry on clay sediment formation*.

Sridharan, A., & Rao, G. V. (1971). Effective Stress Theory of Shrinkage Phenomena. In *Canadian Geotechnical Journal Published by* (Vol. 8, Issue 4).

Sridharan, A., Rao, G. V., & Pandian, R. S. (1973). Volume Change Behaviour of Partly Saturated Clays During Soaking and the Role of Effective Stress Concept. *Soils and Foundations*, *13*(3), 1–15. https://doi.org/10.3208/sandf1972.13.3_1

Sridharan, A., & Sivapullaiah, P. V. (2005). Mini compaction test apparatus for fine grained soils. *Geotechnical Testing Journal*, *28*(3), 240–246. https://doi.org/10.1520/gtj12542

Sridharan, & Rao. (1973). *Mechanism controlling volume change of saturated clays and the role of the effective stress concept*.

Sridharan, & Rao. (1979). *Shear strength behaviour of saturated clays and the role of effective stress concept*.

Suksiripattanapong, C., Horpibulsuk, S., Yeanyong, C., & Arulrajah, A. (2021). Evaluation of polyvinyl alcohol and high calcium fly ash based geopolymer for the improvement of soft Bangkok clay. *Transportation Geotechnics*, *27*. https://doi.org/10.1016/j.trgeo.2020.100476

Sun, D., Sheng, D., & Sloan, S. W. (2007). Elastoplastic modelling of hydraulic and stress-strain behaviour of unsaturated soils. *Mechanics of Materials*, *39*(3), 212–221. https://doi.org/10.1016/j.mechmat.2006.05.002

Sun, D., Sheng, D., & Xu, Y. (2007). Collapse behaviour of unsaturated compacted soil with different initial densities. *Canadian Geotechnical Journal*, *44*(6), 673–686. https://doi.org/10.1139/T07-023

Thorel, L., Ferber, V., Caicedo, B., & Khokhar, I. M. (2011). Physical modelling of wetting-induced collapse in embankment base. *Geotechnique*, *61*(5), 409–420. https://doi.org/10.1680/geot.10.P.029

Thu, T. M., Rahardjo, H., & Leong, E. C. (2007). Elastoplastic model for unsaturated soil with incorporation of the soil-water characteristic curve. *Canadian Geotechnical Journal*, *44*(1), 67–77. https://doi.org/10.1139/T06-091

Thyagaraj, T., & Das, A. P. (2017). Physico-chemical effects on collapse behaviour of compacted red soil. *Geotechnique*, *67*(7), 559–571. https://doi.org/10.1680/jgeot.15.P.240

Tiwari, B., Asce, A. M., & Marui, H. (2005). *A New Method for the Correlation of Residual Shear Strength of the Soil with Mineralogical Composition*. https://doi.org/10.1061/ASCE1090-02412005131:91139

Vilar, O. M., & Rodrigues, R. A. (2011). Collapse behavior of soil in a Brazilian region affected by a rising water table. *Canadian Geotechnical Journal*, *48*(2), 226–233. https://doi.org/10.1139/T10-065

Vitale, E., Russo, G., Dell'agli, G., Ferone, C., & Bartolomeo, C. (2017). Mechanical behaviour of soil improved by alkali activated binders. *Environments - MDPI*, *4*(4), 1–10. https://doi.org/10.3390/environments4040080

Wahid, A. S., Gajo, A., & di Maggio, R. (2011a). Chemo-mechanical effects in kaolinite. Part 1: Prepared samples. *Geotechnique*, *61*(6), 439–447. https://doi.org/10.1680/geot.8.P.067

Wahid, A. S., Gajo, A., & di Maggio, R. (2011b). Chemo-mechanical effects in kaolinite. Part 2: exposed samples and chemical and phase analyses. *Geotechnique*, *61*(6), 449–457. https://doi.org/10.1680/geot.8.P.068

Wang, H., Li, H., & Yan, F. (2005). Synthesis and mechanical properties of metakaolinite-based geopolymer. *Colloids and Surfaces A: Physicochemical and Engineering Aspects*, *268*(1–3), 1–6. https://doi.org/10.1016/j.colsurfa.2005.01.016

Wang, S., & Wu, H. (2006). Environmental-benign utilisation of fly ash as low-cost adsorbents. In *Journal of Hazardous Materials* (Vol. 136, Issue 3, pp. 482–501). https://doi.org/10.1016/j.jhazmat.2006.01.067

Wang, Y. H., & Siu, W. K. (2006a). Structure characteristics and mechanical properties of kaolinite soils. I. Surface charges and structural characterizations. *Canadian Geotechnical Journal*, *43*(6), 587-600.*Canadian Geotechnical Journal*, *43*(6), 601–617. https://doi.org/10.1139/T06-027

Wang, Y. H., & Siu, W. K. (2006b). Structure characteristics and mechanical properties of kaolinite soils. II. Effects of structure on mechanical properties.

Canadian Geotechnical Journal, *43*(6), 601–617. https://doi.org/10.1139/T06-027

Wei, C. (2014). A Theoretical Framework for Modeling the Chemomechanical Behavior of Unsaturated Soils. *Vadose Zone Journal*, *13*(9), vzj2013.07.0132. https://doi.org/10.2136/vzj2013.07.0132

Wheeler, S. J., Sharma, R. J., & Buisson, M. S. R. (2003). Coupling of hydraulic hysteresis and stress-strain behaviour in unsaturated soils. *Géotechnique*, *53*(1), 41–54.

Wheeler, S. J., & Sivakumar, V. (1995). An elasto-plastic critical state framework for unsaturated soil. *Géotechnique*, *45*(1), 35–53. https://doi.org/https://doi.org/10.1680/geot.1995.45.1.35

Wilkinson, A., Haque, A., & Kodikara, J. (2010). Stabilisation of clayey soils with industrial by-products: Part A. *Proceedings of the Institution of Civil Engineers: Ground Improvement*, *163*(3), 149–163. https://doi.org/10.1680/grim.2010.163.3.149

Xie, W. L., Li, P., Vanapalli, S. K., & Wang, J. D. (2018). Prediction of the wetting-induced collapse behaviour using the soil-water characteristic curve. *Journal of Asian Earth Sciences*, *151*, 259–268. https://doi.org/10.1016/j.jseaes.2017.11.009

Xu, H., & Van Deventer, J. S. J. (2002). *Microstructural characterisation of geopolymers synthesised from kaolinite/stilbite mixtures using XRD, MAS-NMR, SEM/EDX, TEM/EDX, and HREM*.

Xu, L., Lan, T., & Mu, Q. (2021). Effects of Structure on the Compression Behavior of Unsaturated Loess. *International Journal of Geomechanics*, *21*(4). https://doi.org/10.1061/(asce)gm.1943-5622.0001967

Xu, Y. (2019). Peak shear strength of compacted GMZ bentonites in saline solution. *Engineering Geology*, *251*, 93–99. https://doi.org/10.1016/j.enggeo.2019.02.009

Yang, D., Yan, R., Ma, T., & Wei, C. (2023). Compressive behavior of kaolinitic clay under chemo-mechanical loadings. *Acta Geotechnica*, *18*(1), 77–94. https://doi.org/10.1007/s11440-022-01554-0

Yao, C., Chen, P., Ma, T., Xia, X., & Wei, C. (2020). Physicochemical effect on shear strength characteristics of clayey soils based on ring-shear experiment. *Canadian Geotechnical Journal*, *57*(12), 1820–1831. https://doi.org/10.1139/cgj-2019-0513

Yavari, N., Tang, A. M., Pereira, J. M., & Hassen, G. (2016). Effect of temperature on the shear strength of soils and the soil–structure interface. In *Canadian Geotechnical Journal* (Vol. 53, Issue 7, pp. 1186–1194). Canadian Science Publishing. https://doi.org/10.1139/cgj-2015-0355

Zhang, Z. H., Zhu, H. J., Zhou, C. H., & Wang, H. (2016). Geopolymer from kaolin in China: An overview. In *Applied Clay Science* (Vol. 119, pp. 31–41). Elsevier Ltd. https://doi.org/10.1016/j.clay.2015.04.023

Appendix A: Formulation of Proposed Framework

Loading-Collapse Yield Function

The elastic deformation along the air-dry re-compression line XY (Fig. 5.2) due to normal stress increments can be written from the equation of a straight line and given by,

$$\Delta e_p = -\kappa(s)\ln\left[\frac{p_y(s)}{p_y(0)}\right] \qquad [A1]$$

where $\kappa(s)$ is the slope of the re-compression line at suction s; $p_y(s)$ is yield stress at suction s; $p_y(0)$ is yield stress at the saturated state.

Likewise, the elasto-plastic deformation along wetting path YB (Fig. 5.2) from an unsaturated state with suction s to a saturated state with suction 0 at normal stress p can be expressed from wetting line LMN as shown in Fig. 9(c),

$$\Delta e_c = -k_{sc}\ln\left[\frac{s+1}{1}\right] \qquad [A2]$$

where k_{sc} is the soaking gradient representing the slope of the wetting line or change in void ratio with a change in suction. From triangle ABC in Fig. 5.2, the slope of the virgin consolidation line is

$$\lambda(0) = \frac{\Delta e_s + \Delta e_p + \Delta e_c}{\ln p_y(s) - \ln p_y(0)} \qquad [A3]$$

where Δe_s is the change in void ratio during swelling due to wetting; Δe_p is elastic deformation due to mechanical loading; Δe_c is plastic collapse due to wetting. Inserting the magnitude of deformation from eq. (A1) and (A2) in the eq. (A3),

$$k_{ss}\ln\left[\frac{s+1}{1}\right] + \kappa(s)\ln\left[\frac{p_y(s)}{p_y(0)}\right] + k_{sc}\ln\left[\frac{s+1}{1}\right] = \lambda(0)\ln\left[\frac{p_y(s)}{p_y(0)}\right]$$

$$\ln\left[\frac{s+1}{1}\right]^{k_{ss}+k_{sc}} + \ln\left[\frac{p_y(s)}{p_y(0)}\right]^{\kappa(s)} = \ln\left[\frac{p_y(s)}{p_y(0)}\right]^{\lambda(0)} \quad \text{[A4]}$$

where parameter $\kappa(s)$ can be assumed to be equal to $\kappa(0)$ (Alonso et al., 1990); k_{ss} is the soaking gradient for the swelling process; k_{sc} is the soaking gradient during the collapse phase. It might be expected that $k_{sc} > k_{ss,}$, as collapsible soils have more volume change during collapse than swelling deformation under low to moderate compaction densities. Although they are obtained under different inundation loads, to simplify eq. (A4) and make a conservative prediction of yield stress $p_y(s)$, the k_{ss} is assumed to be equal to k_{sc} in the eq. (A4),

$$\ln\left[\frac{s+1}{1}\right]^{2k_{sc}} + \ln\left[\frac{p_y(s)}{p_y(0)}\right]^{\kappa(0)} = \ln\left[\frac{p_y(s)}{p_y(0)}\right]^{\lambda(0)}$$

$$p_y(s) = p_y(0)\left[\frac{s+1}{1}\right]^{\frac{2k_{sc}}{[\lambda(0)-\kappa(0)]}} \quad \text{[A5]}$$

Prediction of NCL Behaviour

Post-yield compression curves at various suction values define a sequence of normal compression lines in (e, p) space. Mathematically, the constitutive equation of NCL can be written as a function of state variables suction s and normal stress p from Fig. 5.2,

$$e = N(s)^{*} - \lambda(s)\ln\left[\frac{p}{p_y(s)}\right] \quad \text{[A6]}$$

where $\lambda(s)$ is the slope of NCL; intercept $N(s)^{*}$ of NCL is the function of suction and defined at normal stress p_o. The normal stress p_o can be selected at the beginning of the consolidation

experiment when an air-dry compacted soil sample is inundated with water to reach a fully saturated state (Fig. 5.2). The expression for intercept $N(s)^*$ at normal stress p_o is expressed by considering deformation along the air-dry re-compression line from p_o to $p_y(s)$ as follows,

$$N(s)^* = N(s) - \kappa(s)\ln\left[\frac{p_y(s)}{p_o}\right] \qquad [A7]$$

where $N(s)$ is an intercept of the air-dry re-compression line at normal stress p_o, this differs from the intercept defined by researchers (Alonso et al., 1990; Wheeler & Sivakumar, 1995) at reference pressure p^c; $\kappa(s)$ is slope of re-compression line for the suction, s. It was assumed that, change in void ratio during swelling from the air-dry state (s) to completely saturated (s=0) state at normal stress p_o,

$$\Delta e_{s\to 0} = N(0) - N(s) = k_{ss}\ln\left[\frac{s+1}{1}\right]$$

As already mentioned earlier, $k_{ss} = k_{sc}$, Thus,

$$N(s) = N(0) - k_{sc}\ln\left[\frac{s+1}{1}\right] \qquad [A8]$$

The equation of the family of normal compression lines for various controlled-suction s, in (e, p) space incorporating wetting behaviour is developed by combining eq. (A6), (A7) and (A8),

$$e = N(0) - k_{sc}\ln\left[\frac{s+1}{1}\right] - \kappa(s)\ln\left[\frac{p_y(s)}{p_o}\right] - \lambda(s)\ln\left[\frac{p}{p_y(s)}\right] \qquad [A9]$$

Appendix B: Derivation of Coulomb's Attractive Force

The Laplace's equation gives the spatial variation of electric potential, ϕ produced by the electric charges having relative di-electric permittivity, ε_r

$$\nabla^2\phi = 0 \qquad \text{[B1]}$$

The solution of eq. (B1) for electric potential produced by disk having radius, a carrying a uniformly distributed surface charge density, ρ in an electrolyte free pore medium having di-electric permittivity, ε_r, along its axis at a distance y is given by well-known equation

$$\phi(y) = \frac{\rho}{2\varepsilon_0\varepsilon_r}\left[\sqrt{a^2+y^2} - y\right] \qquad \text{[B2]}$$

where ε_0 is vacuum permittivity. The corresponding electric field generated by the disc at distance, y

$$E(y) = -\frac{d\phi}{dy} = \frac{\rho}{2\varepsilon_0\varepsilon_r}\left[1 - \frac{y}{\sqrt{a^2+y^2}}\right] \qquad \text{[B3]}$$

Now, consider the elemental charge *dq* of length *ds*, thickness *t*, and surface area *dA* on the edge of another vertical disc as shown in Fig. B1. The force experienced by the elemental charge, *dq* due the electric field generated by horizontal disc is

$dF = E(y)dq = \frac{\rho}{2\varepsilon_0\varepsilon_r}\left[1 - \frac{y}{\sqrt{a^2+y^2}}\right]\rho t ds$; where $dq = \rho_e dA = \rho_e t ds$ and ρ_e is edge charge density; The total attractive coulomb force, F_{ef} experienced by the charges along the edge of the vertical disc is

$$F_{ef} = \int dF = \frac{\rho}{2\varepsilon_0\varepsilon_r}\left[1 - \frac{y}{\sqrt{a^2+y^2}}\right]\rho_e t\int_0^{2\pi a} ds = \frac{\pi a t \rho\rho_e}{\varepsilon_0\varepsilon_r}\left[1 - \frac{y}{\sqrt{a^2+y^2}}\right] \qquad \text{[B4]}$$

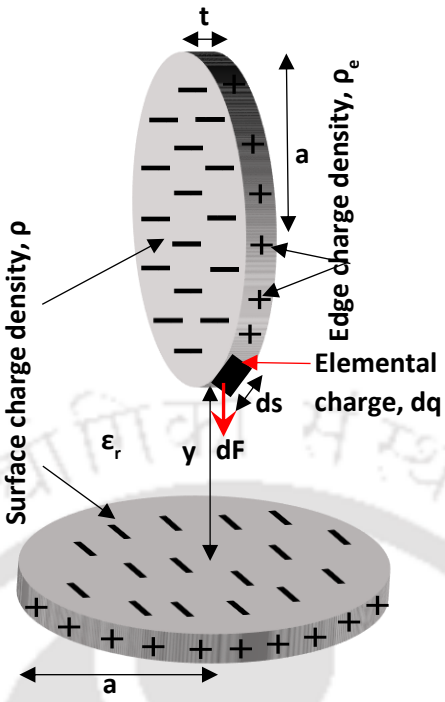

Fig. B1. Estimation of attractive coulomb force in case of edge-to-face interaction between the kaolinite particles (pH < IEP_{edge}).